Applications Of Two-Dimensional Layered Materials in Eradication of Multi-Drug Resistant

Organisms and Natural Enzyme Mimicking Catalysis

by

Sanchari Saha

A Dissertation Presented in Partial Fulfillment
of the Requirements for the Degree
Doctor of Philosophy

Approved June 2021 by the
Graduate Supervisory Committee:

Alexander Green, Chair
Qing Hua Wang
Nicholas Stephanopoulos

ARIZONA STATE UNIVERSITY

August 2021

ABSTRACT

The severe resistance of bacteria and fungi towards common antibiotic drugs has led to the increasing prevalence of infections due to multi-drug resistant microbes, which is one of the most serious issue faced by the healthcare system worldwide. These drug-resistant bacteria have led to significant health problems and fatalities whereas drug-resistance fungi possess significant threat to humans, livestock, and crops globally. Furthermore, this drug resistance leads to the formation of biofilms, which are thick layers of microbes embedded in extracellular polymeric matrix. They adhere to both living and nonliving surfaces, making it harder to contain or eradicate these pathogens. The conventional strategy for combating these pathogenic bacteria and fungi has its limitations and new antimicrobials are constantly required to fight the growing resistant mechanisms. Hence, there is an immediate need for an alternative strategy to combat these drug-resistant isolates.

Herein, this dissertation reports the development of novel potent antimicrobial agent based on tow-dimensional layered nanomaterials dispersed in biocompatible oligonucleotide, biomolecules, polymers, and surfactant. These synthesized novel nanomaterials successfully eliminated multidrug-resistant microbes with synergistic efforts of physical interaction, membrane disintegration, depolarization and intrinsic antimicrobial properties leading to cell death. These systems were highly effective against a broad spectrum of microbes including drug-resistant gram-positive, gram-negative bacteria and fungal isolates. Furthermore, they were successful in eradication of mature biofilm as well as inhibition of biofilms on several medically relevant surfaces. Overall, these novel systems have exceptional potential as a promising alternative solution in solving current problems faced by the healthcare system sue to these pathogenic microbes.

For the next direction, a different avenue was explored where a novel system based on two-dimensional layered material with antibacterial properties was analyzed for enzyme-like activity. These nanomaterials with intrinsic enzyme-like properties are commonly known as nanozymes have many advantages over natural enzymes such as low cost, scalability and high stability. A class of ultra-high temperature ceramics known as metal diborides were synthesized in biocompatible surfactant followed by analysis of their enzymatic activity and antibacterial activity.

Results demonstrate this novel system possesses a unique combination of exceptionally high affinity towards hydrogen peroxide and high activity per cost. Furthermore, it is extremely potent against pathogenic bacteria and has a high degree of biocompatibility. Hence, this new system opens the door for future possible applications in biomedicine with further research.

ACKNOWLEDGMENTS

TABLE OF CONTENTS

LIST OF FIGURES

CHAPTER 1

INTRODUCTION

1.1 Growing resistance and of impact of multidrug-resistant organisms

Multidrug-resistant organisms (MDROs) are organisms like bacteria and fungi that develop the ability to circumvent drugs designed to kill them. Despite advances in technology and continuing research studies, infectious diseases continue to be one of the most critical global health challenges of this era.[1] These rising resistance levels have been attributed to the overuse and misuse of antibiotics.[2] According to the Centers for Disease Control and Prevention (CDC) infections caused by these drug resistant pathogens are difficult, and sometimes impossible to treat. The CDC and the World Health Organization (WHO) assert that the human race has entered a "post-antibiotic era" due to the growing resistance.[3] A survey by the IDSA Emergence Infections Network discovered more than 60% of patients had had a multidrug-resistant (MDR) bacterial infection in the previous year.[4] It has been reported that methicillin resistant staphylococcus aureus (MRSA) is responsible for more deaths in the U.S. each year than Parkinson's disease, emphysema, and homicide combined.[2, 5] The global emergence of strains like vancomycin-resistant enterococci (VRE), *Streptococcus pneumoniae* and *Mycobacterium tuberculosis*, among others have the potential to cause future epidemics.[6-7] Gram-negative pathogens are particularly dangerous, in some cases gaining resistance to almost all antibiotic drug options available.[5-7] For example, the emergence of MDR gram-negative bacilli has affected practices in every field of medicine.[7] Among all MDR gram-negative infections occurring in health care systems, *Klebsiella pneumoniae* (*K. pneumoniae*) , *Pseudomonas aeruginosa (P. aeruginosa),* and *Acinetobacter baumannii (A. baumannii) are the leading cause for them*.[7] Resistance against drugs specifically leads to biofilm formation. Biofilms are communities of aggregated bacterial cells which form over time, embedded in a self-produced extracellular polymeric matrix and prone to spreading across multiple surfaces.[8] Biofilms target weakened immune systems and are implicated in many chronic bacterial and fungal infections.[9] Apart from MDR bacteria and biofilms, invasive fungal diseases pose imminent threat to humans.[10] The most common fungal infections arise from

Candida, *Aspergillus*, *Pneumocystis*, and *Cryptococcus* spp. It has been estimated that these fungal species can cause around 1.4 million fatalities annually around the globe.[11] Compared to other microbial pathogens *Candida* spp. are ranked fourth among for causing invasive bloodstream infections, after other common bacterial pathogens.[12] Infections caused by *Aspergillus* spp. are the most common in transplant patients and immunocompromised individuals.[13] About 30–50% of invasive aspergillosis patients still die, and the mortality from candidemia also remains high at ~50%.[14]

Hence, these above mentioned isolates of both bacteria and fungi place a substantial negative impact on healthcare system and financial burden worldwide.[2, 6-7] On an average each year, health care systems spend around $10,000 to $40,000 to treat each patient infected by MDR infections. A recent report estimates that cumulative loss of US$ 2.9 trillion by 2050 can be expected due to MDR pathogens and subsequent management.[15] Individuals most affected by these MDR bacteria commonly known as nosocomial infections are clinical patients after surgery, premature infants, cancer patients and transplantation patients.[15-16] Increasing drug resistance potentially threatens the success of surgical procedures and targets immune-compromised individuals. It is estimated that around 38.7-50.9% infections are on post-surgical patients and 26.8% of patients suffer from drug-resistant chemotherapy which are resistant to conventional drugs.[15] With such fast-growing drug resistance, the discovery and development of new antimicrobials is costly and requires time-consuming effort.[1] Additionally, for these MDR infections, high doses of antimicrobials are necessary which is toxic.[17] Hence, there is a need for development of alternative strategies.

1.2 Nanomaterials in combatting MDR infections

Nanomaterials (NMs) can be applied as a potential alternative strategy to manage infections caused by MDR pathogens.[18-20] NMs can overcome the limitations of conventional antimicrobial drugs by circumventing the common resistance mechanisms of MRDOs like enzyme

inactivation, reduction of drug permeability, target modification and increased elimination through efflux pumps (**Figure 2.1**).[21] This is due to their unique physical and chemical properties like high surface-volume ratio increasing interaction area targeting organisms.[17, 22-23] NMs also have the ability to penetrate organisms by physical contact and destabilizing membrane potential or hindering molecular pathways by generating reactive oxygen species (**Figure 2.1**).[24-26] Hence, NMs have the potential to reduce or eliminate the evolution of MDROs.[27] Moreover, NMs supplemented with antimicrobial agents show enhanced activity in terms of antimicrobial efficacy and biocompatibility due to synergistic effects.[21, 23] NMs are therefore regarded as next-generation antibiotics.[17]
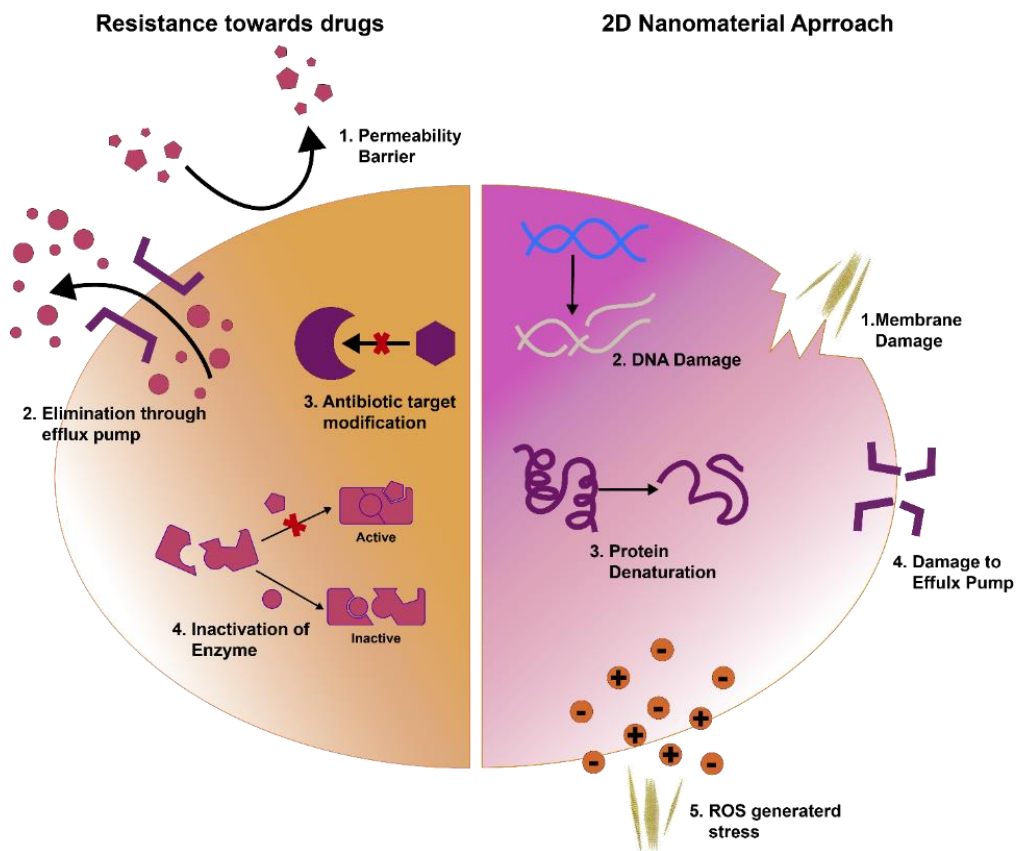
Figure 1.1 Mechanism of antibacterial resistance as compared to nanomaterials.[17]

1.3 Nanomaterials

Nanomaterials (NMs) can be broadly classified into three categories: (1) zero-dimensional (0D) commonly known as nanoparticles (NPs), (2) one-dimensional (1D) like nanotubes and

nanofibers and finally (3) Two-dimensional (2D) resembling large but thin sheets of layered materials (**Figure 2.1**).[28-29] One of the most fundamental advantages of NMs is their dimensionality, which generates totally different properties compared to their bulk form.[29-30] Based on the scope of my research, we will focus on 2D NMs and their properties. Graphene was the first 2D materials discovered in 2004 with predicted properties of a one-atom thick layer of sp^2 carbons arranged in a hexagonal lattice.[31] In light of the unique and tunable properties of graphene, studies have been extended to other layered materials which can be classified into two categories: (1) van der Waals layered materials with weak van der Waals forces holding the planes together and (2) non van der Waals layered materials containing covalent out-of-plane bonds.[32-35]
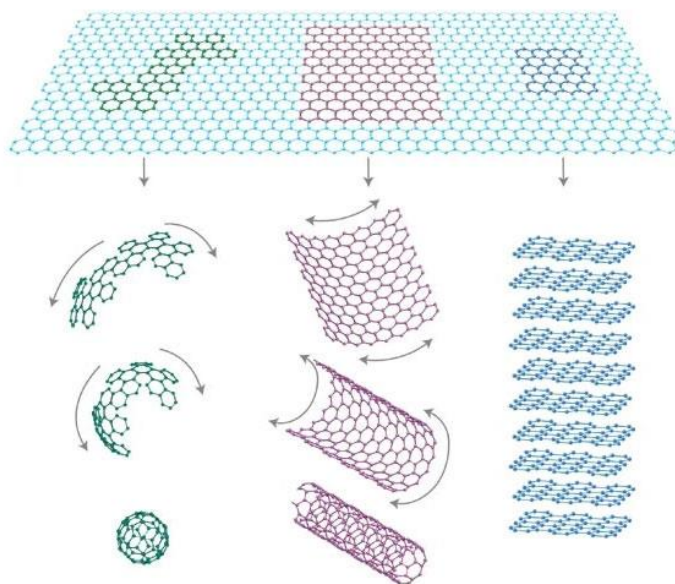
Figure 1.2 Graphene is a carbon containing nanomaterial possessing all 3 dimensionalities. It can be wrapped up into 0D buckyballs (right), rolled into 1D nanotubes (middle) or stacked into 2D graphite nanosheets (left).[36]

1.3.1 Two-dimensional van der Waals material

Structurally 2D van der Waals NMs have single layers of neutral charge which are stacked together by weak van der Waals forces.[37-38] These layered NMs have strong-in-plane covalent bonds and weak out-of-plane van der Waals forces.[39] Owing to their unique structure they can be

4

separated into atomically thin layers with stable structures.[39-40] Graphene is one of the most interesting 2D materials owing to its atomic structure and high carrier mobility.[41] Owing to the success of graphene, 2D nanostructures are being increasingly researched due to their superior physical, chemical, catalytic and electrical properties in their layered form compared with their bulk precursors and their potential applications in various fields, ranging from electronics to medicine.[38, 40, 42] Researchers have synthesized several 2D layered materials with unique properties like transition metal dichalcogenides (TMDs),[37, 43-44] black phosphorus (BP),[45-46] carbon nitride (C_3N_4),[47] metal oxides,[48] hexagonal boron nitride (h-BN),[49] 2D metal organic frameworks (MOFs)[50] and MXenes[51] (**Figure 1.3**). Unlike graphene whose zero bandgap possess a lot of limitations, these new 2d nanomaterials show enhanced properties and can behave like insulators (e.g. *h*-BN) or semiconductors (e.g. TMDs).[30] By exploiting the electrical and surface properties of these layers, novel tunable NMs have been produced which are atomically thin to few layers.[40]
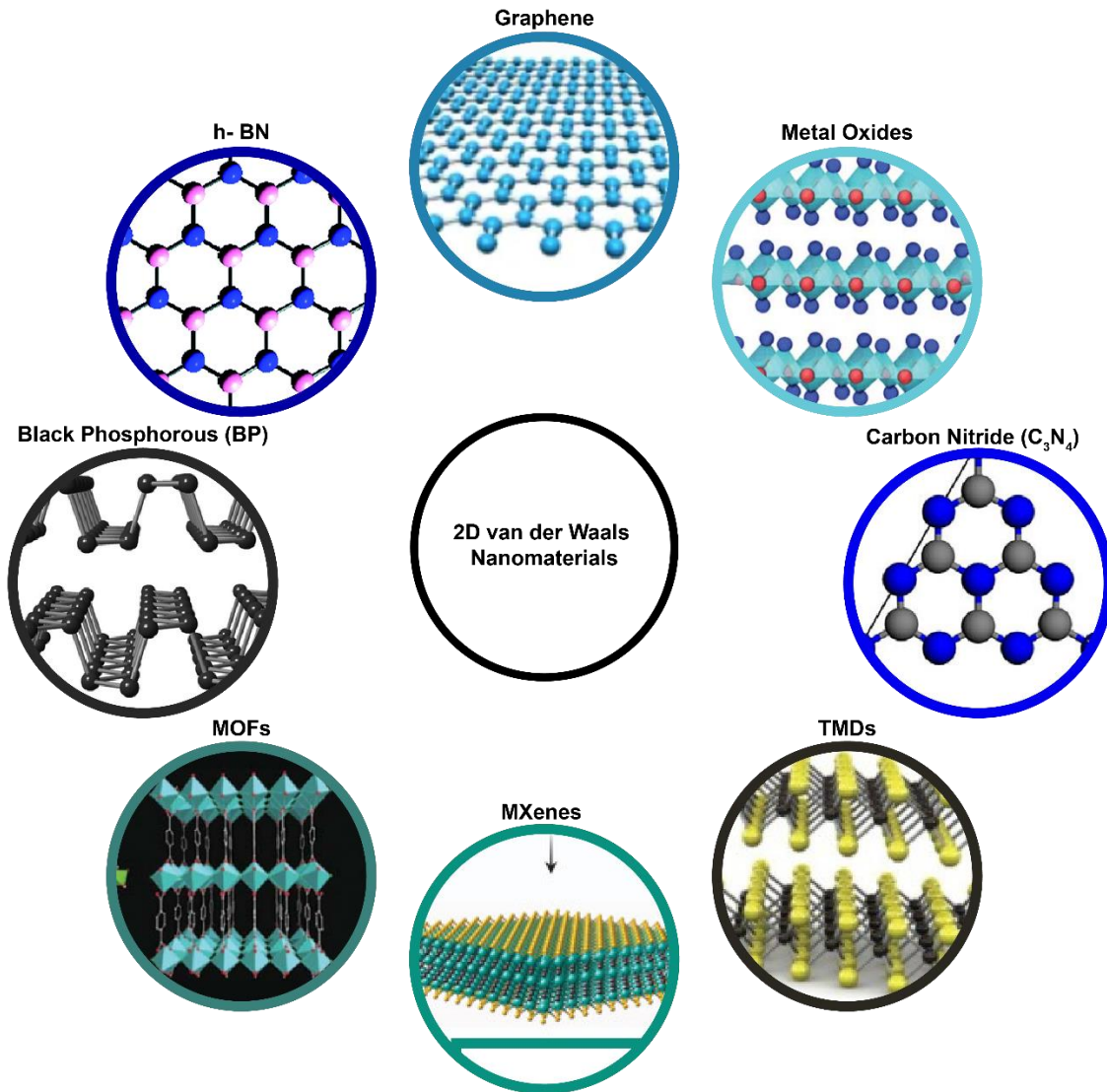
Figure 1.3. Two-dimensional (2D) layered van der Waals materials.[52-59]

1.3.2   Non-van der Waals material

Along with the rise of 2D van der Waals materials, many 2D inorganic materials have been synthesized and studied for novel applications.[35] Researchers have found metal oxides as one of the most versatile 2D materials because of their bandgap ranging from insulators to semiconductors.[60] This led to the discovery of iron oxides (hematene) and their derivatives as a non van der Waals material with diverse applications that includes sensing,[61] magnetic storage media[62] and specifically catalysis (**Figure 1.4A**).[63] Recently another class of ceramic materials

known as metal diborides with crystal structures consisting of alternative boron and metal planes held together with ionic/covalent bond have been researched (**Figure 1.4B**).[64-66] The layered structure of metal diborides with their graphene-like boron sheets have generated stable dispersions of 2D ultrathin nanosheets in several solvents using ultrasonication-assisted exfoliation (**Figure 1.4C**).[66] Results showed these metal diborides are flexible, scalable and tunable layered materials highly potent for further analysis and applications in biomedical fields.
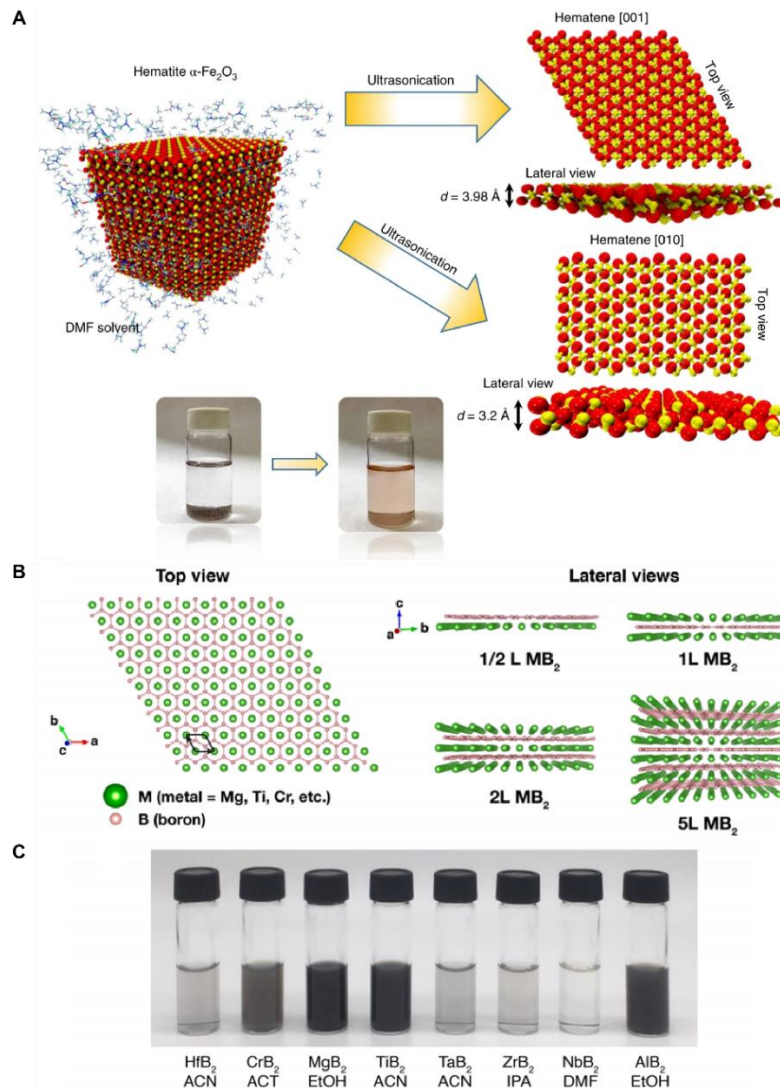
Figure 1.4. Synthesis and characterization of non van der Waals materials. (A) Schematic of the exfoliation of bulk hematite a non van der Waals material in DMF to produce hematene.

Showing two different crystallographic planes. The optical images of bulk hematite (left) and exfoliated in DMF (right).[35] (B) Structure of non van der Waals metal diborides in top view and lateral views at thicknesses of layers. One unit cell with a and b axes is outlined in the top view.[66] (C) Optical images of metal diboride dispersions into layers in various organic solvents.[66]

1.4 TMCs and their synthesis

Transition metal dichalcogenides (TMDs), with the formula MX_2 (where M = transition metal and X = chalcogen), have unique chemical, physical and electronic properties, ranging from insulators to semiconductors (e.g., Ti, Hf, Zr, Mo, and W dichalcogenides) to metallic or semi-metallic (V, Nb, and Ta dichalcogenides).[67] These properties arise from the progressive filling of the nonbonding d bands by the transition metal electrons.[67] Owing to their out-of-plane weak van der Waals bonds, synthesis of these 2D NMs is straightforward. The fabrication methods can be classified into two categories: (1) top-down and (2) bottom-up (**Figure 1.5**).[68]

The bottom-up approaches' biggest advantage is in producing large scale 2D nanosheets for various applications.[68] Among all the methods, chemical vapor deposition (CVD) is one of the most efficient ways of synthesizing uniform nanosheets with controlled thicknesses (**Figure 1.5B**).[69-71] Although this requires extremely high temperature due to high melting point of individual elements of these materials as well as costly equipment.[61] Top down approaches are affordable, scalable and tunable methods to obtain single- to few-layered materials (**Figure 1.5C-E**).[38, 64, 67-68] They consist of mechanical exfoliation,[72] liquid-phase exfoliation[65] or ion intercalation.[73] Liquid-phase exfoliation method is one of the most common top-down methods and produces large-scale single- to few-layered nanosheets, which resulted into major advances in the field.[64, 68, 73] Although with liquid exfoliation it is hard to control the number of layers and surface area of nanosheets, the method is extremely tunable and can enable functionalization with various solvents,[74] surfactants[75] and polymers.[26] We have successfully synthesized novel 2D layered materials for various biomedical applications.
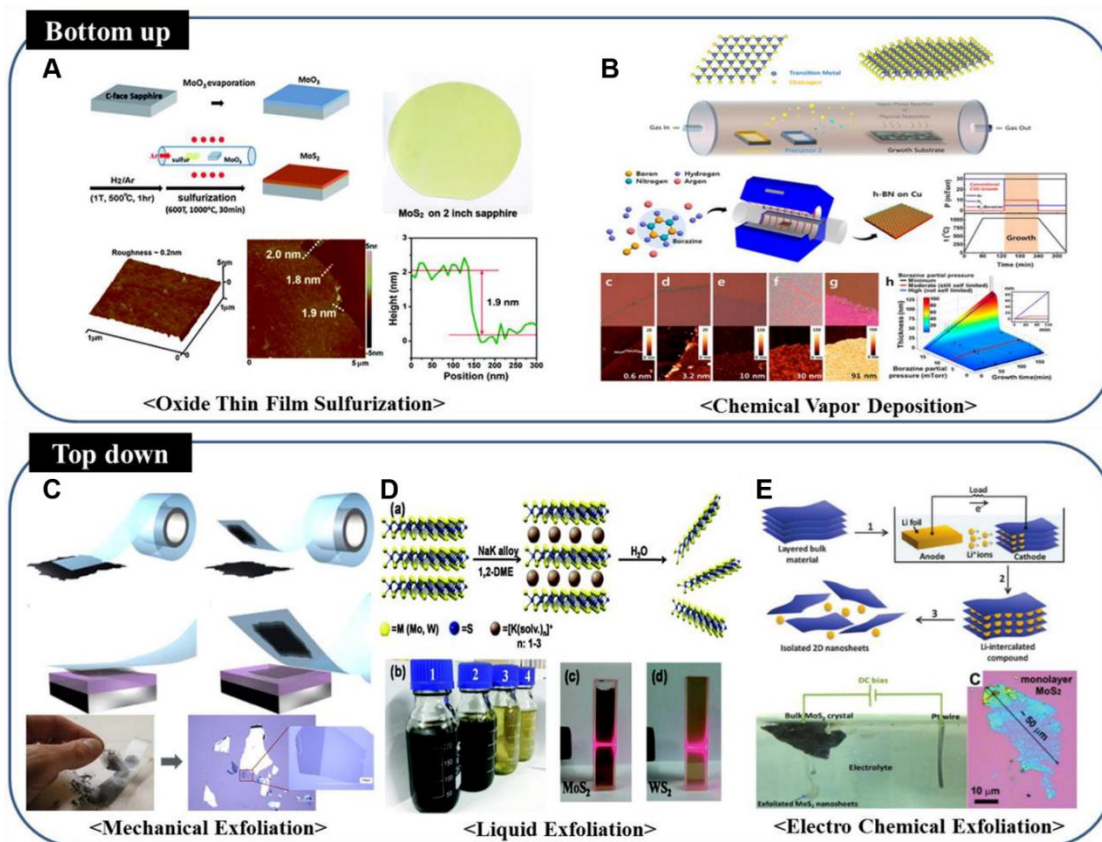
Figure 1.5. TMCs and their synthesis methods. (A, B) Bottom-up approaches to produce large-area high quality 2D nanosheets (A) Oxide thin film sulfurization and (B) Chemical vapor deposition. (C-E) top-down approaches of scalable synthesis of NMs. (C) mechanical exfoliation. (D) Liquid phase exfoliation. (E) Electrochemical exfoliation/ion intercalation.[68]

1.5 Biomedical applications of TMCs

Their ease of synthesis, unique properties and flexible surface modification abilities have made TMDs one of the most versatile NMs with great potential in the biomedical field.[69] TMDs have strong light absorption ability in the near-infrared region making them a very good photothermal agent as well as cancer therapy *in vivo*.[76-77] Due to their high surface-to volume ratio, large numbers of possible anchor sites, and high loading capacity through physical adsorption or chemical functionalization along with its high stability, TMDs are excellent candidates for drug delivery.[78-80]

Owing to its enhanced mechanical strength they are promising bone regeneration scaffolds used for tissue engineering.[81] The unique chemical composition and direct band gap of layered TMDs makes them a highly potent bioimaging agent.[82-83] Furthermore, tunable properties of TMDs like mechanical,[69] catalytic[84] and antimicrobial properties[26, 85-86] along with high biocompatibility make them an attractive alternative for medical device fabrication. Hence with detailed research and specific modifications, TMDs are promising NMs for vast range of biomedical applications (**Figure 1.6**).[69] In this dissertation we have synthesized and characterized novel biocompatible 2D TMD molybdenum diselenide ($MoSe_2$) along with detailed study of them as a broad-spectrum antimicrobial agent against MDR bacteria and fungi.
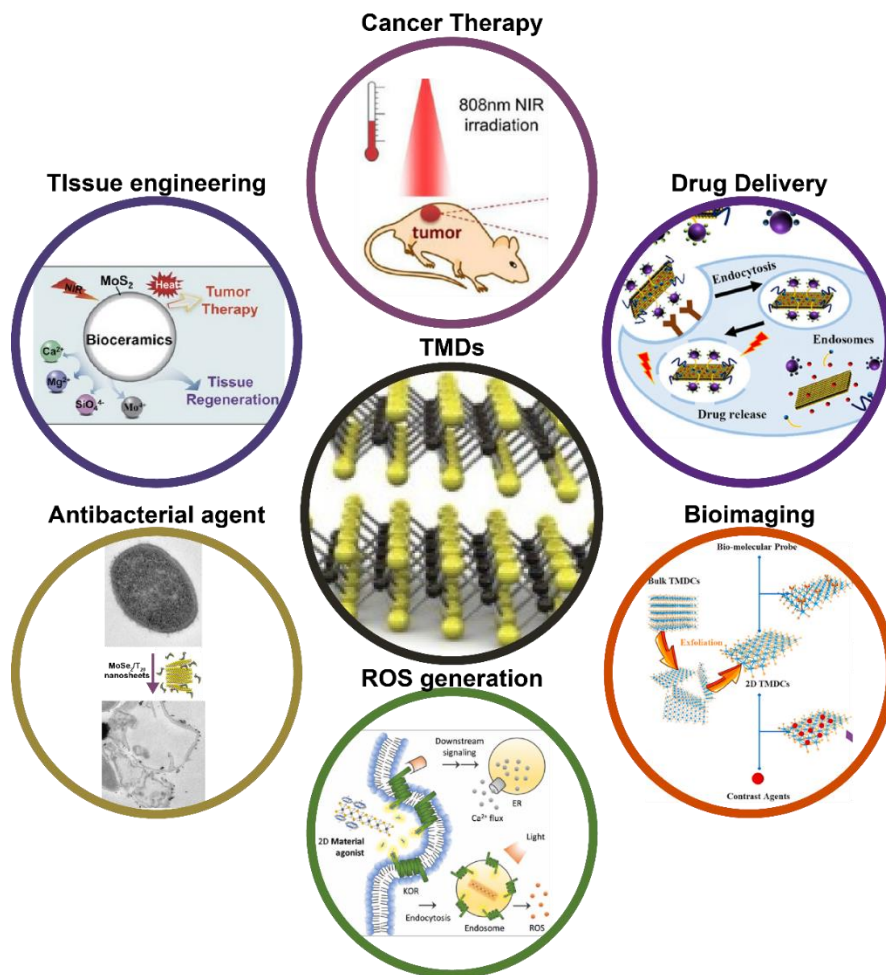
Figure 1.6. Schematic representation of TMCs in biomedical applications.[69, 76, 79, 81, 85-87]

1.6 Nanozymes

Nanozymes are nanomaterials with enzyme-like properties have attracted increasing interest over the past decade because of their ability to overcome the limitations of natural enzymes such as low stability, high cost, and difficult storage and can have a lot of potential applications (**Figure 1.7A**).[87] Since the discovery of ferromagnetic nanoparticles with intrinsic horseradish peroxidase-like activity in 2007, a large number of NMs have been reported which show enzyme mimetic activity (**Figure 1.7B**).[88] For example, iron oxide magnetic nanoparticles (Fe_3O_4 NPs) show pH-dependent peroxidase-like and catalase-like activities; Prussian blue NPs (PB NPs) possess multi-enzymatic activity;[89] and manganese oxide (Mn_3O_4) NPs can mimic all three cellular antioxidant enzymes including superoxide dismutase, catalase, and glutathione peroxidase among them. Molybdenum (Mo) based nanomaterials have also been reported with multi-enzymatic activity (**Figure 1.7C**).[84, 90-91] Other 2D TMDs have also shown peroxidase like activity like $MoSe_2$.[92-94] By taking advantage of the unique physiochemical properties of NMs and further detailed research, a broad range of applications from detection, biosensing to substituting traditional enzymes in living cells can be achieved thereby bridging nanotechnology and biology.[95] In this dissertation we have introduced and explored the enzymatic activity of the non van der Waals layered material hafnium diboride (HfB_2).
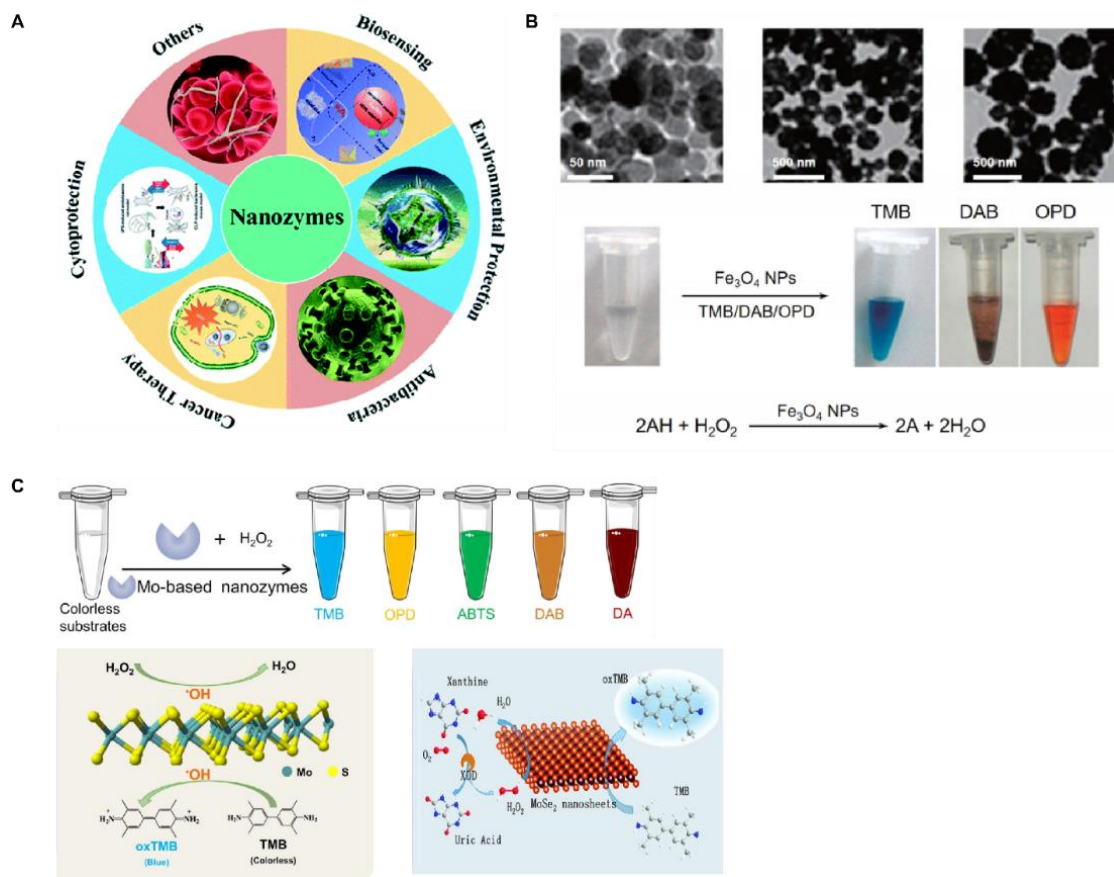
Figure 1.7. Nanozymes. (A) Recent applications of nanozymes in biosensing.[96] (B) TEM images of nanozyme Fe_3O_4 MNPs of different sizes (top). Catalysis by Fe_3O_4 MNPs of various peroxidase substrates in the presence of H_2O_2 (middle). Scheme of the mechanism of catalysis by Fe_3O_4 MNPs where AH is the substrate (bottom).[88] (C) Peroxidase-like activity of TMC molybdenum (Mo)-based nanozymes with various chromogenic substrates (top). The catalytic mechanisms of Mo-based nanozymes: Fenton-like reactions (left) and electron transfer reactions (right).[84]

1.7 Dissertation overview

This dissertation focuses on the engineering of 2D layered nanomaterials by taking advantage of their versatile physiochemical properties followed by eradication of multidrug resistant bacteria and fungi as well as the enzyme mimicking activity of these innovative materials. In Chapter 2 we screen a range of TMDs to test their antibacterial efficacy when encapsulated by single-stranded DNA (ssDNA), inspired by our previous work.[86] Then we developed a novel

nanomaterial consisting of MoSe$_2$ nanosheets, the cationic polymer poly-L-lysine (PLL) and the nonionic block co-polymer Pluronic F77. This showed enhanced antibacterial activity through the synergistic effect of sharp 2D nanosheets of MoSe$_2$ and cationic charge of PLL along with the stabilizing power of Pluronic F77 in biological media. It successfully eradicated MoSe$_2$/PLL/F77 against both gram-positive and gram-negative bacteria showing a broad-spectrum NM which is target specific due to its positive charge and enhanced biocompatibility and high efficiency at a very low concentration. In Chapter 3 we demonstrated the ability of MoSe$_2$/PLL/F77 to eradicate and inhibit biofilms altogether. Since, biofilms have an extracellular matrix, it is much more difficult to eliminate them or prevent them from spreading. MoSe$_2$/PLL/F77 not only successfully killed them, but they also prevented the growth and spreading of biofilms on various medically relevant surfaces when coated with MoSe$_2$/PLL/F77, getting us one step closer to its potential application. In Chapter 4 we tested the antifungal efficacy of MoSe$_2$ wrapped in chitosan (CS), a known naturally occurring antifungal polymer. With the combination of MoSe$_2$/CS we observed a highly biocompatible material which was successful in 100% elimination of both yeast-like fungi as well as filamentous fungi which are lot harder to kill. We also were able to eradicate a new class of fungal isolates designated by the CDC as drug-resistant, *Candida auris*. These strains are responsible for serious invasive infections and multiple hospital outbreaks globally.[97] Additionally, detailed analysis of the antifungal mechanism of MoSe$_2$/CS against fungi was done for a better understanding of how MoSe$_2$ works. In Chapter 5 we synthesized and analyzed metal diborides, a new class of non van der Waals material for biomedical application. These high-temperature ceramic materials are structurally close to graphene and TMDs. Previously in our lab a detailed study of structural properties, mechanical properties and scalable synthesis of metal diborides was performed.[64-66] Hence, we further explored the possibility of using them in biomedical applications owing to its biocompatibility. We observed among all the metal diborides, HfB$_2$ showed excellent peroxidase-like activity with extremely high affinity for hydrogen peroxide. Furthermore, it was highly potent as an antibacterial agent against both gram-negative *E. coli* and MDR gram-positive *S. aureus.* Finally, Chapter 6 concludes this dissertation and provides possible future directions which can bridge

nanotechnology with biological applications, thereby solving a lot of current healthcare issues with

promising alternative solutions.

1.8 References

1.   Huh, A. J.; Kwon, Y. J., "Nanoantibiotics": A new paradigm for treating infectious diseases using nanomaterials in the antibiotics resistant era. *Journal of Controlled Release* **2011,** *156* (2), 128-145.

2.   Ventola, C. L., The antibiotic resistance crisis: part 1: causes and threats. *P T* **2015,** *40* (4), 277-283.

3.   Michael, C. A.; Dominey-Howes, D.; Labbate, M., The antimicrobial resistance crisis: causes, consequences, and management. *Frontiers in public health* **2014,** *2*, 145-145.

4.   Spellberg, B.; Gilbert, D. N., The Future of Antibiotics and Resistance: A Tribute to a Career of Leadership by John Bartlett. *Clinical Infectious Diseases* **2014,** *59* (suppl_2), S71-S75.

5.   Gross, M., Antibiotics in crisis. *Current biology : CB* **2013,** *23* (24), R1063-5.

6.   Rossolini, G. M.; Arena, F.; Pecile, P.; Pollini, S., Update on the antibiotic resistance crisis. *Current Opinion in Pharmacology* **2014,** *18*, 56-60.

7.   Zhabiz, G.; Omar, B.; Donald Gene, P., Bacteriophage therapy: a potential solution for the antibiotic resistance crisis. *The Journal of Infection in Developing Countries* **2014,** *8* (02).

8.   Cepas, V.; López, Y.; Muñoz, E.; Rolo, D.; Ardanuy, C.; Martí, S.; Xercavins, M.; Horcajada, J. P.; Bosch, J.; Soto, S. M., Relationship Between Biofilm Formation and Antimicrobial Resistance in Gram-Negative Bacteria. *Microbial Drug Resistance* **2018,** *25* (1), 72-79.

9.   Hathroubi, S.; Mekni, M. A.; Domenico, P.; Nguyen, D.; Jacques, M., Biofilms: Microbial Shelters Against Antibiotics. *Microbial Drug Resistance* **2016,** *23* (2), 147-156.

10.   Sanglard, D., Emerging Threats in Antifungal-Resistant Fungal Pathogens. *Frontiers in Medicine* **2016,** *3* (11).

11.   Brown, G. D.; Denning, D. W.; Gow, N. A. R.; Levitz, S. M.; Netea, M. G.; White, T. C., Hidden Killers: Human Fungal Infections. *Science Translational Medicine* **2012,** *4* (165), 165rv13-165rv13.

12.   Wisplinghoff, H.; Bischoff, T.; Tallent, S. M.; Seifert, H.; Wenzel, R. P.; Edmond, M. B., Nosocomial bloodstream infections in US hospitals: analysis of 24,179 cases from a prospective nationwide surveillance study. *Clinical infectious diseases : an official publication of the Infectious Diseases Society of America* **2004,** *39* (3), 309-17.

13.   Kontoyiannis, D. P.; Marr, K. A.; Park, B. J.; Alexander, B. D.; Anaissie, E. J.; Walsh, T. J.; Ito, J.; Andes, D. R.; Baddley, J. W.; Brown, J. M.; Brumble, L. M.; Freifeld, A. G.; Hadley, S.; Herwaldt, L. A.; Kauffman, C. A.; Knapp, K.; Lyon, G. M.; Morrison, V. A.; Papanicolaou, G.; Patterson, T. F.; Perl, T. M.; Schuster, M. G.; Walker, R.; Wannemuehler, K. A.; Wingard, J. R.; Chiller, T. M.; Pappas, P. G., Prospective surveillance for invasive fungal infections in hematopoietic stem cell transplant recipients, 2001-2006: overview of the Transplant-Associated Infection Surveillance Network (TRANSNET) Database. *Clinical infectious diseases : an official publication of the Infectious Diseases Society of America* **2010,** *50* (8), 1091-100.

14. Denning, D. W.; Bromley, M. J., How to bolster the antifungal pipeline. *Science* **2015,** *347* (6229), 1414.

15. Friedman, N. D.; Temkin, E.; Carmeli, Y., The negative impact of antibiotic resistance. *Clinical microbiology and infection : the official publication of the European Society of Clinical Microbiology and Infectious Diseases* **2016,** *22* (5), 416-22.

16. Thabit, A. K.; Crandon, J. L.; Nicolau, D. P., Antimicrobial resistance: impact on clinical and economic outcomes and the need for new antimicrobials. *Expert opinion on pharmacotherapy* **2015,** *16* (2), 159-77.

17. Lee, N.-Y.; Ko, W.-C.; Hsueh, P.-R., Nanoparticles in the Treatment of Infections Caused by Multidrug-Resistant Organisms. *Front Pharmacol* **2019,** *10*, 1153-1153.

18. Muzammil, S.; Hayat, S.; Fakhar, E. A. M.; Aslam, B.; Siddique, M. H.; Nisar, M. A.; Saqalein, M.; Atif, M.; Sarwar, A.; Khurshid, A.; Amin, N.; Wang, Z., Nanoantibiotics: Future nanotechnologies to combat antibiotic resistance. *Frontiers in bioscience (Elite edition)* **2018,** *10*, 352-374.

19. Natan, M.; Banin, E., From Nano to Micro: using nanotechnology to combat microorganisms and their multidrug resistance. *FEMS microbiology reviews* **2017,** *41* (3), 302-322.

20. Singh, R.; Smitha, M. S.; Singh, S. P., The role of nanotechnology in combating multi-drug resistant bacteria. *Journal of nanoscience and nanotechnology* **2014,** *14* (7), 4745-56.

21. Baptista, P. V.; McCusker, M. P.; Carvalho, A.; Ferreira, D. A.; Mohan, N. M.; Martins, M.; Fernandes, A. R., Nano-Strategies to Fight Multidrug Resistant Bacteria-"A Battle of the Titans". *Front Microbiol* **2018,** *9*, 1441-1441.

22. Beyth, N.; Houri-Haddad, Y.; Domb, A.; Khan, W.; Hazan, R., Alternative Antimicrobial Approach: Nano-Antimicrobial Materials. *Evidence-Based Complementary and Alternative Medicine* **2015,** *2015*, 246012.

23. Pelgrift, R. Y.; Friedman, A. J., Nanotechnology as a therapeutic tool to combat microbial resistance. *Adv Drug Deliv Rev* **2013,** *65* (13-14), 1803-1815.

24. Hemeg, H. A., Nanomaterials for alternative antibacterial therapy. *International journal of nanomedicine* **2017,** *12*, 8211-8225.

25. Rai, M. K.; Deshmukh, S. D.; Ingle, A. P.; Gade, A. K., Silver nanoparticles: the powerful nanoweapon against multidrug-resistant bacteria. *Journal of applied microbiology* **2012,** *112* (5), 841-52.

26. Roy, S.; Mondal, A.; Yadav, V.; Sarkar, A.; Banerjee, R.; Sanpui, P.; Jaiswal, A., Mechanistic Insight into the Antibacterial Activity of Chitosan Exfoliated MoS2 Nanosheets: Membrane Damage, Metabolic Inactivation, and Oxidative Stress. *ACS Applied Bio Materials* **2019,** *2* (7), 2738-2755.

27. Slavin, Y. N.; Asnis, J.; Häfeli, U. O.; Bach, H., Metal nanoparticles: understanding the mechanisms behind antibacterial activity. *Journal of Nanobiotechnology* **2017,** *15* (1), 65.

28. Guo, H.-W.; Hu, Z.; Liu, Z.-B.; Tian, J.-G., Stacking of 2D Materials. *Advanced Functional Materials* **2021,** *31* (4), 2007810.

29.   Mas-Ballesté, R.; Gómez-Navarro, C.; Gómez-Herrero, J.; Zamora, F., 2D materials: to graphene and beyond. *Nanoscale* **2011,** *3* (1), 20-30.

30.   Gupta, A.; Sakthivel, T.; Seal, S., Recent development in 2D materials beyond graphene. *Progress in Materials Science* **2015,** *73*, 44-126.

31.   Novoselov, K. S.; Geim, A. K.; Morozov, S. V.; Jiang, D.; Zhang, Y.; Dubonos, S. V.; Grigorieva, I. V.; Firsov, A. A., Electric Field Effect in Atomically Thin Carbon Films. *Science* **2004,** *306* (5696), 666.

32.   Bizeto, M. A.; Shiguihara, A. L.; Constantino, V. R. L., Layered niobate nanosheets: building blocks for advanced materials assembly. *Journal of Materials Chemistry* **2009,** *19* (17), 2512-2525.

33.   Ma, R.; Liu, Z.; Li, L.; Iyi, N.; Sasaki, T., Exfoliating layered double hydroxides in formamide: a method to obtain positively charged nanosheets. *Journal of Materials Chemistry* **2006,** *16* (39), 3809-3813.

34.   Osada, M.; Sasaki, T., Exfoliated oxide nanosheets: new solution to nanoelectronics. *Journal of Materials Chemistry* **2009,** *19* (17), 2503-2511.

35.   Puthirath Balan, A.; Radhakrishnan, S.; Woellner, C. F.; Sinha, S. K.; Deng, L.; Reyes, C. d. l.; Rao, B. M.; Paulose, M.; Neupane, R.; Apte, A.; Kochat, V.; Vajtai, R.; Harutyunyan, A. R.; Chu, C.-W.; Costin, G.; Galvao, D. S.; Martí, A. A.; van Aken, P. A.; Varghese, O. K.; Tiwary, C. S.; Malie Madom Ramaswamy Iyer, A.; Ajayan, P. M., Exfoliation of a non-van der Waals material from iron ore hematite. *Nature Nanotechnology* **2018,** *13* (7), 602-609.

36.   Geim, A. K.; Novoselov, K. S., The rise of graphene. *Nature Materials* **2007,** *6* (3), 183-191.

37.   Ambrosi, A.; Pumera, M., Exfoliation of layered materials using electrochemistry. *Chemical Society Reviews* **2018,** *47* (19), 7213-7224.

38.   Butler, S. Z.; Hollen, S. M.; Cao, L.; Cui, Y.; Gupta, J. A.; Gutiérrez, H. R.; Heinz, T. F.; Hong, S. S.; Huang, J.; Ismach, A. F.; Johnston-Halperin, E.; Kuno, M.; Plashnitsa, V. V.; Robinson, R. D.; Ruoff, R. S.; Salahuddin, S.; Shan, J.; Shi, L.; Spencer, M. G.; Terrones, M.; Windl, W.; Goldberger, J. E., Progress, Challenges, and Opportunities in Two-Dimensional Materials Beyond Graphene. *ACS Nano* **2013,** *7* (4), 2898-2926.

39.   Kang, K.; Chen, S.; Yang, E.-H., 12 - Synthesis of transition metal dichalcogenides. In *Synthesis, Modeling, and Characterization of 2D Materials, and Their Heterostructures*, Yang, E.-H.; Datta, D.; Ding, J.; Hader, G., Eds. Elsevier: 2020; pp 247-264.

40.   Ajayan, P.; Kim, P.; Banerjee, K., Two-dimensional van der Waals materials. *Physics Today* **2016,** *69*, 38-44.

41.   Geim, A. K.; MacDonald, A. H., Graphene: Exploring carbon flatland. *Physics Today* **2007,** *60* (8), 35-41.

42.   Novoselov, K. S.; Jiang, D.; Schedin, F.; Booth, T. J.; Khotkevich, V. V.; Morozov, S. V.; Geim, A. K., Two-dimensional atomic crystals. *Proceedings of the National Academy of Sciences of the United States of America* **2005,** *102* (30), 10451.

43.   Chia, X.; Eng, A. Y. S.; Ambrosi, A.; Tan, S. M.; Pumera, M., Electrochemistry of Nanostructured Layered Transition-Metal Dichalcogenides. *Chemical Reviews* **2015,** *115* (21), 11941-11966.

44.   Zhang, H.; Liu, C.-X.; Qi, X.-L.; Dai, X.; Fang, Z.; Zhang, S.-C., Topological insulators in Bi2Se3, Bi2Te3 and Sb2Te3 with a single Dirac cone on the surface. *Nature Physics* **2009,** *5* (6), 438-442.

45.   Du, H.; Lin, X.; Xu, Z.; Chu, D., Recent developments in black phosphorus transistors. *Journal of Materials Chemistry C* **2015,** *3* (34), 8760-8775.

46.   Gusmão, R.; Sofer, Z.; Pumera, M., Black Phosphorus Rediscovered: From Bulk Material to Monolayers. *Angewandte Chemie International Edition* **2017,** *56* (28), 8052-8072.

47.   Mansor, N.; Jia, J.; Miller, T.; Suter, T.; Belen Jorge, A.; Gibbs, C.; Shearing, P. R.; McMillan, P. F.; Mattevi, C.; Shaffer, M.; Brett, D. J. L., Graphitic Carbon Nitride-Graphene Hybrid Nanostructure as a Catalyst Support for Polymer Electrolyte Membrane Fuel Cells. *ECS Transactions* **2016,** *75* (14), 885-897.

48.   Osada, M.; Sasaki, T., Two-Dimensional Dielectric Nanosheets: Novel Nanoelectronics From Nanocrystal Building Blocks. *Advanced Materials* **2012,** *24* (2), 210-228.

49.   Golberg, D.; Bando, Y.; Huang, Y.; Terao, T.; Mitome, M.; Tang, C.; Zhi, C., Boron Nitride Nanotubes and Nanosheets. *ACS Nano* **2010,** *4* (6), 2979-2993.

50.   Dong, R.; Feng, X., Making large single crystals of 2D MOFs. *Nature Materials* **2021,** *20* (2), 122-123.

51.   Khazaei, M.; Mishra, A.; Venkataramanan, N. S.; Singh, A. K.; Yunoki, S., Recent advances in MXenes: From fundamentals to applications. *Current Opinion in Solid State and Materials Science* **2019,** *23* (3), 164-178.

52.   Lloyd-Hughes, J.; Jeon, T.-I., A Review of the Terahertz Conductivity of Bulk and Nano-Materials. *Journal of Infrared, Millimeter, and Terahertz Waves* **2012,** *33* (9), 871-925.

53.   Zhang, F.; Zhu, J.; Zhang, D.; Schwingenschlögl, U.; Alshareef, H. N., Two-Dimensional SnO Anodes with a Tunable Number of Atomic Layers for Sodium Ion Batteries. *Nano Letters* **2017,** *17* (2), 1302-1311.

54.   Zhu, B.; Zhang, J.; Jiang, C.; Cheng, B.; Yu, J., First principle investigation of halogen-doped monolayer g-C3N4 photocatalyst. *Applied Catalysis B: Environmental* **2017,** *207*, 27-34.

55.   He, Z.; Que, W., Molybdenum disulfide nanomaterials: Structures, properties, synthesis and recent progress on hydrogen evolution reaction. *Applied Materials Today* **2016,** *3*, 23-56.

56.   Hong, W.; Wyatt, B. C.; Nemani, S. K.; Anasori, B., Double transition-metal MXenes: Atomistic design of two-dimensional carbides and nitrides. *MRS Bulletin* **2020,** *45* (10), 850-861.

57.   Jeremias, F. Synthesis and Characterization of Metal-Organic Frameworks for Heat Transformation Applications. 2015.

58.   Du, H.; Lin, X.; Xu, Z.; Chu, D., Recent Development in Black Phosphorus Transistors. *J. Mater. Chem. C* **2015,** *3*.

59.   Wang, J.; Ma, F.; Sun, M., Graphene, hexagonal boron nitride, and their heterostructures: properties and applications. *RSC Advances* **2017,** *7* (27), 16801-16822.

60.   Kan, E.; Li, M.; Hu, S.; Xiao, C.; Xiang, H.; Deng, K., Two-Dimensional Hexagonal Transition-Metal Oxide for Spintronics. *The Journal of Physical Chemistry Letters* **2013,** *4* (7), 1120-1125.

61.   Chen, J.; Xu, L.; Li, W.; Gou, X., α-Fe2O3 Nanotubes in Gas Sensor and Lithium-Ion Battery Applications. *Advanced Materials* **2005,** *17* (5), 582-586.

62.   Zeng, H.; Li, J.; Liu, J. P.; Wang, Z. L.; Sun, S., Exchange-coupled nanocomposite magnets by nanoparticle self-assembly. *Nature* **2002,** *420* (6914), 395-398.

63.   Gao, L.; Fan, K.; Yan, X., Iron Oxide Nanozyme: A Multifunctional Enzyme Mimetic for Biomedical Applications. *Theranostics* **2017,** *7* (13), 3207-3227.

64.   Gilliam, M. S.; Yousaf, A.; Guo, Y.; Li, D. O.; Momenah, A.; Wang, Q. H.; Green, A. A., Evaluating the Exfoliation Efficiency of Quasi-2D Metal Diboride Nanosheets Using Hansen Solubility Parameters. *Langmuir* **2021,** *37* (3), 1194-1205.

65.   Guo, Y.; Gupta, A.; Gilliam, M. S.; Debnath, A.; Yousaf, A.; Saha, S.; Levin, M. D.; Green, A. A.; Singh, A. K.; Wang, Q. H., Exfoliation of boron carbide into ultrathin nanosheets. *Nanoscale* **2021,** *13* (3), 1652-1662.

66.   Yousaf, A.; Gilliam, M. S.; Chang, S. L. Y.; Augustin, M.; Guo, Y.; Tahir, F.; Wang, M.; Schwindt, A.; Chu, X. S.; Li, D. O.; Kale, S.; Debnath, A.; Liu, Y.; Green, M. D.; Santos, E. J. G.; Green, A. A.; Wang, Q. H., Exfoliation of Quasi-Two-Dimensional Nanosheets of Metal Diborides. *The Journal of Physical Chemistry C* **2021,** *125* (12), 6787-6799.

67.   Novoselov, K. S.; Mishchenko, A.; Carvalho, A.; Castro Neto, A. H., 2D materials and van der Waals heterostructures. *Science* **2016,** *353* (6298), aac9439.

68.   Han, S. A.; Sohn, A.; Kim, S.-W., Recent advanced in energy harvesting and storage applications with two-dimensional layered materials. *FlatChem* **2017,** *6*, 37-47.

69.   Anju, S.; Mohanan, P. V., Biomedical applications of transition metal dichalcogenides (TMDCs). *Synthetic Metals* **2021,** *271*, 116610.

70.   Lee, Y.-H.; Zhang, X.-Q.; Zhang, W.; Chang, M.-T.; Lin, C.-T.; Chang, K.-D.; Yu, Y.-C.; Wang, J. T.-W.; Chang, C.-S.; Li, L.-J.; Lin, T.-W., Synthesis of Large-Area MoS2 Atomic Layers with Chemical Vapor Deposition. *Advanced Materials* **2012,** *24* (17), 2320-2325.

71.   Wu, S.; Huang, C.; Aivazian, G.; Ross, J. S.; Cobden, D. H.; Xu, X., Vapor–Solid Growth of High Optical Quality MoS2 Monolayers with Near-Unity Valley Polarization. *ACS Nano* **2013,** *7* (3), 2768-2772.

72.   Huang, Y.; Pan, Y.-H.; Yang, R.; Bao, L.-H.; Meng, L.; Luo, H.-L.; Cai, Y.-Q.; Liu, G.-D.; Zhao, W.-J.; Zhou, Z.; Wu, L.-M.; Zhu, Z.-L.; Huang, M.; Liu, L.-W.; Liu, L.; Cheng, P.; Wu, K.-H.; Tian, S.-B.; Gu, C.-Z.; Shi, Y.-G.; Guo, Y.-F.; Cheng, Z. G.; Hu, J.-P.; Zhao, L.; Yang, G.-H.; Sutter, E.; Sutter, P.; Wang, Y.-L.; Ji, W.; Zhou, X.-J.; Gao, H.-J., Universal mechanical exfoliation of large-area 2D crystals. *Nature Communications* **2020,** *11* (1), 2453.

73.   Nicolosi, V.; Chhowalla, M.; Kanatzidis, M. G.; Strano, M. S.; Coleman, J. N., Liquid Exfoliation of Layered Materials. *Science* **2013,** *340* (6139), 1226419.

74.   Cunningham, G.; Lotya, M.; Cucinotta, C. S.; Sanvito, S.; Bergin, S. D.; Menzel, R.; Shaffer, M. S. P.; Coleman, J. N., Solvent Exfoliation of Transition Metal Dichalcogenides: Dispersibility of Exfoliated Nanosheets Varies Only Weakly between Compounds. *ACS Nano* **2012,** *6* (4), 3468-3480.

75.   Wang, N.; Xu, Q.; Xu, S.; Qi, Y.; Chen, M.; Li, H.; Han, B., High-efficiency exfoliation of layered materials into 2D nanosheets in switchable CO2/Surfactant/H2O system. *Scientific reports* **2015,** *5*, 16764.

76.   Yin, W.; Yan, L.; Yu, J.; Tian, G.; Zhou, L.; Zheng, X.; Zhang, X.; Yong, Y.; Li, J.; Gu, Z.; Zhao, Y., High-Throughput Synthesis of Single-Layer MoS2 Nanosheets as a Near-Infrared Photothermal-Triggered Drug Delivery for Effective Cancer Therapy. *ACS Nano* **2014,** *8* (7), 6922-6933.

77.   Qian, X.; Shen, S.; Liu, T.; Cheng, L.; Liu, Z., Two-dimensional TiS2 nanosheets for in vivo photoacoustic imaging and photothermal cancer therapy. *Nanoscale* **2015,** *7* (14), 6380-6387.

78.   Li, B. L.; Li, R.; Zou, H. L.; Ariga, K.; Li, N. B.; Leong, D. T., Engineered functionalized 2D nanoarchitectures for stimuli-responsive drug delivery. *Materials Horizons* **2020,** *7* (2), 455-469.

79.   Shi, J.; Zhang, H.; Chen, Z.; Xu, L.; Zhang, Z., A multi-functional nanoplatform for efficacy tumor theranostic applications. *Asian journal of pharmaceutical sciences* **2017,** *12* (3), 235-249.

80.   Liu, T.; Wang, C.; Gu, X.; Gong, H.; Cheng, L.; Shi, X.; Feng, L.; Sun, B.; Liu, Z., Drug Delivery with PEGylated MoS2 Nano-sheets for Combined Photothermal and Chemotherapy of Cancer. *Advanced Materials* **2014,** *26* (21), 3433-3440.

81.   Wang, X.; Li, T.; Ma, H.; Zhai, D.; Jiang, C.; Chang, J.; Wang, J.; Wu, C., A 3D-printed scaffold with MoS2 nanosheets for tumor therapy and tissue regeneration. *NPG Asia Materials* **2017,** *9* (4), e376-e376.

82.   Dou, W. T.; Kong, Y.; He, X. P.; Chen, G. R.; Zang, Y.; Li, J.; Tian, H., GPCR Activation and Endocytosis Induced by a 2D Material Agonist. *ACS Appl Mater Interfaces* **2017,** *9* (17), 14709-14715.

83.   Ma, Y. H.; Dou, W. T.; Pan, Y. F.; Dong, L. W.; Tan, Y. X.; He, X. P.; Tian, H.; Wang, H. Y., Fluorogenic 2D Peptidosheet Unravels CD47 as a Potential Biomarker for Profiling Hepatocellular Carcinoma and Cholangiocarcinoma Tissues. *Advanced materials (Deerfield Beach, Fla.)* **2017,** *29* (5).

84.   Zu, Y.; Yao, H.; Wang, Y.; Yan, L.; Gu, Z.; Chen, C.; Gao, L.; Yin, W., The age of bioinspired molybdenum-involved nanozymes: Synthesis, catalytic mechanisms, and biomedical applications. *VIEW* **2021,** *n/a* (n/a), 20200188.

85.   Zhou, X.; Sun, H.; Bai, X., Two-Dimensional Transition Metal Dichalcogenides: Synthesis, Biomedical Applications and Biosafety Evaluation. *Frontiers in Bioengineering and Biotechnology* **2020,** *8* (236).

86.   Debnath, A.; Saha, S.; Li, D. O.; Chu, X. S.; Ulissi, Z. W.; Green, A. A.; Wang, Q. H., Elimination of Multidrug-Resistant Bacteria by Transition Metal Dichalcogenides Encapsulated by Synthetic Single-Stranded DNA. *ACS Applied Materials & Interfaces* **2021,** *13* (7), 8082-8094.

87.   Meng, S.; Zhang, Y.; Wang, H.; Wang, L.; Kong, T.; Zhang, H.; Meng, S., Recent advances on TMDCs for medical diagnosis. *Biomaterials* **2021,** *269*, 120471.

88.   Gao, L.; Zhuang, J.; Nie, L.; Zhang, J.; Zhang, Y.; Gu, N.; Wang, T.; Feng, J.; Yang, D.; Perrett, S.; Yan, X., Intrinsic peroxidase-like activity of ferromagnetic nanoparticles. *Nature Nanotechnology* **2007,** *2* (9), 577-583.

89.   Feng, K.; Zhang, J.; Dong, H.; Li, Z.; Gu, N.; Ma, M.; Zhang, Y., Prussian Blue Nanoparticles Having Various Sizes and Crystallinities for Multienzyme Catalysis and Magnetic Resonance Imaging. *ACS Applied Nano Materials* **2021**.

90.   Chen, T.; Zou, H.; Wu, X.; Liu, C.; Situ, B.; Zheng, L.; Yang, G., Nanozymatic Antioxidant System Based on MoS2 Nanosheets. *ACS Applied Materials & Interfaces* **2018,** *10* (15), 12453-12462.

91.   Yu, J.; Ma, D.; Mei, L.; Gao, Q.; Yin, W.; Zhang, X.; Yan, L.; Gu, Z.; Ma, X.; Zhao, Y., Peroxidase-like activity of MoS2 nanoflakes with different modifications and their application for H2O2 and glucose detection. *Journal of Materials Chemistry B* **2018,** *6* (3), 487-498.

92.   Wu, X.; Chen, T.; Wang, J.; Yang, G., Few-layered MoSe2 nanosheets as an efficient peroxidase nanozyme for highly sensitive colorimetric detection of H2O2 and xanthine. *Journal of Materials Chemistry B* **2018,** *6* (1), 105-111.

93.   Kalantar-zadeh, K.; Ou, J. Z.; Daeneke, T.; Strano, M. S.; Pumera, M.; Gras, S. L., Two-Dimensional Transition Metal Dichalcogenides in Biosystems. *Advanced Functional Materials* **2015,** *25* (32), 5086-5099.

94.   Huang, X.-W.; Wei, J.-J.; Liu, T.; Zhang, X.-L.; Bai, S.-M.; Yang, H.-H., Silk fibroin-assisted exfoliation and functionalization of transition metal dichalcogenide nanosheets for antibacterial wound dressings. *Nanoscale* **2017,** *9* (44), 17193-17198.

95.   Liang, M.; Yan, X., Nanozymes: From New Concepts, Mechanisms, and Standards to Applications. *Accounts of Chemical Research* **2019,** *52* (8), 2190-2200.

96.   Huang, Y.; Ren, J.; Qu, X., Nanozymes: Classification, Catalytic Mechanisms, Activity Regulation, and Applications. *Chemical Reviews* **2019,** *119* (6), 4357-4412.

97.   Forsberg, K.; Woodworth, K.; Walters, M.; Berkow, E. L.; Jackson, B.; Chiller, T.; Vallabhaneni, S., Candida auris: The recent emergence of a multidrug-resistant fungal pathogen. *Medical mycology* **2019,** *57* (1), 1-12.

CHAPTER 2

Elimination of multi-drug resistant bacteria with the help of transition metal chalcogenides

2.1 Introduction

The increase in multi-drug resistant (MDR) infections have emerged as a global health hazard which make many current available antibiotics ineffective.[1] According to World Health Organization (WHO), MDR infections comprise some of the greatest threats to global health, food security, and development today, resulting into 700,000 deaths annually.[2-3] It has been reported that by the year 2050, mortality rate will be 10 million individuals per year.[2-3] Individuals most affected by these MDR bacteria are clinical patients after surgery, premature infants, cancer patients and transplantation patients.[4-5] Hence, finding an alternative to overcome this problem is an urgent necessity. Among all the species of bacteria, the Infectious Disease Society of America (IDSA) has identified six different species to be most harmful due to their resistance mechanism, emergence of new resistant species and virulence.[3] They are referred to as 'ESKAPE' pathogens where each letter represents each species namely, *Enterococcus faecium* (*E. faecium*), *Staphylococcus aureus* (*S. aureus*), *Klebsiella pneumoniae* (*K. pneumoniae*), *Acinetobacter baumannii* (*A. baumannii*), *Pseudomonas aeruginosa* (*P. aeruginosa*) and Enterobacter species.[6-7] This group consists of both gram-negative and gram-positive pathogenic species that are resistant to one or more conventional antibiotics. These ESKAPE pathogens commonly lead to fatality, especially among post-surgical patients, immunocompromised individual and infants.[8]

The growth of resistance is attributed to the overuse and misuse of the conventional antibiotics and over the past two decades they have become ineffective against a broad spectrum of bacteria.[9] Furthermore, the rise of new mutated strains every few months have made it impossible to contain and efficiently treat these infections.[10-13] Thus alternative strategies are needed to combat the rise of MDR bacteria. Researchers are exploring next-generation strategies to circumvent the resistance mechanism of bacteria unlike the approach of traditional antibiotics.[14-15] Alternative strategies include antimicrobial peptides (AMP),[14, 16] metal oxide nanomaterials[17] and nanoparticles.[18] Among these AMPs are shorter sequences of peptides which are cationic in nature

and target negatively charged bacteria cell membrane with high specificity.[19] The electrostatic interaction between positively charged AMPs and negatively charged bacteria leads to cell disruption and finally cell death.[19-20] Owing to its toxicity at higher concentration towards mammalian cells the scope of applying it as a potential antibacterial drug is limited.[19, 21-22] Furthermore lack of scalability, cost of production, stability and resistance mechanism of bacteria against them hinders their use as well.[23-24] Whereas, antibacterial agents like nanoparticles,[16] metal and metal oxides,[25] carbon-based nanomaterials (CBNs),[26] and biosurfactants[27] rely on their unique physio-chemical properties and high surface-to-volume ratio commonly known as nanoantibiotics.[28-30] These nanoantibiotics target bacteria by disruption of cell membrane, generation of oxidative stress and membrane depolarization making it far more effective against the growing resistant mechanism of these bacteria.[28-29, 31-32] While they are highly effective they have some limitations like toxicity at higher concentration and difficult synthesis methodologies.[33] Hence, we require nanotechnology-enabled antibacterial systems that are highly effective against MDR bacteria, while being simple to synthesize and biocompatible towards mammalian cells.

Recent studies have shown two-dimensional (2D) transition-metal chalcogenides (TMCs), a type of layered material have unique potential in medical applications.[34-35] TMCs have exhibited great promise in terms of antimicrobial activity due to their large surface area, generation of reactive oxygen species and high biocompatibility attributed to their properties in 2D state and hydrophobicity compared to CBNs.[35-40] It has been previously reported that polymers like oligonucleotides,[36, 38] AMPs,[41] and chitosan[40] are good dispersing agent producing 2D nanosheets of TMCs which are biocompatible making it highly suitable as antibacterial agent. Hence, we synthesized and characterized different TMCs in single stranded (ss) DNA inspired by our previous work.[38] Furthermore, we screened the antibacterial efficiency of these synthesized TMCs to identify the most efficient TMD. We observed complete eradication of bacteria by 2D TMD, molybdenum diselenide ($MoSe_2$) at a concentration of 100 µg ml^{-1} after 4 h of incubation.

To increase the efficiency and target MDR bacteria with higher specificity, we further integrated two antimicrobial components, AMPs and 2D $MoSe_2$, into a single system to synergistically combat MDR bacteria. In this chapter, we report the synthesis and characterization

of stable 2D TMC complexes of molybdenum diselenide ($MoSe_2$) encapsulated by the cationic AMP poly-L-lysine. The incorporation of PLL on nanomaterial surfaces reduces non-specific peptide interactions with mammalian cells while enhancing specific interactions with the negatively charged bacterial cell membrane. We hypothesized that the presence of cationic peptides on the surface of $MoSe_2$, a two-dimensional material with intrinsic antibacterial activity, would increase the local concentrations of the cationic peptides thereby requiring lesser concentration of the AMP making it more biocompatible. It also enables $MoSe_2$ to exhibit enhanced antibacterial efficiency at a much lower concentration as compared to $MoSe_2$/ssDNA which is negatively charged due to phosphate bonds on the backbone of DNA.[38] For further stabilization of the $MoSe_2$/PLL solution at higher salt concentration we incorporated nonionic biocompatible block copolymer Pluronic F77 to provide steric stabilization. Hence, $MoSe_2$/PLL/F77 showed high efficiency in eradicating bacteria. Hence, owing to its cationic nature it was also highly proficient against both gram-positive and gram-negative 'ESKAPE' strains, at a lower minimum bactericidal concentration (MBC) of 50 µg ml^{-1}. Furthermore, it was highly biocompatible towards both mammalian cells and red blood cells. $MoSe_2$/PLL/F77 also inhibited any significant development of resistance towards gram-positive and gram-negative bacteria after 20 serial passages as compared to known clinical antibiotics. Additionally, with the help of transmission electron microscopy (TEM) and scanning electron microscopy (SEM) we evaluated the antibacterial mechanism of $MoSe_2$/PLL/F77 demonstrating multimodal antibacterial mechanism which includes electrostatic interactions with bacterial cell membrane, followed by disturbance to membrane potential, oxidative stress and finally cell death.

2.2 Preparation and characterization of 2D TMCs

A scalable, affordable and tunable method of synthesizing 2D TMCs materials from bulk powders is liquid phase exfoliation of TMCs through ultra-sonication.[42] In the liquid phase exfoliation, ultrasonic waves generate cavitation bubbles that collapse, releasing sufficient energy to break apart layered materials causing exfoliation of bulk materials into 2D nanoflakes.[42-43] For a successful exfoliation bulk crystals are exposed to energetic forces like ultra-sonication and vibration to overcome the weak van der Waals forces that hold together these layered materials.[44-45] Inspired by previous work on the use of surfactant and oligonucleotides for the colloidal

stabilization of nanomaterials,[36, 46-47] we first conducted studies dispersing the TMCs in various ssDNA sequences.[38] These experiments have shown that TMCs can be stably dispersed by optimal ssDNA sequences in aqueous solution. In these dispersions, the ssDNA adsorbs to the surface of the TMC nanosheets through non-covalent π-π stacking interactions involving both purine and pyrimidine bases of the DNA molecules. This interaction enables the sugar-phosphate backbone of ssDNA to orient away from the surface of the TMC to establish a negatively charged hydrophilic outer layer stabilizes the nanosheets in aqueous solution. Hence to analyze the antibacterial efficacy of TMCs having different compositions, we used the T_{20} sequence of ssDNA which proved to be the most efficient in dispersing TMCs, $MoSe_2$ and MoS_2.[38] For this study, we dispersed eight different TMCs (molybdenum disulfide (MoS_2), molybdenum diselenide ($MoSe_2$), tungsten disulfide (WS_2), tungsten diselenide (WSe_2), tin sulfide (SnS), tin diselenide (SnS), bismuth disulfide (Bi_2S_3) and bismuth diselenide (Bi_2Se_3)) in ssDNA T_{20}.

We took bulk powders of eight different TMCs MoS_2, $MoSe_2$, WS_2, WSe_2, Bi_2S_3, Bi_2Se_3, SnSe, and SnS, and ultra-sonicated them for 2 h in aqueous solutions containing 1.6 mg ml^{-1} T_{20} ssDNA sequence. The concentration of the TDMCs were determined using ICP-MS and optical images were also taken (**Figure 2.1A**). $MoSe_2$ in ssDNA had a dark brown color with mass concentration of 0.806 mg ml^{-1}. Whereas MoS_2 and WS_2 had a dark green color with concentrations of 0.15 mg ml^{-1}, 0.16 mg ml^{-1}, respectively. WSe_2, SnSe, SnS, Bi_2Se_3 and Bi_2S_3 were light brown in color with concentrations 0.29 mg ml^{-1} 1, 0.19 mg ml^{-1}, 0.13 mg ml^{-1}, 0.10 mg ml^{-1} and 0.16 mg ml^{-1}, respectively. UV-vis spectra of the nanomaterial dispersions were acquired in the range of 400-900 nm at room temperature (**Figure 2.1B**). Characteristic adsorption peaks for excitonic transitions were observed at the locations marked by asterisks (*****). No significant peaks were observed for Bi_2Se_3 and Bi_2S_3 (**Figure 2.1B**). The aqueous stability of the nanomaterial dispersions was determined by measuring zeta potential for MoS_2, $MoSe_2$, WS_2 and WSe_2. For ssDNA dispersions the value ranged from -20 mV to -40 mV (**Figure S2.1**). The nanosheets were negatively charged because of the phosphate backbone of ssDNA, which stabilizes the sheets and prevents their aggregation through electrostatic repulsion. TEM images were also taken to study the morphology of the resulting TMC nanosheets (**Figure 2.1C**). The biopolymer dispersions

produced materials with thin nanosheet structures. Typical lateral dimensions of the flakes were ~100 nm by ~100 nm for $MoSe_2$ and MoS_2, ~300 nm by ~200 nm for WSe_2, ~250 nm by ~150 nm for WS_2, ~250 nm by ~200 nm for Bi_2Se_3 and Bi_2S_3, ~250 nm by ~250 nm for SnSe, and ~350 nm by ~200 nm for SnS.
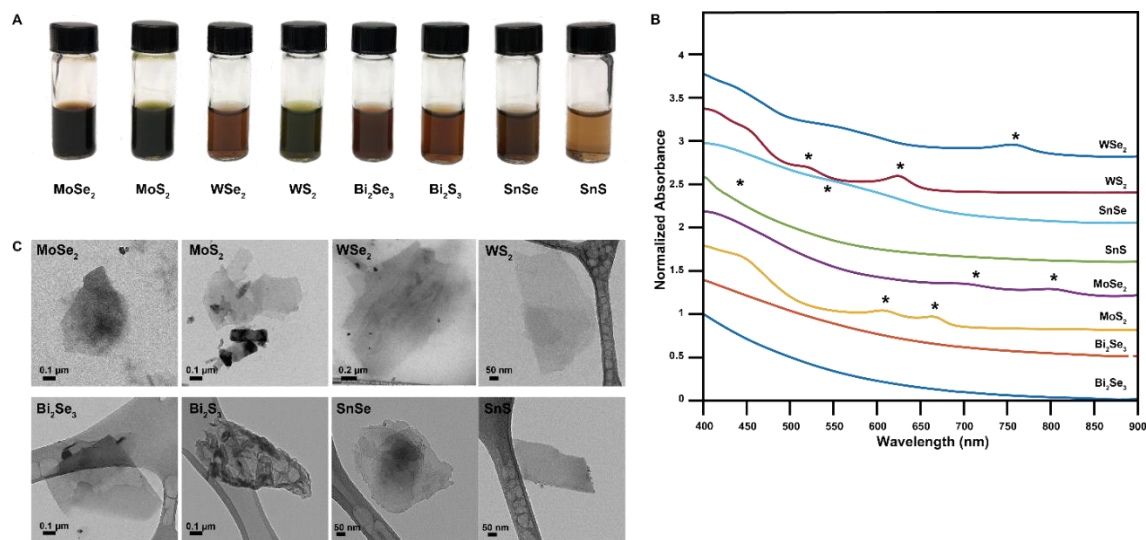
Figure 2.1: Characterization of TMCs. (A) Exfoliation of TMCs in ssDNA solution as a dispersing agent. (B) Characterization of different TMCs using UV-vis spectroscopy in ssDNA solution. Excitonic peaks (*) over a range of wavelength from 300 nm to 900 nm. (C) TEM images of TMCs dispersed in ssDNA. (D) TEM image showing dispersed $MoSe_2$/CS nanosheets.

2.3 Screening of antibacterial activity of TMCs

To study the difference in antimicrobial effects of all eight above-mentioned TMCs dispersed in ssDNA (**Figure 2.2A**), we treated *Escherichia coli* (*E. coli*) MG1655, a non-pathogenic K12 strain with different concentrations of the TMC nanosheets for 4 h. After treatment, the efficiency of individual TMCs were determined through the microdilution method. Out of the eight compounds, $MoSe_2$/ssDNA was the most promising antimicrobial agent, with 99.97% eradication of *E. coli* at a concentration of 50 µg ml^{-1}. MoS_2/ssDNA and WSe_2/ssDNA were the next most-effective material, killing over 98.62% and 98.52% of the bacteria at 50 µg ml^{-1} concentration, respectively. WS_2/ssDNA showed 97.77% but not as effective as WSe_2/ssDNA, which is in agreement with previous studies as well.[37] Bi_2S_3/ssDNA, Bi_2Se_3/ssDNA and SnS/ssDNA showed

the least amount of activity with 97.66%, 97.67% and 94.40% respectively. Lastly SnSe/ssDNA proved unstable, showing signs of aggregation beyond 24 h, and measurements of its antimicrobial activity were inconclusive (**Figure 2.2A**).

Since MoSe$_2$ provided significantly higher antibacterial activity compared to the other TMCs, we also performed a comparison to study the antibacterial effectiveness of MoSe$_2$/ssDNA compared to the most widely used 2D antimicrobial graphene oxide (GO).[48] The experiment showed that MoSe$_2$/ssDNA provided substantially enhanced activity compared to GO (**Figure 2.2B**). At a concentration of 100 µg ml^{-1}, MoSe$_2$/ssDNA completely (100%) eradicated the *E. coli* culture, whereas GO eliminated only 79.76% of the cells.
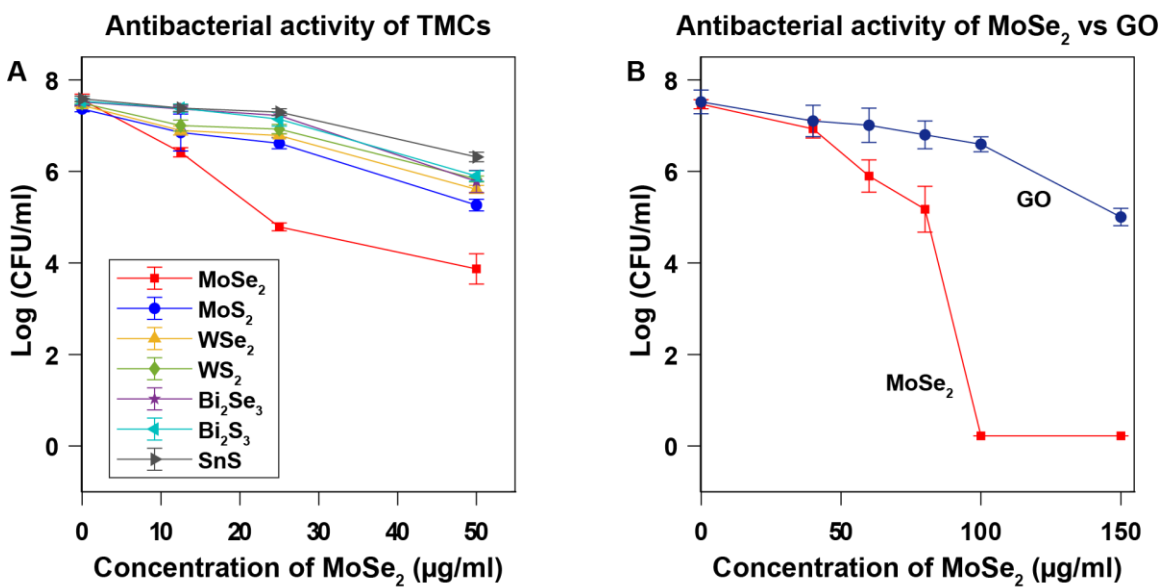
Figure 2.2: Antibacterial screening of TMCs. (A) CFUs at different concentrations were used to determine MBC values of different TMCs against K-12 *E. coli* (gram-negative) strain. MoSe$_2$ was determined at to have highest antibacterial efficiency at 50 µg ml^{-1} of nanomaterial. (B) Comparison of antibacterial activity between MoSe$_2$ and GO against K-12 *E. coli* strain. All experiments were done in triplicate. Dashed line (at the bottom) indicates complete eradication of bacteria cells.

2.4 Antibacterial activity and biocompatibility test

2.4.1 Antibacterial activity against MDR bacteria

Previous reports suggest that cationic polypeptide, poly-L-lysine (PLL) has the ability to interact with the negatively charged bacterial cell membrane whereas, hydrophobic butyl chains enabled it to interact with the surface of the 2D TMCs like $MoSe_2$.[49-51] We thus investigated nanosheet formulations combining both PLL and $MoSe_2$ in the hopes of obtaining higher antibacterial activity. $MoSe_2$ was ultrasonicated in presence of PLL for 2 hours. PLL helped stabilize the $MoSe_2$ layers via electrostatic interactions, after ultrasonication breaks through the weak van der Waals interactions of the layers resulting in successful exfoliation (**Figure S2.2A**). Stabilization was confirmed by zeta potential measurements showing +41 mV positive charge of the resulting solution (**Figure S2.3A**). Despite the high stability of the $MoSe_2$/PLL in the colloidal suspension, we observed aggregation in solutions having high salt concentrations. To further stabilize our material in buffer media, we introduced the known biocompatible nonionic block copolymer Pluronic F77,[52-53] which provided additional stabilization to the nanosheets using steric repulsion. Zeta potential measurements of the colloidal dispersions showed a reduced zeta potential of +21 mV (**Figure S2.3A**). After successful stabilization of $MoSe_2$ nanosheets using PLL and Pluronic-F77, excess polymer was removed from the solutions using dialysis for 24 h. An optical image of the colloidal solution shows a dark brown colored solution (**Figure S2.3B**). We evaluated the morphology of the nanomaterial using TEM (**Figure S2.2B**). The morphological analysis of $MoSe_2$/PLL/F77 using TEM, demonstrated successful exfoliation and thin flake-like structures of dispersed nanomaterial with lateral dimensions in the range of 50-100 nm. The polymer content on the surface of $MoSe_2$ was further determined using thermogravimetric analysis (TGA). The TGA analysis of $MoSe_2$/PLL/F77 demonstrated presence of 22% polymer on the surface of $MoSe_2$ (**Figure S2.2B**)

After successful synthesis of $MoSe_2$/PLL/F77, we evaluated the antibacterial efficiency of $MoSe_2$/PLL/F77 against multidrug resistant (MDR) gram-negative and gram-positive bacteria known as 'ESKAPE' strains.[6] Minimal bactericidal concentrations (MBC) were evaluated using microdilution and colony counting after incubating the material for 2 h at 37 °C. $MoSe_2$/PLL/F77 completely eradicated both gram-positive and gram-negative strains at 50 µg ml^{-1} (**Figure 2.3A** and **2.3B**). It was equally effective against both types of bacterial strains showing its broad-

spectrum antibacterial efficacy. We also observed that MoSe$_2$/PLL/F77 was far more effective at a lower MBC concentration of MoSe$_2$ with reduced incubation time compared to MoSe$_2$/ssDNA. This confirms that the addition of a cationic PLL enhanced the killing of bacteria by synergistically working with the MoSe$_2$ nanoflakes. Furthermore, both *P. aeruginosa* and *K. pneumoniae* were successfully killed at a considerably low concentration of 50 µg ml^{-1}. Usually, it is harder to treat these species owing to their thick extracellular layer and low permeability of antibiotics, thus demonstrating the potency of MoSe$_2$/PLL/F77 as an antibacterial agent.[54-55]

2.4.2 Biocompatibility

We then determined the biocompatibility of MoSe$_2$/PLL/F77 on mammalian RAW 264.7 cells using the alamarBlue assay. This fluorescence-based assay measures the metabolic activity of cells based on oxidation-reduction chemistry where the indicator to changes the color in response to chemical reduction of growth medium (DMEM) resulting from the cell growth.[56] Results show above 90% mammalian cell viability at a concentration as high as 200 µg ml^{-1} (**Figure 2.3C**). We also tested MoSe$_2$/PLL/F77 against human red blood cells (RBCs) using hemolysis assays. The hemolysis assay measures the cytotoxicity of different materials by determining the extent of cell lysis. After incubation of MoSe$_2$/PLL/F77 with RBCs for 2 h, no significant hemolysis was observed, with below ~30% hemolysis of RBC observed at concentrations as high as 200 µg ml^{-1} (**Figure 2.3D**). Concentrations which cause less than 50% (indicated by the dashed line) hemolysis of red blood cells are considered hemocompatible.[16]

2.4.3 Resistance study

Overuse of antibiotics has led to the evolution of bacteria strains which led to resistance mechanisms making these antibiotics redundant. Hence, we evaluated the growth of bacteria in presence of antibiotics imipenem, gentamicin, rifampin, PLL and MoSe$_2$/PLL/F77. We studied resistance development in *P. aeruginosa* and *S. aureus*. Both the strains were treated with antibiotics for 16 hours, MIC was determined at 0.5 x MIC concentrations. Therein, colonies from the treatment were used for the next round of exposure to the antibacterial compounds. This procedure was carried out for 20 serial passages. No resistance development was observed for

MoSe$_2$/PLL/F77 after 20 serial passages (**Figure S 2.4**). We observed both *P. aeruginosa* and *S. aureus* developed resistance to PLL after 8 passages and a 4-fold increase in dosage. For *P. aeruginosa*, we treated the bacteria with two clinically approved antibiotics: imipenem and gentamicin with more than 4-fold increase in dosage after 10 passages ((**Figure S 2.4A**). Similarly, *S. aureus* developed resistance to the rifampicin after 8 passages with more than 4-fold increase in dosage (**Figure S 2.4B**). Whereas MoSe$_2$/PLL/F77 showed no development of resistance confirming that 2D TMC, MoSe$_2$ is a useful antibacterial agent against growing resistance.
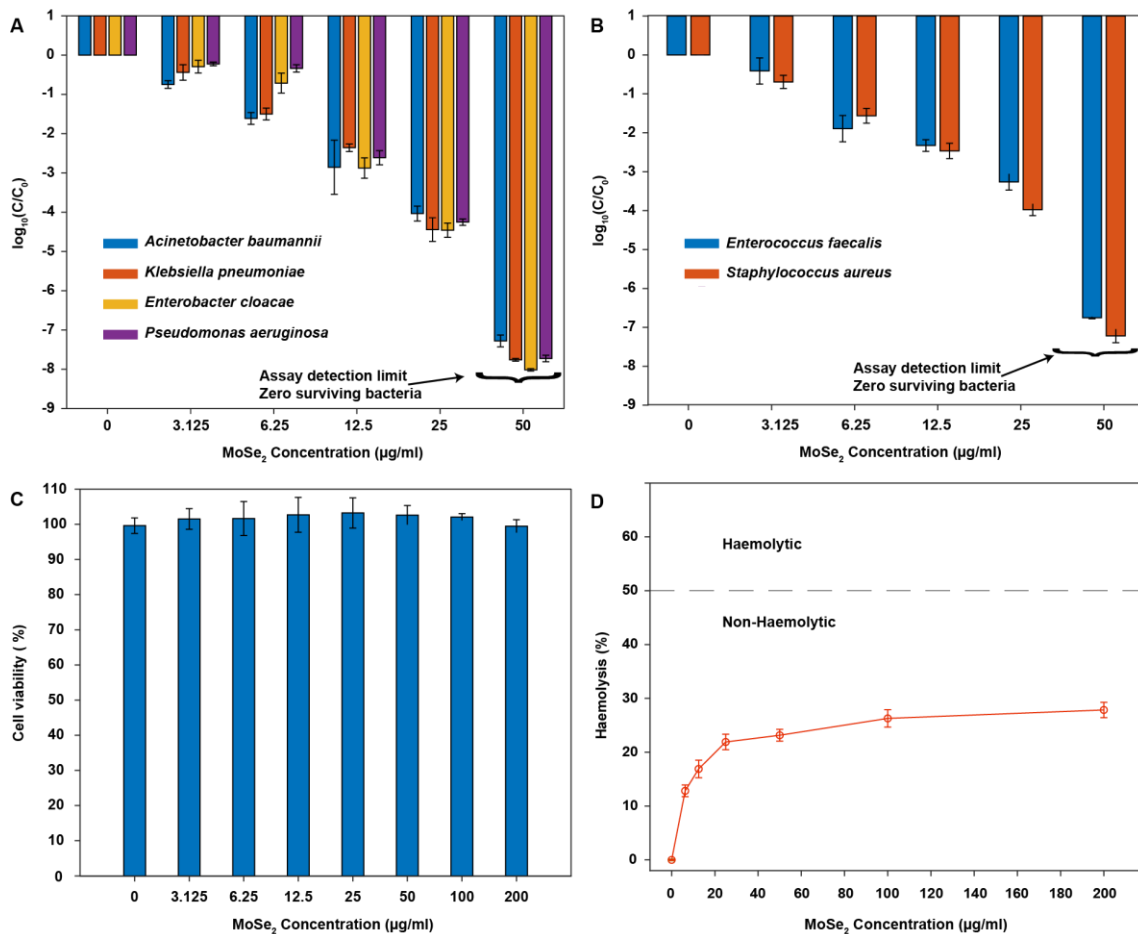
Figure 2.3: Antibacterial activity and biocompatibility of MoSe$_2$/PLL/F77. (A) Minimum bactericidal concentrations (MBC) of MoSe$_2$/PLL/F77 against gram-positive multidrug-resistant.

(MDR) 'ESKAPE' strains. (B) MBCs of MoSe$_2$/PLL/F77 against gram-negative MDR 'ESKAPE' strains. (C) Percent mammalian cell viability of HEK 293 after treatment with MoSe$_2$/PLL/F77 showing. (D) Percent hemolysis of whole human red blood cells (RBCs) on treatment with MoSe$_2$/PLL/F77. All experiments were performed in triplicate. (Experiments were performed by Abhishek Debnath).

2.5 Morphological study

To evaluate effects of MoSe$_2$/PLL/F77 on bacteria cells, we analyzed the morphology of bacteria cells using SEM and TEM (**Figure 2.4**). We analyzed morphology of gram-negative *A. baumannii* and gram-positive *S. aureus* bacteria at a concentration of 50 µg ml^{-1} (1 x MBC) of MoSe$_2$. The untreated cells were considered control and were compared with cells after treatment with the material. SEM images showed both the bacterial strains having intact morphology in the absence of MoSe$_2$/PLL/F77 (**Figure 2.4A** and **2.4C**). After treatment with 1 x MBC of MoSe$_2$/PLL/F77, the bacterial cell membrane demonstrated distinct membrane damage, disruptive features and interaction with nanomaterials (**Figure 2.4B and 2.4D**). Further analysis of the cross-sectional view in the TEM images of the control samples showed that the cytoplasm was intact with unbroken cell membranes and healthy cells (**Figure 2.4E and 2.4G**). Whereas, treated samples show sharp-edged MoSe$_2$ nanoflakes encapsulating the bacteria cells along with ruptured cell membrane and leaking of cytoplasm (**Figure 2.4F and 2.4H**). The localization of nanomaterials around the bacteria can be attributed to the strong electrostatic interactions between MoSe$_2$/PLL/F77 and the negatively charged phospholipids of bacterial outer membrane. The presence of these nanoflakes generates physical stress which can destabilize and reduce the rigidity of the cell membrane, leading to disruption and membrane damage. The high turgor pressure inside the cell combined with these interactions with the membrane enables the rupture of cell wall, cytoplasmic leakage and finally cell death. Hence, we validate that MoSe$_2$/PLL/F77 weakens, damages, inhibits and kills both gram-positive and gram-negative bacterial strains.
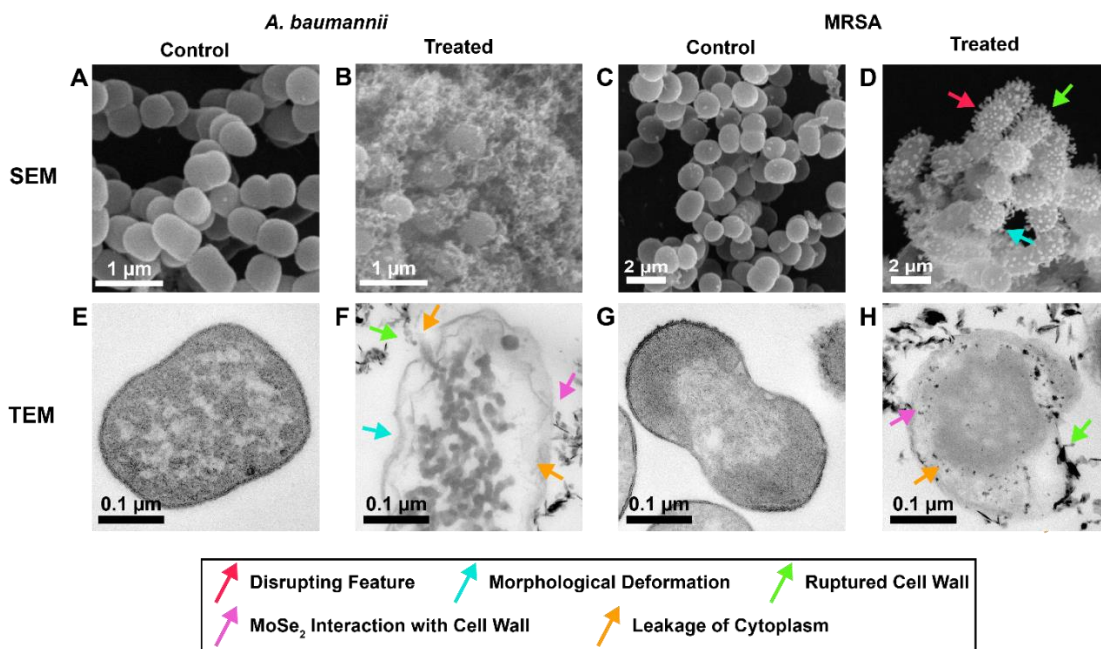
Figure 2.4. Morphology of cells of MoSe$_2$/PLL/F77 against *A. baumannii* and *S. aureus*. (A, C) SEM images of healthy control cells of *A. baumannii* (A) and *S. aureus* (C). (B, D) SEM images showing disruptive features (**red arrows**), morphological deformation (**cyan arrows**) and broken outer membrane (**green arrows**) of *A. baumannii* (B) and *S. aureus* (D) in the presence of MoSe$_2$/PLL/F77. (E, G) TEM images of control cells of *A. baumannii* (E) and *S. aureus* (G) with intact cytoplasm. (F, H) TEM images of *A. baumannii* (F) and *S. aureus* (H) in the presence of MoSe$_2$/CS showing MoSe$_2$ flakes interacting with cell wall (**pink arrows**), leading to rupturing of the cell wall (**green arrows**) and cytoplasmic leakage (**orange arrows**).

2.6 Conclusion

We synthesized several TMC compositions in ssDNA and characterized them with the help UV-vis spectroscopy and TEM. We observed the synthesis of 2D nanosheets which we screened to analyze their antibacterial efficacy. We observed that among all TMCs MoSe$_2$ nanosheets were dispersed in ssDNA most efficiently. We also compared the antibacterial activity against a known 2D material, GO and observed MoSe$_2$ to be ~21% more effective against gram-negative strain *E. coli* at 100 μg ml^{-1} within 4 h of treatment. We also successfully designed and fabricated a novel target-specific antibacterial agent where MoSe$_2$ was prepared by liquid phase exfoliation

encapsulated in cationic AMP, PLL and nonionic Pluronic F77 (MoSe$_2$/PLL/F77). Electron microscopy of the synthesized nanosheets showed a high degree of exfoliation of bulk MoSe$_2$ into monolayer and few-layer nanosheets of various sizes. Evaluation of the antibacterial activity of the MoSe$_2$/PLL/F77 nanosheets revealed their exceptional ability to eradicate MDR gram-positive and gram-negative bacteria within 50 µg ml^{-1} of MoSe$_2$/PLL/F77 after treatment of 2 h. We also tested the toxicity of the material with alamarBlue assay and hemolysis assay which clearly showed it to be highly biocompatible at concentration as high as 200 µg ml^{-1}. Furthermore, TEM and SEM of the treated bacteria cell showed multimodal action of MoSe$_2$/PLL/F77 which includes membrane disruption, leaking of cytoplasm and disintegration leading to cell death. Additionally, we tested our material for development of resistance over 20 serial passage of *P. aeruginosa* and *S. aureus.* We observed no development of resistance was observed by bacteria while parallel experiments with clinical antibiotics showed rapid resistance development. The remarkable antibacterial performance and inhibition of resistance shows the ability of MoSe$_2$/PLL/F77 as a potent antibacterial system with the capacity to combat a broad spectrum of different drug-resistant bacterial pathogens. In the future, MoSe$_2$/PLL/F77 has the possibility of further researching them against biofilms which is the lead cause of nosocomial infections. It can also be analyzed for several biomedical applications like wound dressings, ultrafiltration of membranes and environmental applications.

2.7 Reference

1.   Chandler, C. I. R., Current accounts of antimicrobial resistance: stabilisation, individualisation and antibiotics as infrastructure. *Palgrave Communications* 2019, *5* (1), 53.

2.   Rice, L. B., Federal Funding for the Study of Antimicrobial Resistance in Nosocomial Pathogens: No ESKAPE. *The Journal of Infectious Diseases* 2008, *197* (8), 1079-1081.

3.   Schultz, F.; Anywar, G.; Tang, H.; Chassagne, F.; Lyles, J. T.; Garbe, L.-A.; Quave, C. L., Targeting ESKAPE pathogens with anti-infective medicinal plants from the Greater Mpigi region in Uganda. *Scientific Reports* 2020, *10* (1), 11935.

4.   Friedman, N. D.; Temkin, E.; Carmeli, Y., The negative impact of antibiotic resistance. *Clinical microbiology and infection : the official publication of the European Society of Clinical Microbiology and Infectious Diseases* 2016, *22* (5), 416-22.

5.   Thabit, A. K.; Crandon, J. L.; Nicolau, D. P., Antimicrobial resistance: impact on clinical and economic outcomes and the need for new antimicrobials. *Expert Opinion on Pharmacotherapy* 2015, *16* (2), 159-177.

6.   Boucher, H. W.; Talbot, G. H.; Bradley, J. S.; Edwards, J. E.; Gilbert, D.; Rice, L. B.; Scheld, M.; Spellberg, B.; Bartlett, J., Bad Bugs, No Drugs: No ESKAPE! An Update from the Infectious Diseases Society of America. *Clinical Infectious Diseases* 2009, *48* (1), 1-12.

7.   Mulani, M. S.; Kamble, E. E.; Kumkar, S. N.; Tawre, M. S.; Pardesi, K. R., Emerging Strategies to Combat ESKAPE Pathogens in the Era of Antimicrobial Resistance: A Review. *Frontiers in Microbiology* 2019, *10* (539).

8.   Santajit, S.; Indrawattana, N., Mechanisms of Antimicrobial Resistance in ESKAPE Pathogens. *BioMed Research International* 2016, *2016*, 2475067.

9.   Ventola, C. L., The antibiotic resistance crisis: part 1: causes and threats. *P T* 2015, *40* (4), 277-283.

10.   Fair, R. J.; Tor, Y., Antibiotics and bacterial resistance in the 21st century. *Perspect Medicin Chem* 2014, *6*, 25-64.

11.   Lee, J. H.; Jeong, S. H.; Cha, S.-S.; Lee, S. H., A lack of drugs for antibiotic-resistant Gram-negative bacteria. *Nature Reviews Drug Discovery* 2007, *6* (11), 938-938.

12.   Taubes, G., The Bacteria Fight Back. *Science* 2008, *321* (5887), 356.

13.   Xu, Z.-Q.; Flavin, M. T.; Flavin, J., Combating multidrug-resistant Gram-negative bacterial infections. *Expert Opinion on Investigational Drugs* 2014, *23* (2), 163-182.

14.   Kohanski, M. A.; Dwyer, D. J.; Collins, J. J., How antibiotics kill bacteria: from targets to networks. *Nat Rev Microbiol* 2010, *8* (6), 423-435.

15.   Taylor, P. W.; Stapleton, P. D.; Paul Luzio, J., New ways to treat bacterial infections. *Drug Discovery Today* 2002, *7* (21), 1086-1091.

16.   Gupta, A.; Landis, R. F.; Li, C.-H.; Schnurr, M.; Das, R.; Lee, Y.-W.; Yazdani, M.; Liu, Y.; Kozlova, A.; Rotello, V. M., Engineered Polymer Nanoparticles with Unprecedented Antimicrobial Efficacy and Therapeutic Indices against Multidrug-Resistant Bacteria and Biofilms. *Journal of the American Chemical Society* 2018, *140* (38), 12137-12143.

17.   Gupta, A.; Mumtaz, S.; Li, C.-H.; Hussain, I.; Rotello, V. M., Combatting antibiotic-resistant bacteria using nanomaterials. *Chem Soc Rev* 2019, *48* (2), 415-427.

18.   Singh, R.; Smitha, M. S.; Singh, S. P., The role of nanotechnology in combating multi-drug resistant bacteria. *Journal of nanoscience and nanotechnology* 2014, *14* (7), 4745-56.

19.   Zasloff, M., Antimicrobial peptides of multicellular organisms. *Nature* 2002, *415* (6870), 389-395.

20.   Brogden, K. A., Antimicrobial peptides: pore formers or metabolic inhibitors in bacteria? *Nature Reviews Microbiology* 2005, *3* (3), 238-250.

21.   Kuroda, K.; DeGrado, W. F., Amphiphilic Polymethacrylate Derivatives as Antimicrobial Agents. *Journal of the American Chemical Society* 2005, *127* (12), 4128-4129.

22.	Palermo, E. F.; Kuroda, K., Structural determinants of antimicrobial activity in polymers which mimic host defense peptides. *Applied Microbiology and Biotechnology* 2010, *87* (5), 1605-1615.

23.	Joo, H.-S.; Otto, M., Mechanisms of resistance to antimicrobial peptides in staphylococci. *Biochimica et Biophysica Acta (BBA) - Biomembranes* 2015, *1848* (11, Part B), 3055-3061.

24.	Kang, S.-J.; Park, S. J.; Mishig-Ochir, T.; Lee, B.-J., Antimicrobial peptides: therapeutic potentials. *Expert Review of Anti-infective Therapy* 2014, *12* (12), 1477-1486.

25.	Shkodenko, L.; Kassirov, I.; Koshel, E., Metal Oxide Nanoparticles Against Bacterial Biofilms: Perspectives and Limitations. *Microorganisms* 2020, *8* (10), 1545.

26.	Maleki Dizaj, S.; Mennati, A.; Jafari, S.; Khezri, K.; Adibkia, K., Antimicrobial activity of carbon-based nanoparticles. *Adv Pharm Bull* 2015, *5* (1), 19-23.

27.	Sambanthamoorthy, K.; Feng, X.; Patel, R.; Patel, S.; Paranavitana, C., Antimicrobial and antibiofilm potential of biosurfactants isolated from lactobacilli against multi-drug-resistant pathogens. *BMC Microbiol* 2014, *14*, 197-197.

28.	Huang, Z.; Zheng, X.; Yan, D.; Yin, G.; Liao, X.; Kang, Y.; Yao, Y.; Huang, D.; Hao, B., Toxicological Effect of ZnO Nanoparticles Based on Bacteria. *Langmuir* 2008, *24* (8), 4140-4144.

29.	Maness, P. C.; Smolinski, S.; Blake, D. M.; Huang, Z.; Wolfrum, E. J.; Jacoby, W. A., Bactericidal activity of photocatalytic TiO(2) reaction: toward an understanding of its killing mechanism. *Appl Environ Microbiol* 1999, *65* (9), 4094-4098.

30.	Weir, E.; Lawlor, A.; Whelan, A.; Regan, F., The use of nanoparticles in anti-microbial materials and their characterization. *Analyst* 2008, *133* (7), 835-845.

31.	Kim, J. S.; Kuk, E.; Yu, K. N.; Kim, J.-H.; Park, S. J.; Lee, H. J.; Kim, S. H.; Park, Y. K.; Park, Y. H.; Hwang, C.-Y.; Kim, Y.-K.; Lee, Y.-S.; Jeong, D. H.; Cho, M.-H., Antimicrobial effects of silver nanoparticles. *Nanomedicine: Nanotechnology, Biology and Medicine* 2007, *3* (1), 95-101.

32.	Li, Q.; Mahendra, S.; Lyon, D. Y.; Brunet, L.; Liga, M. V.; Li, D.; Alvarez, P. J. J., Antimicrobial nanomaterials for water disinfection and microbial control: Potential applications and implications. *Water Research* 2008, *42* (18), 4591-4602.

33.	Ding, X.; Duan, S.; Ding, X.; Liu, R.; Xu, F.-J., Versatile Antibacterial Materials: An Emerging Arsenal for Combatting Bacterial Pathogens. *Advanced Functional Materials* 2018, *28* (40), 1802140.

34.	Yang, Y.; Liu, T.; Cheng, L.; Song, G.; Liu, Z.; Chen, M., MoS2-Based Nanoprobes for Detection of Silver Ions in Aqueous Solutions and Bacteria. *ACS Applied Materials & Interfaces* 2015, *7* (14), 7526-7533.

35.	Zhang, W.; Mou, Z.; Wang, Y.; Chen, Y.; Yang, E.; Guo, F.; Sun, D.; Wang, W., Molybdenum disulfide nanosheets loaded with chitosan and silver nanoparticles effective antifungal activities: in vitro and in vivo. *Materials Science and Engineering: C* 2019, *97*, 486-497.

36.	Bang, G. S.; Cho, S.; Son, N.; Shim, G. W.; Cho, B.-K.; Choi, S.-Y., DNA-Assisted Exfoliation of Tungsten Dichalcogenides and Their Antibacterial Effect. *ACS Applied Materials & Interfaces* 2016, *8* (3), 1943-1950.

37.   Benincasa, M.; Pacor, S.; Wu, W.; Prato, M.; Bianco, A.; Gennaro, R., Antifungal Activity of Amphotericin B Conjugated to Carbon Nanotubes. *ACS Nano* 2011, *5* (1), 199-208.

38.   Debnath, A.; Saha, S.; Li, D. O.; Chu, X. S.; Ulissi, Z. W.; Green, A. A.; Wang, Q. H., Elimination of Multidrug-Resistant Bacteria by Transition Metal Dichalcogenides Encapsulated by Synthetic Single-Stranded DNA. *ACS Applied Materials & Interfaces* 2021, *13* (7), 8082-8094.

39.   Kurapati, R.; Muzi, L.; de Garibay, A. P. R.; Russier, J.; Voiry, D.; Vacchi, I. A.; Chhowalla, M.; Bianco, A., Enzymatic Biodegradability of Pristine and Functionalized Transition Metal Dichalcogenide MoS2 Nanosheets. *Advanced Functional Materials* 2017, *27* (7), 1605176.

40.   Roy, S.; Mondal, A.; Yadav, V.; Sarkar, A.; Banerjee, R.; Sanpui, P.; Jaiswal, A., Mechanistic Insight into the Antibacterial Activity of Chitosan Exfoliated MoS2 Nanosheets: Membrane Damage, Metabolic Inactivation, and Oxidative Stress. *ACS Applied Bio Materials* 2019, *2* (7), 2738-2755.

41.   Wu, C.; Liu, J.; Liu, B.; He, S.; Dai, G.; Xu, B.; Zhong, W., NIR light-responsive short peptide/2D NbSe2 nanosheets composite hydrogel with controlled-release capacity. *Journal of Materials Chemistry B* 2019, *7* (19), 3134-3142.

42.   Nicolosi, V.; Chhowalla, M.; Kanatzidis, M. G.; Strano, M. S.; Coleman, J. N., Liquid Exfoliation of Layered Materials. *Science* 2013, *340* (6139), 1226419.

43.   Dular, M.; Stoffel, B.; Širok, B., Development of a cavitation erosion model. *Wear* 2006, *261* (5), 642-655.

44.   Coleman, J. N.; Lotya, M.; O'Neill, A.; Bergin, S. D.; King, P. J.; Khan, U.; Young, K.; Gaucher, A.; De, S.; Smith, R. J.; Shvets, I. V.; Arora, S. K.; Stanton, G.; Kim, H.-Y.; Lee, K.; Kim, G. T.; Duesberg, G. S.; Hallam, T.; Boland, J. J.; Wang, J. J.; Donegan, J. F.; Grunlan, J. C.; Moriarty, G.; Shmeliov, A.; Nicholls, R. J.; Perkins, J. M.; Grieveson, E. M.; Theuwissen, K.; McComb, D. W.; Nellist, P. D.; Nicolosi, V., Two-Dimensional Nanosheets Produced by Liquid Exfoliation of Layered Materials. *Science* 2011, *331* (6017), 568.

45.   Hernandez, Y.; Nicolosi, V.; Lotya, M.; Blighe, F. M.; Sun, Z.; De, S.; McGovern, I. T.; Holland, B.; Byrne, M.; Gun'Ko, Y. K.; Boland, J. J.; Niraj, P.; Duesberg, G.; Krishnamurthy, S.; Goodhue, R.; Hutchison, J.; Scardaci, V.; Ferrari, A. C.; Coleman, J. N., High-yield production of graphene by liquid-phase exfoliation of graphite. *Nature Nanotechnology* 2008, *3* (9), 563-568.

46.   Ayán-Varela, M.; Pérez-Vidal, Ó.; Paredes, J. I.; Munuera, J. M.; Villar-Rodil, S.; Díaz-González, M.; Fernández-Sánchez, C.; Silva, V. S.; Cicuéndez, M.; Vila, M.; Martínez-Alonso, A.; Tascón, J. M. D., Aqueous Exfoliation of Transition Metal Dichalcogenides Assisted by DNA/RNA Nucleotides: Catalytically Active and Biocompatible Nanosheets Stabilized by Acid–Base Interactions. *ACS Applied Materials & Interfaces* 2017, *9* (3), 2835-2845.

47.   Vovusha, H.; Sanyal, B., Adsorption of nucleobases on 2D transition-metal dichalcogenides and graphene sheet: a first principles density functional theory study. *RSC Advances* 2015, *5* (83), 67427-67434.

48.   Liu, S.; Zeng, T. H.; Hofmann, M.; Burcombe, E.; Wei, J.; Jiang, R.; Kong, J.; Chen, Y., Antibacterial Activity of Graphite, Graphite Oxide, Graphene Oxide, and Reduced Graphene Oxide: Membrane and Oxidative Stress. *ACS Nano* 2011, *5* (9), 6971-6980.

49.   Findlay, B.; Zhanel, G. G.; Schweizer, F., Cationic Amphiphiles, a New Generation of Antimicrobials Inspired by the Natural Antimicrobial Peptide Scaffold. *Antimicrobial Agents and Chemotherapy* 2010, *54* (10), 4049.

50.   Hale, J. D. F.; Hancock, R. E. W., Alternative mechanisms of action of cationic antimicrobial peptides on bacteria. *Expert Review of Anti-infective Therapy* 2007, *5* (6), 951-959.

51.   Powers, J.-P. S.; Hancock, R. E. W., The relationship between peptide structure and antibacterial activity. *Peptides* 2003, *24* (11), 1681-1691.

52.   Li, J.; Zhang, K.; Ruan, L.; Chin, S. F.; Wickramasinghe, N.; Liu, H.; Ravikumar, V.; Ren, J.; Duan, H.; Yang, L.; Chan-Park, M. B., Block Copolymer Nanoparticles Remove Biofilms of Drug-Resistant Gram-Positive Bacteria by Nanoscale Bacterial Debridement. *Nano Letters* 2018, *18* (7), 4180-4187.

53.   Pitto-Barry, A.; Barry, N. P. E., Pluronic® block-copolymers in medicine: from chemical and biological versatility to rationalisation and clinical advances. *Polymer Chemistry* 2014, *5* (10), 3291-3297.

54.   Campos, M. A.; Vargas, M. A.; Regueiro, V.; Llompart, C. M.; Albertí, S.; Bengoechea, J. A., Capsule polysaccharide mediates bacterial resistance to antimicrobial peptides. *Infect Immun* 2004, *72* (12), 7107-7114.

55.   Llobet, E.; Tomás, J. M.; Bengoechea, J. A., Capsule polysaccharide is a bacterial decoy for antimicrobial peptides. *Microbiology* 2008, *154* (12), 3877-3886.

56.   Bonnier, F.; Keating, M. E.; Wróbel, T. P.; Majzner, K.; Baranska, M.; Garcia-Munoz, A.; Blanco, A.; Byrne, H. J., Cell viability assessment using the Alamar blue assay: A comparison of 2D and 3D cell culture models. *Toxicology in Vitro* 2015, *29* (1), 124-131.

Chapter 3

Eradication and inhibition of bacterial biofilms using 2D MoSe$_2$ wrapped in biopolymers

3.1 Introduction

Pathogenic bacteria and fungi are an ever-growing global threat to human health,[1] and the rapid evolution of pathogenic bacteria into multi-drug resistant (MDR) ones also pose a significant danger to healthcare and food supplies.[2-4] Existing clinical antibiotics have become ineffective against many MDR bacteria due to misuse and overuse.[5-6] When antibiotics fail to kill bacteria, they adhere to living or inanimate surfaces leading to the formation of biofilms.[5] Biofilms are communities of microbes found either attached to a surface or buried firmly in an extracellular matrix (ECM) as aggregates.[7] The outer layer of the biofilm, containig ECM, made up of polysaccharides, DNA and peptides, and provides a protective coating.[8-9] They have proven to be extremely adaptable and resilient in the environment and very hard to kill. Moreover, the biofilms are responsible for causing a broad range of chronic diseases and due to the emergence of antibiotic resistance in bacteria it has really become difficult to treat.[7] Thus far, only a few molecules such as proline, arginine, phenylalanine and tryptophan containing agents have demonstrated effective killing against biofilms by targeting the stress response in bacteria.[10-11] Hence, commonly available antibiotics are ineffective for treating these biofilm related infections ineffective, due to their higher values of minimum inhibitory concentration (MIC) and minimum biofilm eradication concentration (MBEC), which may result in *in-vivo* toxicity.[7] Currently, biofilm growth has become a global issue in healthcare recognized as nosocomial diseases, which are leading to growing fatalities.[12-13] Nosocomial diseases are spread through the medical environment or people coming in contact with healthcare settings.[14] Biofilm infections of the teeth, lungs, skin, heart and urinary tract are highly lethal.[15-17] In fact, biofilm infections are source of 60% of post-surgical complications and 80% of deaths caused by infections.[18-19] Nearly 80% of all medical devices and surgical implants such as intravenous and urinary catheters, dentures, breast implants, contact lenses and pacemakers are known to have been infected by pathogenic bacteria.[20-25] Nosocomial diseases are prevalent all over the world, and on average 8.7% hospital patients at a time are infected by nosocomial diseases worldwide. Currently approximately 2 million people in the United States, 30,000 people

in Europe, 25% to 40% of patients in India and over 1.4 million in the rest of the world suffer from post-surgical complications due to nosocomial diseases leading to billions of dollars being spent annually.[15, 26-27] Hence, there is an urgent need to tackle biofilms and their role in nosocomial infections.

In the recent years, nanometer-sized antimicrobial agents have shown promising potential in combating MDR bacteria due to their greater activity, large surface to volume ratio, and ability to control their physiochemical properties.[5] Thus, they have a potential future in controlling and treating pathogenic biofilms on various medical devices and implants.[28] The nanomaterials showing antibiofilm activity so far are metals and their oxides,[29-31] inorganic materials and nanoparticles,[32-36] two dimensional (2D) nanomaterials,[37-40] peptides[41] or combinations of these.[41-44] In addition, biopolymers or nanoparticle/nanomaterial-polymer composites are being explored in an effort to make these nanomaterials less toxic.[40, 44-49] Recently, near-infrared light (nIR) or alternating magnetic fields coupled with nanomaterials like gold nanorods and 2D transition metal dichalcogenides (TMCs) are being investigated to eradicate biofilms.[15, 49-51] Despite the immense progress in exploring these novel antibiofilm agents, their direct use has been limited due to complexity of preparation, short term effect, toxicity, lack of clinical applicability and high cost.[28] Thus, there is an immediate requirement for a cost-effective nanomaterial that can be easily synthesized, is highly biocompatible and can be used as a potent coating on biomedical instruments or implants.

Since the discovery of graphene in 2004,[52-53] 2D nanomaterials have received significant attention due their ultrathin dimensions, and exceptional physical and chemical properties.[54-58] Since then, ultrathin TMCs have been investigated and further explored in various fields like catalysis,[59-61] sensors,[62-63] energy storage,[64-65] environmental remediation[66-67] and nanomedicine.[68-71] Owing to their large surface area, stability, and high biocompatibility, they have many advantages as alternative materials for biomedical applications.[68, 70] In recent years, their antimicrobial properties have been investigated in depth.[72] Additionally, it has been reported that atomically thin TMCs are capable of bacterial membrane damage due to their sharp edges and presence of abundant active sites lead to reactive oxygen species (ROS) generation.[73-75] Unlike

antibiotics, 2D materials exhibit a physical antimicrobial mechanism, which reduces the chances of pathogenic MDR to grow resistance towards them.[76] Few-layer TMD nanosheets can be produced in a high yield and cost-effective manner in large quantities by liquid phase exfoliation,[77-79] specifically, with solvents matching the surface energy of TMCs.[49] However, organic solvents are often toxic to cells,[49] so biocompatible water-soluble surfactants,[78] biomacromolecules[79-82] and polymers[83-86] must be used to stabilize the nanosheets to prevent them from reaggregating,[78] although the yield of nanosheets using these dispersants tend to be lower than with organic solvents. Previously, poly-L-lysine (PLL) has been reported to reduce the toxicity of single-walled carbon nanotube (SWNT) when processed on its surface.[87] PLL is a well-established polycationic biopolymer known to show antimicrobial activity.[88] Furthermore, PLL has successfully exfoliated bulk TMCs in aqueous medium with high yield at a low cost in our lab previously showing great antibacterial efficacy against a range of MDR bacteria.[89]

In this paper, we report a synthesis of 2D molybdenum diselenide ($MoSe_2$) in the presence of 0.2 mg ml^{-1} of the cationic peptide polymer PLL with the help of liquid phase exfoliation (LPE) to enhance the eradication of MDR biofilms. The $MoSe_2$ nanosheets were stabilized in water and other physiological media with the help of 0.5% (wt/v%) biocompatible polymer Pluronic F77. We observed that $MoSe_2$/PLL/F77 dispersions demonstrated efficient killing of several pathogenic bacteria: methicillin-resistant *Staphylococcus aureus* (MRSA), *Acinetobacter baumannii* (*A. baumannii*) and *Pseudomonas aeruginosa* (*P. aeruginosa*). The concentrations of $MoSe_2$/PLL/F77 required to kill each of these bacteria were quite low (75 µg ml^{-1}, 50 µg ml^{-1} and 75 µg ml^{-1}, respectively). This was achieved without any external stimulus like near infrared (nIR) light,[15, 90] antibacterial drugs,[40] complex ligands,[46] or biocidal nanoparticles.[44] It successfully eradicated both gram-positive and gram-negative bacterial biofilms at a concentration of 150 µg ml^{-1}. After treatment with $MoSe_2$/PLL/F77 we observed significant decrease in biofilm mass and metabolic activity. Confocal microscopy and electron microscopy were done to qualitatively and quantitatively demonstrate greater than 90% destruction and inhibition in growth and maturation of biofilms. The $MoSe_2$/PLL/F77 dispersion was also successfully coated over various surfaces pertinent to surgical tools like implants, catheters, and pacemakers. These coatings were long-lasting and highly

effective in inhibiting biofilm growth, with less than ~6.57% surviving cells. We used energy dispersive x-ray analysis (EDX) to detect the presence of Mo and Se elements inhibiting biofilm formation on different surfaces. The therapeutic potential of $MoSe_2$/PLL/F77 nanosheets was evaluated by analyzing its cytotoxicity toward mammalian cells, demonstrating more than 90% viability. These results indicate that $MoSe_2$/PLL/F77 nanosheets are highly efficient antibiofilm agents with a high degree of biocompatibility toward mammalian cells which can be used as coatings to prevent biofilm growth in hospitals and public settings.

3.2 2D $MoSe_2$/PLL/F77 synthesis and characterization

$MoSe_2$/PLL/F77 was prepared via ultrasonication of bulk molybdenum diselenide ($MoSe_2$) powder in solution phase in a two-step process using 0.2 mg ml^{-1} PLL followed by 0.5% Pluronic F77. The resulting dispersion has a dark brown color (Figure 1A). UV-vis spectra and TEM were used to characterize the structure and composition of $MoSe_2$/PLL/F77. The concentration of $MoSe_2$/PLL/F77 was ~0.3 mg ml^{-1} determined using ICP-MS. UV-vis spectra of the $MoSe_2$ dispersions were acquired in the range of 500-900 nm at room temperature. Characteristic adsorption peaks for excitonic transitions were observed at 700 nm and 800 nm marked by asterisks (*) in Figure 1B. TEM measurements indicate the biopolymer dispersions contained thin nanosheet structures (Figure 1C). Typical lateral sizes of the $MoSe_2$ flakes were ~50 nm by ~150 nm.
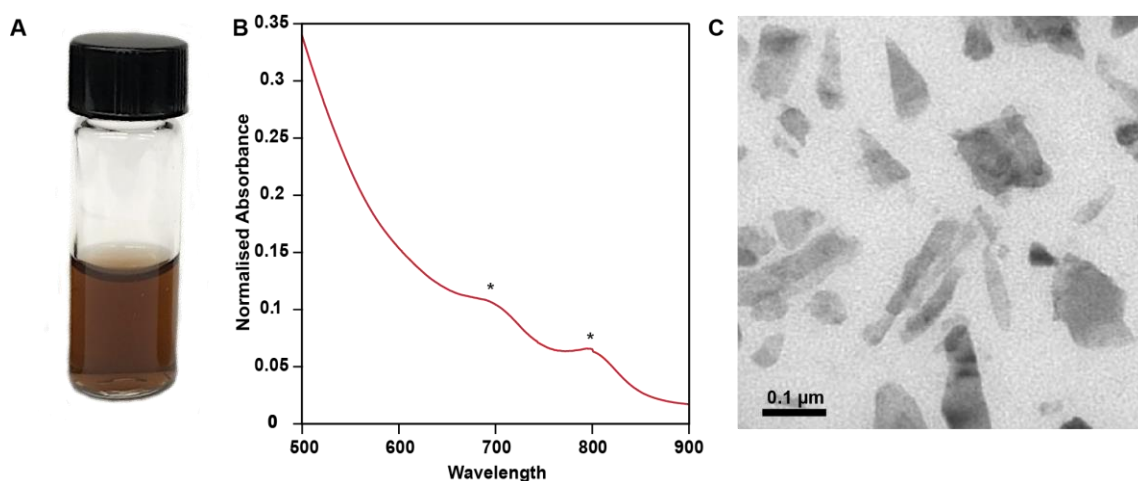
Figure 3.1. Characterization of $MoSe_2$/PLL/F77 nanosheets. (A) Glass vial containing $MoSe_2$/PLL/F77 has a dark brown color. (B) UV-vis of $MoSe_2$/PLL/F77 having characteristic

40

excitonic peaks at 700 nm and 800 nm. (C) TEM images showing MoSe$_2$/PLL/F77 nanosheets with lateral dimensions of ~50 nm by ~150 nm.

3.3 Effect of MoSe$_2$/PLL/F77 on bacterial biofilm

The minimum bactericidal concentration (MBC) is the minimum concentration of material required to completely kill bacterial cells, while the minimum biofilm eradication concentration (MBEC) is the minimum concentration of material required to completely eradicate an existing biofilm. MBC and MBEC values were determined for MRSA, A. baumannii and P. aeruginosa using the microdilution test in TSB medium. To determine MBC, overnight cultures of bacteria was treated with different concentrations of MoSe2/PLL/F77 ranging from 0 to 100 µg ml-1. MRSA and P. aeruginosa were found to have MBC values of 75 µg ml-1, whereas A. baumannii had a value of 50 µg ml-1 (Figure 2A). To determine MBEC, biofilms of each strain were grown on a 96-well plate for 48 h and treated with different concentrations of MoSe2/PLL/F77 ranging from 50 µg ml-1 to 200 µg ml-1. Results show that all three strains have MBEC values of 150 µg ml^{-1} (Figure 2B).

To quantify biofilm formation and viability, gram-positive MRSA bacteria and gram-negative *A. baumannii* bacterial were used to perform the CV assay and the XTT assay. CV is a basic dye consisting of hexamethyl pararosaniline chloride, and binds to the negatively charged molecules and stains the bacteria cell as well as the surrounding ECM. The results shown in Figure 2C indicate that the remaining biofilm mass decreases gradually as the concentration of MoSe$_2$/PLL/F77 was increased. The biofilm mass decreases to 25% of the mass of the untreated biofilm at 125 µg ml^{-1} (Figure 2C), and further decreases to 20% at 200 µg ml^{-1}. This supports the concept of electrostatic interaction between the positively charged MoSe$_2$/PLL/F77 and negatively charged ECM leading to detachment or damage of the biofilm leading to mass loss from the surface.

The XTT assay is an effective way to determine the metabolic activity or the viability of the bacteria cell. The colorless tetrazolium salt turns bright orange upon reduction when in contact with undamaged cell surface due to trans membrane-plasma membrane electron transfer and indicates a metabolically active bacterial cell. The results shown in Figure 2D agree with the CV assay showing a drastic decrease in the metabolic activity of the bacteria with increasing MoSe$_2$/PLL/F77 concentration. The metabolic activity of the bacteria decreases to 7% at 125 µg ml^{-1} and eventually

to 0 at 200 µg ml^{-1} (Figure 2D). The results also indicate that, despite the residual biomass left as observed in the CV assay, there is little to no metabolic activity left in the biofilm when treated with 125 µg ml^{-1} of MoSe$_2$/PLL/F77. This points to the fact that even though there is some biomass left after electrostatic interaction, they are damaged and killed, with no metabolic activity.
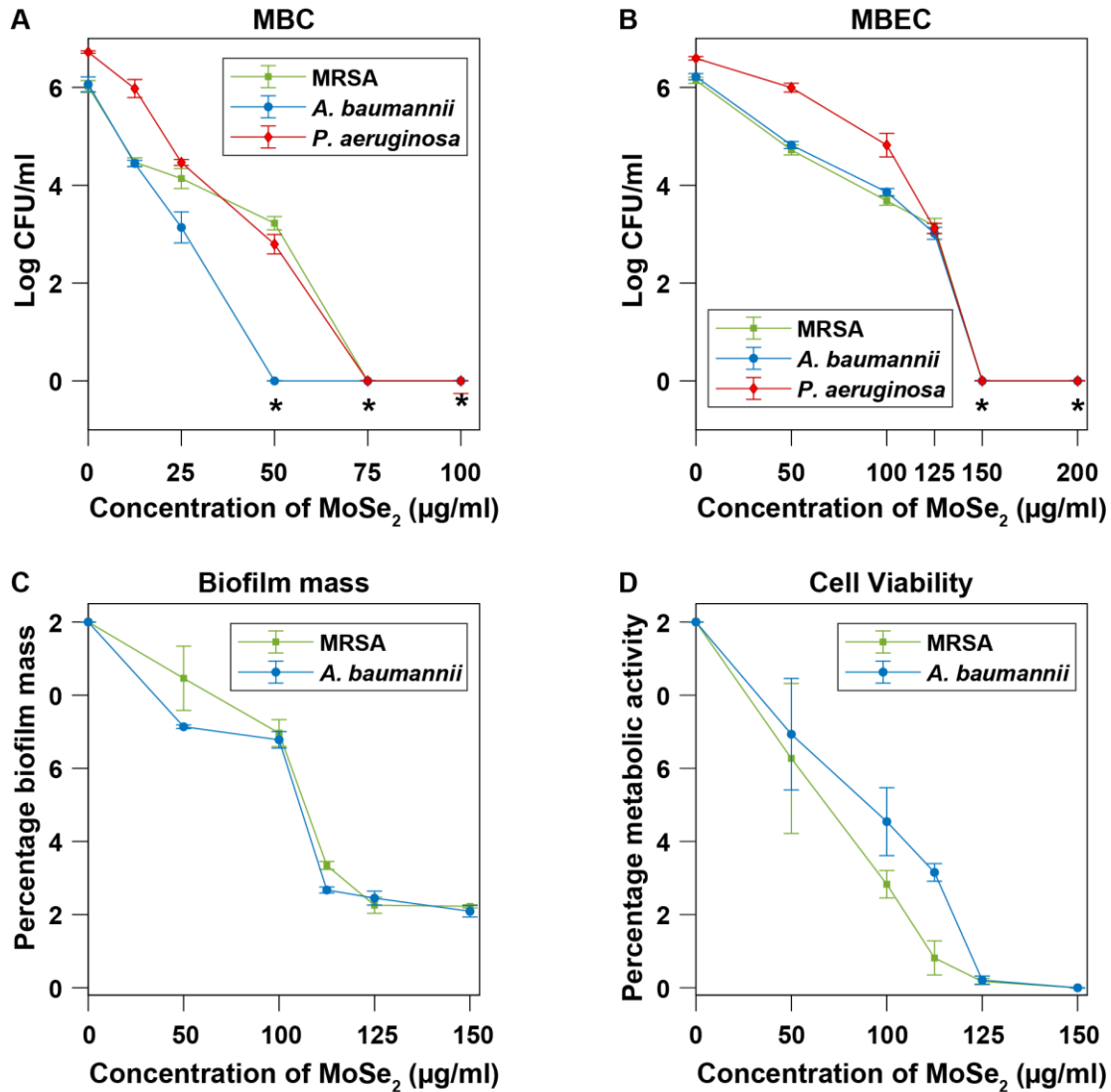
Figure 3.2. Quantitative measurement of biofilm eradication in presence of MoSe$_2$ /PLL/F77 solution. (A) MBC of MRSA, *Acinetobacter baumannii* (*A. baumannii*) and *Pseudomonas aeruginosa* (*P. aeruginosa*) in solution. (B) MBEC of MRSA, *A. baumannii* and *P. aeruginosa* biofilm. (C) Crystal violet assay to determine the relative biofilm mass left in presence of MoSe$_2$ /PLL/F77. (D) XTT assay to determine the relative cell viability in presence of MoSe$_2$ /PLL/F77.

3.4 Eradication of mature bacterial biofilm

CSLM was performed to visualize the biofilm coverage and the live-to-dead cell ratio after treating with $MoSe_2/PLL/F77$. All three strains of bacteria were grown for 48 h to form a biofilm. Biofilm-containing control slides as well as slides treated with 150 µg ml^{-1} of $MoSe_2/PLL/F77$ were treated with SYTO9 green-fluorescent nucleic acid stain and the red-fluorescent PI. SYTO9 can label the entire population of cells, both healthy and damaged. In contrast, PI can only penetrate bacteria with damaged membranes. When stained with both, PI causes a reduction in SYTO9 stain fluorescence once it penetrates the cell. Thus, green fluorescence indicates live cells and red fluorescent indicates dead or damaged cells. From the confocal images (Figure 3A-F), it is verified that the control slide in the absence of $MoSe_2/PLL/F77$ shows ~95.49%, ~94.63% and ~89.2% percent of live cells for MRSA, *A. baumannii* and *P. aeruginosa* respectively. In contrast, the $MoSe_2/PLL/F77$ treated slides only show ~14.55%, ~12.15% and ~14.17% viable cells left (Figure S1A). Thus, biofilms are damaged and inactivated in the presence of $MoSe_2/PLL/F77$.

Along with CSLM, SEM imaging was also done on control and treated samples to microscopically view the biofilm change. Biofilms were first grown on MBEC assay plates with stubs for 48 h followed by treatment with $MoSe_2/PLL/F77$ at a concentration 150 µg ml^{-1} for 6 h. The samples were then processed to observe the change in biofilm morphology in the control from treated samples. Samples without $MoSe_2/PLL/F77$ showed thick layers of biofilm expanding over the surface (Figure 3G-I) while the treated samples lacked healthy cells, biofilm, or ECM (Figure 3J-L). After treating MRSA, *A. baumannii* and *P. aeruginosa* biofilms with $MoSe_2/PLL/F77$, the SEM images showed only ~6.89%, ~6.58% and ~4.42% cells remaining compared to their control samples respectively (Figure S1B) which was manually determined on three images taken from different regions (Figure S1C-E). The cells had apparent deformities and images showed $MoSe_2/PLL/F77$ was wrapped around the cells, demonstrating damaging of cells and destruction of biofilm growth and ECM, respectively.
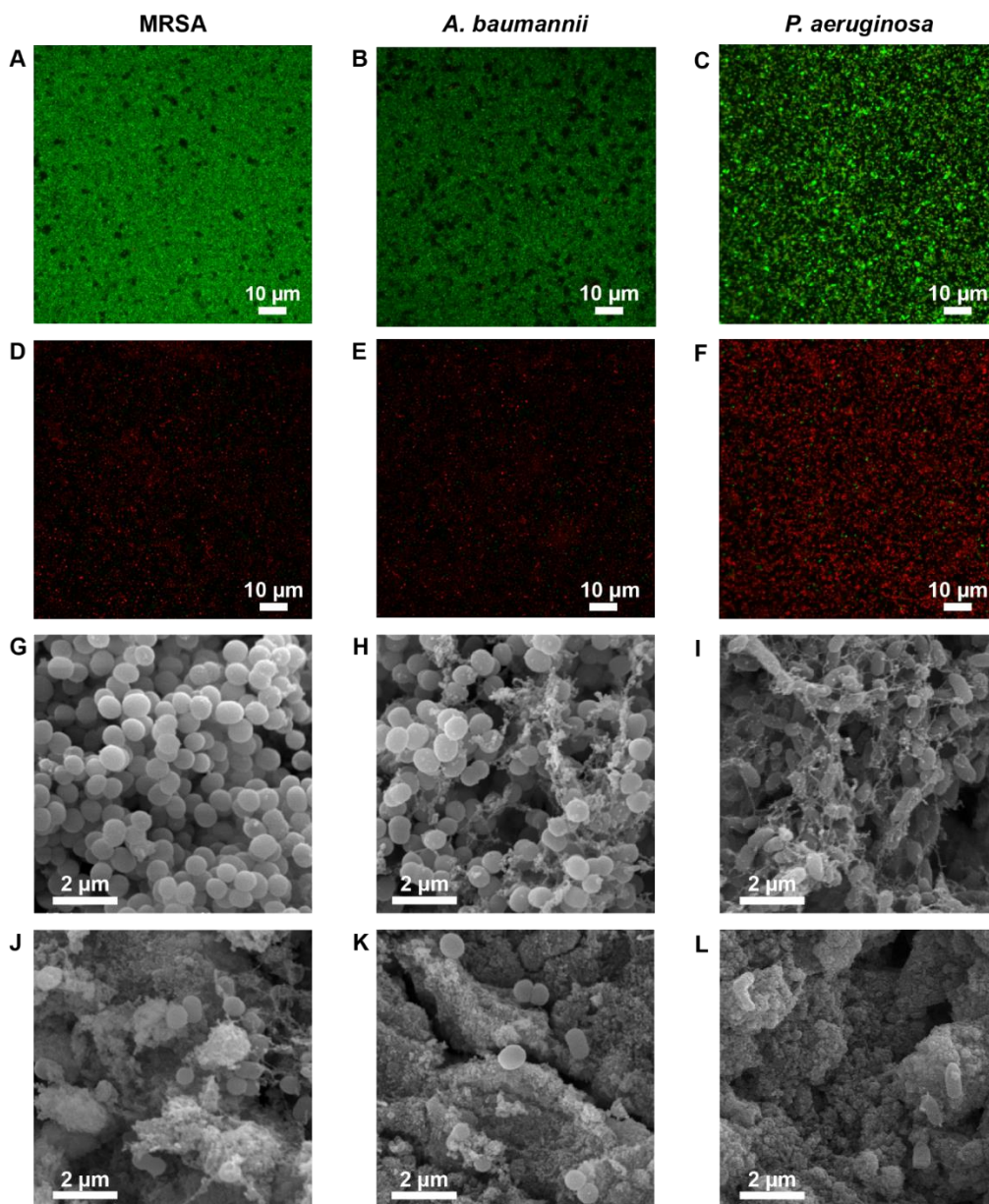
Figure 3.3. Analysis of effects of MoSe$_2$/PLL/F77 solution on biofilm growth. (A-C) Confocal images of the MRSA (A), *A. baumannii* (B), and *P. aeruginosa* (C) untreated control films. (D-F) Confocal images of MRSA (A), *A. baumannii* (B), and *P. aeruginosa* (C) biofilms treated with ~150 µg ml^{-1} of MoSe$_2$/PLL/F77. (G-I) SEM images of MRSA (G), *A. baumannii* (H), and *P. aeruginosa* (I) cells in absence of MoSe$_2$/PLL/F77. (J-L) SEM images of MRSA (J), *A. baumannii* (K), and *P. aeruginosa* (L) treated with ~150 µg ml^{-1} of MoSe$_2$/PLL/F77.

3.5 MoSe$_2$/PLL/F77 coating to inhibit biofilm growth

Biofilm growth and nosocomial infections can be caused by pathogenic bacteria harbored on medical instruments like implants, catheters, and pacemakers. Hence, the capacity of surfaces coated with MoSe$_2$/PLL/F77 to deter bacterial growth were examined. The medically relevant surfaces PMMA, which is used to coat denture strips; hydrophilic PTFE, which is used to coat catheters; and medical grade Ti alloy used in implants and pacemakers were coated with MoSe$_2$/PLL/F77 and exposed to bacteria. MRSA, *A. baumannii*, and *P. aeruginosa* biofilms were grown on uncoated and MoSe$_2$/PLL/F77-coated surfaces, followed by SEM imaging to see the differences in the growth. The MoSe$_2$/PLL/F77 coatings successfully repressed cell growth on all the materials, with massive differences in the final biofilm formation between control surfaces and coated surfaces (Figure 4A-F). PMMA-coated glass slides showed only ~6.53%, ~5.39%, and ~5.69% bacteria cells for MRSA, *A. baumannii* and *P. aeruginosa*, respectively, on coated samples compared to the uncoated samples (Figure S2A-C). Hydrophilic PTFE showed ~3.93%, ~5.02%, and ~6.57% bacteria cells for MRSA, *A. baumannii* and *P. aeruginosa*, respectively, on coated samples compared to the uncoated samples respectively (Figure S2D-F). Medical grade Ti alloy had ~3.28%, 4.30%, and ~2.66% bacteria cells of MRSA, *A. baumannii*, and *P. aeruginosa* on coated samples compared to the uncoated samples respectively (Figure S2G-I). This calculation was done by counting cells in three SEM images taken from different regions. Photographs and SEM images of PMMA glass slide, hydrophilic PTFE membrane and Ti alloy before and after coating with MoSe$_2$/PLL/F77 showed significant differences in appearance and color, clearly showing the presence of the coating (Figure S3). We also observed the coating to be robust and uniform even after multiple washes and incubation in liquid medium (Figure S3A-C). Although it was less robust on smoother surfaces like glass slides.

	MRSA	*A. baumannii*	*P. aeruginosa*

A

B

C

D

E

F
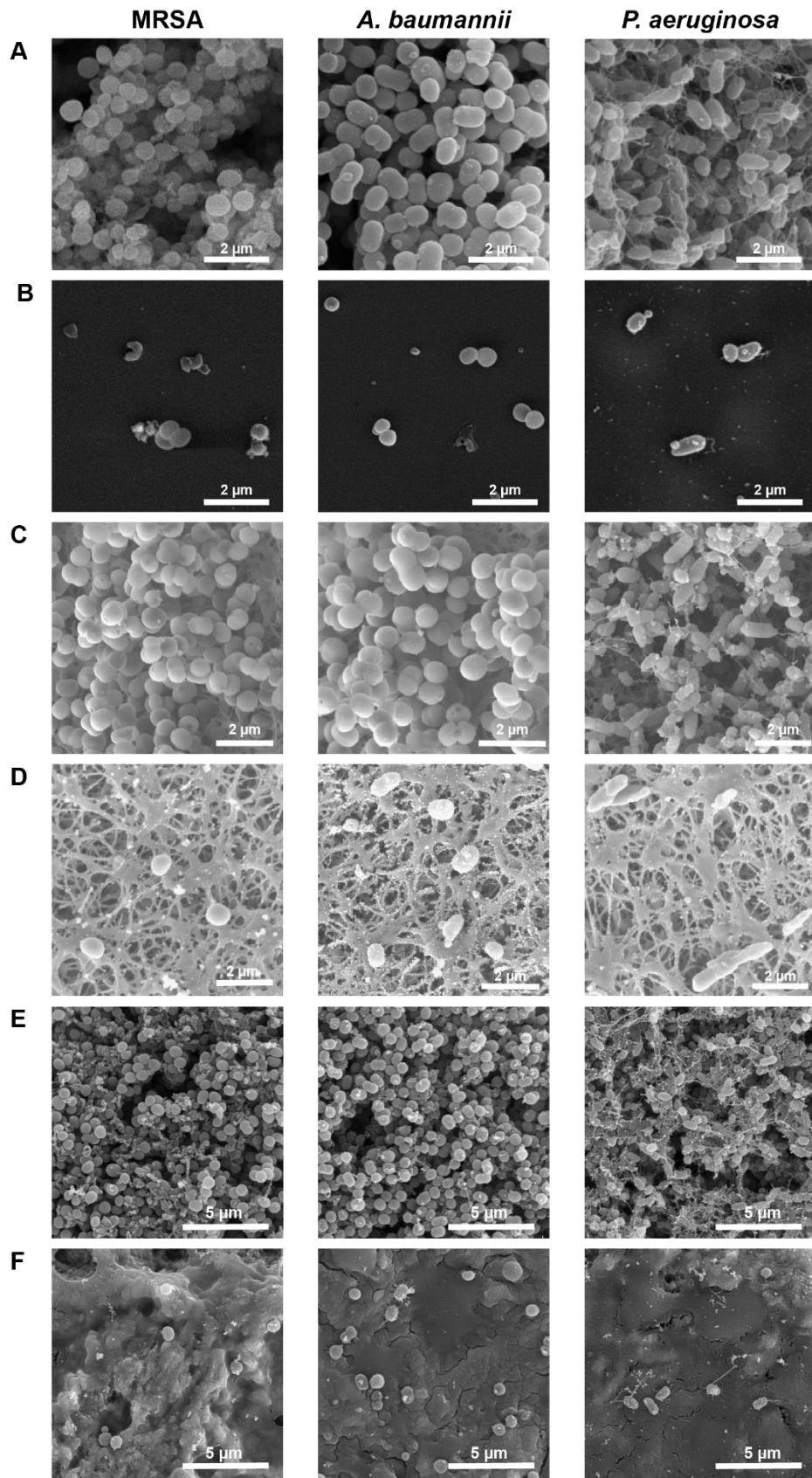
Figure 3.4. Inhibition of biofilm growth on different surfaces precoated with MoSe$_2$/PLL/F77.
(A, B) Biofilm growth of MRSA, *A. baumannii*, and *P. aeruginosa* on an uncoated (A) and coated (B) PMMA surface respectively. (C, D) Biofilm growth of MRSA, *A. baumannii*, and *P. aeruginosa* on uncoated (C) and coated (D) hydrophilic PTFE surface. (E, F) Biofilm growth of MRSA, *A. baumannii*, and *P. aeruginosa* on uncoated (E) and coated (F) medical grade Ti-alloy. (I) Comparing number of cells present on coated and uncoated surface of medical grade Ti-alloy.

To demonstrate the efficiency of the coating, MoSe$_2$/PLL/F77 was coated on the lower half of the MBEC assay plate stubs while the top half was kept uncoated (Figure 5A). Subsequently, biofilm growth was initiated along the entire stub for 48 h and processed for SEM imaging to observe the efficacy of the coating. Despite being on the same stub and treated under the same conditions, the uncoated part of the stub showed complete coverage by biofilm formation while the MoSe$_2$/PLL/F77-coated region had few individual cells to none, present (Figure 5C-E). MRSA, *A. baumanni*, and *P. aeruginosa* biofilms had ~4.08%, 4.19%, and 5.84% bacteria cells on the bottom coated region compared to the top uncoated region (Figure S4 D-G) which was manually determined on three images taken from different regions. To ensure that the bottom region was coated with MoSe$_2$/PLL/F77, EDX was performed on the coated as well as the uncoated region and compared for all three strains of bacteria (Figure S4A-C). Both the uncoated (bottom) and coated (top) region showed presence of carbon (C), oxygen (O) and sodium (Na). Phosphorous (P) and calcium (Ca) peaks are attributed to the hydroxyapatite MBEC plates. EDX also had trace amounts of palladium (Pd) and gold (Au) from the sputter coating. The coated region showed strong presence of ~8 and ~17 atomic percent of molybdenum (Mo) and selenium (Se), respectively (Figure 5B and Table S2), while there was negligible Mo or Se present in the uncoated regions. It was also observed that the percentage of C decreases significantly on the coated region to ~40 atomic percent as opposed to ~80 atomic percent in the uncoated region due to the extensive biofilm (Figure 5B and Table S2).
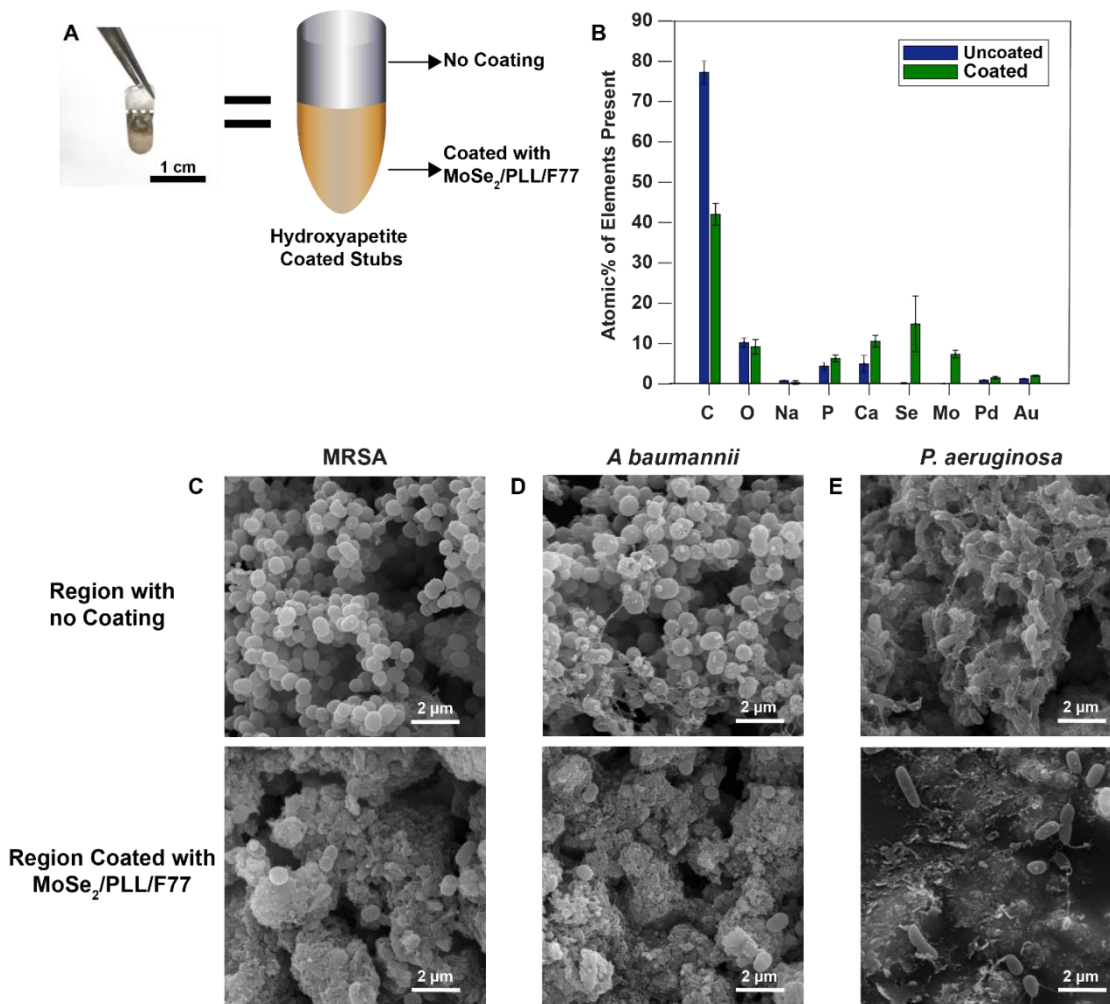
Figure 3.5. Analysis of biofilm growth on same object partially precoated with on MoSe₂/PLL/F77. (A) Photograph of the MBEC stub with top half uncoated and bottom half coated with MoSe₂/PLL/F77, along with a schematic diagram. (B) The atomic percentages of each element on the uncoated and coated region of the same stub from EDX measurements. (C-E) SEM images showing MRSA (C), *A. baumannii* (D), and *P. aeruginosa* (E) biofilm growth on top uncoated portion of MBEC (region with no coating) versus lack of biofilm growth on the bottom coated region of the same MBEC stub that is coated with MoSe₂/PLL/F77.

3.6 Biocompatibility test

In order to ensure the biocompatibility of these coated surfaces, the viability of mammalian HEK 293 cells were tested with alamarBlue assay and the cytotoxicity of the coating was observed with LDH assay. Resazurin present in alamarBlue solution indicates oxidation-reduction that is demonstrated by a colorimetric change. The reduced resorufin gives a fluorescent pink color, with the intensity proportional to the percentage of viable cells respiring. Thus, the change in color indicates the oxidation due to respiration, thus quantitatively measuring the viability of mammalian cells in presence of the coated substrate. The results show 95-100 % viability of mammalian cells (Figure 6A).

The supernatant was collected before treating the mammalian cells with alamarBlue followed by the LDH assay. Lactate dehydrogenase is a cytosolic enzyme secreted by damaged mammalian cells. The secreted LDH can be quantified by catalyzing the enzymatic reaction where tetrazolium salt is converted to a red formazan product. The level of formazan is proportional to percent of damaged cells. The results show ~4% cytotoxicity at 50 μg ml^{-1} of MoSe$_2$/PLL/F77 and a ~10% cytotoxicity at 200 μg ml^{-1} (Figure 6B). The low cytotoxic over a wide range of MoSe$_2$/PLL/F77 concentrations further demonstrates its biocompatibility.
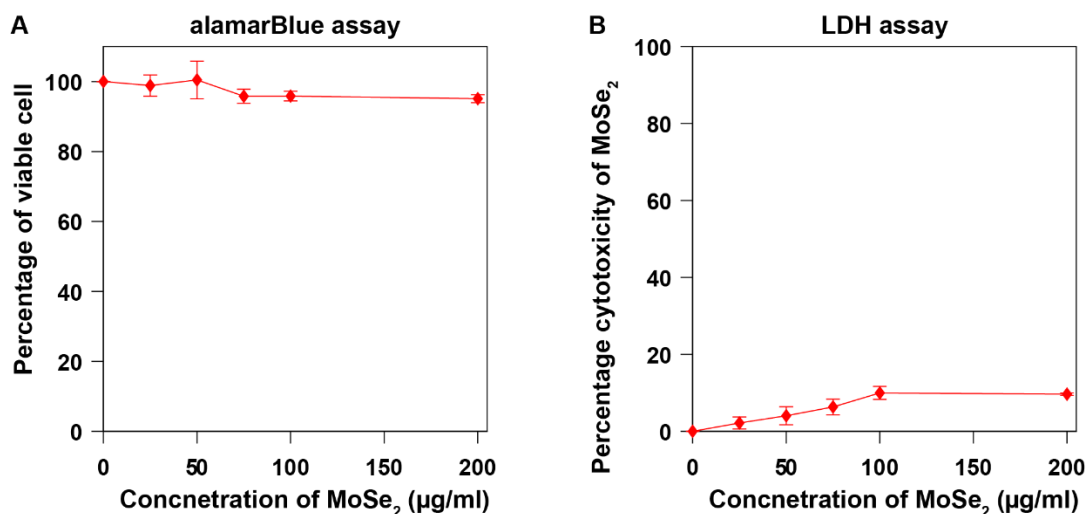
Figure 3.6. Biocompatibility test for MoSe$_2$/PLL/F77 coating. (A) Viability of HEK 293 mammalian cells tested with the help alamarBlue assay in presence of MoSe$_2$/PLL/F77 coated

hydrophilic PTFE membrane. (B) Percent cytotoxicity generated by MoSe₂/PLL/F77 coated hydrophilic PTFE membrane on HEK 293 cells.

3.7 Discussion

Biofilms are organized colonies of microbes (e.g., bacteria, fungi, or yeasts) that form heterogeneous bodies on living and non-living surfaces by secreting extracellular polymeric substances (EPS) to form ECM. These substances protect individual cells from such as antibacterial agents making it difficult to treat biofilm-related infections.[28] In this paper, we prepared MoSe₂ nanosheets encapsulated in cationic polymer PLL with the help of ultrasonication to electrostatically interact with negatively charged outer layer of bacteria. We used Pluronic F77 to stabilize the nanosheets in solution. Our results show excellent antibacterial activity, consistent with our previous results, with high biocompatibility and no antibacterial resistance for over 20 passages.[91] Both gram-positive and gram-negative bacteria were completely killed at 75 μg ml⁻¹ and 50 μg ml⁻¹ within 2 h of incubation.

The formation of biofilms leads to a rigid hydrated EPS secreted by bacteria, which is difficult for most particles or drugs to penetrate. The ECM varies in composition from strain to strain, but they are principally composed of DNA, lipids, and humic substances making them negatively charged.[37] Owing to the negatively charged matrix covering the biofilm, the cationic MoSe₂/PLL/F77 is attracted to ECM, leading to interaction of negatively charged ECM and positively charged PLL.[89] Also, the atomically thin nature of 2D MoSe₂ nanosheets can effectively perforate through the thick ECM layer to reach the cells underneath, causing membrane disruption and triggering cell death. Various other reports of antibiofilm agents typically focus on inhibition of initial biofilm formation;[92] however, removal of established biofilm remains a challenging problem. With the help of the MBEC assay we successfully destroyed 100% of the mature biofilms of MRSA, *A. baumannii* and *P. aeruginosa* at 150 μg ml⁻¹ concentration (Figure 2A and 2B).

The performance achieved in our results compare quite favorably with the existing literature. Previous antibiofilm studies with carbon-based nanomaterials like graphene quantum dots (GQDs) showed 48.85% destroyed at 500 μg ml⁻¹ concentration after 24 h incubation against *S. aureus* strains.[93] Graphene oxide was able to kill 20.16% and 10.22% *S. aureus* and *P.*

aeruginosa biofilm respectively.[37] In our results, MoSe$_2$/PLL/F77 destroyed 93.1% and 95.57% of MRSA and *P. aeruginosa*, respectively. When GO was coupled with silver nanoparticle (AgNPs) which are known antibacterial agents, the concentration required to kill 98% *P. aeruginosa* was 25 µg ml^{-1} but after 12 h of incubation.[41] Polyethyleneimine and AgNP-decorated GO nanocomposite (GO−PEI−Ag) showed further enhanced antibiofilm destruction of 89.96% *E.coli* and 93.45% *S. aureus* at just 10 µg/ml within 2 hour.[44] Our MoSe$_2$/PLL/F77 material was able to eradicate 100% mature bacterial biofilm within 6 h of incubation time with 150 µg ml^{-1}. The antibacterial activity of TMDCs have also been reported in the literature, where molybdenum disulfide-penicillin-near infrared (MoS$_2$-Pen-NIR) killed only ~86.15% *S. aureus* with 0.171 mg ml^{-1} (MoSe$_2$) + 0.366 mg ml^{-1} (Pen) within 6 h whereas MoSe$_2$/PLL/F77 killed 100% of *S. aureus* with 150 µg ml^{-1} within the same timeframe.[49] Chitosan (CS)-MoS$_2$ nanosheets loaded with antibiotics tetracycline hydrochloride (CM-TH) managed to only destroy ~80% at 80 µg ml^{-1} after treating it for 16-18 h.[40] Another report showed 80% killing with CS-MoS$_2$ with 225 µg ml^{-1}.[87]

Surface contamination due to the development of bacterial biofilms is a critical problem with nosocomial infections. Hence, there are extensive efforts to develop enhanced antimicrobial materials that can efficiently suppress bacterial adhesion and biofilm formation.[48] One of the most relevant issues is bacterial colonization of medical devices and implants after surgery that has a significant impact on both the patient health and the costs related to the treatment of the infection.[15] Hence, we showed successful coating of medically relevant surfaces with MoSe$_2$/PLL/F77: PMMA, which is used to coat denture strips; hydrophilic PTFE, which is used to coat catheters; and medical grade Ti alloy used in implants and pacemakers. All three MDR bacterial strains in this study (gram-positive (MRSA) and gram-negative (*A. baumannii*, and *P. aeruginosa*)) have completely suppressed biofilm growth with >94% killing of bacterial cells on the coated surfaces. A previous report has shown MoS$_2$ surfaces (MoS$_{2SUR}$) produced using MoS$_2$ particles (MoS$_{2PAR}$) inhibited 28.5% and 38.4% *S. aureus* and *P. aeruginosa* respectively with 20% concentration after 24 h.[94] Lanthanum hydroxide and graphene oxide nanocomposites (La@GO) managed to inhibit 100% of gram-negative *E. coli* within 2 h at a much higher concentration of 500 µg

51

ml^{-1}.[95] Various polymers have also been used like ultra-high molecular weight (uHMW) poly(N,N-dimethylacrylamide) (PDMA) inhibited >99.3% biofilm formation of *S, aureus* with 2 mg ml^{-1} dopamine and 10 mg ml^{-1} PDMA after 48 h.[47]

Overall, MoSe$_2$/PLL/F77 was able to eradicate both gram-positive and gram-negative bacterial biofilm at comparable concentration within just 6 h of time. It efficiently coated different medically relevant surfaces like PMMA glass slides, hydrophilic PTFE membranes and Ti-alloys. It was evident from the EDX data which demonstrates the presence of ~7% Mo and ~15% Se on the bottom coated region and the absence of them in the top uncoated region. Furthermore, increased carbon (C) percentage of ~77% on the uncoated surface shows the presence of biofilm which decreases down to ~42% in presence of biofilm coating. We hypothesize this comes from the remaining biomass attached to the surface observed from the CV assay (biomass left ~20%) even though the metabolic activity decreases to 0 as determined by the XTT assay. MoSe$_2$/PLL/F77 also proved to be biocompatible (>95%) with low toxicity (<10%) towards mammalian cells making it a highly suitable candidates for antimicrobial coatings. Thus, MoSe$_2$/PLL/F77 has great potential to be used as an antibiofilm agent as well as a coating for various surfaces to prevent the growth and spread of nosocomial infections.

3.8 Conclusion

MoSe$_2$ nanosheets dispersed in PLL and 0.5% F77 (MoSe$_2$/PLL/F77) were prepared by simple liquid phase exfoliation method. TEM imaging of the exfoliated nanosheets showed monolayer and few-layer nanosheets of various sizes, and UV-vis spectra showed the clear excitonic peaks of MoSe$_2$. Evaluation of the antibacterial activity of the MoSe$_2$/PLL/F77 nanosheets revealed their exceptional ability to kill both gram-positive (MRSA) and gram-negative (*A. baumannii and P. aeruginosa*) bacteria with MBC values of 50 to 75 µg ml^{-1} within 2 h. With the help of the MBEC assay, biofilm eradication concentration was determined to be 150 µg ml^{-1} within 6 h of exposure to MoSe$_2$/PLL/F77. The CV assay showed a significant decrease in biofilm mass (below 25%) and 0% metabolic activity after exposure of mature biofilms to MoSe$_2$/PLL/F77 for 6 h. We also demonstrated successful inhibition of biofilm growth on several medically relevant

coated surfaces (PMMA-coated glass slides, hydrophilic PTFE membranes and medical grade Ti-alloy) with only below ~6% surviving bacterial cell demonstrating the high efficacy of the $MoSe_2$/PLL/F77 coating. To substantiate our claim, we showed presence and absence of biofilm on a single surface which inhibits biofilm growth >94% on the $MoSe_2$/PLL/F77 coated region whereas the uncoated region is covered with biofilm. Furthermore, EDX analysis on the partially coated surface showed presence of Mo and Se elements on the coated region as opposed to increased presence of carbon on the uncoated region signifying presence of biomass, thereby proving the presence and effects of $MoSe_2$/PLL/F77 coating on biofilm growth. Finally, the high biocompatibility (>95%) of $MoSe_2$/PLL/F77 with mammalian cells with lower than 10% cytotoxicity of $MoSe_2$ makes it an ideal antibiofilm agent. The high antibacterial performance of the $MoSe_2$/PLL/F77 nanosheets with its ability to coat various surfaces introduces future possibilities for further exploiting them in developing antibiofilm coatings, wound dressings, and membranes for potential applications in health care settings which can further prevent and inhibit the growth of MDR biofilms.

3.9 References

1. Miao, H.; Teng, Z.; Wang, C.; Chong, H.; Wang, G., Recent Progress in Two-Dimensional Antimicrobial Nanomaterials. *Chemistry – A European Journal* **2019,** *25* (4), 929-944.

2. Liu, C.; Kong, D.; Hsu, P.-C.; Yuan, H.; Lee, H.-W.; Liu, Y.; Wang, H.; Wang, S.; Yan, K.; Lin, D.; Maraccini, P. A.; Parker, K. M.; Boehm, A. B.; Cui, Y., Rapid water disinfection using vertically aligned MoS2 nanofilms and visible light. *Nature Nanotechnology* **2016,** *11* (12), 1098-1104.

3. Meredith, H. R.; Srimani, J. K.; Lee, A. J.; Lopatkin, A. J.; You, L., Collective antibiotic tolerance: mechanisms, dynamics and intervention. *Nature Chemical Biology* **2015,** *11* (3), 182-188.

4. Tu, Y.; Lv, M.; Xiu, P.; Huynh, T.; Zhang, M.; Castelli, M.; Liu, Z.; Huang, Q.; Fan, C.; Fang, H.; Zhou, R., Destructive extraction of phospholipids from Escherichia coli membranes by graphene nanosheets. *Nature Nanotechnology* **2013,** *8* (8), 594-601.

5. Huh, A. J.; Kwon, Y. J., "Nanoantibiotics": A new paradigm for treating infectious diseases using nanomaterials in the antibiotics resistant era. *Journal of Controlled Release* **2011,** *156* (2), 128-145.

6. Rice, L. B., Federal Funding for the Study of Antimicrobial Resistance in Nosocomial Pathogens: No ESKAPE. *The Journal of Infectious Diseases* **2008,** *197* (8), 1079-1081.

7.   Roy, R.; Tiwari, M.; Donelli, G.; Tiwari, V., Strategies for combating bacterial biofilms: A focus on anti-biofilm agents and their mechanisms of action. *Virulence* **2018,** *9* (1), 522-554.

8.   Olsen, I., Biofilm-specific antibiotic tolerance and resistance. *European Journal of Clinical Microbiology & Infectious Diseases* **2015,** *34* (5), 877-886.

9.   Tursi, S. A.; Tükel, Ç., Curli-Containing Enteric Biofilms Inside and Out: Matrix Composition, Immune Recognition, and Disease Implications. *Microbiology and Molecular Biology Reviews* **2018,** *82* (4), e00028-18.

10.   Arciola, C. R.; Campoccia, D.; Speziale, P.; Montanaro, L.; Costerton, J. W., Biofilm formation in Staphylococcus implant infections. A review of molecular mechanisms and implications for biofilm-resistant materials. *Biomaterials* **2012,** *33* (26), 5967-5982.

11.   Brogden, K. A., Antimicrobial peptides: pore formers or metabolic inhibitors in bacteria? *Nature Reviews Microbiology* **2005,** *3* (3), 238-250.

12.   Costerton, J. W.; Stewart, P. S.; Greenberg, E. P., Bacterial Biofilms: A Common Cause of Persistent Infections. *Science* **1999,** *284* (5418), 1318.

13.   Davey, M. E.; O'Toole, G. A., Microbial biofilms: from ecology to molecular genetics. *Microbiol Mol Biol Rev* **2000,** *64* (4), 847-867.

14.   Hocevar, S. N.; Edwards, J. R.; Horan, T. C.; Morrell, G. C.; Iwamoto, M.; Lessa, F. C., Device-Associated Infections among Neonatal Intensive Care Unit Patients: Incidence and Associated Pathogens Reported to the National Healthcare Safety Network, 2006–2008. *Infection Control & Hospital Epidemiology* **2015,** *33* (12), 1200-1206.

15.   de Miguel, I.; Prieto, I.; Albornoz, A.; Sanz, V.; Weis, C.; Turon, P.; Quidant, R., Plasmon-Based Biofilm Inhibition on Surgical Implants. *Nano Letters* **2019,** *19* (4), 2524-2529.

16.   Hall-Stoodley, L.; Costerton, J. W.; Stoodley, P., Bacterial biofilms: from the Natural environment to infectious diseases. *Nature Reviews Microbiology* **2004,** *2* (2), 95-108.

17.   Jung, C.-J.; Yeh, C.-Y.; Shun, C.-T.; Hsu, R.-B.; Cheng, H.-W.; Lin, C.-S.; Chia, J.-S., Platelets Enhance Biofilm Formation and Resistance of Endocarditis-Inducing Streptococci on the Injured Heart Valve. *The Journal of Infectious Diseases* **2012,** *205* (7), 1066-1075.

18.   Scott, R. D., The Direct medical costs of healthcare-associated infections in U.S. hospitals and the benefits of prevention. *Cdc* **2009**.

19.   van Kleef, E.; Robotham, J. V.; Jit, M.; Deeny, S. R.; Edmunds, W. J., Modelling the transmission of healthcare associated infections: a systematic review. *BMC Infect Dis* **2013,** *13*, 294-294.

20.   Elder, M. J.; Stapleton, F.; Evans, E.; Dart, J. K. G., Biofilm-related infections in ophthalmology. *Eye* **1995,** *9* (1), 102-109.

21.   Pajkos, A.; Deva, A. K.; Vickery, K.; Cope, C.; Chang, L.; Cossart, Y. E., Detection of subclinical infection in significant breast implant capsules. *Plastic and reconstructive surgery* **2003,** *111* (5), 1605-11.

22.   Rogers, J.; Norkett, D. I.; Bracegirdle, P.; Dowsett, A. B.; Walker, J. T.; Brooks, T.; Keevil, C. W., Examination of biofilm formation and risk of infection associated with the use of urinary catheters with leg bags. *The Journal of hospital infection* **1996,** *32* (2), 105-15.

23.   Ruellan, K.; Frijns, J. H. M.; Bloemberg, G. V.; Hautefort, C.; Van den Abbeele, T.; Lamers, G. E. M.; Herman, P.; Ba Huy, P. T.; Kania, R. E., Detection of Bacterial Biofilm on Cochlear Implants Removed Because of Device Failure, Without Evidence of Infection. *Otology & Neurotology* **2010,** *31* (8).

24.   Sandoe, J. A. T.; Witherden, I. R.; Cove, J. H.; Heritage, J.; Wilcox, M. H., Correlation between enterococcal biofilm formation in vitro and medical-device-related infection potential in vivo. *Journal of Medical Microbiology* **2003,** *52* (7), 547-550.

25.   Viola, G. M.; Darouiche, R. O., Cardiovascular Implantable Device Infections. *Current Infectious Disease Reports* **2011,** *13* (4), 333-342.

26.   Gasser, M.; Zingg, W.; Cassini, A.; Kronenberg, A., Attributable deaths and disability-adjusted life-years caused by infections with antibiotic-resistant bacteria in Switzerland. *The Lancet. Infectious diseases* **2019,** *19* (1), 17-18.

27.   Mehta, Y.; Gupta, A.; Todi, S.; Myatra, S.; Samaddar, D. P.; Patil, V.; Bhattacharya, P. K.; Ramasubban, S., Guidelines for prevention of hospital acquired infections. *Indian J Crit Care Med* **2014,** *18* (3), 149-163.

28.   Ramasamy, M.; Lee, J., Recent Nanotechnology Approaches for Prevention and Treatment of Biofilm-Associated Infections on Medical Devices. *BioMed Research International* **2016,** *2016*, 1851242.

29.   Colon, G.; Ward, B. C.; Webster, T. J., Increased osteoblast and decreased Staphylococcus epidermidis functions on nanophase ZnO and TiO2. *Journal of Biomedical Materials Research Part A* **2006,** *78A* (3), 595-604.

30.   Jones, N.; Ray, B.; Ranjit, K. T.; Manna, A. C., Antibacterial activity of ZnO nanoparticle suspensions on a broad spectrum of microorganisms. *FEMS Microbiology Letters* **2008,** *279* (1), 71-76.

31.   Lee, J.-H.; Kim, Y.-G.; Cho, M. H.; Lee, J., ZnO nanoparticles inhibit Pseudomonas aeruginosa biofilm formation and virulence factor production. *Microbiological Research* **2014,** *169* (12), 888-896.

32.   Gupta, A.; Landis, R. F.; Li, C.-H.; Schnurr, M.; Das, R.; Lee, Y.-W.; Yazdani, M.; Liu, Y.; Kozlova, A.; Rotello, V. M., Engineered Polymer Nanoparticles with Unprecedented Antimicrobial Efficacy and Therapeutic Indices against Multidrug-Resistant Bacteria and Biofilms. *Journal of the American Chemical Society* **2018,** *140* (38), 12137-12143.

33.   Haghighi, F.; Mohammadi, S. R.; Mohammadi, P.; Hosseinkhani, S.; Shidpour, R. In *Antifungal Activity of TiO 2 nanoparticles and EDTA on Candida albicans Biofilms*, 2013.

34.   Inbakandan, D.; Kumar, C.; Abraham, L. S.; Kirubagaran, R.; Venkatesan, R.; Khan, S. A., Silver nanoparticles with anti microfouling effect: A study against marine biofilm forming bacteria. *Colloids and Surfaces B: Biointerfaces* **2013,** *111*, 636-643.

35.   Murthy, P. S.; Venugopalan, V. P.; Arunya, D. D.; Dhara, S.; Pandiyan, R.; Tyagi, A. K. In *Antibiofilm activity of nano sized CuO*, International Conference on Nanoscience, Engineering and Technology (ICONSET 2011), 28-30 Nov. 2011; 2011; pp 580-583.

36.   Yu, Q.; Li, J.; Zhang, Y.; Wang, Y.; Liu, L.; Li, M., Inhibition of gold nanoparticles (AuNPs) on pathogenic biofilm formation and invasion to host cells. *Scientific Reports* **2016,** *6* (1), 26667.

37.   Di Giulio, M.; Zappacosta, R.; Di Lodovico, S.; Di Campli, E.; Siani, G.; Fontana, A.; Cellini, L., Antimicrobial and Antibiofilm Efficacy of Graphene Oxide against Chronic Wound Microorganisms. *Antimicrob Agents Chemother* **2018,** *62* (7), e00547-18.

38.   Kang, S.; Pinault, M.; Pfefferle, L. D.; Elimelech, M., Single-Walled Carbon Nanotubes Exhibit Strong Antimicrobial Activity. *Langmuir* **2007,** *23* (17), 8670-8673.

39.   Liu, S.; Cao, S.; Guo, J.; Luo, L.; Zhou, Y.; Lin, C.; Shi, J.; Fan, C.; Lv, M.; Wang, L., Graphene oxide–silver nanocomposites modulate biofilm formation and extracellular polymeric substance (EPS) production. *Nanoscale* **2018,** *10* (41), 19603-19611.

40.   Zhang, X.; Zhang, W.; Liu, L.; Yang, M.; Huang, L.; Chen, K.; Wang, R.; Yang, B.; Zhang, D.; Wang, J., Antibiotic-loaded MoS2nanosheets to combat bacterial resistance via biofilm inhibition. *Nanotechnology* **2017,** *28* (22), 225101.

41.   Wang, Y.; Kadiyala, U.; Qu, Z.; Elvati, P.; Altheim, C.; Kotov, N. A.; Violi, A.; VanEpps, J. S., Anti-Biofilm Activity of Graphene Quantum Dots via Self-Assembly with Bacterial Amyloid Proteins. *ACS Nano* **2019,** *13* (4), 4278-4289.

42.   Geilich, B. M.; Webster, T. J., Reduced adhesion of Staphylococcus aureus to ZnO/PVC nanocomposites. *Int J Nanomedicine* **2013,** *8*, 1177-1184.

43.   Some, S.; Ho, S.-M.; Dua, P.; Hwang, E.; Shin, Y. H.; Yoo, H.; Kang, J.-S.; Lee, D.-k.; Lee, H., Dual Functions of Highly Potent Graphene Derivative–Poly-l-Lysine Composites To Inhibit Bacteria and Support Human Cells. *ACS Nano* **2012,** *6* (8), 7151-7161.

44.   Zhao, R.; Kong, W.; Sun, M.; Yang, Y.; Liu, W.; Lv, M.; Song, S.; Wang, L.; Song, H.; Hao, R., Highly Stable Graphene-Based Nanocomposite (GO–PEI–Ag) with Broad-Spectrum, Long-Term Antimicrobial Activity and Antibiofilm Effects. *ACS Applied Materials & Interfaces* **2018,** *10* (21), 17617-17629.

45.   Landis, R. F.; Li, C.-H.; Gupta, A.; Lee, Y.-W.; Yazdani, M.; Ngernyuang, N.; Altinbasak, I.; Mansoor, S.; Khichi, M. A. S.; Sanyal, A.; Rotello, V. M., Biodegradable Nanocomposite Antimicrobials for the Eradication of Multidrug-Resistant Bacterial Biofilms without Accumulated Resistance. *Journal of the American Chemical Society* **2018,** *140* (19), 6176-6182.

46.   Li, J.; Zhang, K.; Ruan, L.; Chin, S. F.; Wickramasinghe, N.; Liu, H.; Ravikumar, V.; Ren, J.; Duan, H.; Yang, L.; Chan-Park, M. B., Block Copolymer Nanoparticles Remove Biofilms of Drug-Resistant Gram-Positive Bacteria by Nanoscale Bacterial Debridement. *Nano Letters* **2018,** *18* (7), 4180-4187.

47.   Mei, Y.; Yu, K.; Lo, J. C. Y.; Takeuchi, L. E.; Hadjesfandiari, N.; Yazdani-Ahmadabadi, H.; Brooks, D. E.; Lange, D.; Kizhakkedathu, J. N., Polymer–Nanoparticle Interaction as a Design Principle in the Development of a Durable Ultrathin Universal Binary Antibiofilm Coating with Long-Term Activity. *ACS Nano* **2018,** *12* (12), 11881-11891.

48.   Park, H.-H.; Sun, K.; Seong, M.; Kang, M.; Park, S.; Hong, S.; Jung, H.; Jang, J.; Kim, J.; Jeong, H. E., Lipid-Hydrogel-Nanostructure Hybrids as Robust Biofilm-Resistant Polymeric Materials. *ACS Macro Letters* **2019,** *8* (1), 64-69.

49.   Zhang, C.; Hu, D.-F.; Xu, J.-W.; Ma, M.-Q.; Xing, H.; Yao, K.; Ji, J.; Xu, Z.-K., Polyphenol-Assisted Exfoliation of Transition Metal Dichalcogenides into Nanosheets as Photothermal Nanocarriers for Enhanced Antibiofilm Activity. *ACS Nano* **2018,** *12* (12), 12347-12356.

50.   Pattani, V. P.; Tunnell, J. W., Nanoparticle-mediated photothermal therapy: A comparative study of heating for different particle types. *Lasers in Surgery and Medicine* **2012,** *44* (8), 675-684.

51.   Vallejo-Fernandez, G.; Whear, O.; Roca, A. G.; Hussain, S.; Timmis, J.; Patel, V.; O'Grady, K., Mechanisms of hyperthermia in magnetic nanoparticles. *Journal of Physics D: Applied Physics* **2013,** *46* (31), 312001.

52.   Geim, A. K., Graphene: Status and Prospects. *Science* **2009,** *324* (5934), 1530.

53.   Novoselov, K. S.; Geim, A. K.; Morozov, S. V.; Jiang, D.; Zhang, Y.; Dubonos, S. V.; Grigorieva, I. V.; Firsov, A. A., Electric Field Effect in Atomically Thin Carbon Films. *Science* **2004,** *306* (5696), 666.

54.   Ding, L.; Wei, Y.; Wang, Y.; Chen, H.; Caro, J.; Wang, H., A Two-Dimensional Lamellar Membrane: MXene Nanosheet Stacks. *Angewandte Chemie International Edition* **2017,** *56* (7), 1825-1829.

55.   Tan, C.; Cao, X.; Wu, X.-J.; He, Q.; Yang, J.; Zhang, X.; Chen, J.; Zhao, W.; Han, S.; Nam, G.-H.; Sindoro, M.; Zhang, H., Recent Advances in Ultrathin Two-Dimensional Nanomaterials. *Chemical Reviews* **2017,** *117* (9), 6225-6331.

56.   Tan, C.; Lai, Z.; Zhang, H., Ultrathin Two-Dimensional Multinary Layered Metal Chalcogenide Nanomaterials. *Advanced Materials* **2017,** *29* (37), 1701392.

57.   Xue, Y.; Zhang, Q.; Wang, W.; Cao, H.; Yang, Q.; Fu, L., Opening Two-Dimensional Materials for Energy Conversion and Storage: A Concept. *Advanced Energy Materials* **2017,** *7* (19), 1602684.

58.   Zhang, H., Ultrathin Two-Dimensional Nanomaterials. *ACS Nano* **2015,** *9* (10), 9451-9469.

59.   Maitra, U.; Gupta, U.; De, M.; Datta, R.; Govindaraj, A.; Rao, C. N. R., Highly Effective Visible-Light-Induced H2 Generation by Single-Layer 1T-MoS2 and a Nanocomposite of Few-Layer 2H-MoS2 with Heavily Nitrogenated Graphene. *Angewandte Chemie International Edition* **2013,** *52* (49), 13057-13061.

60.   Pan, L.; Liu, Y.-T.; Xie, X.-M.; Ye, X.-Y., Facile and Green Production of Impurity-Free Aqueous Solutions of WS2 Nanosheets by Direct Exfoliation in Water. *Small* **2016,** *12* (48), 6703-6713.

61.   Shi, Y.; Wang, J.; Wang, C.; Zhai, T.-T.; Bao, W.-J.; Xu, J.-J.; Xia, X.-H.; Chen, H.-Y., Hot Electron of Au Nanorods Activates the Electrocatalysis of Hydrogen Evolution on MoS2 Nanosheets. *Journal of the American Chemical Society* **2015,** *137* (23), 7365-7370.

62.   Hizir, M. S.; Robertson, N. M.; Balcioglu, M.; Alp, E.; Rana, M.; Yigit, M. V., Universal sensor array for highly selective system identification using two-dimensional nanoparticles. *Chemical Science* **2017,** *8* (8), 5735-5745.

63.   Sun, X.; Fan, J.; Fu, C.; Yao, L.; Zhao, S.; Wang, J.; Xiao, J., WS2 and MoS2 biosensing platforms using peptides as probe biomolecules. *Scientific Reports* **2017,** *7* (1), 10290.

64.   Li, W.; Yang, Y.; Weber, J. K.; Zhang, G.; Zhou, R., Tunable, Strain-Controlled Nanoporous MoS2 Filter for Water Desalination. *ACS Nano* **2016,** *10* (2), 1829-1835.

65.   Wang, J.-Z.; Lu, L.; Lotya, M.; Coleman, J. N.; Chou, S.-L.; Liu, H.-K.; Minett, A. I.; Chen, J., Development of MoS2–CNT Composite Thin Film from Layered MoS2 for Lithium Batteries. *Advanced Energy Materials* **2013,** *3* (6), 798-805.

66.   Ai, K.; Ruan, C.; Shen, M.; Lu, L., MoS2 Nanosheets with Widened Interlayer Spacing for High-Efficiency Removal of Mercury in Aquatic Systems. *Advanced Functional Materials* **2016,** *26* (30), 5542-5549.

67.   Sun, L.; Ying, Y.; Huang, H.; Song, Z.; Mao, Y.; Xu, Z.; Peng, X., Ultrafast Molecule Separation through Layered WS2 Nanosheet Membranes. *ACS Nano* **2014,** *8* (6), 6304-6311.

68.   Chimene, D.; Alge, D. L.; Gaharwar, A. K., Two-Dimensional Nanomaterials for Biomedical Applications: Emerging Trends and Future Prospects. *Advanced Materials* **2015,** *27* (45), 7261-7284.

69.   Jia, X.; Bai, J.; Ma, Z.; Jiang, X., BSA-exfoliated WSe2 nanosheets as a photoregulated carrier for synergistic photodynamic/photothermal therapy. *Journal of Materials Chemistry B* **2017,** *5* (2), 269-278.

70.   Liu, T.; Shi, S.; Liang, C.; Shen, S.; Cheng, L.; Wang, C.; Song, X.; Goel, S.; Barnhart, T. E.; Cai, W.; Liu, Z., Iron Oxide Decorated MoS2 Nanosheets with Double PEGylation for Chelator-Free Radiolabeling and Multimodal Imaging Guided Photothermal Therapy. *ACS Nano* **2015,** *9* (1), 950-960.

71.   Yin, W.; Yan, L.; Yu, J.; Tian, G.; Zhou, L.; Zheng, X.; Zhang, X.; Yong, Y.; Li, J.; Gu, Z.; Zhao, Y., High-Throughput Synthesis of Single-Layer MoS2 Nanosheets as a Near-Infrared Photothermal-Triggered Drug Delivery for Effective Cancer Therapy. *ACS Nano* **2014,** *8* (7), 6922-6933.

72.   Xia, M.-Y.; Xie, Y.; Yu, C.-H.; Chen, G.-Y.; Li, Y.-H.; Zhang, T.; Peng, Q., Graphene-based nanomaterials: the promising active agents for antibiotics-independent antibacterial applications. *Journal of Controlled Release* **2019,** *307*, 16-31.

73.   Gupta, A.; Sakthivel, T.; Seal, S., Recent development in 2D materials beyond graphene. *Progress in Materials Science* **2015,** *73*, 44-126.

74.   Kim, T. I.; Kwon, B.; Yoon, J.; Park, I.-J.; Bang, G. S.; Park, Y.; Seo, Y.-S.; Choi, S.-Y., Antibacterial Activities of Graphene Oxide–Molybdenum Disulfide Nanocomposite Films. *ACS Applied Materials & Interfaces* **2017,** *9* (9), 7908-7917.

75.   Yang, X.; Li, J.; Liang, T.; Ma, C.; Zhang, Y.; Chen, H.; Hanagata, N.; Su, H.; Xu, M., Antibacterial activity of two-dimensional MoS2 sheets. *Nanoscale* **2014,** *6* (17), 10126-10133.

76.   Pang, X.; Xiao, Q.; Cheng, Y.; Ren, E.; Lian, L.; Zhang, Y.; Gao, H.; Wang, X.; Leung, W.; Chen, X.; Liu, G.; Xu, C., Bacteria-Responsive Nanoliposomes as Smart Sonotheranostics for Multidrug Resistant Bacterial Infections. *ACS Nano* **2019,** *13* (2), 2427-2438.

77.   Coleman, J. N.; Lotya, M.; O'Neill, A.; Bergin, S. D.; King, P. J.; Khan, U.; Young, K.; Gaucher, A.; De, S.; Smith, R. J.; Shvets, I. V.; Arora, S. K.; Stanton, G.; Kim, H.-Y.; Lee, K.; Kim, G. T.; Duesberg, G. S.; Hallam, T.; Boland, J. J.; Wang, J. J.; Donegan, J. F.; Grunlan, J. C.; Moriarty, G.; Shmeliov, A.; Nicholls, R. J.; Perkins, J. M.; Grieveson, E. M.; Theuwissen, K.; McComb, D. W.; Nellist, P. D.; Nicolosi, V., Two-Dimensional Nanosheets Produced by Liquid Exfoliation of Layered Materials. *Science* **2011,** *331* (6017), 568.

78.   Smith, R. J.; King, P. J.; Lotya, M.; Wirtz, C.; Khan, U.; De, S.; O'Neill, A.; Duesberg, G. S.; Grunlan, J. C.; Moriarty, G.; Chen, J.; Wang, J.; Minett, A. I.; Nicolosi, V.; Coleman, J. N., Large-Scale Exfoliation of Inorganic Layered Compounds in Aqueous Surfactant Solutions. *Advanced Materials* **2011,** *23* (34), 3944-3948.

79.   Zong, L.; Li, M.; Li, C., Bioinspired Coupling of Inorganic Layered Nanomaterials with Marine Polysaccharides for Efficient Aqueous Exfoliation and Smart Actuating Hybrids. *Advanced Materials* **2017,** *29* (10), 1604691.

80.   Guan, G.; Xia, J.; Liu, S.; Cheng, Y.; Bai, S.; Tee, S. Y.; Zhang, Y.-W.; Han, M.-Y., Electrostatic-Driven Exfoliation and Hybridization of 2D Nanomaterials. *Advanced Materials* **2017,** *29* (32), 1700326.

81.   Guan, G.; Zhang, S.; Liu, S.; Cai, Y.; Low, M.; Teng, C. P.; Phang, I. Y.; Cheng, Y.; Duei, K. L.; Srinivasan, B. M.; Zheng, Y.; Zhang, Y.-W.; Han, M.-Y., Protein Induces Layer-by-Layer Exfoliation of Transition Metal Dichalcogenides. *Journal of the American Chemical Society* **2015,** *137* (19), 6152-6155.

82.   Ravula, S.; Essner, J. B.; Baker, G. A., Kitchen-Inspired Nanochemistry: Dispersion, Exfoliation, and Hybridization of Functional MoS2 Nanosheets Using Culinary Hydrocolloids. *ChemNanoMat* **2015,** *1* (3), 167-177.

83.   Jia, W.; Tang, B.; Wu, P., Nafion-assisted exfoliation of MoS2 in water phase and the application in quick-response NIR light controllable multi-shape memory membrane. *Nano Research* **2018,** *11* (1), 542-553.

84.   Roy, S.; Mondal, A.; Yadav, V.; Sarkar, A.; Banerjee, R.; Sanpui, P.; Jaiswal, A., Mechanistic Insight into the Antibacterial Activity of Chitosan Exfoliated MoS2 Nanosheets: Membrane Damage, Metabolic Inactivation, and Oxidative Stress. *ACS Applied Bio Materials* **2019,** *2* (7), 2738-2755.

85.   Vega-Mayoral, V.; Backes, C.; Hanlon, D.; Khan, U.; Gholamvand, Z.; O'Brien, M.; Duesberg, G. S.; Gadermaier, C.; Coleman, J. N., Photoluminescence from Liquid-Exfoliated WS2 Monomers in Poly(Vinyl Alcohol) Polymer Composites. *Advanced Functional Materials* **2016,** *26* (7), 1028-1039.

86.   Yuan, Y.; Li, R.; Liu, Z., Establishing Water-Soluble Layered WS2 Nanosheet as a Platform for Biosensing. *Analytical Chemistry* **2014,** *86* (7), 3610-3615.

87.   Lin, D. W.; Bettinger, C. J.; Ferreira, J. P.; Wang, C. L.; Bao, Z., A Cell-Compatible Conductive Film from a Carbon Nanotube Network Adsorbed on Poly-l-lysine. *ACS Nano* **2011,** *5* (12), 10026-10032.

88.   Colville, K.; Tompkins, N.; Rutenberg, A. D.; Jericho, M. H., Effects of Poly(l-lysine) Substrates on Attached Escherichia coli Bacteria. *Langmuir* **2010,** *26* (4), 2639-2644.

89.   Debnath, A., Saha, S., Wang, Q. H., and Green, A. A, Eradication of Multidrug-Resistant Bacteria Using Poly-L-Lysine-Encapsulated 2D Molybdenum Didelenide Nanosheets. **2021 (in preperation)**.

90.   Singh, S. P.; Ramanan, S.; Kaufman, Y.; Arnusch, C. J., Laser-Induced Graphene Biofilm Inhibition: Texture Does Matter. *ACS Applied Nano Materials* **2018,** *1* (4), 1713-1720.

91.   Debnath, A.; Saha, S.; Li, D. O.; Chu, X. S.; Ulissi, Z. W.; Green, A. A.; Wang, Q. H., Elimination of Multidrug-Resistant Bacteria by Transition Metal Dichalcogenides Encapsulated by Synthetic Single-Stranded DNA. *ACS Applied Materials & Interfaces* **2021,** *13* (7), 8082-8094.

92.   Mei, L.; Zhu, S.; Yin, W.; Chen, C.; Nie, G.; Gu, Z.; Zhao, Y., Two-dimensional nanomaterials beyond graphene for antibacterial applications: current progress and future perspectives. *Theranostics* **2020,** *10* (2), 757-781.

93.   Joseph, R.; Naugolny, A.; Feldman, M.; Herzog, I. M.; Fridman, M.; Cohen, Y., Cationic Pillararenes Potently Inhibit Biofilm Formation without Affecting Bacterial Growth and Viability. *Journal of the American Chemical Society* **2016,** *138* (3), 754-757.

94.   Amin, M.; Rowley-Neale, S.; Shalamanova, L.; Lynch, S.; Wilson-Nieuwenhuis, J. T.; El Mohtadi, M.; Banks, C. E.; Whitehead, K. A., Molybdenum Disulfide Surfaces to Reduce Staphylococcus aureus and Pseudomonas aeruginosa Biofilm Formation. *ACS Applied Materials & Interfaces* **2020,** *12* (18), 21057-21069.

95.   Zheng, H.; Ji, Z.; Roy, K. R.; Gao, M.; Pan, Y.; Cai, X.; Wang, L.; Li, W.; Chang, C. H.; Kaweeteerawat, C.; Chen, C.; Xia, T.; Zhao, Y.; Li, R., Engineered Graphene Oxide Nanocomposite Capable of Preventing the Evolution of Antimicrobial Resistance. *ACS Nano* **2019,** *13* (10), 11488-11499.

CHAPTER 4

Eradication of Fungi Using MoSe$_2$/Chitosan Nanosheets

4.1 Introduction

Fungal diseases have emerged as one of the leading causes of deaths across the world.[1] Along with the significant threat to human health, these fungal pathogens can cause considerable economic losses.[2] The treatment of fungal diseases is increasingly challenging due to the emergence of antifungal drug resistance,[3] leading to a high mortality rate.[4] In the past few years, fungal diseases have infected over a billion patients per year worldwide, leading to more than 1.5 million fatalities.[1-2, 4] Recent global estimates have found that ~3,000,000 cases of chronic pulmonary aspergillosis, ~223,100 cases of cryptococcal meningitis complicating HIV/AIDS, ~700,000 cases of invasive candidiasis, ~250,000 cases of invasive aspergillosis and over 10,000,000 cases of fungal asthma occur annually.[5] Fungal disease can also damage plants and crops, causing major losses in agricultural activities and food production.[6] Animal pathogenic fungi are threatening bats, amphibians and reptiles with extinction.[7] It is estimated that fungi are the highest threat for animal-host and plant-host species, representing the major cause (approximately 65%) of pathogen-driven host loss.[8] In this complex scenario, it is now increasingly clear that climate change has resulted in increased incidences of fungal diseases.[9] Furthermore, there is an emerging pathogen *Candida auris* (*C. auris*) that has been associated with nosocomial outbreaks on five continents.[10] This new species of yeast was first discovered in Japan in 2009[11] and has garnered massive attention due to its worldwide spread, its ability to cause epidemics in healthcare settings, and its resilience against enhanced infection prevention and control (IPC) measures.[12] *C. auris* frequently occurs in critically ill patients exhibiting innate and evolving resistance to common anti-fungal drugs and displays higher minimum inhibitory concentrations (MICs) than usual,[13-14] leading to its recognition as multi-drug resistant (MDR). Hence, the global emergence of *C. auris* validates a new threat that will require enhanced antifungal agents and prevention control measures across the world.[12, 15-16] Current therapeutics to treat fungal diseases remain insufficient as compared to antibiotics, and novel therapeutic alternatives are promptly required.[17] Based on all these factors, concerns over a pandemic of fungal origin in the near future have been raised.[7]

Currently, therapeutic options for antifungal drugs are limited to Amphotericin B, azoles, echinocandins and 5-flucytosine. However, pathogenic fungi have several well-characterized resistance mechanisms leading to the gradual inefficacy of these drugs.[13, 17-21] Although researchers are investigating novel ways to target these resistant fungal pathogens, they are evolving and growing new resistant genes at a much faster rate. Hence, alternative approaches are needed to strengthen the antifungal pipeline.[1] In recent years, nanomaterials have been used to form novel antimicrobial agents with distinctive chemical and physical properties.[17, 22] Nanomaterials like silver (Ag),[22-23] zinc oxide (ZnO),[24] titanium dioxide (TiO$_2$),[24] iron oxide (Fe$_3$O$_4$),[25] copper oxide (CuO),[26] magnesium oxide (MgO),[27] and nitric oxide (NO) nanoparticles[28] have displayed antibacterial activity. However, their toxicity has proven to be challenging for applications in the biomedical field.[29] One-dimensional (1D) single walled carbon nanotubes (SWCNTs) displayed antifungal activity against *Fusarium graminearum* and *Fusarium poae* but at very high concentrations of 500 µg ml^{-1} with less than 96% killing efficiency.[30] However, CNTs when conjugated with antifungal drugs like amphotericin B showed relatively good killing efficiency at 80 µg ml^{-1} against *Candida albicans*.[31] Two-dimensional (2D) nanomaterials have attracted a great deal of attention in the past decade as potential antimicrobial agents.[32] Carbon-based nanomaterials (CBNs) such as graphene and graphene oxide have been studied extensively for their antimicrobial properties,[33-34] due to their extremely high mechanical strength, large surface to volume ratio and prominent physicochemical properties in interaction with bacteria.[35] Lately, transition-metal dichalcogenides (TMDCs) have also shown unique potential in the biomedical field.[36-37] In particular, they have exhibited great promise in antimicrobial activity due to their large surface area, hydrophobicity and high biocompatibility attributed to their 2D structure and better biocompatibility compared to CBNs.[31, 37-44] Molybdenum disulfide (MoS$_2$) modified with chitosan (CS) and silver nanoparticles (MoS$_2$-CS-AgNPs) was able to inhibit the growth of plant fungi *Saccharomyces uvarum* and *Aspergillus niger*, at low concentrations of 6.8 µg ml^{-1} and 4.2 µg ml^{-1}, respectively, but only after long incubation times of 72 h.[37] A nanocomposite of AgNPs coupled with zinc oxide (Ag@ZnO) showed complete killing (MFC) of *C. krusei* at 250 µg ml^{-1} after 18 h of incubation.[45] Recently, our group conducted a detailed study of liquid exfoliated TMDC nanosheets

encapsulated in synthetic single-stranded DNA and found that molybdenum diselenide (MoSe$_2$) showed excellent antibacterial efficiency against many strains of MDR bacteria currently.[46]

However, there have been relatively few studies on the antifungal potential of TMDCs.[37, 47-49] At the same time, there has been a growing interest in the development and use of biological materials to combat the growing resistance of microbial strains to drugs.[50-51] Chitosan (CS) is a cationic polysaccharide that is nontoxic, biocompatible and biodegradable since it is derived from the shells of crustaceans, and has diverse therapeutic properties including antimicrobial activity.[37, 39, 52] CS has been known to inhibit mRNA synthesis once it enters the cell cytoplasm, thus triggering cell death, and making it a good antifungal agent. The cationic nature of CS allows it to interact with the negatively charged fungal cell wall making it highly target-specific, and it can increase the permeability of cell membranes causing leakage of the cytoplasm. Chitosan also acts as a chelating agent that binds with trace elements present in the cells, thereby inhibiting fungal cell growth.[53-54] In addition, the incorporation of nanoparticles into CS matrices can markedly improve antimicrobial activities and enhance biocompatibility.[37, 39, 55-56] Thus, the combination of CS and 2D materials have excellent potential as antifungal agents to combat pathogenic fungi. In this paper, we report the antifungal activity of 2D MoSe$_2$ nanosheets formed by liquid phase exfoliation in a 0.5% (w/v%) low-molecular-weight (LMW) CS aqueous solution. The resulting MoSe$_2$ nanosheets are encapsulated in CS (MoSe$_2$/CS) and exhibit exceptional antifungal activity. Moreover they do so without any requiring any modifications, such as surface functionalization with complex ligands,[37] biocidal nanoparticles,[57] photosensitizers,[58] or antifungal drugs,[31] and in the absence of any external stimulus such as near infrared (nIR) light,[59] that have been reported in the literature. Both unicellular and filamentous fungi were successfully inhibited at low concentrations of MoSe$_2$/CS between 37 to 75 µg ml^{-1}. The effects of MoSe$_2$/CS nanosheets on the membrane structure and integrity of fungal cells were investigated through a series of carefully designed experiments, which showed more than 95% of cells had membranes that were depolarized and disintegrated. High resolution imaging via confocal scanning laser microscopy (CSLM), transmission electron microscopy (TEM), and scanning electron microscopy (SEM) were used to directly show physical disruption of the lipid bilayer occurring on the fungal cells as a result of interaction with the

MoSe$_2$/CS nanosheets. The therapeutic potential of MoSe$_2$/CS nanosheets was evaluated by analyzing its cytotoxicity toward mammalian cells, demonstrating more than 90% viability of mammalian cells and human red blood cells until 75 µg ml^{-1} of MoSe$_2$/CS. These results indicate that MoSe$_2$/CS nanosheets are highly efficient antifungal agents with a high degree of biocompatibility toward mammalian cells, and the antifungal action is a combination of membrane damage, membrane depolarization and metabolic inactivation. The MoSe$_2$/CS nanosheets were also used to kill several strains of the highly pathogenic and multidrug-resistant fungus *Candida auris*.
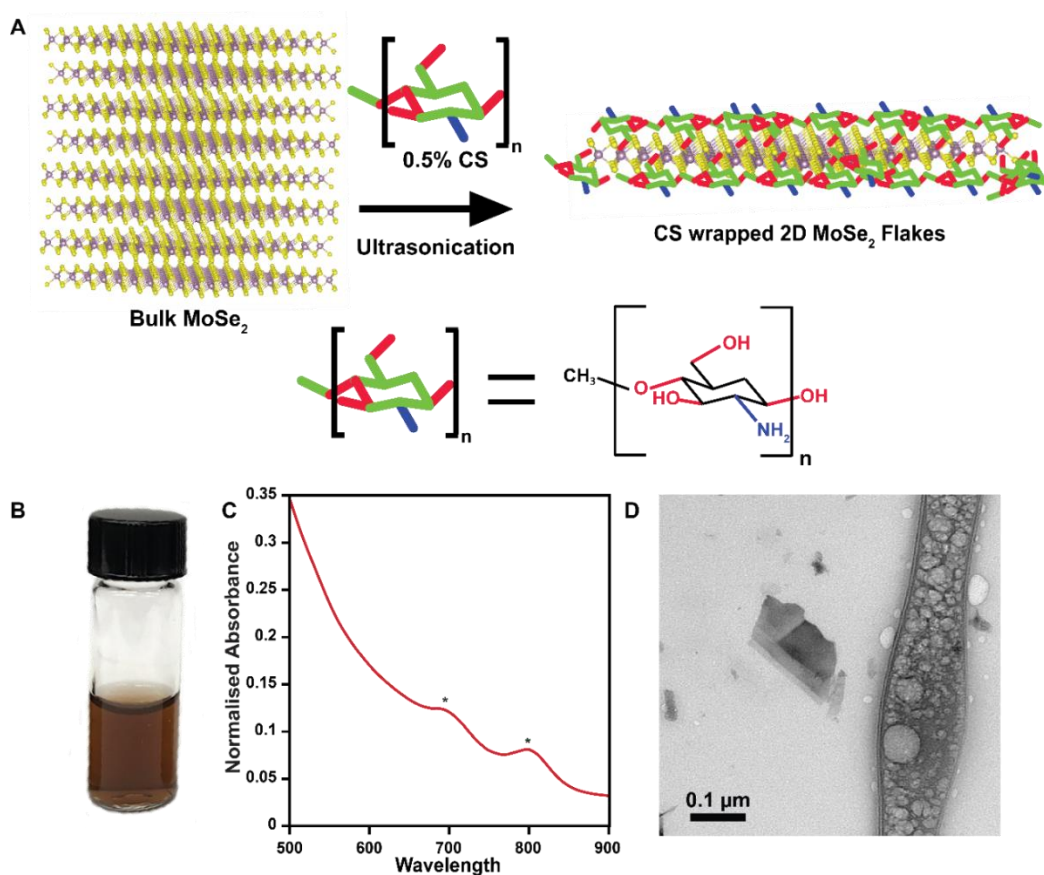
Figure 4.1. Synthesis and characterization of MoSe$_2$/CS. (A) Schematic illustration of exfoliation of bulk MoSe$_2$ in 0.5% CS solution to form MoSe$_2$ nanosheets encapsulated in CS. The structure of CS is shown at bottom. Yellow spheres are Se atoms, and purple spheres are Mo atoms. (B) Glass vial containing a dark brown MoSe$_2$/CS dispersion. (C) UV-vis spectrum of MoSe$_2$/CS having

characteristic excitonic peaks (*) at ~700 nm and ~800 nm. (D) TEM image showing dispersed MoSe$_2$/CS nanosheets.

4.2 Preparation and characterization of 2D MoSe$_2$/CS

Chitosan (CS) is a linear polysaccharide composed of β-(1-4)-linked D-glucosamine and N-acetyl-D-glucosamine arrayed in a random order. Acetyl moieties within N-acetyl-D-glucosamine provide a bulky group keeping the nanosheets from aggregating due to steric repulsion, whereas the amine groups (-NH$_2$) in D-glucosamine act as a hydrophilic outer layer to interface with the surrounding aqueous solution. Bulk MoSe$_2$ powder was dispersed in 0.5% (w/v) low-molecular-weight CS in 1% acetic acid using ultrasonication (**Figure 1A**) to form CS-wrapped MoSe$_2$ nanosheets. The resulting dispersion had a dark brown appearance (**Figure 1B**) and a concentration of ~0.32 mg ml^{-1}. Visible to near-infrared absorbance spectroscopy was performed to identify the characteristic peaks of MoSe$_2$ at approximately 700 nm and 800 nm (**Figure 1C**). Transmission electron microscopy (TEM) images (**Figure 1D**) showed the 2D nature of the dispersed nanosheets. They had mono- to few-layer thickness, with the largest nanosheet in **Figure 1D** having lateral dimensions ~70 nm by ~200 nm.

4.3 Antifungal activity of MoSe$_2$/CS

Fungi can be classified into two categories: (1) unicellular fungi, including *S. cerevisiae*, *C. parapsilosis*, *I. orientalis, C. albicans*, *C. neoformans*, and *C. gattii*; and (2) filamentous fungi, including *A. fumigatus*. The minimum fungicidal concentration (MFC) values of MoSe$_2$/CS were determined for both categories using the microdilution method (see Experimental Methods section for more details) as shown in **Figure 2**. The MFC values of biosafety level 1 (BSL-1) strains *S. cerevisiae*, C*. parapsilosis* and *I. orientalis* were determined to be 12.5 µg ml^{-1}, 6.25 µg ml^{-1} and 6.25 µg ml^{-1}, respectively of MoSe$_2$, dispersed in 5 mg ml^{-1}of CS (**Figure 2A-C** and **Table 1**). The more resistant pathogenic BSL-2 fungi *C. albicans*, *C. gattii*, and *C. neoformans* required higher concentrations, with MFCs at 75 µg ml^{-1} (**Figure 2D-F** and **Table 1**).

The minimum inhibitory concentration (MIC) values for the unicellular fungi *S. cerevisiae, C. albicans* and filamentous fungi *A. fumigatus* were measured according to the procedure

described in the Experimental Methods section, and were found to be 3.125, 37.5 and 12.5 µg ml^{-1}, respectively (**Figure 2G-I**). The microdilution test for MFC determination was not performed on *A. fumigatus* due to its filamentous nature and lack of individual colonies. The MICs of other strains including *C. parapsilosis*, *I. orientalis*, *C. neoformans*, *C. gattii*, *F. verticillioides* and *F. falciforme* were determined to be 0.78, 0.78,1.56, 1.56, 0.5 and 0.5 µg ml^{-1}, respectively (**Figure S1** and **Table 1**).

The killing efficiency of MoSe$_2$/CS was compared to 0.5% CS as a control. The 0.5% CS solution alone managed to kill only 95.75% of *S. cerevisiae*, 80.68% of C*. parapsilo* and 79.0% of *I. orientalis* at similar concentration of MoSe$_2$ applied (**Figure 2A-C**). On the other hand, in the case of BSL-2 fungi *C. albicans*, *C. gattii*, and *C. neoformans*, the 0.5% CS could only eliminate 58.6%, 56.8% and 63.0% of these fungi strains, respectively (**Figure 2D-F**). Hence, we can conclude that 0.5% CS was far less potent against these strains and that the combined effect of MoSe$_2$ and CS results in the high killing efficiency of MoSe$_2$/CS at lower concentrations.

Table 4.1. MIC and MFC values of MoSe$_2$/CS against different fungal strains.

Fungal Strain	Type	BSL Level	Incubation time (h)	MFC (µg ml^{-1})	MIC (µg ml^{-1})
S. *cerevisiae*	Unicellular	1	3	12.5	3.125
C. *parapsilosis*	Unicellular	1	3	6.25	0.78
I. orientalis	Unicellular	1	3	6.25	0.78
C. albicans	Unicellular	2	3	75	37.5
C. *neoformans*	Unicellular	2	3	75	1.56
C. gattii	Unicellular	2	3	75	1.56
A. fumigatus	Filamentous	2	3	-	12.5
F. *verticillioides*	Filamentous	2	3	-	0.5
F. falciforme	Filamentous	2	3	-	0.5
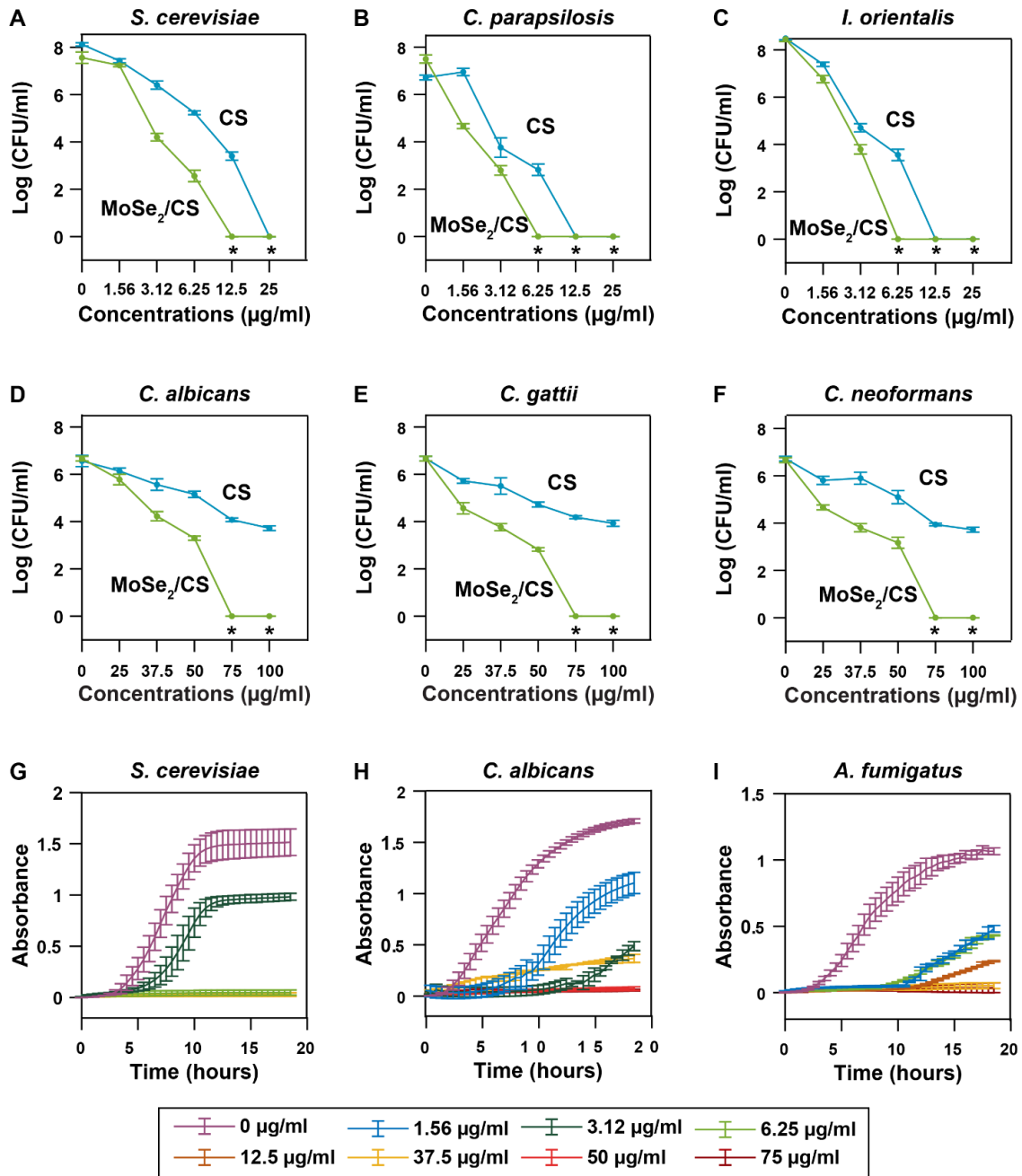
Figure 4.2. Antifungal activity of MoSe₂/CS against unicellular and filamentous fungi. (A, B,

C) CFUs at different concentrations were used to determine MFC of BSL-1 S. *cerevisiae* (A), C.

parapsilosis (B) and *I. orientalis* (C) was determined to be 12.5, 6.25 and 6.25 µg ml⁻¹, respectively,

using the microdilution method. (E, F, G) MFC of BSL-2 *C. albicans* (E), *C. neoformans* (F), and *C.*

gattii (G) were determined to be 75 µg ml⁻¹. (G, H, I) Absorbance over time to determine MIC of

unicellular *S. cerevisiae* (BSL-1) (G), *C. albicans* (BSL-2) (H) and filamentous *A. fumigatus* (BSL-

2) (I) were determined to be 3.125, 37.5 and 12.5 μg ml^{-1}, respectively. * indicates complete eradication of fungal cells.

4.4 Biocompatibility test

To test the effect of MoSe$_2$/CS on mammalian cells, we performed several biocompatibility assays (see Experimental Methods section for more details). The hemolysis assay was performed by incubating human red blood cells (RBCs) with different concentrations of MoSe$_2$/CS. The same volume of 0.5% CS solution in separate samples were used as controls (**Figure 3A**). After incubation for 3 h, only ~1.5% to 9% lysis of RBCs was observed for MoSe$_2$/CS for concentrations as high as 150 μg ml^{-1} (indicated by the red dashed line). Materials that induce up to 5% hemolysis of RBC (indicated by the red dashed line in **Figure 5A)** are considered to be biocompatible. Therefore, we can conclude that MoSe$_2$/CS can be considered as fairly biocompatible up to 150 μg ml^{-1}.[60] Meanwhile, the 0.5% CS had a much stronger effect, causing lysis of ~7% to 50% when added at the same volumes as the MoSe$_2$/CS preparations (**Figure 3A**). The surfactant Triton X is also used as a positive control for complete lysis of RBCs.

The viability of the human embryonic kidney cell line HEK 293 was tested using the XTT and alamarBlue viability assays with MoSe$_2$/CS dispersions at different concentrations (**Figure 3B-C**). The colorimetric XTT assay results indicate that after incubation for 3 h with MoSe$_2$/CS at concentrations ranging from 0 to 75 μg ml^{-1}, more than 90% of cells were viable which is considered to be biocompatible (indicated by the red dashed line in **Figure 5B** and **C**). In fact, the MoSe$_2$/CS nanosheets were more biocompatible than the CS alone. We also used the fluorescence-based alamarBlue assay. In the presence of MoSe$_2$/CS at different concentrations, the portion of viable cells is above ~90% (indicated by the red line) compared to ~70-98% biocompatibility of 0.5% CS alone (**Figure 5C**). Hence, the above results all demonstrate the biocompatibility of MoSe$_2$/CS at concentrations above the MFC level, and the XTT assay further shows that the viability of cells in 0.5% CS solution is less than in MoSe$_2$/CS at concentrations ranging from 37.5 to 100 μg ml^{-1}.
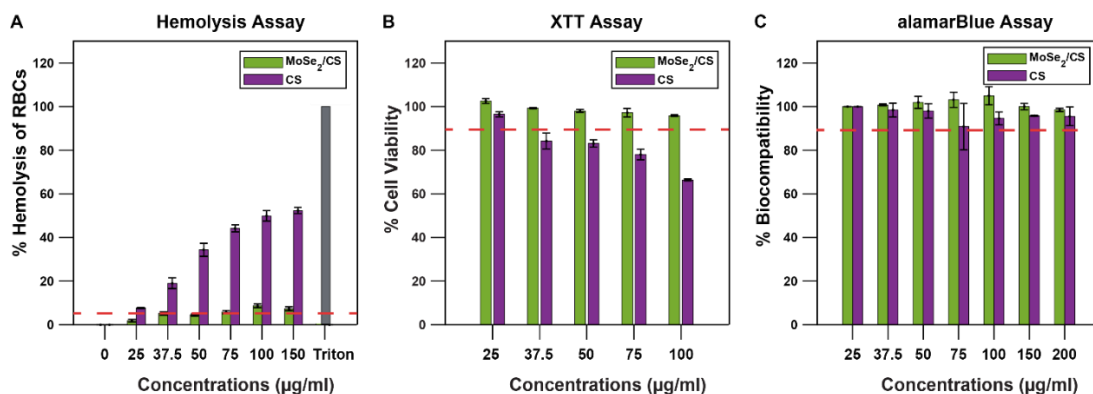
Figure 4.3. Biocompatibility test for MoSe₂/CS solution. (A) Hemolysis assay to determine the toxicity of MoSe₂/CS and 0.5% CS alone against RBCs. Percent hemolysis below the red dashed line (5% lysis) is considered non-toxic.[60] (B) Percent cell viability of HEK293 cells when treated with different concentrations of MoSe₂/CS and 0.5% CS alone. Percent viability above the red dashed line at 90% is considered biocompatible. (C) Percent biocompatibility of HEK293 mammalian cells tested with the alamarBlue assay in the presence of MoSe₂/CS and 0.5% CS alone. Percent viability above the red dashed line at 90% is considered biocompatible.

4.5 Confocal scanning laser microscopy (CSLM)

Fluorescence imaging using confocal scanning laser microscopy (CSLM) was conducted on the unicellular fungi *C. albicans* and the filamentous fungi *A. fumigatus* to visualize the fungal cells and their viability after treatment with MoSe₂/CS (**Figure 5**). Intense green fluorescence results from ConA binding to polysaccharides including alpha-mannopyranosyl and alpha-glucopyranosyl residues and indicates the cell walls of the fungi, while the bright red fluorescence is due to the FUN 1 cell stain staining localized in dense aggregates in the cytoplasm of metabolically active cells (**red arrows**). Metabolically inactive cells are indicated by the absence of bright red aggregates (**white arrows**). Fungal cells were treated with MoSe₂/CS at the concentrations of 0 μg ml⁻¹ (negative control), 25 μg ml⁻¹, 50 μg ml⁻¹, and 100 μg ml⁻¹ with 3 h incubation. A stark difference is observed between samples that were treated with 0 μg ml⁻¹ and those treated with 50 μg ml⁻¹ and 100 μg ml⁻¹ of MoSe₂/CS. The negative control sample has substantially more red fluorescent aggregates as compared to samples treated with 25 μg ml⁻¹,

clearly indicating that MoSe$_2$/CS at 25 µg ml^{-1} shows some antifungal activity. Samples treated with 50 µg ml^{-1} and 100 µg ml^{-1} show close to no red fluorescence, indicating inactive cells or dead cells due to the MoSe$_2$/CS treatment.
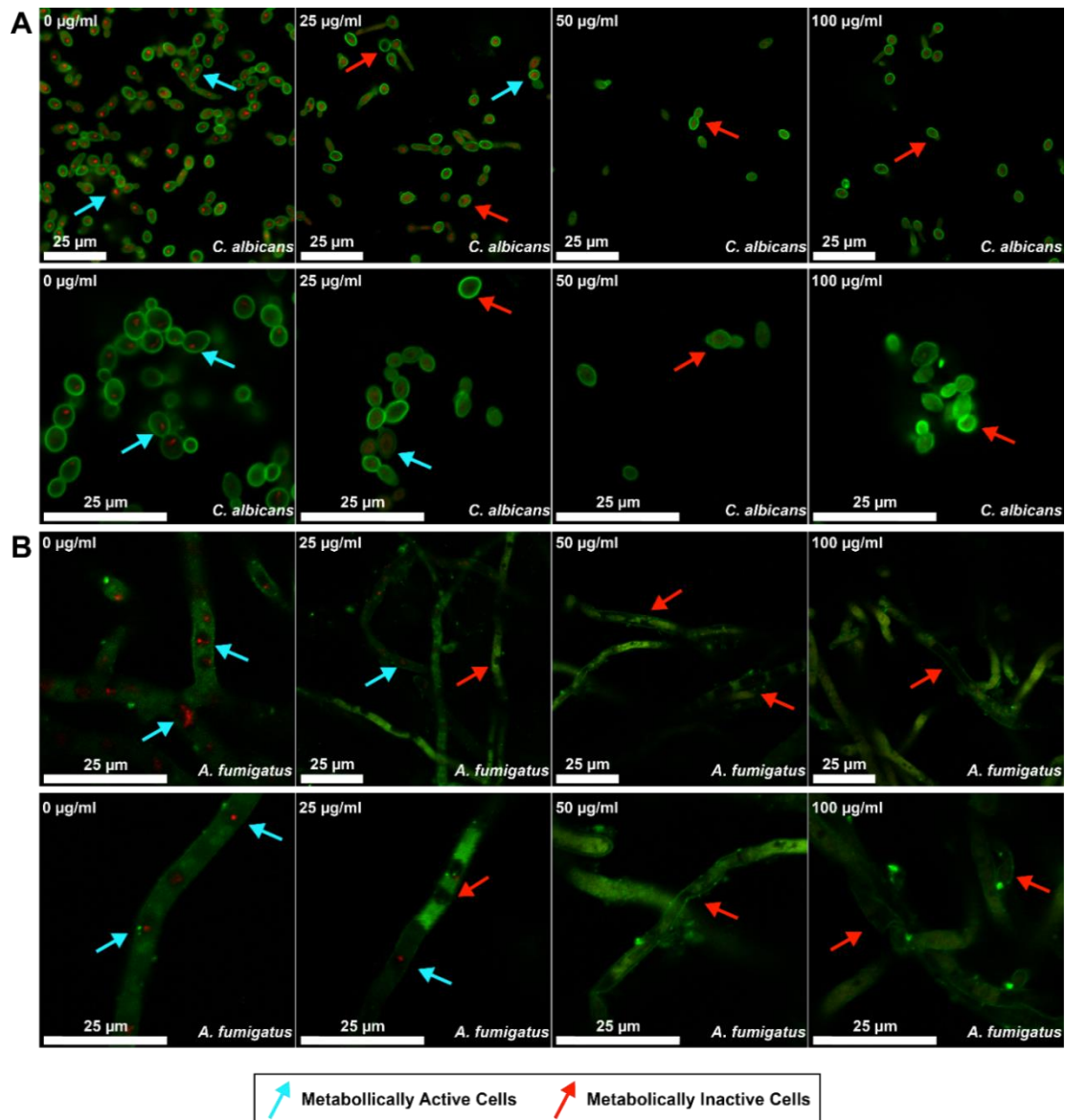
Figure 4.4. Fluorescence imaging of fungal cells by confocal scanning laser microscopy (CSLM). The structures appearing green (Con A stain) are the fungal cell walls and those appearing red (FUN 1 stain) are metabolically active cytoplasm. The viable cells are marked with **blue arrows**. The absence of red aggregates in the cells signifies loss of viability or dead cells (**red arrows**). (A) *C. albicans* (unicellular) cells after treatment with MoSe$_2$/CS at 0 (negative control), 25, 50, and

100 µg ml^{-1} for 3 h of incubation. The two rows of images are at different magnification levels (B) *A. fumigatus* (filamentous) cells after treatment with MoSe$_2$/CS at 0 (negative control), 25, 50, and 100 µg ml^{-1} for 3 h incubation.

4.6 Changes in fungal cell morphology

To observe the changes in morphology after treating the fungal cells with MoSe$_2$/CS at the MFC, TEM and SEM imaging was performed on *C. albicans* and *A. fumigatus* (**Figure 5**). Cells were prepared for microscopy according to the protocols described in the Methods section. The treated fungi were compared to untreated control samples of fungi that were subjected to the same sample preparation conditions in the absence of MoSe$_2$/CS. A stark difference was observed between the treated and untreated fungi. SEM imaging showed the untreated *C. albicans* had intact unicellular cells and the untreated *A. fumigatus* had healthy filaments (**Figure 5A** and **C**). In contrast, the treated cells showed distinct membrane damage, breaking of filaments and deformed cells (**Figure 5B** and **D**). The cross-sectional view in TEM images of the control samples showed that the cytoplasm was intact with unbroken cell membranes and healthy cells (**Figure 5E** and **G**). The treated samples showed sharp-edged MoSe$_2$/CS nanosheets assembling around the fungal cells and filaments, broken outer cell walls and leaking of cytoplasm leading to deformation of cells (**Figure 5F** and **H**). These observations indicate that the positively charged MoSe$_2$/CS complexes localize around the negative outer membranes due to electrostatic interactions. The presence of these complexes weakens the cell wall, destabilizing and reducing its rigidity, leading to disruption and membrane damage. The high turgor pressure inside the cell combined with these disturbances to the membrane enables the breaking of the cell wall and cytoplasmic leakage. Hence, MoSe$_2$/CS weakens, damages, inhibits and kills both unicellular and filamentous fungi.

A–H: SEM and TEM micrographs of *C. albicans* and *A. fumigatus*.
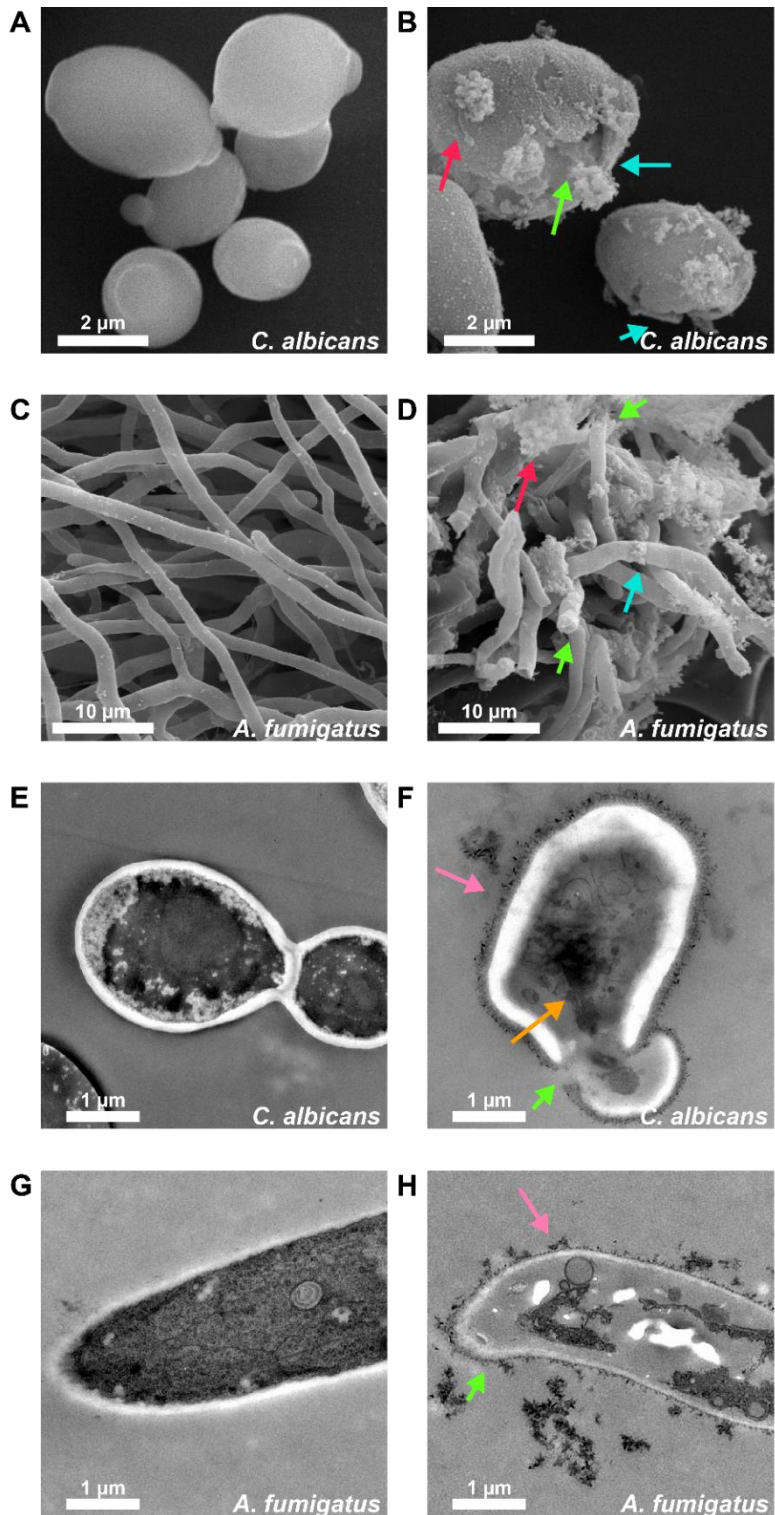
Legend:
- Red arrow — Disrupting Feature
- Cyan arrow — Morphological Deformation
- Green arrow — Ruptured Cell Wall
- Pink arrow — MoSe$_2$/CS Interaction with Cell Wall
- Orange arrow — Leakage of Cytoplasm

Figure 4.5. Cell morphology of *C. albicans* and *A. fumigatus* after treatment with MoSe$_2$/CS. (A, C) SEM images of healthy control cells of *C. albicans* (A) and *A. fumigatus* (C). (B, D) SEM images after treatment with MoSe$_2$/CS for 3 h showing disruptive features (**red arrows**), morphological deformation (**cyan arrows**) and broken outer membrane (**green arrows**) of *C. albicans* (B) and *A. fumigatus* (D) in the presence of MoSe$_2$/CS. (E, G) TEM images of control cells of *C. albicans* (E) and *A. fumigatus* (G) with intact cytoplasm. (F, H) TEM images after treatment with MoSe$_2$/CS for 3 h of *C. albicans* (F) and *A. fumigatus* (H) in the presence of MoSe$_2$/CS showing MoSe$_2$ flakes interacting with cell wall (**pink arrows**), leading to rupturing of the cell wall (**green arrows**) and cytoplasmic leakage (**orange arrows**).

4.7 Fungal Membrane Potential and Membrane Integrity

To determine the effect of MoSe$_2$/CS on the fungal cell membranes, and thereby elucidate its inactivation mechanisms, we conducted flow cytometry experiments to measure the transmembrane potential and membrane integrity of the fungi. Many antifungal agents have been known to exert fungicidal effects through destabilization of the transmembrane potential of cell membranes, subsequently leading to the physical disruption of the lipid bilayer or membrane damage.

The membrane potential was investigated with the probe DiBAC$_4$ which preferentially enters cells whose membrane potential has collapsed to fluorescently label them. The amount of depolarization was indicated by the degree of fluorescence: the higher the fluorescence, the higher the depolarization. Cell counts are shown as a function of the DiBAC$_4$ fluorescence in **Figure 6A** for a negative control (no MoSe$_2$/CS), cells treated with 50 and 100 µg ml^{-1} of MoSe$_2$/CS, and a positive control (cold absolute ethanol). The calculated proportion of damaged and undamaged cells are shown in the bar plots in **Figure 6B**. The cells in the negative control sample having a DiBAC$_4$ fluorescence peak at ~1.4 were healthy cells with normal transmembrane potential. After incubation for 3 h with MoSe$_2$/CS at concentrations of 50 and 100 µg ml^{-1} the percentages of depolarized cells are 99.9% and 98.0%, respectively. Interestingly, the depolarization due to

positive control (cold absolute ethanol) was 80.0%, indicating that the $MoSe_2$/CS was able to change the membrane potential even more strongly than ethanol.

The effect of $MoSe_2$/CS nanosheets on membrane integrity was validated by measuring the uptake efficiency of a membrane-impermeable dye, propidium iodide (PI), by fungal cells treated by $MoSe_2$/CS at different concentrations. PI can enter cells only if the membrane is damaged or compromised. Upon entering cells, PI binds to single and double-stranded nucleic acids and produces a strong red fluorescence. *C. albicans* was treated with $MoSe_2$/CS nanosheets at concentrations of 50 and 100 µg ml^{-1} and with cold absolute ethanol (positive control) for 3 h (**Figure 6C**). The higher the PI fluorescence, the higher the disintegration of the membrane. The calculated proportion of cells with damage to the membrane integrity were 99.4%, 99.1% and 99.1% respectively, as shown in the bar plots in **Figure 6D**. The negative control without any $MoSe_2$/CS again has fully intact cells. This experiment clearly showed that the $MoSe_2$/CS nanosheets upon interacting with the fungal cells caused extensive membrane damage, which resulted in the leakage of the dye molecules. The results of the PI uptake assay confirmed the potential of $MoSe_2$/CS nanosheets to cause physical disruption of the lipid bilayer leaking the cytoplasm, thereby causing cell death.
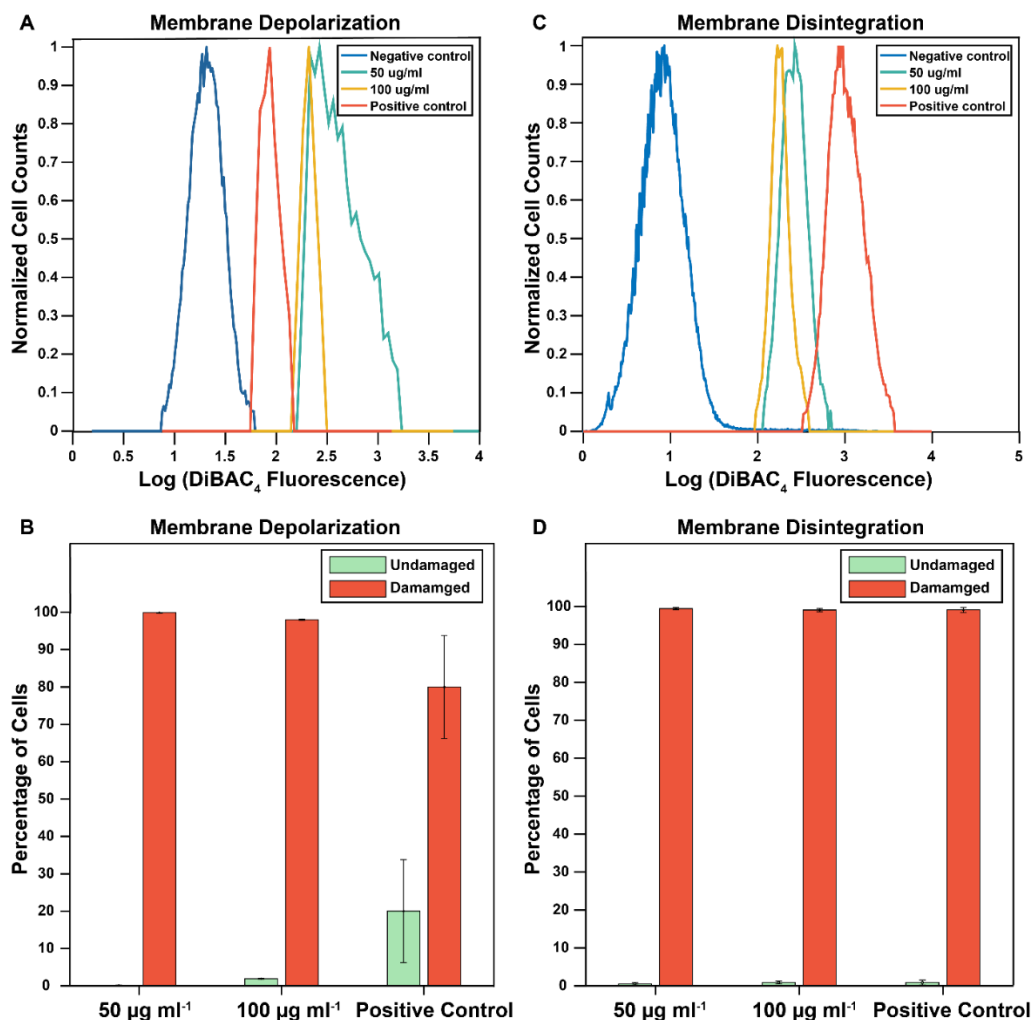
Figure 4.6. Membrane depolarization and membrane disintegration of *C. albicans* cells. (A) Plot of normalized event number in flow cytometry as a function of DiBAC$_4$ (green) fluorescence intensity of 4 different samples together showing the extent of depolarization of *C. albicans* cells upon treatment with negative control, 50 and 100 µg ml^{-1} of MoSe$_2$/CS and cold absolute ethanol (positive control) after 3 h incubation. (B) Bar plots of the proportion of cells with depolarization for the samples shown in panel (A). (B) Plot of normalized event number in flow cytometry as a function of PI (red) fluorescence intensity of 4 different samples together showing the extent of depolarization of *C. albicans* cells upon treatment with negative control, 50 and 100 µg ml^{-1} of MoSe$_2$/CS and cold absolute ethanol (positive control) after 3 h incubation. (D) Bar plots of the proportion of disintegrated cells for the samples shown in panel (C).

4.8 Treatment of *Candida auris* (*C. auris*)

Since its discovery in 2009,[11] *C. auris* has been detected in more than 30 countries.[16] In contrast to other *Candida* species, *C. auris* spreads easily in healthcare settings causing nosocomial outbreaks.[14, 61] The prevalence of C. auris is increasing due to its ability to persist both in the human host and on various surfaces, and its resistance to common disinfection protocols.[12, 62] It exhibits intrinsic resistance to common antifungal drugs like fluconazole[13] and variable susceptibility to other azole antifungal drugs, 5-flucytosine,[20] amphotericin B,[19] and echinocandins.[18, 20-21] It displays higher MICs than usual,[13-14, 16] leading to its classification as being multi-drug resistant (MDR).[15] In most cases, invasive infection with *C. auris* occurs in critically ill patients, i.e., those in intensive care facilities and undergoing invasive procedures.[63-64] This, along with its unknown mechanism of resistance, has led to the pandemic potential of *C. auris* by causing an expanding range of nosocomial infections worldwide.[11, 13-14]

In this study, MoSe$_2$/CS was used to treat nine different strains from the *C. auris* panel identified by the CDC with the most resistance against all three classes of antifungal drugs. In addition, the following strains are able to survive on a range of surface types and their rate of recovery was higher than any other fungal strains, indicating the potential consequence of environmental contamination.[65-66] Hence, they were categorized as multidrug resistant *C. auris* panel by CDC & FDA AR Isolate Bank. The MFC of MoSe$_2$/CS was determined using the microdilution method against three different *C. auris* isolates (0386, 0388, 0389), *C. duobushaemulonii* (0394), *C. haemulonii* (0395), *K. ohmeri* (0396), *C. krusei* (0397), *C. lusitaniae* (0398) and *S. cerevisiae* (0399). MFC of *C. auris* strains and *C. krusei* were all found to be between 100 and 150 µg ml^{-1}, as shown in **Figure 7A-D** and summarized in **Table 2**. The MFC for more susceptible isolates *C. duobushaemulonii*, *C. haemulonii*, *K. ohmeri*, *C. lusitaniae* and *S. cerevisiae* were determined to be between 25 µg ml^{-1} and 50 µg ml^{-1}respectively, as shown in **Figure S7** and summarized in **Table 2**. MIC measurements for *C. auris* (0389) and *C. krusei* strains revealed that they were inhibited at 50 and 25 µg ml^{-1}, respectively (**Figure 7E and F**). Each experiment was

done in triplicate and compared with 0.5% CS in the absence of MoSe$_2$. The results show excellent

efficacy of MoSe$_2$/CS against all the isolates.

Table 4.2. MIC and MFC values of MoSe$_2$/CS against different fungal strains of *C. auris* panel.

Fungal Strain	Type	Biosafety Level	Incubation time (h)	MFC (µg ml^{-1})	MIC (µg ml^{-1})
C. auris (0386)	Unicellular	2	3	150	-
C. auris (0388)	Unicellular	2	3	100	-
C. auris (0389)	Unicellular	2	3	150	50
C. krusei (0397)	Unicellular	2	3	125	25
C. duobushaemulonii (0394)	Unicellular	2	3	50	-
C. haemulonii (0395)	Unicellular	2	3	37.5	-
K. ohmeri (0396)	Unicellular	2	3	37.5	-
C. lusitaniae (0398)	Unicellular	2	3	37.5	-
S. cerevisiae (0399)	Unicellular	2	3	37.5	-
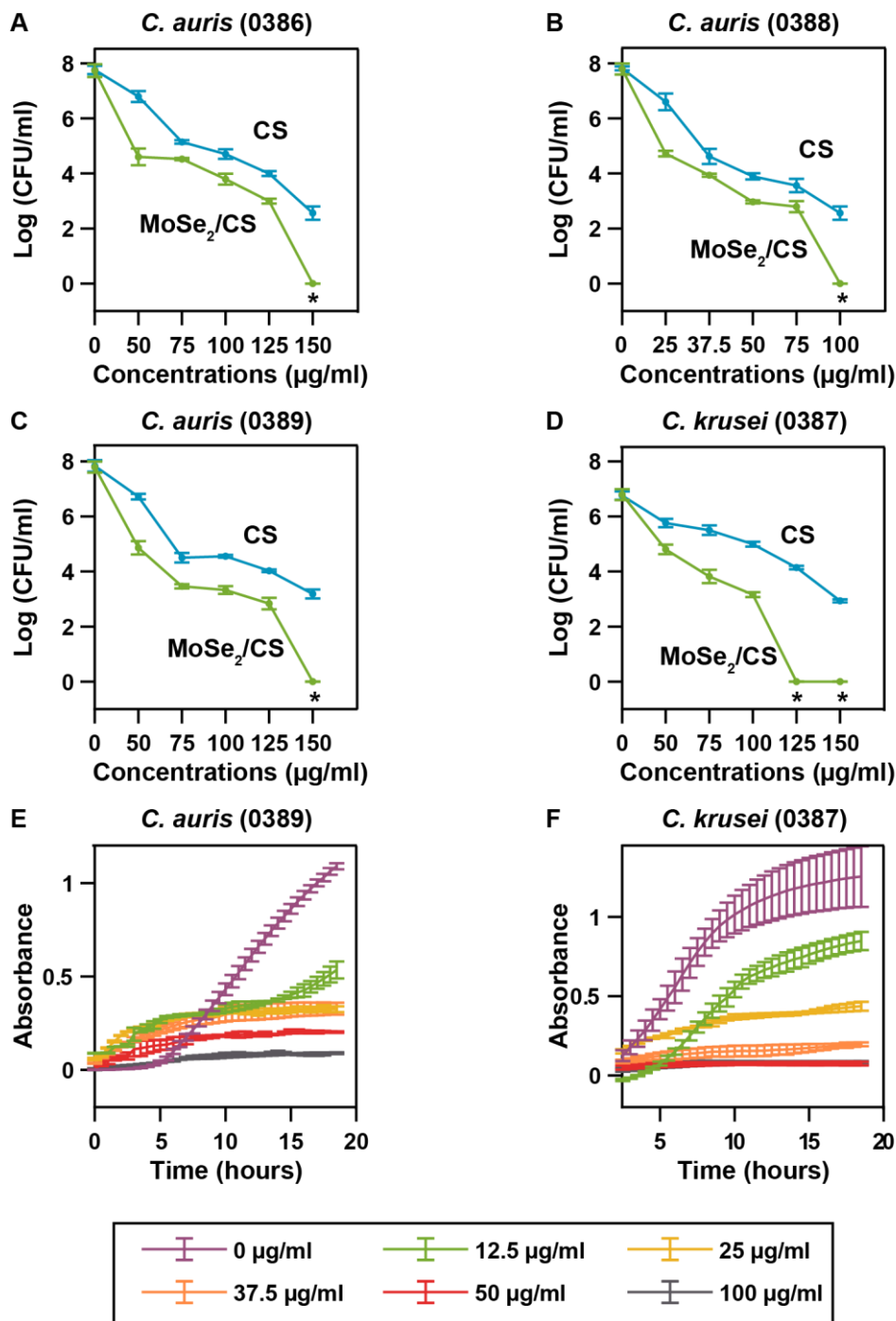
Figure 4.7. Antifungal activity of MoSe₂/CS against *C. auris* panel. (A, B, C and D) CFUs at different concentrations to determine the MFC of BSL-2 *C. auris* panel including *C. auris* (0386), *C. auris* (0388), *C. auris* (0389) and *C. krusei* (0387) were determined to be 150, 100, 150 and 125 μg ml⁻¹, respectively, using the microdilution method. (E and F) Absorbance over time to determine

MICs of *C. auris* (0389) and *C. krusei* (0387) (BSL-2), were found to be 50 and 25 µg ml^{-1} respectively. * indicates complete eradication of fungal cells.

4.9 Discussion

In this study, we prepared MoSe$_2$ nanosheets encapsulated in chitosan that completely eradicated (i.e.100% killing) both unicellular and filamentous fungi within 3 h of incubation at a various range of concentrations. Our results show superior performance in terms of MFC and MIC values and a short incubation duration compared to previous reports of various nanomaterials and nanoparticles acting as antifungal agents (see Supporting Information **Table S1** for comparisons). Antifungal studies with carbon-based nanomaterials like SWCNTs after incubation for 3 h showed killing efficiency up to ~96% at a concentration of 500 µg ml^{-1} against *Fusarium graminearum* and *Fusarium poae*.[31] In comparison, our MoSe$_2$/CS nanosheets against *C. albicans* had an MFC value of 75 µg ml^{-1} over the same incubation time. Reduced graphene oxide (rGO) manages to inhibit (MIC) only 50% of *Aspergillus niger* after 7 days of incubation at 50 µg ml^{-1}.[48] In comparison, our MoSe$_2$/CS inhibited the growth of *A. fumigatus* at a far lower concentration of 12.5 µg ml^{-1}. GO coupled with other nanomaterials like silver nanoparticles (AgNPs) shows increased inhibition in terms of MIC against *C. albicans* at 8 µg ml^{-1} but only after a far longer incubation period of 18 h. Low molecular weight CS (LMWCS) has shown good antifungal efficiency against *C. albicans* with an MIC <40 µg ml^{-1}, similar to the MoSe$_2$/CS MIC of 37.5 µg ml^{-1}. However, the incubation period for LMWCS was considerably longer at 24 h instead of 3 h for our work.[53] The antifungal activity of another TMDC material, MoS$_2$, has also been reported previously, but only when modified with both CS and AgNPs (MoS$_2$-CS-Ag), making it highly effective at just 6.8 µg ml^{-1} against *Saccharomyces uvarum* and 4.2 µg ml^{-1} against *Aspergillus niger*. However, both these organisms were less virulent BSL-1 strains and were incubated for 72 h,[37] a far longer duration than our 3 h incubation time. A synthetic polymer with antimicrobial properties designed for potential use in medical devices showed promise against several organisms but did not demonstrate any efficacy against *C. auris*.[67]

Overall, the MoSe$_2$/CS nanosheets here were tested against a wide range of fungal strains from BSL-1 to BSL-2 and demonstrated the capacity to completely eradicate them at varying concentrations. With MoSe$_2$/CS we observe complete eradication of various strains in *C. auris* panel. In addition, there seems to be a correlation between the susceptibility of these *C. auris* isolates toward conventional antifungal drugs and toward MoSe$_2$/CS. The isolates that exhibit higher MIC values when treated by known drugs like amphotericin B, fluconazole and flucytosine (i.e. *C. auris* (0389)) also exhibited higher MFC when treated by MoSe$_2$/CS, whereas *C. duobushaemulonii* or *C. haemulonii* with lower MIC values were more susceptible towards MoSe$_2$/CS in the panel (**Table S2**). *C. auris* also showed higher MFC and MIC as compared to the *C. albicans* we tested before. Hence, MoSe$_2$/CS proved efficient against a panel of drug resistant fungal strains, making them a potent antifungal agent for potential use in healthcare settings.

To understand how MoSe$_2$/CS inactivates fungal cells, we evaluated the transmembrane potential and membrane integrity of *C. albicans* under treatment with the nanosheets. MoSe$_2$/CS successfully depolarized 99.9% of cells at a concentration of only 50 µg ml^{-1}. Even the cold absolute ethanol (positive control) was only able to depolarize 80.0% of the cells (**Figure 6C)**. A previous study on *C. albicans* to examine the depolarization effects due to carbon nanotubes functionalized with amphotericin B (fCNTs-AMB)[31] showed effective depolarization was achieved by incubating for a much longer period of 16 h at 10 µg ml^{-1} concentration found depolarization of 92.7% of cells. Similarly, the extent of membrane damage after 3 h of incubation is significant, as shown by the shift in MoSe$_2$/CS-treated cells compared to the control cells. The fast rate of damage within 3 h of incubation with *C. albicans* with MoSe$_2$/CS shows a very high level of membrane damage, with 99.4% and 99.1% of cells disintegrated for 50 and 100 µg ml^{-1} of MoSe$_2$/CS, respectively (**Figure 6D**). In previous work with carbon nanotubes, 10 µg ml^{-1} of fCNTs-AMB incubated with *C. albicans* for 16 h led to membrane damage in 80% of cells.[31] MoSe$_2$/CS acts even faster than lytic antimicrobial peptides[21] with a shorter exposure time of 3 h revealing evident depolarization and permeabilization effects. Such rapid depolarization with MoSe$_2$/CS treated cells is likely due to the electrostatic interaction of the cationic CS polymer with the negatively charged chitin on the fungal

cell surface.

Other recent studies on the nature of interaction between bacterial membranes and other types of 2D nanosheets can offer insights into our MoSe$_2$/CS system. MoS$_2$ nanosheets have been shown to attach to the surface of the bacterial cell membrane and insert themselves into the membrane through the formation of indentations on the membrane surface.[68] The mechanism of action of CS-MoS$_2$ nanosheets against bacteria was observed to be a multistep process that started with the attachment of the positively charged CS to the bacterial cell surface via electrostatic interactions, leading to embedding of the MoS$_2$ nanosheets into the membrane through formation of dents.[39] For fungi exposed to our MoSe$_2$/CS system, the strong electrostatic interaction between MoSe$_2$/CS nanosheets and the combination of polyglucan and chitin molecules in the fungal membrane initiates the antifungal activity. This CS-driven interaction helps the thin 2D MoSe$_2$ nanosheets puncture the cell membrane, which in turn destabilizes the turgor pressure of the cell and leads to cytoplasmic leakage.[68] This synergistic effect leads to rapid depolarization of cell membrane, which then modifies the membrane permeability initiating disintegration of the cell membrane. Furthermore, the CS that enters the cell cytoplasm via the MoSe$_2$ nanosheets can also inhibit mRNA synthesis and inactivate the metabolism of the cell.

4.10 Conclusion

MoSe$_2$ nanosheets dispersed in chitosan (MoSe$_2$/CS) were prepared by liquid phase exfoliation. Electron microscopy of the synthesized nanosheets showed a high degree of exfoliation of bulk MoSe$_2$ into monolayer and few-layer nanosheets of various sizes. Evaluation of the antifungal activity of the MoSe$_2$/CS nanosheets revealed their exceptional ability to inhibit the growth of both unicellular and filamentous fungi leading to complete eradication with a brief three-hour incubation period. The MFC concentrations of MoSe$_2$/CS required to eradicate both unicellular and filamentous fungi ranged from 6.25 to 75 µg ml^{-1} of MoSe$_2$ dispersed in 5 mg ml^{-1} of CS. The concentrations at which these different strains were inhibited ranged from 0.5 to 37.5 µg ml^{-1} of MoSe$_2$ in 5 mg ml^{-1} of CS. Detailed investigations of the mechanism of antifungal action showed that the MoSe$_2$/CS nanosheets induced fungal cell death through a combined action of membrane

damage, membrane depolarization, metabolic inactivation, and cytoplasmic leakage. The MoSe$_2$/CS nanosheets were also found to possess high biocompatibility toward mammalian cells. They were also highly potent against a panel of MDR *C. auris* fungi at a range of concentrations from 37.5 to 150 μg ml^{-1} within 3 h incubation time. The highly effective antifungal action of the chitosan exfoliated MoSe$_2$/CS nanosheets were observed without the need for any additional surface functionalization of the nanosheets with complex ligands, biocidal nanoparticles, antimicrobial peptides, photosensitizers, or antibiotics, and they do not need any nIR assisted photothermal action. The remarkable antifungal performance of the MoSe$_2$/CS nanosheets introduces future possibilities for further exploiting them in developing antifungal coatings, wound dressings, and ultrafiltration membranes for potential biomedical and environmental applications.

4.11 Reference

1.   Lee, Y.; Puumala, E.; Robbins, N.; Cowen, L. E., Antifungal Drug Resistance: Molecular Mechanisms in Candida albicans and Beyond. *Chemical Reviews* **2021,** *121* (6), 3390-3411.

2.   Armstrong-James, D.; Meintjes, G.; Brown, G. D., A neglected epidemic: fungal infections in HIV/AIDS. *Trends in microbiology* **2014,** *22* (3), 120-7.

3.   Cowen, L. E.; Sanglard, D.; Howard, S. J.; Rogers, P. D.; Perlin, D. S., Mechanisms of Antifungal Drug Resistance. *Cold Spring Harbor perspectives in medicine* **2014,** *5* (7), a019752.

4.   Brown, G. D.; Denning, D. W.; Gow, N. A. R.; Levitz, S. M.; Netea, M. G.; White, T. C., Hidden Killers: Human Fungal Infections. *Science Translational Medicine* **2012,** *4* (165), 165rv13.

5.   Bongomin, F.; Gago, S.; Oladele, R. O.; Denning, D. W., Global and Multi-National Prevalence of Fungal Diseases-Estimate Precision. *Journal of fungi (Basel, Switzerland)* **2017,** *3* (4).

6.   Savary, S.; Ficke, A.; Aubertot, J.-N.; Hollier, C., Crop losses due to diseases and their implications for global food production losses and food security. *Food Security* **2012,** *4* (4), 519-537.

7.   Casadevall, A., Don't Forget the Fungi When Considering Global Catastrophic Biorisks. *Health security* **2017,** *15* (4), 341-342.

8.   Fisher, M. C.; Henk, D. A.; Briggs, C. J.; Brownstein, J. S.; Madoff, L. C.; McCraw, S. L.; Gurr, S. J., Emerging fungal threats to animal, plant and ecosystem health. *Nature* **2012,** *484* (7393), 186-194.

9.   Garcia-Solache, M. A.; Casadevall, A., Global Warming Will Bring New Fungal Diseases for Mammals. *mBio* **2010,** *1* (1), e00061-10.

10.   Jeffery-Smith, A.; Taori, S. K.; Schelenz, S.; Jeffery, K.; Johnson, E. M.; Borman, A.; Manuel, R.; Brown, C. S., Candida auris: a Review of the Literature. *Clinical microbiology reviews* **2018,** *31* (1).

11.   Satoh, K.; Makimura, K.; Hasumi, Y.; Nishiyama, Y.; Uchida, K.; Yamaguchi, H., Candida auris sp. nov., a novel ascomycetous yeast isolated from the external ear canal of an inpatient in a Japanese hospital. *Microbiology and immunology* **2009,** *53* (1), 41-4.

12.   Rhodes, J.; Fisher, M. C., Global epidemiology of emerging Candida auris. *Current opinion in microbiology* **2019,** *52*, 84-89.

13.   Lockhart, S. R.; Etienne, K. A.; Vallabhaneni, S.; Farooqi, J.; Chowdhary, A.; Govender, N. P.; Colombo, A. L.; Calvo, B.; Cuomo, C. A.; Desjardins, C. A.; Berkow, E. L.; Castanheira, M.; Magobo, R. E.; Jabeen, K.; Asghar, R. J.; Meis, J. F.; Jackson, B.; Chiller, T.; Litvintseva, A. P., Simultaneous Emergence of Multidrug-Resistant Candida auris on 3 Continents Confirmed by Whole-Genome Sequencing and Epidemiological Analyses. *Clinical infectious diseases : an official publication of the Infectious Diseases Society of America* **2017,** *64* (2), 134-140.

14.   Schelenz, S.; Hagen, F.; Rhodes, J. L.; Abdolrasouli, A.; Chowdhary, A.; Hall, A.; Ryan, L.; Shackleton, J.; Trimlett, R.; Meis, J. F.; Armstrong-James, D.; Fisher, M. C., First hospital outbreak of the globally emerging Candida auris in a European hospital. *Antimicrob Resist Infect Control* **2016,** *5*, 35-35.

15.   Chowdhary, A.; Anil Kumar, V.; Sharma, C.; Prakash, A.; Agarwal, K.; Babu, R.; Dinesh, K. R.; Karim, S.; Singh, S. K.; Hagen, F.; Meis, J. F., Multidrug-resistant endemic clonal strain of Candida auris in India. *European journal of clinical microbiology & infectious diseases : official publication of the European Society of Clinical Microbiology* **2014,** *33* (6), 919-26.

16.   Spivak, E. S.; Hanson, K. E., Candida auris: an Emerging Fungal Pathogen. *Journal of clinical microbiology* **2018,** *56* (2).

17.   Coelho, C.; Casadevall, A., Cryptococcal therapies and drug targets: the old, the new and the promising. *Cellular microbiology* **2016,** *18* (6), 792-9.

18.   Chowdhary, A.; Prakash, A.; Sharma, C.; Kordalewska, M.; Kumar, A.; Sarma, S.; Tarai, B.; Singh, A.; Upadhyaya, G.; Upadhyay, S.; Yadav, P.; Singh, P. K.; Khillan, V.; Sachdeva, N.; Perlin, D. S.; Meis, J. F., A multicentre study of antifungal susceptibility patterns among 350 Candida auris isolates (2009-17) in India: role of the ERG11 and FKS1 genes in azole and echinocandin resistance. *The Journal of antimicrobial chemotherapy* **2018,** *73* (4), 891-899.

19.   Escandón, P.; Chow, N. A.; Caceres, D. H.; Gade, L.; Berkow, E. L.; Armstrong, P.; Rivera, S.; Misas, E.; Duarte, C.; Moulton-Meissner, H.; Welsh, R. M.; Parra, C.; Pescador, L. A.; Villalobos, N.; Salcedo, S.; Berrio, I.; Varón, C.; Espinosa-Bode, A.; Lockhart, S. R.; Jackson, B. R.; Litvintseva, A. P.; Beltran, M.; Chiller, T. M., Molecular Epidemiology of Candida auris in Colombia Reveals a Highly Related, Countrywide Colonization With Regional Patterns in Amphotericin B Resistance. *Clinical infectious diseases : an official publication of the Infectious Diseases Society of America* **2019,** *68* (1), 15-21.

20.   Rhodes, J.; Abdolrasouli, A.; Farrer, R. A.; Cuomo, C. A.; Aanensen, D. M.; Armstrong-James, D.; Fisher, M. C.; Schelenz, S., Genomic epidemiology of the UK outbreak of the emerging human fungal pathogen Candida auris. *Emerging microbes & infections* **2018,** *7* (1), 43.

21.   Berkow, E. L.; Lockhart, S. R., Activity of CD101, a long-acting echinocandin, against clinical isolates of Candida auris. *Diagnostic microbiology and infectious disease* **2018,** *90* (3), 196-197.

22.   Franci, G.; Falanga, A.; Galdiero, S.; Palomba, L.; Rai, M.; Morelli, G.; Galdiero, M., Silver nanoparticles as potential antibacterial agents. *Molecules (Basel, Switzerland)* **2015,** *20* (5), 8856-74.

23.   Mallakpour, S.; Abdolmaleki, A.; Borandeh, S.; Sabzalian, M., One pot fabrication of optically active and efficient antibacterial poly(amide-benzimidazole-imide)/Ag bionanocomposite. *Journal of Polymer Research* **2015,** *22*.

24.   Rajendran, S. P.; Sengodan, K., Synthesis and Characterization of Zinc Oxide and Iron Oxide Nanoparticles Using<i> Sesbania grandiflora</i> Leaf Extract as Reducing Agent. *Journal of Nanoscience* **2017,** *2017*, 8348507.

25.   Sankaralingam, K.; Kadirvelu, K., Green synthesis of Iron oxide nanoparticles using Lagenaria siceraria and evaluation of its Antimicrobial activity. *Defence Life Science Journal* **2017,** *2*, 422.

26.   Jadhav, M. S.; Kulkarni, S.; Raikar, P.; Barretto, D. A.; Vootla, S. K.; Raikar, U. S., Green biosynthesis of CuO & Ag–CuO nanoparticles from Malus domestica leaf extract and evaluation of antibacterial, antioxidant and DNA cleavage activities. *New Journal of Chemistry* **2018,** *42* (1), 204-213.

27.   Karthik, K.; Dhanuskodi, S.; Seetharaman, P. K.; Chandrakasan, G.; Sivaramakrishnan, S., Microwave Assisted Green Synthesis of MgO Nanorods and Their Antibacterial and Anti-breast Cancer Activities. *Materials Letters* **2017,** *206*, 217-220.

28.   Martinez, L. R.; Han, G.; Chacko, M.; Mihu, M. R.; Jacobson, M.; Gialanella, P.; Friedman, A. J.; Nosanchuk, J. D.; Friedman, J. M., Antimicrobial and healing efficacy of sustained release nitric oxide nanoparticles against Staphylococcus aureus skin infection. *The Journal of investigative dermatology* **2009,** *129* (10), 2463-9.

29.   Bahadar, H.; Maqbool, F.; Niaz, K.; Abdollahi, M., Toxicity of Nanoparticles and an Overview of Current Experimental Models. *Iranian biomedical journal* **2016,** *20* (1), 1-11.

30.   Wang, X.; Liu, X.; Chen, J.; Han, H.; Yuan, Z., Evaluation and mechanism of antifungal effects of carbon nanomaterials in controlling plant fungal pathogen. *Carbon* **2014,** *68*, 798-806.

31.   Benincasa, M.; Pacor, S.; Wu, W.; Prato, M.; Bianco, A.; Gennaro, R., Antifungal activity of amphotericin B conjugated to carbon nanotubes. *ACS nano* **2011,** *5* (1), 199-208.

32.   Miao, H.; Teng, Z.; Wang, C.; Chong, H.; Wang, G., Recent Progress in Two-Dimensional Antimicrobial Nanomaterials. *Chemistry – A European Journal* **2019,** *25* (4), 929-944.

33.   Zhu, Y.; Murali, S.; Cai, W.; Li, X.; Suk, J. W.; Potts, J. R.; Ruoff, R. S., Graphene and Graphene Oxide: Synthesis, Properties, and Applications. *Advanced Materials* **2010,** *22* (35), 3906-3924.

34.   Mallakpour, S.; Abdolmaleki, A.; Borandeh, S., Covalently functionalized graphene sheets with biocompatible natural amino acids. *Applied Surface Science* **2014,** *307*, 533-542.

35.   Mohammed, H.; Kumar, A.; Bekyarova, E.; Al-Hadeethi, Y.; Zhang, X.; Chen, M.; Ansari, M. S.; Cochis, A.; Rimondini, L., Antimicrobial Mechanisms and Effectiveness of Graphene and Graphene-Functionalized Biomaterials. A Scope Review. *Frontiers in Bioengineering and Biotechnology* **2020,** *8* (465).

36.   Yang, Y.; Liu, T.; Cheng, L.; Song, G.; Liu, Z.; Chen, M., MoS2-Based Nanoprobes for Detection of Silver Ions in Aqueous Solutions and Bacteria. *ACS Applied Materials & Interfaces* **2015,** *7* (14), 7526-7533.

37.   Zhang, W.; Mou, Z.; Wang, Y.; Chen, Y.; Yang, E.; Guo, F.; Sun, D.; Wang, W., Molybdenum disulfide nanosheets loaded with chitosan and silver nanoparticles effective antifungal activities: in vitro and in vivo. *Materials science & engineering. C, Materials for biological applications* **2019,** *97*, 486-497.

38.   Kurapati, R.; Muzi, L.; de Garibay, A. P. R.; Russier, J.; Voiry, D.; Vacchi, I. A.; Chhowalla, M.; Bianco, A., Enzymatic Biodegradability of Pristine and Functionalized Transition Metal Dichalcogenide MoS2 Nanosheets. *Advanced Functional Materials* **2017,** *27* (7), 1605176.

39.   Roy, S.; Mondal, A.; Yadav, V.; Sarkar, A.; Banerjee, R.; Sanpui, P.; Jaiswal, A., Mechanistic Insight into the Antibacterial Activity of Chitosan Exfoliated MoS2 Nanosheets: Membrane Damage, Metabolic Inactivation, and Oxidative Stress. *ACS Applied Bio Materials* **2019,** *2* (7), 2738-2755.

40.   Pandit, S.; Karunakaran, S.; Boda, S. K.; Basu, B.; De, M., High Antibacterial Activity of Functionalized Chemically Exfoliated MoS2. *ACS Applied Materials & Interfaces* **2016,** *8* (46), 31567-31573.

41.   Cao, F.; Ju, E.; Zhang, Y.; Wang, Z.; Liu, C.; Li, W.; Huang, Y.; Dong, K.; Ren, J.; Qu, X., An Efficient and Benign Antimicrobial Depot Based on Silver-Infused MoS2. *ACS nano* **2017,** *11* (5), 4651-4659.

42.   Liu, X.; Duan, G.; Li, W.; Zhou, Z.; Zhou, R., Membrane destruction-mediated antibacterial activity of tungsten disulfide (WS2). *RSC Advances* **2017,** *7* (60), 37873-37880.

43.   Rasool, K.; Helal, M.; Ali, A.; Ren, C. E.; Gogotsi, Y.; Mahmoud, K. A., Antibacterial Activity of Ti3C2Tx MXene. *ACS nano* **2016,** *10* (3), 3674-3684.

44.   Bang, G. S.; Cho, S.; Son, N.; Shim, G. W.; Cho, B.-K.; Choi, S.-Y., DNA-Assisted Exfoliation of Tungsten Dichalcogenides and Their Antibacterial Effect. *ACS Applied Materials & Interfaces* **2016,** *8* (3), 1943-1950.

45.   Das, B.; Khan, M. I.; Jayabalan, R.; Behera, S. K.; Yun, S.-I.; Tripathy, S. K.; Mishra, A., Understanding the Antifungal Mechanism of Ag@ZnO Core-shell Nanocomposites against Candida krusei. *Scientific Reports* **2016,** *6* (1), 36403.

46.   Debnath, A.; Saha, S.; Li, D. O.; Chu, X. S.; Ulissi, Z. W.; Green, A. A.; Wang, Q. H., Elimination of Multidrug-Resistant Bacteria by Transition Metal Dichalcogenides Encapsulated by Synthetic Single-Stranded DNA. *ACS Applied Materials & Interfaces* **2021,** *13* (7), 8082-8094.

47.   Alimardani, V.; Abolmaali, S.; Borandeh, S., Antifungal and Antibacterial Properties of Graphene-based Nanomaterials: A Mini-review. *Journal of Nanostructures* **2019,** *9*, 402-413.

48.   Sawangphruk, M.; Srimuk, P.; Chiochan, P.; Sangsri, T.; Siwayaprahm, P., Synthesis and antifungal activity of reduced graphene oxide nanosheets. *Carbon* **2012,** *50* (14), 5156-5161.

49.   Bhatt, V. K.; Patel, M.; Pataniya, P. M.; Iyer, B. D.; Sumesh, C. K.; Late, D. J., Enhanced Antifungal Activity of WS2/ZnO Nanohybrid against Candida albicans. *ACS Biomaterials Science & Engineering* **2020,** *6* (11), 6069-6075.

50.   Amato, D. V.; Amato, D. N.; Blancett, L. T.; Mavrodi, O. V.; Martin, W. B.; Swilley, S. N.; Sandoz, M. J.; Shearer, G.; Mavrodi, D. V.; Patton, D. L., A bio-based pro-antimicrobial polymer network via degradable acetal linkages. *Acta biomaterialia* **2018,** *67*, 196-205.

51.   Fan, X.; Ngo, H.; Wu, C., Natural and Bio-based Antimicrobials: A Review. In *Natural and Bio-Based Antimicrobials for Food Applications*, American Chemical Society: 2018; Vol. 1287, pp 1-24.

52.   Shankar, S.; Rhim, J.-W., Preparation of sulfur nanoparticle-incorporated antimicrobial chitosan films. *Food Hydrocolloids* **2018,** *82*, 116-123.

53.   Park, Y.; Kim, M. H.; Park, S. C.; Cheong, H.; Jang, M. K.; Nah, J. W.; Hahm, K. S., Investigation of the antifungal activity and mechanism of action of LMWS-chitosan. *Journal of microbiology and biotechnology* **2008,** *18* (10), 1729-34.

54.   Ing, L. Y.; Zin, N. M.; Sarwar, A.; Katas, H., Antifungal Activity of Chitosan Nanoparticles and Correlation with Their Physical Properties. *International Journal of Biomaterials* **2012,** *2012*, 632698.

55.   Sundaram, J.; Pant, J.; Goudie, M. J.; Mani, S.; Handa, H., Antimicrobial and Physicochemical Characterization of Biodegradable, Nitric Oxide-Releasing Nanocellulose–Chitosan Packaging Membranes. *Journal of Agricultural and Food Chemistry* **2016,** *64* (25), 5260-5266.

56.   Kumar, S.; Ye, F.; Dobretsov, S.; Dutta, J., Chitosan Nanocomposite Coatings for Food, Paints, and Water Treatment Applications. *Applied Sciences* **2019,** *9*, 2409.

57.   Li, C.; Wang, X.; Chen, F.; Zhang, C.; Zhi, X.; Wang, K.; Cui, D., The antifungal activity of graphene oxide-silver nanocomposites. *Biomaterials* **2013,** *34* (15), 3882-90.

58.   Hu, Y.; Qi, X.; Sun, H.; Lu, Y.; Hu, Y.; Chen, X.; Liu, K.; Yang, Y.; Mao, Z.; Wu, Z.; Zhou, X., Photodynamic therapy combined with antifungal drugs against chromoblastomycosis and the effect of ALA-PDT on Fonsecaea in vitro. *PLoS neglected tropical diseases* **2019,** *13* (10), e0007849.

59.   Zhang, Y.; Huang, P.; Wang, D.; Chen, J.; Liu, W.; Hu, P.; Huang, M.; Chen, X.; Chen, Z., Near-infrared-triggered antibacterial and antifungal photodynamic therapy based on lanthanide-doped upconversion nanoparticles. *Nanoscale* **2018,** *10* (33), 15485-15495.

60.   Liu, J.; Li, F.; Zheng, J.; Li, B.; Zhang, D.; Jia, L., Redox/NIR dual-responsive MoS(2) for synergetic chemo-photothermal therapy of cancer. *J Nanobiotechnology* **2019,** *17* (1), 78-78.

61.   Chowdhary, A.; Sharma, C.; Meis, J. F., Candida auris: A rapidly emerging cause of hospital-acquired multidrug-resistant fungal infections globally. *PLoS pathogens* **2017,** *13* (5), e1006290.

62.   Abdolrasouli, A.; Armstrong-James, D.; Ryan, L.; Schelenz, S., In vitro efficacy of disinfectants utilised for skin decolonisation and environmental decontamination during a hospital outbreak with Candida auris. *Mycoses* **2017,** *60* (11), 758-763.

63.   Vallabhaneni, S.; Kallen, A.; Tsay, S.; Chow, N.; Welsh, R.; Kerins, J.; Kemble, S. K.; Pacilli, M.; Black, S. R.; Landon, E.; Ridgway, J.; Palmore, T. N.; Zelzany, A.; Adams, E. H.; Quinn, M.; Chaturvedi, S.; Greenko, J.; Fernandez, R.; Southwick, K.; Furuya, E. Y.; Calfee, D. P.; Hamula, C.; Patel, G.; Barrett, P.; Lafaro, P.; Berkow, E. L.; Moulton-Meissner, H.; Noble-Wang, J.; Fagan, R. P.; Jackson, B. R.; Lockhart, S. R.; Litvintseva, A. P.; Chiller, T. M., Investigation of the First Seven Reported Cases of Candida auris, a Globally Emerging Invasive, Multidrug-Resistant Fungus-United States, May 2013-August 2016. *American journal of transplantation : official journal of the American Society of Transplantation and the American Society of Transplant Surgeons* **2017,** *17* (1), 296-299.

64.   Lee, W. G.; Shin, J. H.; Uh, Y.; Kang, M. G.; Kim, S. H.; Park, K. H.; Jang, H. C., First three reported cases of nosocomial fungemia caused by Candida auris. *Journal of clinical microbiology* **2011,** *49* (9), 3139-42.

65.   Piedrahita, C. T.; Cadnum, J. L.; Jencson, A. L.; Shaikh, A. A.; Ghannoum, M. A.; Donskey, C. J., Environmental Surfaces in Healthcare Facilities are a Potential Source for Transmission of Candida auris and Other Candida Species. *Infection control and hospital epidemiology* **2017,** *38* (9), 1107-1109.

66.   Welsh, R. M.; Bentz, M. L.; Shams, A.; Houston, H.; Lyons, A.; Rose, L. J.; Litvintseva, A. P., Survival, Persistence, and Isolation of the Emerging Multidrug-Resistant Pathogenic Yeast Candida auris on a Plastic Health Care Surface. *Journal of clinical microbiology* **2017,** *55* (10), 2996-3005.

67.   Saeed, S.; Rashid, N.; Jones, P. G.; Ali, M.; Hussain, R., Synthesis, characterization and biological evaluation of some thiourea derivatives bearing benzothiazole moiety as potential antimicrobial and anticancer agents. *European journal of medicinal chemistry* **2010,** *45* (4), 1323-31.

68.   Wu, R.; Ou, X.; Tian, R.; Zhang, J.; Jin, H.; Dong, M.; Li, J.; Liu, L., Membrane destruction and phospholipid extraction by using two-dimensional MoS(2) nanosheets. *Nanoscale* **2018,** *10* (43), 20162-20170.

CHAPTER 5

Peroxidase-like Activity of Hafnium Diboride Nanozyme with Antibacterial Properties

5.1 Introduction

Enzymes are biological catalysts found in nature that play crucial roles in the functioning of all living things.[1] Many applications like water purification, pharmaceutical and food industries also use natural enzymes for specific reactions.[2-4] However, natural enzymes have limitations including high cost, difficult synthesis processes and low stability.[5] In light of these drawbacks, more cost-effective alternative artificial enzymes have been developed, and are also typically more stable.[6] Artificial enzymes developed from nanomaterials having enzyme-like activity were first coined as "nanozymes" in 2004, followed by the discovery of the peroxidase-like activity of ferromagnetic nanoparticles (Fe_3O_4 NPs) in 2007.[6-8] They have the capability to address the limitations of natural enzymes and conventional artificial enzymes by being more affordable, stable, tunable, and scalable in production.[9]

Natural enzymes are generally divided into several classes based on the type of reaction they catalyze and are often named for the substrates on which they act. For example, oxidoreductases are enzymes that catalyze redox reactions, and include oxidase, peroxidase, catalase, superoxide dismutase and nitrate reductase. Nanozymes are similarly named according to the enzymes that they mimic.[10] Peroxidase catalyzes the reduction of H_2O_2 and the oxidation of substrates like 3,3,5,5-tetramethylbenzidine (TMB).[6] Natural peroxidases such as horseradish peroxidase (HRP) are used in a wide range of applications from wastewater treatment to enzyme immunoassays.[11-12] The advantages of HRP are high turnover number and small size, but it is very expensive and highly sensitive to degradation.[13] Hence nanozymes are being investigated favored for biomedical applications ranging from biosensing, cancer therapy, to antibacterial activity.[14] Many varieties of nanozymes have been reported in the literature including nanoparticles (NPs),[15-16] nanosheets,[17-19] nanocubes,[20] quantum dots,[21] nanofibers[22-23] and nanotubes.[24] For example, iron oxide (Fe_3O_4) NPs show pH-dependent peroxidase-like and catalase-like activities with high turnover number.[6] Manganese oxide (Mn_3O_4) NPs show multi-enzymatic properties including performing the same catalytic action as superoxide dismutase, catalase, and glutathione peroxidase.[25] Prussian blue

NPs, copper manganese nanoflakes ($CuMnO_2$) nanoflakes and vanadium oxide (V_3O_{16}) nanomaterials also show multi-enzymatic activity.[26-28] Taking advantage of the intrinsic properties of nanomaterials have led to a broad range of applications of nanozymes for *in vitro* detection to replace specific enzymes in biological systems.[7]

Two-dimensional (2D) materials are composed of atomic layers held together by different intermolecular forces.[29] Most 2D materials have van der Waals (vdW) attractive forces like electrostatic interactions and hydrophobic interactions between atomic layers.[30] On the other hand, some layered nanomaterials are known as non-vdW 2D materials because of mixture of ionic and covalent interactions occur between layers.[31] 2D materials have previously been reported to show catalytic activity. Among 2D nanomaterials, boron (B) and nitrogen (N) doped graphene show affordable catalytic activity.[13] Molybdenum diselenide ($MoSe_2$) liquid exfoliated in silk fibroin has shown both catalytic as well as antibacterial activity.[18] Molybdenum disulfide (MoS_2) also displayed comparable catalytic activity in both nanosheet and nanofiber forms.[23, 32]

Metal diborides (MB_2) are ultra-high temperature ceramics[33] that exhibit exceptional thermal, chemical, and mechanical stability, which we have recently exfoliated into 2D nanosheets.[34-35] Their layered crystal structures consist of hexagonal layers of boron atoms separated by metal layers that are held together by mixed ionic-covalent type bonding (**Figure 1**).[36] We assessed MB_2 materials like ZrB_2, CrB_2 and TaB_2 for their ability to be exfoliated in several surfactant solutions and screened for their peroxidase activity. Among these, HfB_2 dispersed in the block copolymer Pluronic F68 was the most promising. In general, nanosheets of 2D materials can be exfoliated and stabilized in dispersants such as organic solvents, polymers, oligonucleotides and surfactants.[37-39] Pluronic F68 is an amphiphilic and biocompatible block-copolymer used in medical applications,[40] and has been previously used to exfoliate and disperse nanomaterials.[41] It is a triblock copolymer with alternating hydrophilic poly(ethylene oxide) (PEO) and hydrophobic poly(propylene oxide) (PPO) blocks (**Figure 1**).

In this work, hafnium diboride (HfB_2) nanosheets were exfoliated and dispersed in F68 by liquid phase exfoliation, and the resulting peroxidase-like activity and antibacterial activity of the F68-encapsulated HfB2 nanosheets (HfB$_2$/F68) were measured. We characterized the morphology,

thickness, and composition of HfB_2/F68 using transmission electron microscopy (TEM), scanning electron microscopy (SEM) and electron dispersive x-ray spectroscopy (EDS). The HfB_2 nanosheets have thicknesses ranging from few- to multilayers. The catalytic activity of the HfB_2/F68 nanozyme towards the oxidation of TMB in the presence and reduction of hydrogen peroxide (H_2O_2) is studied in detail. The detailed kinetics and catalytic performance were analyzed using the Michaelis Menten equation. We observed high binding affinity of HfB_2/F68 towards H_2O_2, and also saw high rates of reaction for both TMB and H_2O_2 substrates. Analysis of the reaction mechanism showed that it follows the ping-pong mechanism like naturally occurring horseradish peroxidase (HRP).

HfB_2/F68 was further analyzed for biomedical applications. We examined the antibacterial activity of HfB_2/F68 nanozyme over various HfB_2 concentrations and incubation times. It was successful in eradicating both gram-negative *Escherichia coli* (*E. coli*) and gram-positive methicillin-resistant *Staphylococcus aureus* (MRSA) with a very low nanozyme concentration of <11 µg ml^{-1} within 5 hours of incubation. It also showed over 80% biocompatibility towards mammalian cells and was completely nonhemolytic even at higher concentrations of the nanozyme. We also conducted an extensive literature survey to compare the performance of the HfB_2/F68 nanozyme with other similar nanozymes, and found it to be extremely affordable and easily synthesizable with very competitive catalytic activity and exceptional antibacterial efficacy.

5.2 Preparation and characterization of 2D HfB_2/F68

Bulk materials layered materials can be separated into layered nanosheets with thicknesses ranging from a few layers down to single layers by liquid phase exfoliation (LPE),[43] where ultrasonic waves are converted into mechanical energy that separate the layers in a liquid medium.[44] Subsequently, dispersing agents in the solution adsorb on the dispersed flakes, thereby stabilizing them by electrostatic repulsion and preventing them from reaggregating.[45] From our previous work with 2D materials, we have used various polymers, surfactants and solvents to successfully exfoliate TMDCs, borides and carbides.[35, 38, 46] In particular, we have conducted extensive studies on metal diborides as quasi-2D nanosheets.[35] Here we exfoliated hafnium diboride (HfB_2)

nanosheets dispersed in Pluronic F68 (**Figure 1**) to study its antimicrobial and nanozyme properties. The HfB$_2$/F68 nanosheets were prepared by bath sonication of 200 mg of HfB$_2$ powder in 5 mL of aqueous F68 solution for 24 h in an ice water bath. The excess unexfoliated material was removed by centrifugation at 5000 rpm for 5 min. The resulting dispersion had a light grey appearance (**Figure 1**) and a concentration of ~30-50 mg ml^{-1} as determined by the extinction coefficient from UV-vis spectroscopy and ICP-MS.

Figure 5.1. Schematic of the liquid phase exfoliation of HfB$_2$ by 3% Pluronic F68.

Exfoliated HfB$_2$/F68 nanoflakes were characterized using atomic force microscopy (AFM), transmission electron microscopy (TEM), high-resolution transmission electron microscopy (HR-TEM) and energy dispersive spectroscopy (EDS). TEM images showed numerous nanosheets of varying sizes (**Figure 2A**). It was employed to determine the surface area of the nanoflakes by measuring 500 nanoflakes and plotting a histogram (**Figure S1A and S1B**). The average area was 503.30 nm^2 (**Figure 2B**). The morphology of the HfB$_2$/F68 nanosheets was studied by AFM (**Figure 2C**). Dispersed nanosheets were spin-coated in silicon wafers followed by annealing treatment to

remove organic residues. The nanoflakes exhibit different thicknesses and surface areas (**Figure S1C and S1D**). Additionally, from the AFM images we can see nanoflakes stacked together. A histogram of the surface area and flake thickness distribution was made from the AFM images using 427 nanoflakes. The average surface area obtained from AFM image was 4000.81 nm^2 (**Figure 2D**). The thickness varied from ~5-42 nm with average thickness of 12.92 nm (**Figure 2E and 2F**). From our results we observed much smaller flakes to be imaged using TEM as compared to AFM evident from average surface area.
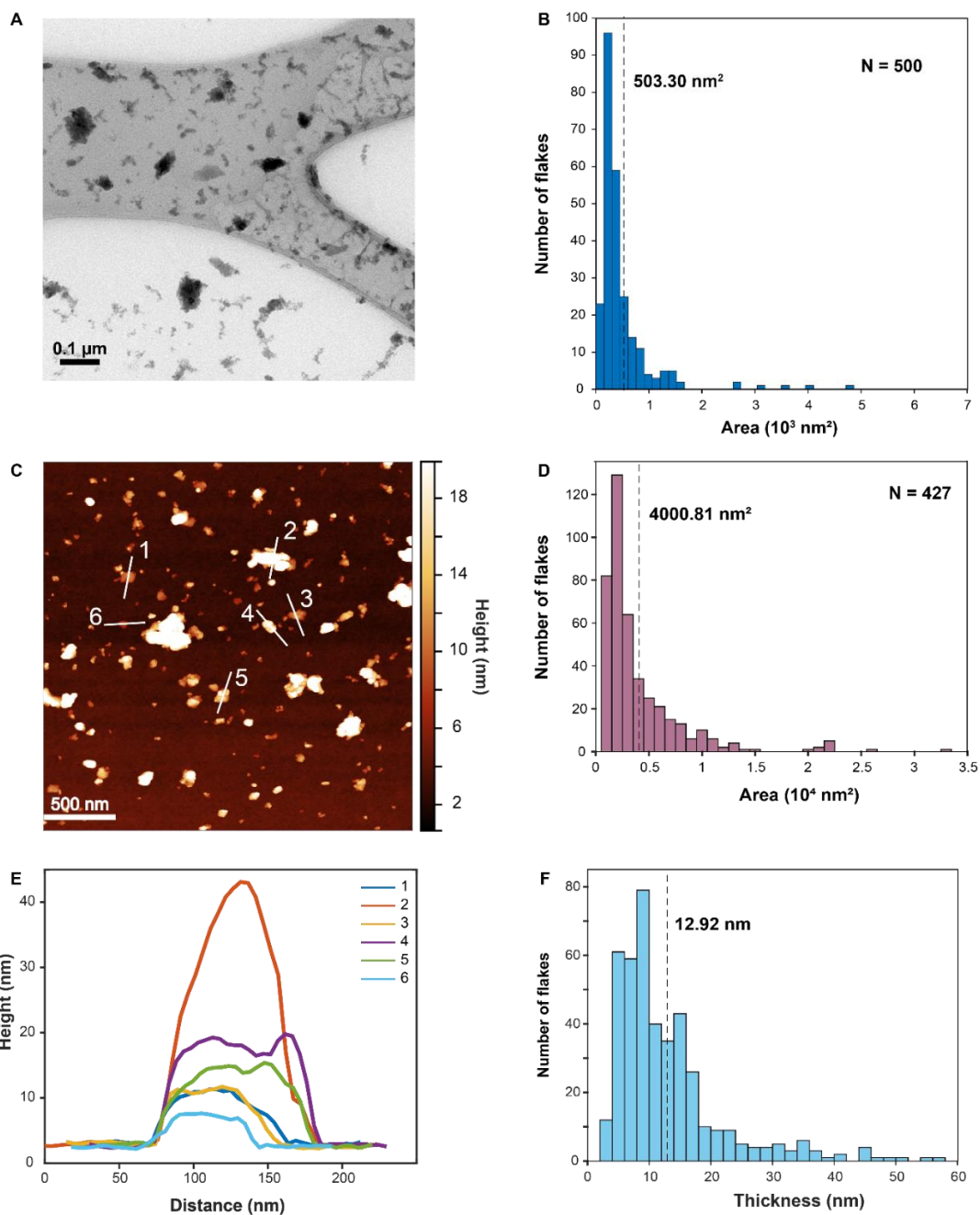
Figure 5.2. Characterization of HfB$_2$ liquid exfoliation by F68. (A) TEM image used for measuring the surface area of the HfB$_2$ nanoflakes. (B) Surface area distribution of 500 nanoflakes using TEM. The average surface area was calculated as 503.30 nm^2. (C) AFM image with varying thickness and surface area distribution of 427 nanoflakes. (D) The average surface area from AFM images was calculated as 4000.81 nm^2. (E) Thickness profile of 6 different individual flakes in (C).

(E) Thickness distribution of 427 nanoflakes showed average thickness was calculated as 12.92 nm.

We also saw presence of few layered nanoflakes from the AFM height distribution confirming presence of 2D nanosheets of HfB_2/F68. HR-TEM images showed the hexagonal atomic order of HfB_2 (**Figure 2b**). The presence of hafnium in the flakes was confirmed from the EDS spectrum (**Figure 2c**), showing the characteristic peak around 2 keV, which is not present when the measurement was taken off the flake. The copper peak at 8 keV corresponds to the grid and there is a small Ti peak caused by some impurities. C and O peaks are also found, and they may correspond to F68 adsorbed on the surface of HfB_2, or some minor oxidation of the HfB_2 flakes during processing.
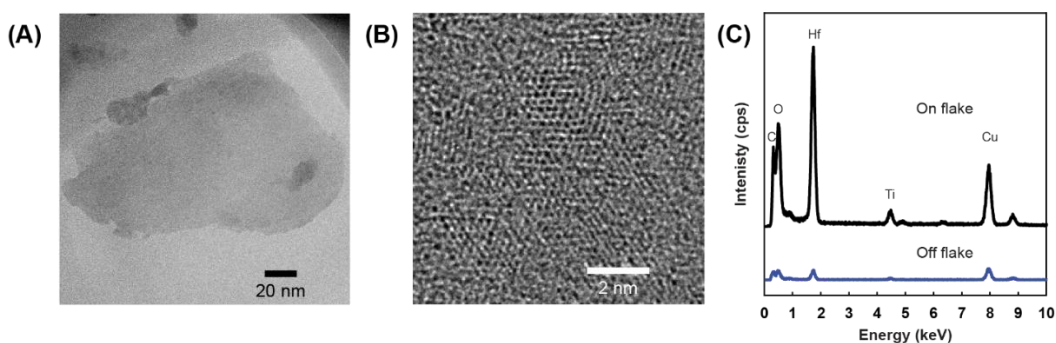
Figure 5.3. HR-TEM and EDS data. (A) TEM image of a HfB_2/F68 nanoflake. (B) HR-TEM image. (C) EDS spectrum on and off the flake.

5.3 Catalytic Activity of HfB_2/F68

TMB is a common chromogenic peroxidase substrate used to study enzyme mimics with peroxidase-like activity due to its high sensitivity and its molar extinction coefficient being the highest among the known colorimetric substrates. TMB can be oxidized by peroxidase in the presence of H_2O_2 to display a blue color with maximum absorbance at 652 nm.[18] The oxidation mechanism for this reaction follows a two-step process of single electron oxidation.[47] The peroxidase-like activity of HfB_2/F68 is shown in **Figure 4** where it acts to oxidize TMB in the presence of H_2O_2. This colorimetric reaction has been analyzed by measuring the absorbance at 652 nm. To verify if the peroxidase-like activity of HfB_2/F68 was the sole contribution from the 2D HfB_2 nanoflakes, we compared the enzymatic activity of the combined material against 3% F68

alone at different concentrations. The results were observed after 30 mins incubation time of the reaction mixture. We observed that enzymatic activity increased with increasing concentration of HfB$_2$/F68, while the 3% F68 failed to activate the reaction (**Figure 4A**). Furthermore, we performed a time-dependent study of different concentrations of HfB$_2$/F68 at three different incubation times. We observed the absorbance increased with increasing time, showing strong enzymatic activity (**Figure 4B**). The reaction was done from a range of 0 to 15 µg ml^{-1}, where absorbance increased with increasing concentration. All the experiments were done in triplicate.
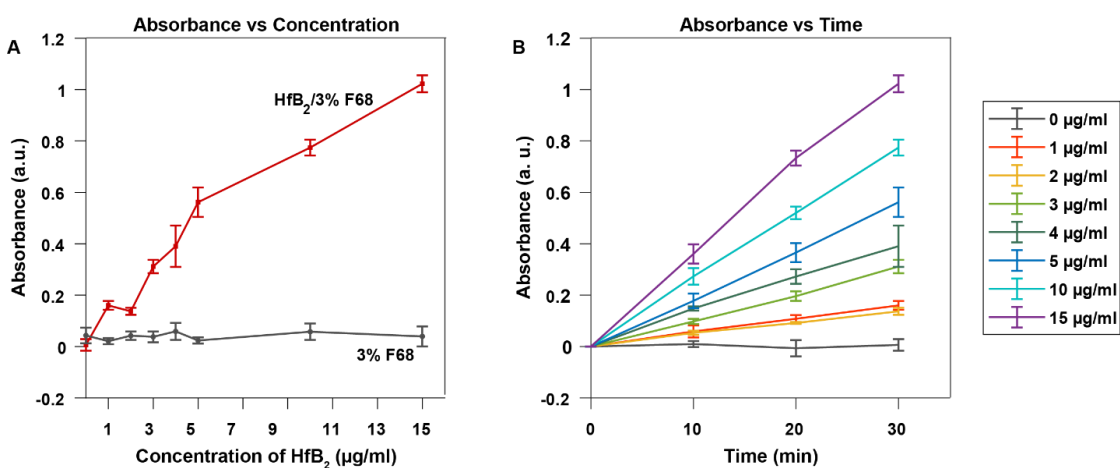
Figure 5.4. Enzymatic activity of nanozyme. (A) Comparison of enzymatic activity of nanozyme HfB$_2$/F68 vs just 3% F68. (B) Concentration dependent study of HfB$_2$ over 30 mins of time. All the experiment were done in triplicate.

We note that we initially performed a screening for peroxidase activity by assessing three commonly used substrates (**Figure S4**): 3,3,5,5-tetramethylbenzidine (TMB), 2,2'-azino-bis (3-ethylbenzothiazoline-6-sulphonic acid) (ABTS) and o-phenylenediamine (OPD) at optimized concentrations. After 30 mins of reaction, the typical color changes for the oxidation of these substrates were clearly visible. TMB, ABTS and OPD upon oxidation turn blue, green and yellow, respectively. Optical images show distinct difference in activity after 3 mins (initial) and 30 mins (final) incubation time (**Figure S2**).

To confirm that the 2D nanosheet morphology of HfB$_2$ is needed for the catalytic reaction, a comparison between exfoliated HfB$_2$ nanoflakes and bulk powder HfB$_2$ was done (**Figure S3**). The

powder sample had a concentration about ~5000 times higher than the exfoliated HfB_2 sample. Despite this, the exfoliated sample showed a more intense blue color after 30 mins corresponding to the higher yield of oxidized TMB. When the bulk material is exfoliated, more surface area and edges are exposed, all contributing to the improved catalytic activity which can only be observed in presence of HfB_2 nanoflakes.

5.4 Optimization of the catalytic reaction

To obtain the optimum performance of the HfB_2/F68 nanozyme, we systematically altered the experimental conditions including concentration of TMB, concentration of H_2O_2, pH, temperature, and concentration of F68 (**Figure 5**). First, the catalytic activity as a function of concentration of TMB is shown in **Figure 5A**. The highest values of catalytic activity occur at a TMB concentration between 5 to 12 mM, with highest relative activity occurring at about 10 mM. The optimal H_2O_2 concentration for the nanozyme activity was found to be at 10 mM, although 80% or more of the maximum activity can be achieved in the entire range of H_2O_2 concentrations that was tested (1 mM to 100 mM) (**Figure 5B**). Like the natural horseradish peroxidase (HRP) and other peroxidase-mimics,[6, 26, 48] the HfB_2/F68 nanozyme achieves high catalytic activity in acidic pH of 4 (**Figure 5C**). The optimal temperature for the peroxidase-like activity was found to be 35 ºC, and more than 60% of relative activity was obtained in the range from 30 ºC to 40 ºC (**Figure 5D**). The concentration of F68 for dispersing the $MoSe_2$ was optimized by testing different mass percentage (w/v%) values of 0.5%, 1%, 2%, 3%, and 4%. We found the highest catalytic activity occurred for 3% F68 at 10 µg ml^{-1} HfB_2 (**Figure 5E**). After completing this series of systematic studies, we found that the optimal conditions for the peroxidase-like activity of the HfB_2/F68 nanozyme were: TMB concentration of 10 mM, H_2O_2 concentration of 10 mM, pH of 4, temperature of 35ºC and 3% F68.
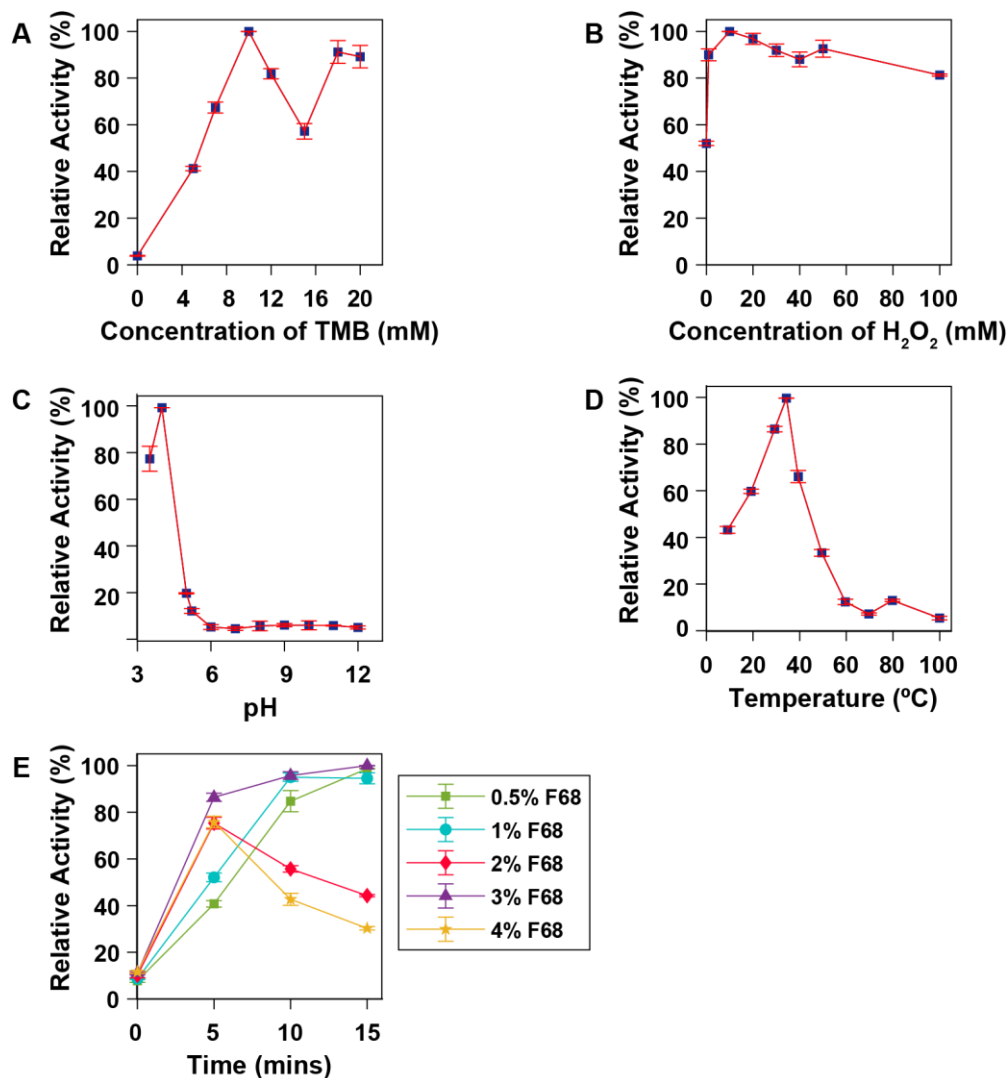
Figure 5.5. Optimal parameters for the peroxidase-like activity. Relative catalytic activity as a function of different conditions. (A) Concentration of F68. (B) HfB₂ concentration. (C) TMB concentration. (D) H₂O₂ concentration and. (E) pH and (F) temperature. The highest activity was set as 100% in each plot and done in triplicate.

5.5 Steady-state kinetics and reaction mechanism

Nanomaterials that mimic naturally occurring enzymes can be measured with the help of Michaelis-Menten kinetic equation. We used steady-state kinetics to obtain insights into the oxidation of TMB and reduction of H_2O_2. We determined the catalytic constants by measuring the initial reaction rates at different substrate concentrations and fitting the data to the Michaelis-Menten equation:

$$V = \frac{V_{max} \times [S]}{(K_M + [S])}$$

(1)

where, V is the initial reaction rate, V_{max} is the maximum rate, K_M is the Michaelis constant, and [S] is the substrate concentration. V_{max} is the maximum rate reached in the reaction and corresponds to the velocity where the substrate is saturated. K_M is a catalytic constant that describes the affinity of the substrate to the catalyst, and it is the concentration at half the maximum velocity V_{max}. To avoid factors that affect catalysis like product inhibition or reverse reactions, the initial rates of the catalytic reaction at different substrate concentrations were recorded.

The kinetics assay of HfB$_2$/F68 was done for both TMB and H$_2$O$_2$ as substrates (**Figure 6**). We observed that both substrates follow the Michaelis-Menten fitting curve. From our experiments we observe that TMB has a maximum velocity of 5.56 x 10^{-4} M/s (**Figure 5a**) and 3.268 x 10^{-4} M/s for H$_2$O$_2$ (**Figure 56**). The Michaelis constants obtained were 0.275 mM (**Figure 6A**) for TMB and 0.229 for H$_2$O$_2$ (**Figure 6B**). Lower values of K$_M$ indicate higher binding affinity between the substrate and the nanozyme. HfB$_2$/F68 seems to have slightly higher binding affinity for H$_2$O$_2$ than for TMB based on the these Michaelis constants. Furthermore, the nanozyme has lower K$_M$ values for both TMB and H$_2$O$_2$ compared to HRP (**Table 1**). Similarly, HfB$_2$/F68 showed faster initial rate as compared to HRP for both the substrates.[6] The higher affinity of TMB and H$_2$O$_2$ can be attributed to lower concentrations of these substrate to reach maximum catalytic activity.

Table 5.1. Comparison Kinetic parameters of HfB$_2$/F68 and HRP.

Catalyst	Substrate	K$_M$ (mM)	V$_{max}$ (M/s)
HfB$_2$/F68	TMB	0.275	5.56 x 10^{-4}
	H$_2$O$_2$	0.229	3.26 x 10^{-4}
HRP[6]	TMB	0.434	1.00 x 10^{-7}
	H$_2$O$_2$	3.7	8.78 x 10^{-8}
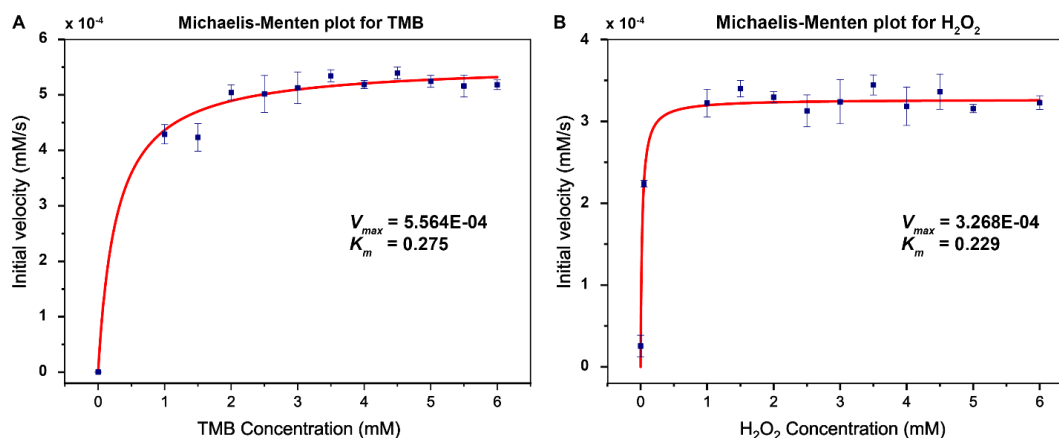
Figure 5.6. Steady-state kinetic experiments. (A) and (B) are Michaelis-Menten plots for TMB and H_2O_2, respectively. The error bars represent the standard error of three repeated measurements.

Details about the reaction mechanism involving TMB and H_2O_2 with the nanozyme can be understood by comparing Lineweaver-Burk plots of both substrates with the natural peroxidase HRP. A well-known mechanism for HRP is called the ping-pong mechanism, which can be confirmed by parallel lines of double-reciprocal plots of the concentration and velocity.[19] The equation for this reaction was the double reciprocal plots of the Michaelis-Menten equation is known as the Lineweaver-Burk plots:

$$\frac{1}{V} = \left(\frac{K_M}{V_{max}}\right)\left(\frac{1}{[S]}\right) + \frac{1}{V_{max}}$$

(2)

The double reciprocal graphs were made by fixing concentrations of one substrate while the varying the concentration of the other substrate (**Figure 7A and 7B**). The resulting lines are parallel to each other for different concentration of that substrate, confirming that the reaction between the substrates and HfB$_2$/F68 follows a ping-pong mechanism. This suggests that one substrate will bind to the catalyst first followed by the release of the product, and then just after the release the second substrate binds and reacts.[49] This mechanism is common among other nanozymes with intrinsic peroxidase-like activity.[19, 23, 50]

To calculate the turnover number or catalytic rate constant (k_{cat}) the following equation was used:

$$k_{cat} = \frac{V_{max}}{[E]}$$

where [E] is the molar concentration of catalyst. The rate constant, also known as the turnover number, measures the amount of substrate converted to product by unit time as the maximum velocity (V_{max}) is reached and represents the ability of forming product after the catalyst binds with the substrate. The calculated k_{cat} for the HfB$_2$/F68 nanozyme was 1.5×10^{-3} s^{-1} and 9.3×10^{-4} s^{-1} for TMB and H$_2$O$_2$, respectively.

The kinetic parameters of the reaction between the nanozyme, TMB and H$_2$O$_2$ substrates were determined. The resulting K_M values showed that the HfB$_2$/F68 nanozyme has higher affinity towards TMB and H$_2$O$_2$ compared to HRP. Furthermore, the higher value of V_{max} shows that HfB$_2$/F68 achieves maximal activity faster than HRP. These results all indicate that nanozyme HfB$_2$/F68 can be successfully used to mimic the naturally occurring peroxidase enzyme HRP with excellent efficiency. The catalytic reaction also follows a ping-pong mechanism involving both substrates.
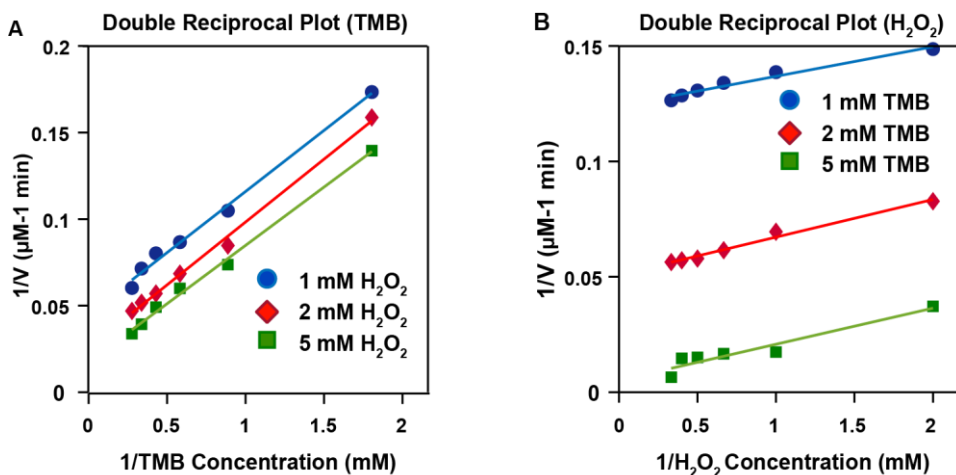
Figure 5.7. Ping-pong mechanism. Double reciprocal plots (Lineweaver-Burk) for (A) TMB and (B) H$_2$O$_2$. The final working concentration of the nanozyme was 10 µg/mL of HfB$_2$, the concentration of F68 was 3%(v/w) and all experiments were conducted at pH 4 and 35°C.

5.6 Antibacterial Activity of HfB$_2$/F68 Nanozyme

The growing antibiotic resistance of bacteria pose a significant challenge for healthcare systems, including in the healing of infected wounds and disinfection of surfaces.[51] Recently, various alternative antimicrobial agents based on nanomaterials have been studied.[18, 38, 52-54] To evaluate the antibacterial activity of HfB$_2$/F68 we chose two well-known strains: gram-negative *E. coli* and multi-drug resistant gram-positive *S. aureus*. The minimum bactericidal concentration (MBC) values of HfB$_2$/F68 were determined for both bacteria using the microdilution method as shown in **Figure 8**. The MBC values of biosafety level 1 (BSL-1) strains *E. coli* was 10 µg ml^{-1} after 4 h of incubation with HfB$_2$/F68 and 7 µg ml^{-1} after 5 h of incubation time (**Figure 8A**). For BSL-2 *S. aureus* the MBC was determined to be 12 µg ml^{-1} and 11 µg ml^{-1} after 4 h and 5 h of incubation respectively (**Figure 8B**). Subsequently we also did a study of antibacterial activity of HfB$_2$/F68 in the presence of H$_2$O$_2$ (**Figure S5**). The range of concentration used for of HfB$_2$/F68 was 0 - 15 µg ml^{-1} and for H$_2$O$_2$ was 0-0.1 mM (as 0.05 mM to 0.1mM is considered biologically relevant).[21, 55] We analyzed the MBC of *E. coli* and *S. aureus* with varying concentrations of HfB$_2$/F68 keeping the concentration of H$_2$O$_2$ at 0.1 mM for different incubation times (**Figure S5A and S5B** respectively). Also, we did the same with different H$_2$O$_2$ concentrations keeping the concentration of HfB$_2$/F68 fixed at 7 µg ml^{-1} and 12 µg ml^{-1} for *E. coli* and *S. aureus* respectively (**Figure S5C and S5D** respectively). The above results show similar antibacterial efficacy with and without the presence of H$_2$O$_2$ showing the ability of HfB$_2$/F68 to be a highly potent antibacterial agent.

5.7 Biocompatibility of HfB$_2$/F68 Nanozyme

The viability of the epithelial cell line A549 in the presence of HfB$_2$/F68 was analyzed with alamarBlue viability assays at different concentrations of HfB$_2$/F68 (**Figure 8C**). The fluorescence-based alamarBlue assay results indicate that after incubation for 24 h with HfB$_2$/F68 at concentrations ranging from 0 to 15 µg ml^{-1}, where 0 µg ml^{-1} indicates the absence of any HfB$_2$ indicating our control, there was more than 80% of the cells remaining viable. Furthermore, at up to 12 µg ml^{-1} of HfB$_2$/F68 concentration, the mammalian cells showed more than 90% cell viability which is considered biocompatible. We also performed the biocompatibility assay in presence of

0.1 mM H_2O_2 and observed a slight decrease in viability of cells down to ~70% at higher concentrations of 15 µg ml^{-1} of HfB$_2$/F68 as compared to just HfB$_2$/F68 (**Figure S5**).

To further examine the biocompatibility of HfB$_2$/F68, we performed a hemolysis assay by incubating whole human red blood cells (RBCs) with different concentrations of HfB$_2$/F68 ranging from 0 to 20 µg ml^{-1}. After incubation for 24 h, only ~3.5% lysis of RBCs was observed for HfB$_2$/F68 for concentrations as high as 20 µg ml^{-1} (**Figure 8D**). Materials that induce up to 5% hemolysis of RBC are considered biocompatible.[56] From optical images as well we can attest to the fact that HfB$_2$/F68 has near to no hemolytic effects on the RBCs (**Figure S6A**). Additionally, we measured the optical absorbance spectra of the samples after incubation over a broad spectrum of wavelengths from 300-700 nm and found very low absorbance from lysed RBCs across a wide range of concentrations of HfB2/F68 (Figure S6B). Only the positive control of Triton X showed significant cell lysis and high optical absorbance. Therefore, we can conclude that HfB$_2$/F68 can be considered biocompatible.
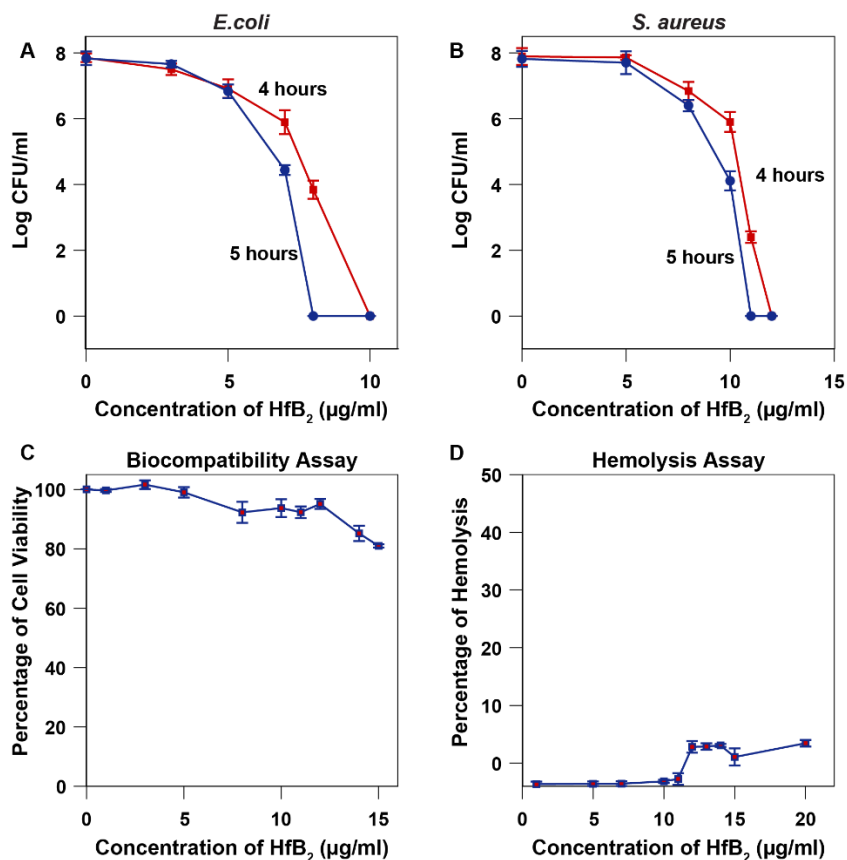
Figure 5.8. Antibacterial activity and biocompatibility of HfB$_2$/F68. (A) CFUs of *E. coli* after treatment with different HfB$_2$/F68 concentrations at 4 and 5 h of incubation times. (B) CFUs of *S. aureus* after treatment with different HfB$_2$/F68 concentrations at 4 and 5 h of incubation times. (C) Percent cell viability of A549 epithelial cells when treated with different concentrations of HfB$_2$/F68. (D) Hemolysis assay to determine the toxicity of HfB$_2$/F68.

5.8 Discussion

In this study, we successfully prepared HfB$_2$ nanosheets exfoliated and dispersed in an aqueous solution of the nonionic surfactant Pluronic F68 by bath sonication. We found 3% F68 concentration to be optimal for highest catalytic efficiency of the resulting HfB$_2$/F68 nanozyme. We hypothesize that a higher concentration of 4% F68 makes the nanoflake exfoliation less effective because of the decrease in surface tension caused by the concentration of dispersing agent.[57] Lower F68 concentrations (0.5%, 1% and 2%) are not as effective as 3% F68 because those concentrations of the dispersing agent are not enough to keep the separated layers of HfB$_2$ stabilized in solution. We also observe 0.5% and 1% of F68 to be more effective than 2% F68 probably because of better adsorption on the HfB$_2$ nanoflake surface (**Figure 5A**).

Understanding the kinetics of a catalytic reaction is essential for all enzymes and enzyme-mimics. In the past, steady-state kinetics and the theory developed by Leonor Michaelis and Maud Leonora Menten have been followed.[58] The modern Michaelis-Menten equation is derived based on the steady-state assumption (***Equation 1***). Insights about the reaction mechanism can be obtained from two relevant kinetic parameters V_{max} and K_M, where K_M is the measure of binding affinity of a specific substrate, and a lower value of K_M correlates to larger binding affinity.[59] The rate of reaction when the enzyme is saturated with substrate is the maximum rate of reaction or V_{max}.[59]

To overcome the drawbacks of natural peroxidases like high cost and low stability, nanozymes with superior catalytic activity are required.[13] A comparison of catalytic performance was conducted and the catalytic rate constants or turnover number (k_{cat}), calculated with the molar concentration of the nanozymes based on reported performance were analyzed (**Table S1**).

Nanozymes from different nanostructures were chosen for the comparison. The affinity of HfB_2/F68 with respect to H_2O_2 and the corresponding catalytic rate constant per mass for different nanozymes was also studied. Most nanozymes have high values of K_M for H_2O_2 corresponding to low affinity for hydrogen peroxide. The affinities of different nanozymes for hydrogen peroxide were plotted (**Figure S6**). Importantly, HfB_2/F68 nanozymes have very high affinity for hydrogen peroxide compared to all the nanozymes in Table S1. Only gold nanoparticles with graphitic carbon nitride (Au/g-C_3N_4) show slightly higher binding affinity value of 0.222 mM towards H_2O_2 as compared to HfB_2/F68 with 0.229 mM.[55] However, HfB_2/F68 has a much higher rate of reaction (V_{max}) with a value of 3.26 x 10^{-4} compared to 1.50 x 10^{-5} reaction rate of Au/g-C_3N_4 (**Table S1**). This is an important result, especially for applications involving reactions with hydrogen peroxide. The cost of HfB_2/F68 is also significantly lower than Au/g-C_3N_4.

One of the main drawbacks of natural enzymes is their high cost which is why lower cost nanozymes are needed. For instance, HRP shows excellent catalytic activity with turnover number (k_{cat}) (**Table S1**) but can cost up to \$3110/gram which is higher than all the nanozymes used in this comparison. Hence, we compared the prices of known nanozymes with their corresponding catalytic efficiency (**Figure S8**). The first reported nanozyme ferromagnetic nanoparticles (Fe_3O_4 MNPs), cost ~\$16/gram which is much more affordable than HRP with a turnover number higher than that of HfB_2/F68. However, they are toxic with low biocompatibility and instability over long times, making them unsuitable for biomedical applications.[6, 60] Other expensive nanozymes involving inert metals like Au and Pt cost ~\$300/gram and shows good catalytic activity (**Table S1**) have far lower binding affinity towards H_2O_2 (**Figure S7 and S8**).[15-16, 55] The most cost effective nanozymes include HfB_2, tungsten oxide (WO_3),[19] Prussian blue (PB NPs),[28] molybdenum diselenide ($MoSe_2$)[18] and molybdenum disufide (MoS_2)[32] with prices lower than \$16/gram. HfB_2 nanozymes, MoS_2 nanofibers (NF), $MoSe_2$ and PB NPs nanoparticles showed optimal results in terms of the relation between activity and cost-effectiveness (**Figure S8**). Moreover, HfB_2 has the highest TMB turnover activity per cost among nanozymes from 2D nanostructures. This might be caused by the low concentration of H_2O_2 required to reach the maximum velocity. We also analyzed the affinity of HfB_2/F68 with respect to TMB, which is lower than the rest of the nanozymes, but it

can achieve high catalytic activity at a much faster rate (**Table S1**). HfB$_2$/F68 excels in the relation between affinity towards H$_2$O$_2$ and catalytic activity compared to other enzyme-mimics. These findings make HfB$_2$/F68 nanozyme a promising candidate for applications involving extreme conditions since it is capable of achieving high activity despite the high concentration of TMB required.

We also analyzed the antibacterial activity of HfB$_2$/F68 nanozyme in the absence (**Figure 8A and 8B**) and presence of H$_2$O$_2$ (**Figure S4**). The results show the extraordinary efficiency of HfB$_2$/F68 at a concentration below 12 µg ml^{-1} against both gram-negative *E. coli* and drug resistant gram-positive *S. aureus* within 5 h of incubation. In the literature, MoSe$_2$ nanozymes synthesized in silk fibroin show wound healing ability with the assistance of 0.1 mM H$_2$O$_2$ at a much higher concentration of 50 µg ml^{-1}.[18] In comparison, graphene quantum dots (GDQs) could only achieve eradication of bacteria at 100 µg ml^{-1} and 1mM H$_2$O$_2$.[21] Gold nanoparticles with ultrathin graphitic carbon nitride (Au/g-C$_3$N$_4$) also displays antibacterial efficiency at comparable concentration of 20 µg ml^{-1} but in the presence of 0.1 mM H$_2$O$_2$ and 8 h of incubation.[55] Hence, HfB$_2$/F68 as a nanozyme can be studied further for various applications to replace natural enzyme owing to its very low cost, ease of synthesis, catalytic efficiency and binding affinity towards H$_2$O$_2$. Furthermore, there is scope for tunability and functionalization to incorporate specificity to increase its efficiency. It can also be used as disinfectants and as antibacterial agent in absence of H$_2$O$_2$ attributed to its very high antibacterial efficacy and biocompatibility.

5.9 Conclusions

In conclusion, we have prepared HfB$_2$ nanosheets dispersed and stabilized in F68, and demonstrated their nanozyme and antibacterial performance. Characterization by microscopy methods showed the nanosheets had average surface area of 1394.3 nm^2 and average thickness of 18.28 nm. The intrinsic peroxidase-like activity of HfB$_2$/F68 was investigated using TMB and H$_2$O$_2$ as substrates. The optimal conditions for the catalytic activity of the HfB$_2$/F68 nanozyme were found to be 10 mM H$_2$O$_2$, 10 mM TMB, pH4, 35℃, and 3% F68. Catalytic parameters were determined by steady state kinetic experiments and the catalytic performance was compared with other nanozymes in the literature, showing that HfB$_2$/F68 has one of the highest affinity towards

H$_2$O$_2$ and highest TMB turnover activity per cost among nanozymes from 2D nanostructures, and is very cost effective and can be produced by a facile and environmentally benign bath sonication method. Steady state kinetic assays also revealed that the reaction mechanism follows a ping-pong mechanism like HRP. The high affinity of the nanozyme for hydrogen peroxide opens the door for future possible applications such as detecting biomolecules that are closely related to the generation of H$_2$O$_2$. Furthermore, the antibacterial assay showed 100% eradication of *E. coli* and *S. aureus* at 7 µg ml^{-1} and 12 µg ml^{-1} of HfB$_2$/F68, respectively, after treatment for 5 h. These MBC values are among the lowest measured from antimicrobial agents from nanomaterials. The HfB$_2$/F68 also showed excellent biocompatibility based on mammalian cell viability and hemolysis assays, which suggests it may be suitable for future use as an antimicrobial agent or in other biomedical applications.

5.10 References

1. Garcia-Viloca, M.; Gao, J.; Karplus, M.; Truhlar, D. G., How Enzymes Work: Analysis by Modern Rate Theory and Computer Simulations. *Science* **2004,** *303* (5655), 186.

2. Jun, L. Y.; Yon, L. S.; Mubarak, N. M.; Bing, C. H.; Pan, S.; Danquah, M. K.; Abdullah, E. C.; Khalid, M., An overview of immobilized enzyme technologies for dye and phenolic removal from wastewater. *Journal of Environmental Chemical Engineering* **2019,** *7* (2), 102961.

3. Parameswaran, B.; Papamichael, E.; Varjani, S.; Raveendran, S., Introduction to Green Bioprocesses: Industrial Enzymes for Food Applications: Enzymes in Industrial Food Processing. 2019; pp 1-8.

4. Shrivastava, A.; Shrivastava, N.; Singh, P. K., Chapter 34 - Enzymes in Pharmaceutical Industry. In *Enzymes in Food Biotechnology*, Kuddus, M., Ed. Academic Press: 2019; pp 591-602.

5. Lin, Y.; Ren, J.; Qu, X., Catalytically Active Nanomaterials: A Promising Candidate for Artificial Enzymes. *Accounts of Chemical Research* **2014,** *47* (4), 1097-1105.

6. Gao, L.; Zhuang, J.; Nie, L.; Zhang, J.; Zhang, Y.; Gu, N.; Wang, T.; Feng, J.; Yang, D.; Perrett, S.; Yan, X., Intrinsic peroxidase-like activity of ferromagnetic nanoparticles. *Nature Nanotechnology* **2007,** *2* (9), 577-583.

7. Liang, M.; Yan, X., Nanozymes: From New Concepts, Mechanisms, and Standards to Applications. *Accounts of Chemical Research* **2019,** *52* (8), 2190-2200.

8. Manea, F.; Houillon, F. B.; Pasquato, L.; Scrimin, P., Nanozymes: Gold-Nanoparticle-Based Transphosphorylation Catalysts. *Angewandte Chemie International Edition* **2004,** *43* (45), 6165-6169.

9.   Manea, F.; Houillon, F. B.; Pasquato, L.; Scrimin, P., Nanozymes: gold-nanoparticle-based transphosphorylation catalysts. *Angewandte Chemie (International ed. in English)* **2004,** *43* (45), 6165-9.

10.   Huang, Y.; Ren, J.; Qu, X., Nanozymes: Classification, Catalytic Mechanisms, Activity Regulation, and Applications. *Chemical Reviews* **2019,** *119* (6), 4357-4412.

11.   Temoçin, Z.; İnal, M.; Gökgöz, M.; Yiğitoğlu, M., Immobilization of horseradish peroxidase on electrospun poly(vinyl alcohol)–polyacrylamide blend nanofiber membrane and its use in the conversion of phenol. *Polymer Bulletin* **2018,** *75* (5), 1843-1865.

12.   Zhang, Z.; Lai, J.; Wu, K.; Huang, X.; Guo, S.; Zhang, L.; Liu, J., Peroxidase-catalyzed chemiluminescence system and its application in immunoassay. *Talanta* **2018,** *180*, 260-270.

13.   Kim, M. S.; Cho, S.; Joo, S. H.; Lee, J.; Kwak, S. K.; Kim, M. I.; Lee, J., N- and B-Codoped Graphene: A Strong Candidate To Replace Natural Peroxidase in Sensitive and Selective Bioassays. *ACS nano* **2019,** *13* (4), 4312-4321.

14.   Wang, X.; Hu, Y.; Wei, H., Nanozymes in bionanotechnology: from sensing to therapeutics and beyond. *Inorganic Chemistry Frontiers* **2016,** *3* (1), 41-60.

15.   Li, W.; Chen, B.; Zhang, H.; Sun, Y.; Wang, J.; Zhang, J.; Fu, Y., BSA-stabilized Pt nanozyme for peroxidase mimetics and its application on colorimetric detection of mercury(II) ions. *Biosensors & bioelectronics* **2015,** *66*, 251-8.

16.   Liu, Y.; Xiang, Y.; Ding, D.; Guo, R., Structural effects of amphiphilic protein/gold nanoparticle hybrid based nanozyme on peroxidase-like activity and silver-mediated inhibition. *RSC Advances* **2016,** *6* (113), 112435-112444.

17.   Chen, T.; Zou, H.; Wu, X.; Liu, C.; Situ, B.; Zheng, L.; Yang, G., Nanozymatic Antioxidant System Based on MoS2 Nanosheets. *ACS Applied Materials & Interfaces* **2018,** *10* (15), 12453-12462.

18.   Huang, X.-W.; Wei, J.-J.; Liu, T.; Zhang, X.-L.; Bai, S.-M.; Yang, H.-H., Silk fibroin-assisted exfoliation and functionalization of transition metal dichalcogenide nanosheets for antibacterial wound dressings. *Nanoscale* **2017,** *9* (44), 17193-17198.

19.   Li, Z.; Liu, X.; Liang, X. H.; Zhong, J.; Guo, L.; Fu, F., Colorimetric determination of xanthine in urine based on peroxidase-like activity of WO(3) nanosheets. *Talanta* **2019,** *204*, 278-284.

20.   Zhu, J.; Peng, X.; Nie, W.; Wang, Y.; Gao, J.; Wen, W.; Selvaraj, J. N.; Zhang, X.; Wang, S., Hollow copper sulfide nanocubes as multifunctional nanozymes for colorimetric detection of dopamine and electrochemical detection of glucose. *Biosensors and Bioelectronics* **2019,** *141*, 111450.

21.   Sun, H.; Gao, N.; Dong, K.; Ren, J.; Qu, X., Graphene Quantum Dots-Band-Aids Used for Wound Disinfection. *ACS nano* **2014,** *8* (6), 6202-6210.

22.   Chen, S.; Wang, Y.; Zhong, M.; Yu, D.; Wang, C.; Lu, X., Fe(III)-Tannic Acid Complex Derived Fe3C Decorated Carbon Nanofibers for Triple-Enzyme Mimetic Activity and Their Biosensing Application. *ACS Biomaterials Science & Engineering* **2019,** *5* (3), 1238-1246.

23.   Yin, W.; Yu, J.; Lv, F.; Yan, L.; Zheng, L. R.; Gu, Z.; Zhao, Y., Functionalized Nano-MoS(2) with Peroxidase Catalytic and Near-Infrared Photothermal Activities for Safe and Synergetic Wound Antibacterial Applications. *ACS nano* **2016,** *10* (12), 11000-11011.

24.   Yang, Y.; Li, T.; Qin, Y.; Zhang, L.; Chen, Y., Construct of Carbon Nanotube-Supported Fe2O3 Hybrid Nanozyme by Atomic Layer Deposition for Highly Efficient Dopamine Sensing. *Frontiers in Chemistry* **2020,** *8* (876).

25.   Singh, N.; Savanur, M. A.; Srivastava, S.; D'Silva, P.; Mugesh, G., A Redox Modulatory Mn3O4 Nanozyme with Multi-Enzyme Activity Provides Efficient Cytoprotection to Human Cells in a Parkinson's Disease Model. *Angewandte Chemie International Edition* **2017,** *56* (45), 14267-14271.

26.   Chen, Y.; Chen, T.; Wu, X.; Yang, G., CuMnO2 nanoflakes as pH-switchable catalysts with multiple enzyme-like activities for cysteine detection. *Sensors and Actuators B: Chemical* **2019,** *279*, 374-384.

27.   Li, H.; Wang, T.; Wang, Y.; Wang, S.; Su, P.; Yang, Y., Intrinsic Triple-Enzyme Mimetic Activity of V6O13 Nanotextiles: Mechanism Investigation and Colorimetric and Fluorescent Detections. *Industrial & Engineering Chemistry Research* **2018,** *57* (6), 2416-2425.

28.   Zhang, W.; Hu, S.; Yin, J.-J.; He, W.; Lu, W.; Ma, M.; Gu, N.; Zhang, Y., Prussian Blue Nanoparticles as Multienzyme Mimetics and Reactive Oxygen Species Scavengers. *Journal of the American Chemical Society* **2016,** *138* (18), 5860-5865.

29.   Lim, H.; Yoon, S. I.; Kim, G.; Jang, A. R.; Shin, H. S., Stacking of Two-Dimensional Materials in Lateral and Vertical Directions. *Chemistry of Materials* **2014,** *26* (17), 4891-4903.

30.   Wang, Q. H.; Kalantar-Zadeh, K.; Kis, A.; Coleman, J. N.; Strano, M. S., Electronics and optoelectronics of two-dimensional transition metal dichalcogenides. *Nature Nanotechnology* **2012,** *7* (11), 699-712.

31.   Puthirath Balan, A.; Radhakrishnan, S.; Woellner, C. F.; Sinha, S. K.; Deng, L.; Reyes, C. d. l.; Rao, B. M.; Paulose, M.; Neupane, R.; Apte, A.; Kochat, V.; Vajtai, R.; Harutyunyan, A. R.; Chu, C.-W.; Costin, G.; Galvao, D. S.; Martí, A. A.; van Aken, P. A.; Varghese, O. K.; Tiwary, C. S.; Malie Madom Ramaswamy Iyer, A.; Ajayan, P. M., Exfoliation of a non-van der Waals material from iron ore hematite. *Nature Nanotechnology* **2018,** *13* (7), 602-609.

32.   Yu, J.; Ma, D.; Mei, L.; Gao, Q.; Yin, W.; Zhang, X.; Yan, L.; Gu, Z.; Ma, X.; Zhao, Y., Peroxidase-like activity of MoS2 nanoflakes with different modifications and their application for H2O2 and glucose detection. *Journal of Materials Chemistry B* **2018,** *6* (3), 487-498.

33.   Sani, E.; Mercatelli, L.; Meucci, M.; Silvestroni, L.; Balbo, A.; Sciti, D., Process and composition dependence of optical properties of zirconium, hafnium and tantalum borides for solar receiver applications. *Solar Energy Materials and Solar Cells* **2016,** *155*, 368-377.

34.   Gilliam, M. S.; Yousaf, A.; Guo, Y.; Li, D. O.; Momenah, A.; Wang, Q. H.; Green, A. A., Evaluating the Exfoliation Efficiency of Quasi-2D Metal Diboride Nanosheets Using Hansen Solubility Parameters. *Langmuir* **2021,** *37* (3), 1194-1205.

35.   Yousaf, A.; Gilliam, M. S.; Chang, S. L. Y.; Augustin, M.; Guo, Y.; Tahir, F.; Wang, M.; Schwindt, A.; Chu, X. S.; Li, D. O.; Kale, S.; Debnath, A.; Liu, Y.; Green, M. D.; Santos, E. J. G.; Green, A. A.; Wang, Q. H., Exfoliation of Quasi-Two-Dimensional Nanosheets of Metal Diborides. *The Journal of Physical Chemistry C* **2021,** *125* (12), 6787-6799.

36.   Wagner, F. R.; Baranov, A. I.; Grin, Y.; Kohout, M., A Position-Space View on Chemical Bonding in Metal Diborides with AlB2 Type of Crystal Structure. *Zeitschrift für anorganische und allgemeine Chemie* **2013,** *639* (11), 2025-2035.

37.   Backes, C.; Higgins, T. M.; Kelly, A.; Boland, C.; Harvey, A.; Hanlon, D.; Coleman, J. N., Guidelines for Exfoliation, Characterization and Processing of Layered Materials Produced by Liquid Exfoliation. *Chemistry of Materials* **2017,** *29* (1), 243-255.

38.   Debnath, A.; Saha, S.; Li, D. O.; Chu, X. S.; Ulissi, Z. W.; Green, A. A.; Wang, Q. H., Elimination of Multidrug-Resistant Bacteria by Transition Metal Dichalcogenides Encapsulated by Synthetic Single-Stranded DNA. *ACS Applied Materials & Interfaces* **2021,** *13* (7), 8082-8094.

39.   Yousaf, A.; Gilliam, M.; Chang, S.; Augustin, M.; Guo, Y.; Tahir, F.; Wang, M.; Schwindt, A.; Chu, X.; Li, D.; Kale, S.; Debnath, A.; Liu, Y.; Green, M.; Santos, E.; Green, A.; Wang, Q. H., *Exfoliation of Two-Dimensional Nanosheets of Metal Diborides*. 2020.

40.   Pitto-Barry, A.; Barry, N. P. E., Pluronic® block-copolymers in medicine: from chemical and biological versatility to rationalisation and clinical advances. *Polymer Chemistry* **2014,** *5* (10), 3291-3297.

41.   Seo, J.-W. T.; Green, A. A.; Antaris, A. L.; Hersam, M. C., High-Concentration Aqueous Dispersions of Graphene Using Nonionic, Biocompatible Block Copolymers. *The Journal of Physical Chemistry Letters* **2011,** *2* (9), 1004-1008.

42.   Nečas, D.; Klapetek, P., Gwyddion: an open-source software for SPM data analysis. *Central European Journal of Physics* **2012,** *10* (1), 181-188.

43.   Hernandez, Y.; Nicolosi, V.; Lotya, M.; Blighe, F. M.; Sun, Z.; De, S.; McGovern, I. T.; Holland, B.; Byrne, M.; Gun'Ko, Y. K.; Boland, J. J.; Niraj, P.; Duesberg, G.; Krishnamurthy, S.; Goodhue, R.; Hutchison, J.; Scardaci, V.; Ferrari, A. C.; Coleman, J. N., High-yield production of graphene by liquid-phase exfoliation of graphite. *Nature Nanotechnology* **2008,** *3* (9), 563-568.

44.   Chatakondu, K.; Green, M. L. H.; Thompson, M. E.; Suslick, K. S., The enhancement of intercalation reactions by ultrasound. *Journal of the Chemical Society, Chemical Communications* **1987,** (12), 900-901.

45.   Gupta, A.; Arunachalam, V.; Vasudevan, S., Water Dispersible, Positively and Negatively Charged MoS2 Nanosheets: Surface Chemistry and the Role of Surfactant Binding. *The Journal of Physical Chemistry Letters* **2015,** *6* (4), 739-744.

46.   Guo, Y.; Gupta, A.; Gilliam, M. S.; Debnath, A.; Yousaf, A.; Saha, S.; Levin, M. D.; Green, A. A.; Singh, A. K.; Wang, Q. H., Exfoliation of boron carbide into ultrathin nanosheets. *Nanoscale* **2021,** *13* (3), 1652-1662.

47.   Marquez, L. A.; Dunford, H. B., Mechanism of the Oxidation of 3,5,3',5'-Tetramethylbenzidine by Myeloperoxidase Determined by Transient- and Steady-State Kinetics. *Biochemistry* **1997,** *36* (31), 9349-9355.

48.   Xia, X.; Zhang, J.; Lu, N.; Kim, M. J.; Ghale, K.; Xu, Y.; McKenzie, E.; Liu, J.; Ye, H., Pd–Ir Core–Shell Nanocubes: A Type of Highly Efficient and Versatile Peroxidase Mimic. *ACS nano* **2015,** *9* (10), 9994-10004.

49.   Porter, D. J.; Bright, H. J., The mechanism of oxidation of nitroalkanes by horseradish peroxidase. *The Journal of biological chemistry* **1983,** *258* (16), 9913-24.

50.   Song, Y.; Qu, K.; Zhao, C.; Ren, J.; Qu, X., Graphene Oxide: Intrinsic Peroxidase Catalytic Activity and Its Application to Glucose Detection. *Advanced Materials* **2010,** *22* (19), 2206-2210.

51.   Ji, H.; Sun, H.; Qu, X., Antibacterial applications of graphene-based nanomaterials: Recent achievements and challenges. *Advanced drug delivery reviews* **2016,** *105* (Pt B), 176-189.

52.   Liu, S.; Zeng, T. H.; Hofmann, M.; Burcombe, E.; Wei, J.; Jiang, R.; Kong, J.; Chen, Y., Antibacterial Activity of Graphite, Graphite Oxide, Graphene Oxide, and Reduced Graphene Oxide: Membrane and Oxidative Stress. *ACS nano* **2011,** *5* (9), 6971-6980.

53.   Rasool, K.; Helal, M.; Ali, A.; Ren, C. E.; Gogotsi, Y.; Mahmoud, K. A., Antibacterial Activity of Ti3C2Tx MXene. *ACS nano* **2016,** *10* (3), 3674-3684.

54.   Roy, S.; Mondal, A.; Yadav, V.; Sarkar, A.; Banerjee, R.; Sanpui, P.; Jaiswal, A., Mechanistic Insight into the Antibacterial Activity of Chitosan Exfoliated MoS2 Nanosheets: Membrane Damage, Metabolic Inactivation, and Oxidative Stress. *ACS Applied Bio Materials* **2019,** *2* (7), 2738-2755.

55.   Wang, Z.; Dong, K.; Liu, Z.; Zhang, Y.; Chen, Z.; Sun, H.; Ren, J.; Qu, X., Activation of biologically relevant levels of reactive oxygen species by Au/g-C(3)N(4) hybrid nanozyme for bacteria killing and wound disinfection. *Biomaterials* **2017,** *113*, 145-157.

56.   Liu, J.; Li, F.; Zheng, J.; Li, B.; Zhang, D.; Jia, L., Redox/NIR dual-responsive MoS(2) for synergetic chemo-photothermal therapy of cancer. *J Nanobiotechnology* **2019,** *17* (1), 78-78.

57.   Notley, S. M., Highly Concentrated Aqueous Suspensions of Graphene through Ultrasonic Exfoliation with Continuous Surfactant Addition. *Langmuir* **2012,** *28* (40), 14110-14113.

58.   Johnson, K. A.; Goody, R. S., The Original Michaelis Constant: Translation of the 1913 Michaelis–Menten Paper. *Biochemistry* **2011,** *50* (39), 8264-8269.

59.   Cho, Y. S.; Lim, H. S., Comparison of various estimation methods for the parameters of Michaelis-Menten equation based on in vitro elimination kinetic simulation data. *Translational and clinical pharmacology* **2018,** *26* (1), 39-47.

60.   Markides, H.; Rotherham, M.; El Haj, A. J., Biocompatibility and Toxicity of Magnetic Nanoparticles in Regenerative Medicine. *Journal of Nanomaterials* **2012,** *2012*, 614094.

CHAPTER 6

CONCLUSIONS AND FUTURE DIRECTIONS

6.1 Conclusions

Two-dimensional (2D) materials of different compositions has been studied extensively in the last two decades since the advent of graphene and its derivatives in 2004.[1–3] These novel 2D materials are used in numerous applications of various fields of research such as biomedicine, biosensing and chemical sensing as well as energy storage and generation, electronics, etc.[4] In this thesis we covered synthesis of biocompatible novel nanomaterials and biological applications of two types of layered materials: (1) 2D van der Waals transition metal chalcogenides (TMCs) and (2) Layered non-van der Waals metal diborides. Layered materials with their unique physical, chemical and electrical properties along with the fact that they are extremely tunable has a lot of potential for application in medical fields addressing current health problems. One of the major limitations of using nanomaterials in biology is their cytotoxicity which we have addressed in this thesis by interfacing biological molecules to produce biocompatible 2D nanomaterials. In conclusion, we have demonstrated simple synthesis of 2D layered materials followed by their characterizations. We demonstrated the antimicrobial activity of the synthesized materials and addressed the challenge of growing resistance of MDR microbes. We also evaluated their mode of action and biocompatibility. Finally, we tested our synthesized metal diborides for intrinsic catalytic activity for future application in biomedicine.

In Chapter 2, we synthesized several TMCs with various compositions in a oligonucleotide sequence of ssDNA with the sequence T_{20} inspired by our previous work.[5] After characterization we observed $MoSe_2$ nanosheets were dispersed in ssDNA most efficiently and was most potent against bacteria. It was even ~21% more effective against GO in eliminating gram-negative strain *E. coli*. To increase the efficacy of antibacterial activity, we successfully designed and fabricated a novel target-specific biocompatible antibacterial agent where $MoSe_2$ was prepared by liquid phase exfoliation encapsulated in cationic polymer PLL and nonionic Pluronic F77 ($MoSe_2$/PLL/F77). Evaluation of the antibacterial activity of the $MoSe_2$/PLL/F77 nanosheets

revealed their exceptional ability to eradicate ESKAPE strains. The multimodal action of MoSe$_2$/PLL/F77 against both gram-positive and gram-negative bacteria was elucidated with the help of SEM and TEM. Additionally, we observed no development of resistance against MoSe$_2$/PLL/F7 even after 20 passages of bacteria. The remarkable antibacterial performance and inhibition of resistance shows the ability of MoSe$_2$/PLL/F77 as a potent antibacterial system with the capacity to combat a broad spectrum of different drug-resistant bacterial pathogens.

In Chapter 3, we further tested MoSe$_2$/PLL/F77 against MDR biofilms which are a leading cause of spreading of MDR infections in hospitals and public places. We observed complete eradication of mature biofilm against both gram-positive and gram-negative drug-resistant bacteria. We also demonstrated successful inhibition of biofilm growth on several medically relevant surfaces (PMMA-coated glass slides, hydrophilic PTFE membranes and medical grade Ti-alloy) coated with MoSe$_2$/PLL/F77 with only below ~6% surviving bacterial cell demonstrating the high efficacy of the MoSe$_2$/PLL/F77 coating. Furthermore, EDX analysis of the coating showed presence of Mo and Se elements on the coated region as opposed to increased presence of carbon on the uncoated region signifying presence of biomass, thereby proving the presence and effects of MoSe$_2$/PLL/F77 coating on biofilm growth. This brings us one-step closure towards practical application in solving problems against growing resistance of MDR bacteria and biofilm.

In Chapter 4, we prepared another novel material consisting of MoSe$_2$ nanosheets dispersed in chitosan (MoSe$_2$/CS) to target MDR fungal strains including *C. auris* panel which has been declared as an imminent threat by CDC. Since, fungal strains are more difficult to treat and with the lack of antifungal drugs available we replaced PLL with chitosan a naturally occurring antifungal polymer. We observed a successful synthesis of 2D MoSe$_2$ nanosheets in presence of CS. They showed exceptional efficiency against growth of both unicellular and filamentous fungi leading to complete eradication. A detailed investigation of the mechanism of antifungal action showed that the MoSe$_2$/CS nanosheets induced fungal cell death through a combined action of membrane damage, membrane depolarization, metabolic inactivation, and cytoplasmic leakage.

The MoSe$_2$/CS nanosheets were also found to possess high biocompatibility toward mammalian cells.

In Chapter 5, we investigated a completely different material metal diborides. They are non-van der Waals layered materials held together by ionic/covalent bonds. Recently the liquid phase exfoliation and structural properties of metal diborides were explored in our lab.[6–8] We further analyzed them for biomedical applications in this dissertation. We successfully synthesized and characterized hafnium diboride (HfB$_2$) nanoflakes in biocompatible block-co polymers Pluronic F68. Size and thickness distributions for the nanoflakes showed nanoflake like property. We examined its catalytic activity and discovered a new nanozyme which showed peroxidase mimicking properties. HfB$_2$/F68 nanozyme possess intrinsic peroxidase-like activity which was investigated with the help of TMB and H$_2$O$_2$ as substrates. Catalytic parameters were determined by steady state kinetic experiments and the catalytic performance was compared with other nanozymes in the literature. Comparison showed that HfB$_2$/F68 has one of the highest affinities towards H$_2$O$_2$ and highest TMB turnover activity per cost between nanozymes when compared with 2D-nanostructures. Steady state kinetic assays also revealed that the reaction mechanism follows a Ping-Pong mechanism like HRP. Furthermore, antibacterial assay showed complete eradication of *E. coli* and MDR *S. aureus* and high biocompatibility.

Thus, the work covered in my thesis explores antimicrobial efficacy of layered materials for future applications in healthcare system to tackle the growing drug-resistance of microbes. We also introduce layered materials as a novel nanozyme with antibacterial ability to eradicate both gram-positive and gram-negative bacteria. I believe that the research in this dissertation paves the path for future solution to the problems faced in the healthcare system and overcome the limitations posed by current approaches. Additionally, with further research of metal diborides

scientists can learn and synthesize various biocompatible materials. It can open new possibilities of applications in biomedicine, catalysis, biosensing and functional electronics.

6.2 Future directions

Recent development in 2D materials and multiple research in the field of biomedical applications have opened up numerous possibilities. Hence, following are the possible direction these projects can lead to in the immediate future.

6.2.1 Surface coating

One of the most critical problems faced by healthcare systems are multi-drug resistant infections (MDR). The primary reason for these infections is their ability to attach and survive on surfaces, both in healthcare settings and on common surfaces.[9] Colonization of these MDR microbes on surgical implants and tools leads to infections and biofilm formation which is the major reason for complications in the use of implants and are the predominant cause for implant failure.[10,11] We demonstrated successful antibacterial coating with the help of $MoSe_2$/PL/F77 on various medically relevant surfaces (PMMA-coated glass slides, hydrophilic PTFE membranes and medical grade Ti-alloy). $MoSe_2$/PL/F77 not only eradicated mature biofilms but also effectively inhibited the growth of biofilm on coated surfaces. Furthermore, with incorporation of viscous material like chitosan (CS), more robust coating can be developed like $MoSe_2$/CS. These coatings on hospitals equipment, medical devices and in general surfaces in public places can avoid the growth and spread of MDR infections.

6.2.2 Wound healing patches

Prolonged time to heal wounds and the possibility of infections in patients suffering from diabetes or post-surgical patients not only gives rise to complications but also makes the entire process expensive.[12,13] Current therapies cannot fully address the impaired healing, provoking wound complications like infections and poor wound closure.[13] Thus, unique properties of nanomaterials and anti-inflammatory properties of biomaterials like antimicrobial peptides (PLL) or polymers (CS) can provide an alternative solutions for next generation of wound nano-therapies. We were able to make free standing films of $MoSe_2$/CS which were excellent in inhibiting growth of bacteria and fungi in solution. Owing to its viscosity, elasticity and hydrophilicity

it can be further analyzed for wound healing patches. Additionally, both MoSe$_2$/PLL/F77 and MoSe$_2$/CS can be incorporated in methylcellulose-based polymers for applications on noninvasive wounds and burn regions for prevention of infection thereby expediting the healing process. Thus, these biocompatible nanomaterials can bridge the gap between scientific knowledge and translate them into commercially available wound healing products.

6.2.3 Lysing of viral capsids

With the onset of SARS-CoV-2 pandemic and other viral diseases, we need fast and simple means of detection which consists of one important step of extraction of RNA/DNA. Often extraction process can be time consuming, expensive, and complicated limiting conventional extraction kits for large-scale extraction process.[14] Hence, we are analyzing the ability of these synthesized nanomaterials for lysing of viral capsids for a fast, affordable, and efficient extraction of RNA/DNA. With our material MoSe$_2$/PLL/F77 and MoSe$_2$/CS we were able to lyse viral capsids in a very short time. Further analysis can achieve binding of the extracted RNA/DNA in buffer comprising of chaotropic agents and organic solvents to separate them from the nanomaterials for rapid large-scale detection, analysis and storage.

6.2.4 Mechanistic study of metal diborides in medical applications

Metal diborides are a class of ultrahigh-temperature ceramic materials showing flexibility and strong mechanical properties in composite form.[6,7] In our research we observed the facile production of HfB$_2$ nanoflakes in aqueous solution of biocompatible Pluronic F68 which has the advantage of an environmentally friendly process of water bath sonication. Researchers can further investigate synthesizing these metal diborides in other biocompatible oligonucleotide, polymers and surfactant to generate higher yield. We also discovered the peroxidase-like activity of HfB$_2$ with high affinity towards H$_2$O$_2$ opening the door for future possible applications in catalysis, ROS production and biomedicine. For instance, detecting biomolecules that are closely related to the generation of H$_2$O$_2$ by creating biosensors made of this nanozyme. Since HfB$_2$/F68 also displayed exceptional antibacterial efficiency, scientist should perform detailed studies into its mechanism of action and cytotoxicity. With its ability to kill microbes and to form strong, flexible composites it can be further examined for future applications as an antimicrobial agent and coatings.

6.3 References

1. Novoselov, K. S.; Geim, A. K.; Morozov, S. V.; Jiang, D.; Zhang, Y.; Dubonos, S. V.; Grigorieva, I. V.; Firsov, A. A., Electric Field Effect in Atomically Thin Carbon Films. *Science* **2004,** *306* (5696), 666.

2. Mas-Ballesté, R.; Gómez-Navarro, C.; Gómez-Herrero, J.; Zamora, F., 2D materials: to graphene and beyond. *Nanoscale* **2011,** *3* (1), 20-30.

3. Banerjee, A. N., Graphene and its derivatives as biomedical materials: future prospects and challenges. *Interface focus* **2018,** *8* (3), 20170056.

4. Rohaizad, N.; Mayorga-Martinez, C. C.; Fojtů, M.; Latiff, N. M.; Pumera, M., Two-dimensional materials in biomedical, biosensing and sensing applications. *Chemical Society Reviews* **2021,** *50* (1), 619-657.

5. Debnath, A.; Saha, S.; Li, D. O.; Chu, X. S.; Ulissi, Z. W.; Green, A. A.; Wang, Q. H., Elimination of Multidrug-Resistant Bacteria by Transition Metal Dichalcogenides Encapsulated by Synthetic Single-Stranded DNA. *ACS Applied Materials & Interfaces* **2021,** *13* (7), 8082-8094.

6. Gilliam, M. S.; Yousaf, A.; Guo, Y.; Li, D. O.; Momenah, A.; Wang, Q. H.; Green, A. A., Evaluating the Exfoliation Efficiency of Quasi-2D Metal Diboride Nanosheets Using Hansen Solubility Parameters. *Langmuir* **2021,** *37* (3), 1194-1205.

7. Yousaf, A.; Gilliam, M. S.; Chang, S. L. Y.; Augustin, M.; Guo, Y.; Tahir, F.; Wang, M.; Schwindt, A.; Chu, X. S.; Li, D. O.; Kale, S.; Debnath, A.; Liu, Y.; Green, M. D.; Santos, E. J. G.; Green, A. A.; Wang, Q. H., Exfoliation of Quasi-Two-Dimensional Nanosheets of Metal Diborides. *The Journal of Physical Chemistry C* **2021,** *125* (12), 6787-6799.

8. Guo, Y.; Gupta, A.; Gilliam, M. S.; Debnath, A.; Yousaf, A.; Saha, S.; Levin, M. D.; Green, A. A.; Singh, A. K.; Wang, Q. H., Exfoliation of boron carbide into ultrathin nanosheets. *Nanoscale* **2021,** *13* (3), 1652-1662.

9. Imani, S. M.; Ladouceur, L.; Marshall, T.; Maclachlan, R.; Soleymani, L.; Didar, T. F., Antimicrobial Nanomaterials and Coatings: Current Mechanisms and Future Perspectives to Control the Spread of Viruses Including SARS-CoV-2. *ACS Nano* **2020,** *14* (10), 12341-12369.

10. Li, X.; Huang, T.; Heath, D. E.; O'Brien-Simpson, N. M.; O'Connor, A. J., Antimicrobial nanoparticle coatings for medical implants: Design challenges and prospects. *Biointerphases* **2020,** *15* (6), 060801.

11. Vasilev, K., Nanoengineered Antibacterial Coatings and Materials: A Perspective. *Coatings* **2019,** *9* (10).

12. Han, G.; Ceilley, R., Chronic Wound Healing: A Review of Current Management and Treatments. *Advances in therapy* **2017,** *34* (3), 599-610.

13. Blanco-Fernandez, B.; Castaño, O.; Mateos-Timoneda, M.; Engel, E.; Pérez-Amodio, S., Nanotechnology Approaches in Chronic Wound Healing. *Advances in wound care* **2021,** *10* (5), 234-256.

14. Klein, S.; Müller, T. G.; Khalid, D.; Sonntag-Buck, V.; Heuser, A.-M.; Glass, B.; Meurer, M.; Morales, I.; Schillak, A.; Freistaedter, A.; Ambiel, I.; Winter, S. L.; Zimmermann, L.; Naumoska, T.; Bubeck, F.; Kirrmaier, D.; Ullrich, S.; Barreto Miranda, I.; Anders, S.; Grimm, D.; Schnitzler, P.;

Knop, M.; Kräusslich, H.-G.; Dao Thi, V. L.; Börner, K.; Chlanda, P., SARS-CoV-2 RNA Extraction Using Magnetic Beads for Rapid Large-Scale Testing by RT-qPCR and RT-LAMP. *Viruses* **2020,** *12* (8), 863.

REFERENCES

Chapter 1

1.   Huh, A. J.; Kwon, Y. J., "Nanoantibiotics": A new paradigm for treating infectious diseases using nanomaterials in the antibiotics resistant era. *Journal of Controlled Release* **2011,** *156* (2), 128-145.

2.   Ventola, C. L., The antibiotic resistance crisis: part 1: causes and threats. *P T* **2015,** *40* (4), 277-283.

3.   Michael, C. A.; Dominey-Howes, D.; Labbate, M., The antimicrobial resistance crisis: causes, consequences, and management. *Frontiers in public health* **2014,** *2*, 145-145.

4.   Spellberg, B.; Gilbert, D. N., The Future of Antibiotics and Resistance: A Tribute to a Career of Leadership by John Bartlett. *Clinical Infectious Diseases* **2014,** *59* (suppl_2), S71-S75.

5.   Gross, M., Antibiotics in crisis. *Current biology : CB* **2013,** *23* (24), R1063-5.

6.   Rossolini, G. M.; Arena, F.; Pecile, P.; Pollini, S., Update on the antibiotic resistance crisis. *Current Opinion in Pharmacology* **2014,** *18*, 56-60.

7.   Zhabiz, G.; Omar, B.; Donald Gene, P., Bacteriophage therapy: a potential solution for the antibiotic resistance crisis. *The Journal of Infection in Developing Countries* **2014,** *8* (02).

8.   Cepas, V.; López, Y.; Muñoz, E.; Rolo, D.; Ardanuy, C.; Martí, S.; Xercavins, M.; Horcajada, J. P.; Bosch, J.; Soto, S. M., Relationship Between Biofilm Formation and Antimicrobial Resistance in Gram-Negative Bacteria. *Microbial Drug Resistance* **2018,** *25* (1), 72-79.

9.   Hathroubi, S.; Mekni, M. A.; Domenico, P.; Nguyen, D.; Jacques, M., Biofilms: Microbial Shelters Against Antibiotics. *Microbial Drug Resistance* **2016,** *23* (2), 147-156.

10.   Sanglard, D., Emerging Threats in Antifungal-Resistant Fungal Pathogens. *Frontiers in Medicine* **2016,** *3* (11).

11.   Brown, G. D.; Denning, D. W.; Gow, N. A. R.; Levitz, S. M.; Netea, M. G.; White, T. C., Hidden Killers: Human Fungal Infections. *Science Translational Medicine* **2012,** *4* (165), 165rv13-165rv13.

12.   Wisplinghoff, H.; Bischoff, T.; Tallent, S. M.; Seifert, H.; Wenzel, R. P.; Edmond, M. B., Nosocomial bloodstream infections in US hospitals: analysis of 24,179 cases from a prospective nationwide surveillance study. *Clinical infectious diseases : an official publication of the Infectious Diseases Society of America* **2004,** *39* (3), 309-17.

13.   Kontoyiannis, D. P.; Marr, K. A.; Park, B. J.; Alexander, B. D.; Anaissie, E. J.; Walsh, T. J.; Ito, J.; Andes, D. R.; Baddley, J. W.; Brown, J. M.; Brumble, L. M.; Freifeld, A. G.; Hadley, S.; Herwaldt, L. A.; Kauffman, C. A.; Knapp, K.; Lyon, G. M.; Morrison, V. A.; Papanicolaou, G.; Patterson, T. F.; Perl, T. M.; Schuster, M. G.; Walker, R.; Wannemuehler, K. A.; Wingard, J. R.; Chiller, T. M.; Pappas, P. G., Prospective surveillance for invasive fungal infections in hematopoietic stem cell transplant recipients, 2001-2006: overview of the Transplant-Associated Infection Surveillance Network (TRANSNET) Database. *Clinical infectious diseases : an official publication of the Infectious Diseases Society of America* **2010,** *50* (8), 1091-100.

14.   Denning, D. W.; Bromley, M. J., How to bolster the antifungal pipeline. *Science* **2015,** *347* (6229), 1414.

15.   Friedman, N. D.; Temkin, E.; Carmeli, Y., The negative impact of antibiotic resistance. *Clinical microbiology and infection : the official publication of the European Society of Clinical Microbiology and Infectious Diseases* **2016,** *22* (5), 416-22.

16.   Thabit, A. K.; Crandon, J. L.; Nicolau, D. P., Antimicrobial resistance: impact on clinical and economic outcomes and the need for new antimicrobials. *Expert opinion on pharmacotherapy* **2015,** *16* (2), 159-77.

17.   Lee, N.-Y.; Ko, W.-C.; Hsueh, P.-R., Nanoparticles in the Treatment of Infections Caused by Multidrug-Resistant Organisms. *Front Pharmacol* **2019,** *10*, 1153-1153.

18.   Muzammil, S.; Hayat, S.; Fakhar, E. A. M.; Aslam, B.; Siddique, M. H.; Nisar, M. A.; Saqalein, M.; Atif, M.; Sarwar, A.; Khurshid, A.; Amin, N.; Wang, Z., Nanoantibiotics: Future nanotechnologies to combat antibiotic resistance. *Frontiers in bioscience (Elite edition)* **2018,** *10*, 352-374.

19.   Natan, M.; Banin, E., From Nano to Micro: using nanotechnology to combat microorganisms and their multidrug resistance. *FEMS microbiology reviews* **2017,** *41* (3), 302-322.

20.   Singh, R.; Smitha, M. S.; Singh, S. P., The role of nanotechnology in combating multi-drug resistant bacteria. *Journal of nanoscience and nanotechnology* **2014,** *14* (7), 4745-56.

21.   Baptista, P. V.; McCusker, M. P.; Carvalho, A.; Ferreira, D. A.; Mohan, N. M.; Martins, M.; Fernandes, A. R., Nano-Strategies to Fight Multidrug Resistant Bacteria-"A Battle of the Titans". *Front Microbiol* **2018,** *9*, 1441-1441.

22.   Beyth, N.; Houri-Haddad, Y.; Domb, A.; Khan, W.; Hazan, R., Alternative Antimicrobial Approach: Nano-Antimicrobial Materials. *Evidence-Based Complementary and Alternative Medicine* **2015,** *2015*, 246012.

23.   Pelgrift, R. Y.; Friedman, A. J., Nanotechnology as a therapeutic tool to combat microbial resistance. *Adv Drug Deliv Rev* **2013,** *65* (13-14), 1803-1815.

24.   Hemeg, H. A., Nanomaterials for alternative antibacterial therapy. *International journal of nanomedicine* **2017,** *12*, 8211-8225.

25.   Rai, M. K.; Deshmukh, S. D.; Ingle, A. P.; Gade, A. K., Silver nanoparticles: the powerful nanoweapon against multidrug-resistant bacteria. *Journal of applied microbiology* **2012,** *112* (5), 841-52.

26.   Roy, S.; Mondal, A.; Yadav, V.; Sarkar, A.; Banerjee, R.; Sanpui, P.; Jaiswal, A., Mechanistic Insight into the Antibacterial Activity of Chitosan Exfoliated MoS2 Nanosheets: Membrane Damage, Metabolic Inactivation, and Oxidative Stress. *ACS Applied Bio Materials* **2019,** *2* (7), 2738-2755.

27.   Slavin, Y. N.; Asnis, J.; Häfeli, U. O.; Bach, H., Metal nanoparticles: understanding the mechanisms behind antibacterial activity. *Journal of Nanobiotechnology* **2017,** *15* (1), 65.

28.   Guo, H.-W.; Hu, Z.; Liu, Z.-B.; Tian, J.-G., Stacking of 2D Materials. *Advanced Functional Materials* **2021,** *31* (4), 2007810.

29.   Mas-Ballesté, R.; Gómez-Navarro, C.; Gómez-Herrero, J.; Zamora, F., 2D materials: to graphene and beyond. *Nanoscale* **2011,** *3* (1), 20-30.

30.   Gupta, A.; Sakthivel, T.; Seal, S., Recent development in 2D materials beyond graphene. *Progress in Materials Science* **2015,** *73*, 44-126.

31.   Novoselov, K. S.; Geim, A. K.; Morozov, S. V.; Jiang, D.; Zhang, Y.; Dubonos, S. V.; Grigorieva, I. V.; Firsov, A. A., Electric Field Effect in Atomically Thin Carbon Films. *Science* **2004,** *306* (5696), 666.

32.   Bizeto, M. A.; Shiguihara, A. L.; Constantino, V. R. L., Layered niobate nanosheets: building blocks for advanced materials assembly. *Journal of Materials Chemistry* **2009,** *19* (17), 2512-2525.

33.   Ma, R.; Liu, Z.; Li, L.; Iyi, N.; Sasaki, T., Exfoliating layered double hydroxides in formamide: a method to obtain positively charged nanosheets. *Journal of Materials Chemistry* **2006,** *16* (39), 3809-3813.

34.   Osada, M.; Sasaki, T., Exfoliated oxide nanosheets: new solution to nanoelectronics. *Journal of Materials Chemistry* **2009,** *19* (17), 2503-2511.

35.   Puthirath Balan, A.; Radhakrishnan, S.; Woellner, C. F.; Sinha, S. K.; Deng, L.; Reyes, C. d. l.; Rao, B. M.; Paulose, M.; Neupane, R.; Apte, A.; Kochat, V.; Vajtai, R.; Harutyunyan, A. R.; Chu, C.-W.; Costin, G.; Galvao, D. S.; Martí, A. A.; van Aken, P. A.; Varghese, O. K.; Tiwary, C. S.; Malie Madom Ramaswamy Iyer, A.; Ajayan, P. M., Exfoliation of a non-van der Waals material from iron ore hematite. *Nature Nanotechnology* **2018,** *13* (7), 602-609.

36.   Geim, A. K.; Novoselov, K. S., The rise of graphene. *Nature Materials* **2007,** *6* (3), 183-191.

37.   Ambrosi, A.; Pumera, M., Exfoliation of layered materials using electrochemistry. *Chemical Society Reviews* **2018,** *47* (19), 7213-7224.

38.   Butler, S. Z.; Hollen, S. M.; Cao, L.; Cui, Y.; Gupta, J. A.; Gutiérrez, H. R.; Heinz, T. F.; Hong, S. S.; Huang, J.; Ismach, A. F.; Johnston-Halperin, E.; Kuno, M.; Plashnitsa, V. V.; Robinson, R. D.; Ruoff, R. S.; Salahuddin, S.; Shan, J.; Shi, L.; Spencer, M. G.; Terrones, M.; Windl, W.; Goldberger, J. E., Progress, Challenges, and Opportunities in Two-Dimensional Materials Beyond Graphene. *ACS Nano* **2013,** *7* (4), 2898-2926.

39.   Kang, K.; Chen, S.; Yang, E.-H., 12 - Synthesis of transition metal dichalcogenides. In *Synthesis, Modeling, and Characterization of 2D Materials, and Their Heterostructures*, Yang, E.-H.; Datta, D.; Ding, J.; Hader, G., Eds. Elsevier: 2020; pp 247-264.

40.   Ajayan, P.; Kim, P.; Banerjee, K., Two-dimensional van der Waals materials. *Physics Today* **2016,** *69*, 38-44.

41.   Geim, A. K.; MacDonald, A. H., Graphene: Exploring carbon flatland. *Physics Today* **2007,** *60* (8), 35-41.

42.   Novoselov, K. S.; Jiang, D.; Schedin, F.; Booth, T. J.; Khotkevich, V. V.; Morozov, S. V.; Geim, A. K., Two-dimensional atomic crystals. *Proceedings of the National Academy of Sciences of the United States of America* **2005,** *102* (30), 10451.

43.   Chia, X.; Eng, A. Y. S.; Ambrosi, A.; Tan, S. M.; Pumera, M., Electrochemistry of Nanostructured Layered Transition-Metal Dichalcogenides. *Chemical Reviews* **2015,** *115* (21), 11941-11966.

44.   Zhang, H.; Liu, C.-X.; Qi, X.-L.; Dai, X.; Fang, Z.; Zhang, S.-C., Topological insulators in Bi2Se3, Bi2Te3 and Sb2Te3 with a single Dirac cone on the surface. *Nature Physics* **2009,** *5* (6), 438-442.

45.   Du, H.; Lin, X.; Xu, Z.; Chu, D., Recent developments in black phosphorus transistors. *Journal of Materials Chemistry C* **2015,** *3* (34), 8760-8775.

46.   Gusmão, R.; Sofer, Z.; Pumera, M., Black Phosphorus Rediscovered: From Bulk Material to Monolayers. *Angewandte Chemie International Edition* **2017,** *56* (28), 8052-8072.

47.   Mansor, N.; Jia, J.; Miller, T.; Suter, T.; Belen Jorge, A.; Gibbs, C.; Shearing, P. R.; McMillan, P. F.; Mattevi, C.; Shaffer, M.; Brett, D. J. L., Graphitic Carbon Nitride-Graphene Hybrid Nanostructure as a Catalyst Support for Polymer Electrolyte Membrane Fuel Cells. *ECS Transactions* **2016,** *75* (14), 885-897.

48.   Osada, M.; Sasaki, T., Two-Dimensional Dielectric Nanosheets: Novel Nanoelectronics From Nanocrystal Building Blocks. *Advanced Materials* **2012,** *24* (2), 210-228.

49.   Golberg, D.; Bando, Y.; Huang, Y.; Terao, T.; Mitome, M.; Tang, C.; Zhi, C., Boron Nitride Nanotubes and Nanosheets. *ACS Nano* **2010,** *4* (6), 2979-2993.

50.   Dong, R.; Feng, X., Making large single crystals of 2D MOFs. *Nature Materials* **2021,** *20* (2), 122-123.

51.   Khazaei, M.; Mishra, A.; Venkataramanan, N. S.; Singh, A. K.; Yunoki, S., Recent advances in MXenes: From fundamentals to applications. *Current Opinion in Solid State and Materials Science* **2019,** *23* (3), 164-178.

52.   Lloyd-Hughes, J.; Jeon, T.-I., A Review of the Terahertz Conductivity of Bulk and Nano-Materials. *Journal of Infrared, Millimeter, and Terahertz Waves* **2012,** *33* (9), 871-925.

53.   Zhang, F.; Zhu, J.; Zhang, D.; Schwingenschlögl, U.; Alshareef, H. N., Two-Dimensional SnO Anodes with a Tunable Number of Atomic Layers for Sodium Ion Batteries. *Nano Letters* **2017,** *17* (2), 1302-1311.

54.   Zhu, B.; Zhang, J.; Jiang, C.; Cheng, B.; Yu, J., First principle investigation of halogen-doped monolayer g-C3N4 photocatalyst. *Applied Catalysis B: Environmental* **2017,** *207*, 27-34.

55.   He, Z.; Que, W., Molybdenum disulfide nanomaterials: Structures, properties, synthesis and recent progress on hydrogen evolution reaction. *Applied Materials Today* **2016,** *3*, 23-56.

56.   Hong, W.; Wyatt, B. C.; Nemani, S. K.; Anasori, B., Double transition-metal MXenes: Atomistic design of two-dimensional carbides and nitrides. *MRS Bulletin* **2020,** *45* (10), 850-861.

57.   Jeremias, F. Synthesis and Characterization of Metal-Organic Frameworks for Heat Transformation Applications. 2015.

58.   Du, H.; Lin, X.; Xu, Z.; Chu, D., Recent Development in Black Phosphorus Transistors. *J. Mater. Chem. C* **2015,** *3*.

59.   Wang, J.; Ma, F.; Sun, M., Graphene, hexagonal boron nitride, and their heterostructures: properties and applications. *RSC Advances* **2017,** *7* (27), 16801-16822.

60.   Kan, E.; Li, M.; Hu, S.; Xiao, C.; Xiang, H.; Deng, K., Two-Dimensional Hexagonal Transition-Metal Oxide for Spintronics. *The Journal of Physical Chemistry Letters* **2013,** *4* (7), 1120-1125.

61.   Chen, J.; Xu, L.; Li, W.; Gou, X., α-Fe2O3 Nanotubes in Gas Sensor and Lithium-Ion Battery Applications. *Advanced Materials* **2005,** *17* (5), 582-586.

62.   Zeng, H.; Li, J.; Liu, J. P.; Wang, Z. L.; Sun, S., Exchange-coupled nanocomposite magnets by nanoparticle self-assembly. *Nature* **2002,** *420* (6914), 395-398.

63.   Gao, L.; Fan, K.; Yan, X., Iron Oxide Nanozyme: A Multifunctional Enzyme Mimetic for Biomedical Applications. *Theranostics* **2017,** *7* (13), 3207-3227.

64.   Gilliam, M. S.; Yousaf, A.; Guo, Y.; Li, D. O.; Momenah, A.; Wang, Q. H.; Green, A. A., Evaluating the Exfoliation Efficiency of Quasi-2D Metal Diboride Nanosheets Using Hansen Solubility Parameters. *Langmuir* **2021,** *37* (3), 1194-1205.

65.   Guo, Y.; Gupta, A.; Gilliam, M. S.; Debnath, A.; Yousaf, A.; Saha, S.; Levin, M. D.; Green, A. A.; Singh, A. K.; Wang, Q. H., Exfoliation of boron carbide into ultrathin nanosheets. *Nanoscale* **2021,** *13* (3), 1652-1662.

66.   Yousaf, A.; Gilliam, M. S.; Chang, S. L. Y.; Augustin, M.; Guo, Y.; Tahir, F.; Wang, M.; Schwindt, A.; Chu, X. S.; Li, D. O.; Kale, S.; Debnath, A.; Liu, Y.; Green, M. D.; Santos, E. J. G.; Green, A. A.; Wang, Q. H., Exfoliation of Quasi-Two-Dimensional Nanosheets of Metal Diborides. *The Journal of Physical Chemistry C* **2021,** *125* (12), 6787-6799.

67.   Novoselov, K. S.; Mishchenko, A.; Carvalho, A.; Castro Neto, A. H., 2D materials and van der Waals heterostructures. *Science* **2016,** *353* (6298), aac9439.

68.   Han, S. A.; Sohn, A.; Kim, S.-W., Recent advanced in energy harvesting and storage applications with two-dimensional layered materials. *FlatChem* **2017,** *6*, 37-47.

69.   Anju, S.; Mohanan, P. V., Biomedical applications of transition metal dichalcogenides (TMDCs). *Synthetic Metals* **2021,** *271*, 116610.

70.   Lee, Y.-H.; Zhang, X.-Q.; Zhang, W.; Chang, M.-T.; Lin, C.-T.; Chang, K.-D.; Yu, Y.-C.; Wang, J. T.-W.; Chang, C.-S.; Li, L.-J.; Lin, T.-W., Synthesis of Large-Area MoS2 Atomic Layers with Chemical Vapor Deposition. *Advanced Materials* **2012,** *24* (17), 2320-2325.

71.   Wu, S.; Huang, C.; Aivazian, G.; Ross, J. S.; Cobden, D. H.; Xu, X., Vapor–Solid Growth of High Optical Quality MoS2 Monolayers with Near-Unity Valley Polarization. *ACS Nano* **2013,** *7* (3), 2768-2772.

72.   Huang, Y.; Pan, Y.-H.; Yang, R.; Bao, L.-H.; Meng, L.; Luo, H.-L.; Cai, Y.-Q.; Liu, G.-D.; Zhao, W.-J.; Zhou, Z.; Wu, L.-M.; Zhu, Z.-L.; Huang, M.; Liu, L.-W.; Liu, L.; Cheng, P.; Wu, K.-H.; Tian, S.-B.; Gu, C.-Z.; Shi, Y.-G.; Guo, Y.-F.; Cheng, Z. G.; Hu, J.-P.; Zhao, L.; Yang, G.-H.; Sutter, E.; Sutter, P.; Wang, Y.-L.; Ji, W.; Zhou, X.-J.; Gao, H.-J., Universal mechanical exfoliation of large-area 2D crystals. *Nature Communications* **2020,** *11* (1), 2453.

73.   Nicolosi, V.; Chhowalla, M.; Kanatzidis, M. G.; Strano, M. S.; Coleman, J. N., Liquid Exfoliation of Layered Materials. *Science* **2013,** *340* (6139), 1226419.

74. Cunningham, G.; Lotya, M.; Cucinotta, C. S.; Sanvito, S.; Bergin, S. D.; Menzel, R.; Shaffer, M. S. P.; Coleman, J. N., Solvent Exfoliation of Transition Metal Dichalcogenides: Dispersibility of Exfoliated Nanosheets Varies Only Weakly between Compounds. *ACS Nano* **2012,** *6* (4), 3468-3480.

75. Wang, N.; Xu, Q.; Xu, S.; Qi, Y.; Chen, M.; Li, H.; Han, B., High-efficiency exfoliation of layered materials into 2D nanosheets in switchable CO2/Surfactant/H2O system. *Scientific reports* **2015,** *5*, 16764.

76. Yin, W.; Yan, L.; Yu, J.; Tian, G.; Zhou, L.; Zheng, X.; Zhang, X.; Yong, Y.; Li, J.; Gu, Z.; Zhao, Y., High-Throughput Synthesis of Single-Layer MoS2 Nanosheets as a Near-Infrared Photothermal-Triggered Drug Delivery for Effective Cancer Therapy. *ACS Nano* **2014,** *8* (7), 6922-6933.

77. Qian, X.; Shen, S.; Liu, T.; Cheng, L.; Liu, Z., Two-dimensional TiS2 nanosheets for in vivo photoacoustic imaging and photothermal cancer therapy. *Nanoscale* **2015,** *7* (14), 6380-6387.

78. Li, B. L.; Li, R.; Zou, H. L.; Ariga, K.; Li, N. B.; Leong, D. T., Engineered functionalized 2D nanoarchitectures for stimuli-responsive drug delivery. *Materials Horizons* **2020,** *7* (2), 455-469.

79. Shi, J.; Zhang, H.; Chen, Z.; Xu, L.; Zhang, Z., A multi-functional nanoplatform for efficacy tumor theranostic applications. *Asian journal of pharmaceutical sciences* **2017,** *12* (3), 235-249.

80. Liu, T.; Wang, C.; Gu, X.; Gong, H.; Cheng, L.; Shi, X.; Feng, L.; Sun, B.; Liu, Z., Drug Delivery with PEGylated MoS2 Nano-sheets for Combined Photothermal and Chemotherapy of Cancer. *Advanced Materials* **2014,** *26* (21), 3433-3440.

81. Wang, X.; Li, T.; Ma, H.; Zhai, D.; Jiang, C.; Chang, J.; Wang, J.; Wu, C., A 3D-printed scaffold with MoS2 nanosheets for tumor therapy and tissue regeneration. *NPG Asia Materials* **2017,** *9* (4), e376-e376.

82. Dou, W. T.; Kong, Y.; He, X. P.; Chen, G. R.; Zang, Y.; Li, J.; Tian, H., GPCR Activation and Endocytosis Induced by a 2D Material Agonist. *ACS Appl Mater Interfaces* **2017,** *9* (17), 14709-14715.

83. Ma, Y. H.; Dou, W. T.; Pan, Y. F.; Dong, L. W.; Tan, Y. X.; He, X. P.; Tian, H.; Wang, H. Y., Fluorogenic 2D Peptidosheet Unravels CD47 as a Potential Biomarker for Profiling Hepatocellular Carcinoma and Cholangiocarcinoma Tissues. *Advanced materials (Deerfield Beach, Fla.)* **2017,** *29* (5).

84. Zu, Y.; Yao, H.; Wang, Y.; Yan, L.; Gu, Z.; Chen, C.; Gao, L.; Yin, W., The age of bioinspired molybdenum-involved nanozymes: Synthesis, catalytic mechanisms, and biomedical applications. *VIEW* **2021,** *n/a* (n/a), 20200188.

85. Zhou, X.; Sun, H.; Bai, X., Two-Dimensional Transition Metal Dichalcogenides: Synthesis, Biomedical Applications and Biosafety Evaluation. *Frontiers in Bioengineering and Biotechnology* **2020,** *8* (236).

86. Debnath, A.; Saha, S.; Li, D. O.; Chu, X. S.; Ulissi, Z. W.; Green, A. A.; Wang, Q. H., Elimination of Multidrug-Resistant Bacteria by Transition Metal Dichalcogenides Encapsulated by Synthetic Single-Stranded DNA. *ACS Applied Materials & Interfaces* **2021,** *13* (7), 8082-8094.

87. Meng, S.; Zhang, Y.; Wang, H.; Wang, L.; Kong, T.; Zhang, H.; Meng, S., Recent advances on TMDCs for medical diagnosis. *Biomaterials* **2021,** *269*, 120471.

88.   Gao, L.; Zhuang, J.; Nie, L.; Zhang, J.; Zhang, Y.; Gu, N.; Wang, T.; Feng, J.; Yang, D.; Perrett, S.; Yan, X., Intrinsic peroxidase-like activity of ferromagnetic nanoparticles. *Nature Nanotechnology* **2007,** *2* (9), 577-583.

89.   Feng, K.; Zhang, J.; Dong, H.; Li, Z.; Gu, N.; Ma, M.; Zhang, Y., Prussian Blue Nanoparticles Having Various Sizes and Crystallinities for Multienzyme Catalysis and Magnetic Resonance Imaging. *ACS Applied Nano Materials* **2021**.

90.   Chen, T.; Zou, H.; Wu, X.; Liu, C.; Situ, B.; Zheng, L.; Yang, G., Nanozymatic Antioxidant System Based on MoS2 Nanosheets. *ACS Applied Materials & Interfaces* **2018,** *10* (15), 12453-12462.

91.   Yu, J.; Ma, D.; Mei, L.; Gao, Q.; Yin, W.; Zhang, X.; Yan, L.; Gu, Z.; Ma, X.; Zhao, Y., Peroxidase-like activity of MoS2 nanoflakes with different modifications and their application for H2O2 and glucose detection. *Journal of Materials Chemistry B* **2018,** *6* (3), 487-498.

92.   Wu, X.; Chen, T.; Wang, J.; Yang, G., Few-layered MoSe2 nanosheets as an efficient peroxidase nanozyme for highly sensitive colorimetric detection of H2O2 and xanthine. *Journal of Materials Chemistry B* **2018,** *6* (1), 105-111.

93.   Kalantar-zadeh, K.; Ou, J. Z.; Daeneke, T.; Strano, M. S.; Pumera, M.; Gras, S. L., Two-Dimensional Transition Metal Dichalcogenides in Biosystems. *Advanced Functional Materials* **2015,** *25* (32), 5086-5099.

94.   Huang, X.-W.; Wei, J.-J.; Liu, T.; Zhang, X.-L.; Bai, S.-M.; Yang, H.-H., Silk fibroin-assisted exfoliation and functionalization of transition metal dichalcogenide nanosheets for antibacterial wound dressings. *Nanoscale* **2017,** *9* (44), 17193-17198.

95.   Liang, M.; Yan, X., Nanozymes: From New Concepts, Mechanisms, and Standards to Applications. *Accounts of Chemical Research* **2019,** *52* (8), 2190-2200.

96.   Huang, Y.; Ren, J.; Qu, X., Nanozymes: Classification, Catalytic Mechanisms, Activity Regulation, and Applications. *Chemical Reviews* **2019,** *119* (6), 4357-4412.

97.   Forsberg, K.; Woodworth, K.; Walters, M.; Berkow, E. L.; Jackson, B.; Chiller, T.; Vallabhaneni, S., Candida auris: The recent emergence of a multidrug-resistant fungal pathogen. *Medical mycology* **2019,** *57* (1), 1-12.

Chapter 2

1.   Chandler, C. I. R., Current accounts of antimicrobial resistance: stabilisation, individualisation and antibiotics as infrastructure. *Palgrave Communications* 2019, *5* (1), 53.

2.   Rice, L. B., Federal Funding for the Study of Antimicrobial Resistance in Nosocomial Pathogens: No ESKAPE. *The Journal of Infectious Diseases* 2008, *197* (8), 1079-1081.

3.   Schultz, F.; Anywar, G.; Tang, H.; Chassagne, F.; Lyles, J. T.; Garbe, L.-A.; Quave, C. L., Targeting ESKAPE pathogens with anti-infective medicinal plants from the Greater Mpigi region in Uganda. *Scientific Reports* 2020, *10* (1), 11935.

4.   Friedman, N. D.; Temkin, E.; Carmeli, Y., The negative impact of antibiotic resistance. *Clinical microbiology and infection : the official publication of the European Society of Clinical Microbiology and Infectious Diseases* 2016, *22* (5), 416-22.

5.   Thabit, A. K.; Crandon, J. L.; Nicolau, D. P., Antimicrobial resistance: impact on clinical and economic outcomes and the need for new antimicrobials. *Expert Opinion on Pharmacotherapy* 2015, *16* (2), 159-177.

6.   Boucher, H. W.; Talbot, G. H.; Bradley, J. S.; Edwards, J. E.; Gilbert, D.; Rice, L. B.; Scheld, M.; Spellberg, B.; Bartlett, J., Bad Bugs, No Drugs: No ESKAPE! An Update from the Infectious Diseases Society of America. *Clinical Infectious Diseases* 2009, *48* (1), 1-12.

7.   Mulani, M. S.; Kamble, E. E.; Kumkar, S. N.; Tawre, M. S.; Pardesi, K. R., Emerging Strategies to Combat ESKAPE Pathogens in the Era of Antimicrobial Resistance: A Review. *Frontiers in Microbiology* 2019, *10* (539).

8.   Santajit, S.; Indrawattana, N., Mechanisms of Antimicrobial Resistance in ESKAPE Pathogens. *BioMed Research International* 2016, *2016*, 2475067.

9.   Ventola, C. L., The antibiotic resistance crisis: part 1: causes and threats. *P T* 2015, *40* (4), 277-283.

10.   Fair, R. J.; Tor, Y., Antibiotics and bacterial resistance in the 21st century. *Perspect Medicin Chem* 2014, *6*, 25-64.

11.   Lee, J. H.; Jeong, S. H.; Cha, S.-S.; Lee, S. H., A lack of drugs for antibiotic-resistant Gram-negative bacteria. *Nature Reviews Drug Discovery* 2007, *6* (11), 938-938.

12.   Taubes, G., The Bacteria Fight Back. *Science* 2008, *321* (5887), 356.

13.   Xu, Z.-Q.; Flavin, M. T.; Flavin, J., Combating multidrug-resistant Gram-negative bacterial infections. *Expert Opinion on Investigational Drugs* 2014, *23* (2), 163-182.

14.   Kohanski, M. A.; Dwyer, D. J.; Collins, J. J., How antibiotics kill bacteria: from targets to networks. *Nat Rev Microbiol* 2010, *8* (6), 423-435.

15.   Taylor, P. W.; Stapleton, P. D.; Paul Luzio, J., New ways to treat bacterial infections. *Drug Discovery Today* 2002, *7* (21), 1086-1091.

16.   Gupta, A.; Landis, R. F.; Li, C.-H.; Schnurr, M.; Das, R.; Lee, Y.-W.; Yazdani, M.; Liu, Y.; Kozlova, A.; Rotello, V. M., Engineered Polymer Nanoparticles with Unprecedented Antimicrobial

Efficacy and Therapeutic Indices against Multidrug-Resistant Bacteria and Biofilms. *Journal of the American Chemical Society* 2018, *140* (38), 12137-12143.

17.   Gupta, A.; Mumtaz, S.; Li, C.-H.; Hussain, I.; Rotello, V. M., Combatting antibiotic-resistant bacteria using nanomaterials. *Chem Soc Rev* 2019, *48* (2), 415-427.

18.   Singh, R.; Smitha, M. S.; Singh, S. P., The role of nanotechnology in combating multi-drug resistant bacteria. *Journal of nanoscience and nanotechnology* 2014, *14* (7), 4745-56.

19.   Zasloff, M., Antimicrobial peptides of multicellular organisms. *Nature* 2002, *415* (6870), 389-395.

20.   Brogden, K. A., Antimicrobial peptides: pore formers or metabolic inhibitors in bacteria? *Nature Reviews Microbiology* 2005, *3* (3), 238-250.

21.   Kuroda, K.; DeGrado, W. F., Amphiphilic Polymethacrylate Derivatives as Antimicrobial Agents. *Journal of the American Chemical Society* 2005, *127* (12), 4128-4129.

22.   Palermo, E. F.; Kuroda, K., Structural determinants of antimicrobial activity in polymers which mimic host defense peptides. *Applied Microbiology and Biotechnology* 2010, *87* (5), 1605-1615.

23.   Joo, H.-S.; Otto, M., Mechanisms of resistance to antimicrobial peptides in staphylococci. *Biochimica et Biophysica Acta (BBA) - Biomembranes* 2015, *1848* (11, Part B), 3055-3061.

24.   Kang, S.-J.; Park, S. J.; Mishig-Ochir, T.; Lee, B.-J., Antimicrobial peptides: therapeutic potentials. *Expert Review of Anti-infective Therapy* 2014, *12* (12), 1477-1486.

25.   Shkodenko, L.; Kassirov, I.; Koshel, E., Metal Oxide Nanoparticles Against Bacterial Biofilms: Perspectives and Limitations. *Microorganisms* 2020, *8* (10), 1545.

26.   Maleki Dizaj, S.; Mennati, A.; Jafari, S.; Khezri, K.; Adibkia, K., Antimicrobial activity of carbon-based nanoparticles. *Adv Pharm Bull* 2015, *5* (1), 19-23.

27.   Sambanthamoorthy, K.; Feng, X.; Patel, R.; Patel, S.; Paranavitana, C., Antimicrobial and antibiofilm potential of biosurfactants isolated from lactobacilli against multi-drug-resistant pathogens. *BMC Microbiol* 2014, *14*, 197-197.

28.   Huang, Z.; Zheng, X.; Yan, D.; Yin, G.; Liao, X.; Kang, Y.; Yao, Y.; Huang, D.; Hao, B., Toxicological Effect of ZnO Nanoparticles Based on Bacteria. *Langmuir* 2008, *24* (8), 4140-4144.

29.   Maness, P. C.; Smolinski, S.; Blake, D. M.; Huang, Z.; Wolfrum, E. J.; Jacoby, W. A., Bactericidal activity of photocatalytic TiO(2) reaction: toward an understanding of its killing mechanism. *Appl Environ Microbiol* 1999, *65* (9), 4094-4098.

30.   Weir, E.; Lawlor, A.; Whelan, A.; Regan, F., The use of nanoparticles in anti-microbial materials and their characterization. *Analyst* 2008, *133* (7), 835-845.

31.   Kim, J. S.; Kuk, E.; Yu, K. N.; Kim, J.-H.; Park, S. J.; Lee, H. J.; Kim, S. H.; Park, Y. K.; Park, Y. H.; Hwang, C.-Y.; Kim, Y.-K.; Lee, Y.-S.; Jeong, D. H.; Cho, M.-H., Antimicrobial effects of silver nanoparticles. *Nanomedicine: Nanotechnology, Biology and Medicine* 2007, *3* (1), 95-101.

32. Li, Q.; Mahendra, S.; Lyon, D. Y.; Brunet, L.; Liga, M. V.; Li, D.; Alvarez, P. J. J., Antimicrobial nanomaterials for water disinfection and microbial control: Potential applications and implications. *Water Research* 2008, *42* (18), 4591-4602.

33. Ding, X.; Duan, S.; Ding, X.; Liu, R.; Xu, F.-J., Versatile Antibacterial Materials: An Emerging Arsenal for Combatting Bacterial Pathogens. *Advanced Functional Materials* 2018, *28* (40), 1802140.

34. Yang, Y.; Liu, T.; Cheng, L.; Song, G.; Liu, Z.; Chen, M., MoS2-Based Nanoprobes for Detection of Silver Ions in Aqueous Solutions and Bacteria. *ACS Applied Materials & Interfaces* 2015, *7* (14), 7526-7533.

35. Zhang, W.; Mou, Z.; Wang, Y.; Chen, Y.; Yang, E.; Guo, F.; Sun, D.; Wang, W., Molybdenum disulfide nanosheets loaded with chitosan and silver nanoparticles effective antifungal activities: in vitro and in vivo. *Materials Science and Engineering: C* 2019, *97*, 486-497.

36. Bang, G. S.; Cho, S.; Son, N.; Shim, G. W.; Cho, B.-K.; Choi, S.-Y., DNA-Assisted Exfoliation of Tungsten Dichalcogenides and Their Antibacterial Effect. *ACS Applied Materials & Interfaces* 2016, *8* (3), 1943-1950.

37. Benincasa, M.; Pacor, S.; Wu, W.; Prato, M.; Bianco, A.; Gennaro, R., Antifungal Activity of Amphotericin B Conjugated to Carbon Nanotubes. *ACS Nano* 2011, *5* (1), 199-208.

38. Debnath, A.; Saha, S.; Li, D. O.; Chu, X. S.; Ulissi, Z. W.; Green, A. A.; Wang, Q. H., Elimination of Multidrug-Resistant Bacteria by Transition Metal Dichalcogenides Encapsulated by Synthetic Single-Stranded DNA. *ACS Applied Materials & Interfaces* 2021, *13* (7), 8082-8094.

39. Kurapati, R.; Muzi, L.; de Garibay, A. P. R.; Russier, J.; Voiry, D.; Vacchi, I. A.; Chhowalla, M.; Bianco, A., Enzymatic Biodegradability of Pristine and Functionalized Transition Metal Dichalcogenide MoS2 Nanosheets. *Advanced Functional Materials* 2017, *27* (7), 1605176.

40. Roy, S.; Mondal, A.; Yadav, V.; Sarkar, A.; Banerjee, R.; Sanpui, P.; Jaiswal, A., Mechanistic Insight into the Antibacterial Activity of Chitosan Exfoliated MoS2 Nanosheets: Membrane Damage, Metabolic Inactivation, and Oxidative Stress. *ACS Applied Bio Materials* 2019, *2* (7), 2738-2755.

41. Wu, C.; Liu, J.; Liu, B.; He, S.; Dai, G.; Xu, B.; Zhong, W., NIR light-responsive short peptide/2D NbSe2 nanosheets composite hydrogel with controlled-release capacity. *Journal of Materials Chemistry B* 2019, *7* (19), 3134-3142.

42. Nicolosi, V.; Chhowalla, M.; Kanatzidis, M. G.; Strano, M. S.; Coleman, J. N., Liquid Exfoliation of Layered Materials. *Science* 2013, *340* (6139), 1226419.

43. Dular, M.; Stoffel, B.; Širok, B., Development of a cavitation erosion model. *Wear* 2006, *261* (5), 642-655.

44. Coleman, J. N.; Lotya, M.; O'Neill, A.; Bergin, S. D.; King, P. J.; Khan, U.; Young, K.; Gaucher, A.; De, S.; Smith, R. J.; Shvets, I. V.; Arora, S. K.; Stanton, G.; Kim, H.-Y.; Lee, K.; Kim, G. T.; Duesberg, G. S.; Hallam, T.; Boland, J. J.; Wang, J. J.; Donegan, J. F.; Grunlan, J. C.; Moriarty, G.; Shmeliov, A.; Nicholls, R. J.; Perkins, J. M.; Grieveson, E. M.; Theuwissen, K.; McComb, D. W.; Nellist, P. D.; Nicolosi, V., Two-Dimensional Nanosheets Produced by Liquid Exfoliation of Layered Materials. *Science* 2011, *331* (6017), 568.

45.	Hernandez, Y.; Nicolosi, V.; Lotya, M.; Blighe, F. M.; Sun, Z.; De, S.; McGovern, I. T.; Holland, B.; Byrne, M.; Gun'Ko, Y. K.; Boland, J. J.; Niraj, P.; Duesberg, G.; Krishnamurthy, S.; Goodhue, R.; Hutchison, J.; Scardaci, V.; Ferrari, A. C.; Coleman, J. N., High-yield production of graphene by liquid-phase exfoliation of graphite. *Nature Nanotechnology* 2008, *3* (9), 563-568.

46.	Ayán-Varela, M.; Pérez-Vidal, Ó.; Paredes, J. I.; Munuera, J. M.; Villar-Rodil, S.; Díaz-González, M.; Fernández-Sánchez, C.; Silva, V. S.; Cicuéndez, M.; Vila, M.; Martínez-Alonso, A.; Tascón, J. M. D., Aqueous Exfoliation of Transition Metal Dichalcogenides Assisted by DNA/RNA Nucleotides: Catalytically Active and Biocompatible Nanosheets Stabilized by Acid–Base Interactions. *ACS Applied Materials & Interfaces* 2017, *9* (3), 2835-2845.

47.	Vovusha, H.; Sanyal, B., Adsorption of nucleobases on 2D transition-metal dichalcogenides and graphene sheet: a first principles density functional theory study. *RSC Advances* 2015, *5* (83), 67427-67434.

48.	Liu, S.; Zeng, T. H.; Hofmann, M.; Burcombe, E.; Wei, J.; Jiang, R.; Kong, J.; Chen, Y., Antibacterial Activity of Graphite, Graphite Oxide, Graphene Oxide, and Reduced Graphene Oxide: Membrane and Oxidative Stress. *ACS Nano* 2011, *5* (9), 6971-6980.

49.	Findlay, B.; Zhanel, G. G.; Schweizer, F., Cationic Amphiphiles, a New Generation of Antimicrobials Inspired by the Natural Antimicrobial Peptide Scaffold. *Antimicrobial Agents and Chemotherapy* 2010, *54* (10), 4049.

50.	Hale, J. D. F.; Hancock, R. E. W., Alternative mechanisms of action of cationic antimicrobial peptides on bacteria. *Expert Review of Anti-infective Therapy* 2007, *5* (6), 951-959.

51.	Powers, J.-P. S.; Hancock, R. E. W., The relationship between peptide structure and antibacterial activity. *Peptides* 2003, *24* (11), 1681-1691.

52.	Li, J.; Zhang, K.; Ruan, L.; Chin, S. F.; Wickramasinghe, N.; Liu, H.; Ravikumar, V.; Ren, J.; Duan, H.; Yang, L.; Chan-Park, M. B., Block Copolymer Nanoparticles Remove Biofilms of Drug-Resistant Gram-Positive Bacteria by Nanoscale Bacterial Debridement. *Nano Letters* 2018, *18* (7), 4180-4187.

53.	Pitto-Barry, A.; Barry, N. P. E., Pluronic® block-copolymers in medicine: from chemical and biological versatility to rationalisation and clinical advances. *Polymer Chemistry* 2014, *5* (10), 3291-3297.

54.	Campos, M. A.; Vargas, M. A.; Regueiro, V.; Llompart, C. M.; Albertí, S.; Bengoechea, J. A., Capsule polysaccharide mediates bacterial resistance to antimicrobial peptides. *Infect Immun* 2004, *72* (12), 7107-7114.

55.	Llobet, E.; Tomás, J. M.; Bengoechea, J. A., Capsule polysaccharide is a bacterial decoy for antimicrobial peptides. *Microbiology* 2008, *154* (12), 3877-3886.

56.	Bonnier, F.; Keating, M. E.; Wróbel, T. P.; Majzner, K.; Baranska, M.; Garcia-Munoz, A.; Blanco, A.; Byrne, H. J., Cell viability assessment using the Alamar blue assay: A comparison of 2D and 3D cell culture models. *Toxicology in Vitro* 2015, *29* (1), 124-131.

Chapter 3

1.   Miao, H.; Teng, Z.; Wang, C.; Chong, H.; Wang, G., Recent Progress in Two-Dimensional Antimicrobial Nanomaterials. *Chemistry – A European Journal* **2019,** *25* (4), 929-944.

2.   Liu, C.; Kong, D.; Hsu, P.-C.; Yuan, H.; Lee, H.-W.; Liu, Y.; Wang, H.; Wang, S.; Yan, K.; Lin, D.; Maraccini, P. A.; Parker, K. M.; Boehm, A. B.; Cui, Y., Rapid water disinfection using vertically aligned MoS2 nanofilms and visible light. *Nature Nanotechnology* **2016,** *11* (12), 1098-1104.

3.   Meredith, H. R.; Srimani, J. K.; Lee, A. J.; Lopatkin, A. J.; You, L., Collective antibiotic tolerance: mechanisms, dynamics and intervention. *Nature Chemical Biology* **2015,** *11* (3), 182-188.

4.   Tu, Y.; Lv, M.; Xiu, P.; Huynh, T.; Zhang, M.; Castelli, M.; Liu, Z.; Huang, Q.; Fan, C.; Fang, H.; Zhou, R., Destructive extraction of phospholipids from Escherichia coli membranes by graphene nanosheets. *Nature Nanotechnology* **2013,** *8* (8), 594-601.

5.   Huh, A. J.; Kwon, Y. J., "Nanoantibiotics": A new paradigm for treating infectious diseases using nanomaterials in the antibiotics resistant era. *Journal of Controlled Release* **2011,** *156* (2), 128-145.

6.   Rice, L. B., Federal Funding for the Study of Antimicrobial Resistance in Nosocomial Pathogens: No ESKAPE. *The Journal of Infectious Diseases* **2008,** *197* (8), 1079-1081.

7.   Roy, R.; Tiwari, M.; Donelli, G.; Tiwari, V., Strategies for combating bacterial biofilms: A focus on anti-biofilm agents and their mechanisms of action. *Virulence* **2018,** *9* (1), 522-554.

8.   Olsen, I., Biofilm-specific antibiotic tolerance and resistance. *European Journal of Clinical Microbiology & Infectious Diseases* **2015,** *34* (5), 877-886.

9.   Tursi, S. A.; Tükel, Ç., Curli-Containing Enteric Biofilms Inside and Out: Matrix Composition, Immune Recognition, and Disease Implications. *Microbiology and Molecular Biology Reviews* **2018,** *82* (4), e00028-18.

10.   Arciola, C. R.; Campoccia, D.; Speziale, P.; Montanaro, L.; Costerton, J. W., Biofilm formation in Staphylococcus implant infections. A review of molecular mechanisms and implications for biofilm-resistant materials. *Biomaterials* **2012,** *33* (26), 5967-5982.

11.   Brogden, K. A., Antimicrobial peptides: pore formers or metabolic inhibitors in bacteria? *Nature Reviews Microbiology* **2005,** *3* (3), 238-250.

12.   Costerton, J. W.; Stewart, P. S.; Greenberg, E. P., Bacterial Biofilms: A Common Cause of Persistent Infections. *Science* **1999,** *284* (5418), 1318.

13.   Davey, M. E.; O'Toole, G. A., Microbial biofilms: from ecology to molecular genetics. *Microbiol Mol Biol Rev* **2000,** *64* (4), 847-867.

14.   Hocevar, S. N.; Edwards, J. R.; Horan, T. C.; Morrell, G. C.; Iwamoto, M.; Lessa, F. C., Device-Associated Infections among Neonatal Intensive Care Unit Patients: Incidence and Associated Pathogens Reported to the National Healthcare Safety Network, 2006–2008. *Infection Control & Hospital Epidemiology* **2015,** *33* (12), 1200-1206.

15.   de Miguel, I.; Prieto, I.; Albornoz, A.; Sanz, V.; Weis, C.; Turon, P.; Quidant, R., Plasmon-Based Biofilm Inhibition on Surgical Implants. *Nano Letters* **2019,** *19* (4), 2524-2529.

16.   Hall-Stoodley, L.; Costerton, J. W.; Stoodley, P., Bacterial biofilms: from the Natural environment to infectious diseases. *Nature Reviews Microbiology* **2004,** *2* (2), 95-108.

17.   Jung, C.-J.; Yeh, C.-Y.; Shun, C.-T.; Hsu, R.-B.; Cheng, H.-W.; Lin, C.-S.; Chia, J.-S., Platelets Enhance Biofilm Formation and Resistance of Endocarditis-Inducing Streptococci on the Injured Heart Valve. *The Journal of Infectious Diseases* **2012,** *205* (7), 1066-1075.

18.   Scott, R. D., The Direct medical costs of healthcare-associated infections in U.S. hospitals and the benefits of prevention. *Cdc* **2009**.

19.   van Kleef, E.; Robotham, J. V.; Jit, M.; Deeny, S. R.; Edmunds, W. J., Modelling the transmission of healthcare associated infections: a systematic review. *BMC Infect Dis* **2013,** *13*, 294-294.

20.   Elder, M. J.; Stapleton, F.; Evans, E.; Dart, J. K. G., Biofilm-related infections in ophthalmology. *Eye* **1995,** *9* (1), 102-109.

21.   Pajkos, A.; Deva, A. K.; Vickery, K.; Cope, C.; Chang, L.; Cossart, Y. E., Detection of subclinical infection in significant breast implant capsules. *Plastic and reconstructive surgery* **2003,** *111* (5), 1605-11.

22.   Rogers, J.; Norkett, D. I.; Bracegirdle, P.; Dowsett, A. B.; Walker, J. T.; Brooks, T.; Keevil, C. W., Examination of biofilm formation and risk of infection associated with the use of urinary catheters with leg bags. *The Journal of hospital infection* **1996,** *32* (2), 105-15.

23.   Ruellan, K.; Frijns, J. H. M.; Bloemberg, G. V.; Hautefort, C.; Van den Abbeele, T.; Lamers, G. E. M.; Herman, P.; Ba Huy, P. T.; Kania, R. E., Detection of Bacterial Biofilm on Cochlear Implants Removed Because of Device Failure, Without Evidence of Infection. *Otology & Neurotology* **2010,** *31* (8).

24.   Sandoe, J. A. T.; Witherden, I. R.; Cove, J. H.; Heritage, J.; Wilcox, M. H., Correlation between enterococcal biofilm formation in vitro and medical-device-related infection potential in vivo. *Journal of Medical Microbiology* **2003,** *52* (7), 547-550.

25.   Viola, G. M.; Darouiche, R. O., Cardiovascular Implantable Device Infections. *Current Infectious Disease Reports* **2011,** *13* (4), 333-342.

26.   Gasser, M.; Zingg, W.; Cassini, A.; Kronenberg, A., Attributable deaths and disability-adjusted life-years caused by infections with antibiotic-resistant bacteria in Switzerland. *The Lancet. Infectious diseases* **2019,** *19* (1), 17-18.

27.   Mehta, Y.; Gupta, A.; Todi, S.; Myatra, S.; Samaddar, D. P.; Patil, V.; Bhattacharya, P. K.; Ramasubban, S., Guidelines for prevention of hospital acquired infections. *Indian J Crit Care Med* **2014,** *18* (3), 149-163.

28.   Ramasamy, M.; Lee, J., Recent Nanotechnology Approaches for Prevention and Treatment of Biofilm-Associated Infections on Medical Devices. *BioMed Research International* **2016,** *2016*, 1851242.

29.   Colon, G.; Ward, B. C.; Webster, T. J., Increased osteoblast and decreased Staphylococcus epidermidis functions on nanophase ZnO and TiO2. *Journal of Biomedical Materials Research Part A* **2006,** *78A* (3), 595-604.

30.   Jones, N.; Ray, B.; Ranjit, K. T.; Manna, A. C., Antibacterial activity of ZnO nanoparticle suspensions on a broad spectrum of microorganisms. *FEMS Microbiology Letters* **2008,** *279* (1), 71-76.

31.   Lee, J.-H.; Kim, Y.-G.; Cho, M. H.; Lee, J., ZnO nanoparticles inhibit Pseudomonas aeruginosa biofilm formation and virulence factor production. *Microbiological Research* **2014,** *169* (12), 888-896.

32.   Gupta, A.; Landis, R. F.; Li, C.-H.; Schnurr, M.; Das, R.; Lee, Y.-W.; Yazdani, M.; Liu, Y.; Kozlova, A.; Rotello, V. M., Engineered Polymer Nanoparticles with Unprecedented Antimicrobial Efficacy and Therapeutic Indices against Multidrug-Resistant Bacteria and Biofilms. *Journal of the American Chemical Society* **2018,** *140* (38), 12137-12143.

33.   Haghighi, F.; Mohammadi, S. R.; Mohammadi, P.; Hosseinkhani, S.; Shidpour, R. In *Antifungal Activity of TiO 2 nanoparticles and EDTA on Candida albicans Biofilms*, 2013.

34.   Inbakandan, D.; Kumar, C.; Abraham, L. S.; Kirubagaran, R.; Venkatesan, R.; Khan, S. A., Silver nanoparticles with anti microfouling effect: A study against marine biofilm forming bacteria. *Colloids and Surfaces B: Biointerfaces* **2013,** *111*, 636-643.

35.   Murthy, P. S.; Venugopalan, V. P.; Arunya, D. D.; Dhara, S.; Pandiyan, R.; Tyagi, A. K. In *Antibiofilm activity of nano sized CuO*, International Conference on Nanoscience, Engineering and Technology (ICONSET 2011), 28-30 Nov. 2011; 2011; pp 580-583.

36.   Yu, Q.; Li, J.; Zhang, Y.; Wang, Y.; Liu, L.; Li, M., Inhibition of gold nanoparticles (AuNPs) on pathogenic biofilm formation and invasion to host cells. *Scientific Reports* **2016,** *6* (1), 26667.

37.   Di Giulio, M.; Zappacosta, R.; Di Lodovico, S.; Di Campli, E.; Siani, G.; Fontana, A.; Cellini, L., Antimicrobial and Antibiofilm Efficacy of Graphene Oxide against Chronic Wound Microorganisms. *Antimicrob Agents Chemother* **2018,** *62* (7), e00547-18.

38.   Kang, S.; Pinault, M.; Pfefferle, L. D.; Elimelech, M., Single-Walled Carbon Nanotubes Exhibit Strong Antimicrobial Activity. *Langmuir* **2007,** *23* (17), 8670-8673.

39.   Liu, S.; Cao, S.; Guo, J.; Luo, L.; Zhou, Y.; Lin, C.; Shi, J.; Fan, C.; Lv, M.; Wang, L., Graphene oxide–silver nanocomposites modulate biofilm formation and extracellular polymeric substance (EPS) production. *Nanoscale* **2018,** *10* (41), 19603-19611.

40.   Zhang, X.; Zhang, W.; Liu, L.; Yang, M.; Huang, L.; Chen, K.; Wang, R.; Yang, B.; Zhang, D.; Wang, J., Antibiotic-loaded MoS2nanosheets to combat bacterial resistance via biofilm inhibition. *Nanotechnology* **2017,** *28* (22), 225101.

41.   Wang, Y.; Kadiyala, U.; Qu, Z.; Elvati, P.; Altheim, C.; Kotov, N. A.; Violi, A.; VanEpps, J. S., Anti-Biofilm Activity of Graphene Quantum Dots via Self-Assembly with Bacterial Amyloid Proteins. *ACS Nano* **2019,** *13* (4), 4278-4289.

42.   Geilich, B. M.; Webster, T. J., Reduced adhesion of Staphylococcus aureus to ZnO/PVC nanocomposites. *Int J Nanomedicine* **2013,** *8*, 1177-1184.

43.   Some, S.; Ho, S.-M.; Dua, P.; Hwang, E.; Shin, Y. H.; Yoo, H.; Kang, J.-S.; Lee, D.-k.; Lee, H., Dual Functions of Highly Potent Graphene Derivative–Poly-l-Lysine Composites To Inhibit Bacteria and Support Human Cells. *ACS Nano* **2012,** *6* (8), 7151-7161.

44.   Zhao, R.; Kong, W.; Sun, M.; Yang, Y.; Liu, W.; Lv, M.; Song, S.; Wang, L.; Song, H.; Hao, R., Highly Stable Graphene-Based Nanocomposite (GO–PEI–Ag) with Broad-Spectrum, Long-Term Antimicrobial Activity and Antibiofilm Effects. *ACS Applied Materials & Interfaces* **2018,** *10* (21), 17617-17629.

45.   Landis, R. F.; Li, C.-H.; Gupta, A.; Lee, Y.-W.; Yazdani, M.; Ngernyuang, N.; Altinbasak, I.; Mansoor, S.; Khichi, M. A. S.; Sanyal, A.; Rotello, V. M., Biodegradable Nanocomposite Antimicrobials for the Eradication of Multidrug-Resistant Bacterial Biofilms without Accumulated Resistance. *Journal of the American Chemical Society* **2018,** *140* (19), 6176-6182.

46.   Li, J.; Zhang, K.; Ruan, L.; Chin, S. F.; Wickramasinghe, N.; Liu, H.; Ravikumar, V.; Ren, J.; Duan, H.; Yang, L.; Chan-Park, M. B., Block Copolymer Nanoparticles Remove Biofilms of Drug-Resistant Gram-Positive Bacteria by Nanoscale Bacterial Debridement. *Nano Letters* **2018,** *18* (7), 4180-4187.

47.   Mei, Y.; Yu, K.; Lo, J. C. Y.; Takeuchi, L. E.; Hadjesfandiari, N.; Yazdani-Ahmadabadi, H.; Brooks, D. E.; Lange, D.; Kizhakkedathu, J. N., Polymer–Nanoparticle Interaction as a Design Principle in the Development of a Durable Ultrathin Universal Binary Antibiofilm Coating with Long-Term Activity. *ACS Nano* **2018,** *12* (12), 11881-11891.

48.   Park, H.-H.; Sun, K.; Seong, M.; Kang, M.; Park, S.; Hong, S.; Jung, H.; Jang, J.; Kim, J.; Jeong, H. E., Lipid-Hydrogel-Nanostructure Hybrids as Robust Biofilm-Resistant Polymeric Materials. *ACS Macro Letters* **2019,** *8* (1), 64-69.

49.   Zhang, C.; Hu, D.-F.; Xu, J.-W.; Ma, M.-Q.; Xing, H.; Yao, K.; Ji, J.; Xu, Z.-K., Polyphenol-Assisted Exfoliation of Transition Metal Dichalcogenides into Nanosheets as Photothermal Nanocarriers for Enhanced Antibiofilm Activity. *ACS Nano* **2018,** *12* (12), 12347-12356.

50.   Pattani, V. P.; Tunnell, J. W., Nanoparticle-mediated photothermal therapy: A comparative study of heating for different particle types. *Lasers in Surgery and Medicine* **2012,** *44* (8), 675-684.

51.   Vallejo-Fernandez, G.; Whear, O.; Roca, A. G.; Hussain, S.; Timmis, J.; Patel, V.; O'Grady, K., Mechanisms of hyperthermia in magnetic nanoparticles. *Journal of Physics D: Applied Physics* **2013,** *46* (31), 312001.

52.   Geim, A. K., Graphene: Status and Prospects. *Science* **2009,** *324* (5934), 1530.

53.   Novoselov, K. S.; Geim, A. K.; Morozov, S. V.; Jiang, D.; Zhang, Y.; Dubonos, S. V.; Grigorieva, I. V.; Firsov, A. A., Electric Field Effect in Atomically Thin Carbon Films. *Science* **2004,** *306* (5696), 666.

54.   Ding, L.; Wei, Y.; Wang, Y.; Chen, H.; Caro, J.; Wang, H., A Two-Dimensional Lamellar Membrane: MXene Nanosheet Stacks. *Angewandte Chemie International Edition* **2017,** *56* (7), 1825-1829.

55.   Tan, C.; Cao, X.; Wu, X.-J.; He, Q.; Yang, J.; Zhang, X.; Chen, J.; Zhao, W.; Han, S.; Nam, G.-H.; Sindoro, M.; Zhang, H., Recent Advances in Ultrathin Two-Dimensional Nanomaterials. *Chemical Reviews* **2017,** *117* (9), 6225-6331.

56.   Tan, C.; Lai, Z.; Zhang, H., Ultrathin Two-Dimensional Multinary Layered Metal Chalcogenide Nanomaterials. *Advanced Materials* **2017,** *29* (37), 1701392.

57.   Xue, Y.; Zhang, Q.; Wang, W.; Cao, H.; Yang, Q.; Fu, L., Opening Two-Dimensional Materials for Energy Conversion and Storage: A Concept. *Advanced Energy Materials* **2017,** *7* (19), 1602684.

58.   Zhang, H., Ultrathin Two-Dimensional Nanomaterials. *ACS Nano* **2015,** *9* (10), 9451-9469.

59.   Maitra, U.; Gupta, U.; De, M.; Datta, R.; Govindaraj, A.; Rao, C. N. R., Highly Effective Visible-Light-Induced H2 Generation by Single-Layer 1T-MoS2 and a Nanocomposite of Few-Layer 2H-MoS2 with Heavily Nitrogenated Graphene. *Angewandte Chemie International Edition* **2013,** *52* (49), 13057-13061.

60.   Pan, L.; Liu, Y.-T.; Xie, X.-M.; Ye, X.-Y., Facile and Green Production of Impurity-Free Aqueous Solutions of WS2 Nanosheets by Direct Exfoliation in Water. *Small* **2016,** *12* (48), 6703-6713.

61.   Shi, Y.; Wang, J.; Wang, C.; Zhai, T.-T.; Bao, W.-J.; Xu, J.-J.; Xia, X.-H.; Chen, H.-Y., Hot Electron of Au Nanorods Activates the Electrocatalysis of Hydrogen Evolution on MoS2 Nanosheets. *Journal of the American Chemical Society* **2015,** *137* (23), 7365-7370.

62.   Hizir, M. S.; Robertson, N. M.; Balcioglu, M.; Alp, E.; Rana, M.; Yigit, M. V., Universal sensor array for highly selective system identification using two-dimensional nanoparticles. *Chemical Science* **2017,** *8* (8), 5735-5745.

63.   Sun, X.; Fan, J.; Fu, C.; Yao, L.; Zhao, S.; Wang, J.; Xiao, J., WS2 and MoS2 biosensing platforms using peptides as probe biomolecules. *Scientific Reports* **2017,** *7* (1), 10290.

64.   Li, W.; Yang, Y.; Weber, J. K.; Zhang, G.; Zhou, R., Tunable, Strain-Controlled Nanoporous MoS2 Filter for Water Desalination. *ACS Nano* **2016,** *10* (2), 1829-1835.

65.   Wang, J.-Z.; Lu, L.; Lotya, M.; Coleman, J. N.; Chou, S.-L.; Liu, H.-K.; Minett, A. I.; Chen, J., Development of MoS2–CNT Composite Thin Film from Layered MoS2 for Lithium Batteries. *Advanced Energy Materials* **2013,** *3* (6), 798-805.

66.   Ai, K.; Ruan, C.; Shen, M.; Lu, L., MoS2 Nanosheets with Widened Interlayer Spacing for High-Efficiency Removal of Mercury in Aquatic Systems. *Advanced Functional Materials* **2016,** *26* (30), 5542-5549.

67.   Sun, L.; Ying, Y.; Huang, H.; Song, Z.; Mao, Y.; Xu, Z.; Peng, X., Ultrafast Molecule Separation through Layered WS2 Nanosheet Membranes. *ACS Nano* **2014,** *8* (6), 6304-6311.

68.   Chimene, D.; Alge, D. L.; Gaharwar, A. K., Two-Dimensional Nanomaterials for Biomedical Applications: Emerging Trends and Future Prospects. *Advanced Materials* **2015,** *27* (45), 7261-7284.

69.   Jia, X.; Bai, J.; Ma, Z.; Jiang, X., BSA-exfoliated WSe2 nanosheets as a photoregulated carrier for synergistic photodynamic/photothermal therapy. *Journal of Materials Chemistry B* **2017,** *5* (2), 269-278.

70.   Liu, T.; Shi, S.; Liang, C.; Shen, S.; Cheng, L.; Wang, C.; Song, X.; Goel, S.; Barnhart, T. E.; Cai, W.; Liu, Z., Iron Oxide Decorated MoS2 Nanosheets with Double PEGylation for Chelator-

Free Radiolabeling and Multimodal Imaging Guided Photothermal Therapy. *ACS Nano* **2015,** *9* (1), 950-960.

71.   Yin, W.; Yan, L.; Yu, J.; Tian, G.; Zhou, L.; Zheng, X.; Zhang, X.; Yong, Y.; Li, J.; Gu, Z.; Zhao, Y., High-Throughput Synthesis of Single-Layer MoS2 Nanosheets as a Near-Infrared Photothermal-Triggered Drug Delivery for Effective Cancer Therapy. *ACS Nano* **2014,** *8* (7), 6922-6933.

72.   Xia, M.-Y.; Xie, Y.; Yu, C.-H.; Chen, G.-Y.; Li, Y.-H.; Zhang, T.; Peng, Q., Graphene-based nanomaterials: the promising active agents for antibiotics-independent antibacterial applications. *Journal of Controlled Release* **2019,** *307*, 16-31.

73.   Gupta, A.; Sakthivel, T.; Seal, S., Recent development in 2D materials beyond graphene. *Progress in Materials Science* **2015,** *73*, 44-126.

74.   Kim, T. I.; Kwon, B.; Yoon, J.; Park, I.-J.; Bang, G. S.; Park, Y.; Seo, Y.-S.; Choi, S.-Y., Antibacterial Activities of Graphene Oxide–Molybdenum Disulfide Nanocomposite Films. *ACS Applied Materials & Interfaces* **2017,** *9* (9), 7908-7917.

75.   Yang, X.; Li, J.; Liang, T.; Ma, C.; Zhang, Y.; Chen, H.; Hanagata, N.; Su, H.; Xu, M., Antibacterial activity of two-dimensional MoS2 sheets. *Nanoscale* **2014,** *6* (17), 10126-10133.

76.   Pang, X.; Xiao, Q.; Cheng, Y.; Ren, E.; Lian, L.; Zhang, Y.; Gao, H.; Wang, X.; Leung, W.; Chen, X.; Liu, G.; Xu, C., Bacteria-Responsive Nanoliposomes as Smart Sonotheranostics for Multidrug Resistant Bacterial Infections. *ACS Nano* **2019,** *13* (2), 2427-2438.

77.   Coleman, J. N.; Lotya, M.; O'Neill, A.; Bergin, S. D.; King, P. J.; Khan, U.; Young, K.; Gaucher, A.; De, S.; Smith, R. J.; Shvets, I. V.; Arora, S. K.; Stanton, G.; Kim, H.-Y.; Lee, K.; Kim, G. T.; Duesberg, G. S.; Hallam, T.; Boland, J. J.; Wang, J. J.; Donegan, J. F.; Grunlan, J. C.; Moriarty, G.; Shmeliov, A.; Nicholls, R. J.; Perkins, J. M.; Grieveson, E. M.; Theuwissen, K.; McComb, D. W.; Nellist, P. D.; Nicolosi, V., Two-Dimensional Nanosheets Produced by Liquid Exfoliation of Layered Materials. *Science* **2011,** *331* (6017), 568.

78.   Smith, R. J.; King, P. J.; Lotya, M.; Wirtz, C.; Khan, U.; De, S.; O'Neill, A.; Duesberg, G. S.; Grunlan, J. C.; Moriarty, G.; Chen, J.; Wang, J.; Minett, A. I.; Nicolosi, V.; Coleman, J. N., Large-Scale Exfoliation of Inorganic Layered Compounds in Aqueous Surfactant Solutions. *Advanced Materials* **2011,** *23* (34), 3944-3948.

79.   Zong, L.; Li, M.; Li, C., Bioinspired Coupling of Inorganic Layered Nanomaterials with Marine Polysaccharides for Efficient Aqueous Exfoliation and Smart Actuating Hybrids. *Advanced Materials* **2017,** *29* (10), 1604691.

80.   Guan, G.; Xia, J.; Liu, S.; Cheng, Y.; Bai, S.; Tee, S. Y.; Zhang, Y.-W.; Han, M.-Y., Electrostatic-Driven Exfoliation and Hybridization of 2D Nanomaterials. *Advanced Materials* **2017,** *29* (32), 1700326.

81.   Guan, G.; Zhang, S.; Liu, S.; Cai, Y.; Low, M.; Teng, C. P.; Phang, I. Y.; Cheng, Y.; Duei, K. L.; Srinivasan, B. M.; Zheng, Y.; Zhang, Y.-W.; Han, M.-Y., Protein Induces Layer-by-Layer Exfoliation of Transition Metal Dichalcogenides. *Journal of the American Chemical Society* **2015,** *137* (19), 6152-6155.

82.   Ravula, S.; Essner, J. B.; Baker, G. A., Kitchen-Inspired Nanochemistry: Dispersion, Exfoliation, and Hybridization of Functional MoS2 Nanosheets Using Culinary Hydrocolloids. *ChemNanoMat* **2015,** *1* (3), 167-177.

83.   Jia, W.; Tang, B.; Wu, P., Nafion-assisted exfoliation of MoS2 in water phase and the application in quick-response NIR light controllable multi-shape memory membrane. *Nano Research* **2018,** *11* (1), 542-553.

84.   Roy, S.; Mondal, A.; Yadav, V.; Sarkar, A.; Banerjee, R.; Sanpui, P.; Jaiswal, A., Mechanistic Insight into the Antibacterial Activity of Chitosan Exfoliated MoS2 Nanosheets: Membrane Damage, Metabolic Inactivation, and Oxidative Stress. *ACS Applied Bio Materials* **2019,** *2* (7), 2738-2755.

85.   Vega-Mayoral, V.; Backes, C.; Hanlon, D.; Khan, U.; Gholamvand, Z.; O'Brien, M.; Duesberg, G. S.; Gadermaier, C.; Coleman, J. N., Photoluminescence from Liquid-Exfoliated WS2 Monomers in Poly(Vinyl Alcohol) Polymer Composites. *Advanced Functional Materials* **2016,** *26* (7), 1028-1039.

86.   Yuan, Y.; Li, R.; Liu, Z., Establishing Water-Soluble Layered WS2 Nanosheet as a Platform for Biosensing. *Analytical Chemistry* **2014,** *86* (7), 3610-3615.

87.   Lin, D. W.; Bettinger, C. J.; Ferreira, J. P.; Wang, C. L.; Bao, Z., A Cell-Compatible Conductive Film from a Carbon Nanotube Network Adsorbed on Poly-l-lysine. *ACS Nano* **2011,** *5* (12), 10026-10032.

88.   Colville, K.; Tompkins, N.; Rutenberg, A. D.; Jericho, M. H., Effects of Poly(l-lysine) Substrates on Attached Escherichia coli Bacteria. *Langmuir* **2010,** *26* (4), 2639-2644.

89.   Debnath, A., Saha, S., Wang, Q. H., and Green, A. A, Eradication of Multidrug-Resistant Bacteria Using Poly-L-Lysine-Encapsulated 2D Molybdenum Didelenide Nanosheets. **2021 (in preperation)**.

90.   Singh, S. P.; Ramanan, S.; Kaufman, Y.; Arnusch, C. J., Laser-Induced Graphene Biofilm Inhibition: Texture Does Matter. *ACS Applied Nano Materials* **2018,** *1* (4), 1713-1720.

91.   Debnath, A.; Saha, S.; Li, D. O.; Chu, X. S.; Ulissi, Z. W.; Green, A. A.; Wang, Q. H., Elimination of Multidrug-Resistant Bacteria by Transition Metal Dichalcogenides Encapsulated by Synthetic Single-Stranded DNA. *ACS Applied Materials & Interfaces* **2021,** *13* (7), 8082-8094.

92.   Mei, L.; Zhu, S.; Yin, W.; Chen, C.; Nie, G.; Gu, Z.; Zhao, Y., Two-dimensional nanomaterials beyond graphene for antibacterial applications: current progress and future perspectives. *Theranostics* **2020,** *10* (2), 757-781.

93.   Joseph, R.; Naugolny, A.; Feldman, M.; Herzog, I. M.; Fridman, M.; Cohen, Y., Cationic Pillararenes Potently Inhibit Biofilm Formation without Affecting Bacterial Growth and Viability. *Journal of the American Chemical Society* **2016,** *138* (3), 754-757.

94.   Amin, M.; Rowley-Neale, S.; Shalamanova, L.; Lynch, S.; Wilson-Nieuwenhuis, J. T.; El Mohtadi, M.; Banks, C. E.; Whitehead, K. A., Molybdenum Disulfide Surfaces to Reduce Staphylococcus aureus and Pseudomonas aeruginosa Biofilm Formation. *ACS Applied Materials & Interfaces* **2020,** *12* (18), 21057-21069.

95.   Zheng, H.; Ji, Z.; Roy, K. R.; Gao, M.; Pan, Y.; Cai, X.; Wang, L.; Li, W.; Chang, C. H.; Kaweeteerawat, C.; Chen, C.; Xia, T.; Zhao, Y.; Li, R., Engineered Graphene Oxide Nanocomposite Capable of Preventing the Evolution of Antimicrobial Resistance. *ACS Nano* **2019,** *13* (10), 11488-11499.

1. Lee, Y.; Puumala, E.; Robbins, N.; Cowen, L. E., Antifungal Drug Resistance: Molecular Mechanisms in Candida albicans and Beyond. *Chemical Reviews* **2021,** *121* (6), 3390-3411.

2. Armstrong-James, D.; Meintjes, G.; Brown, G. D., A neglected epidemic: fungal infections in HIV/AIDS. *Trends in microbiology* **2014,** *22* (3), 120-7.

3. Cowen, L. E.; Sanglard, D.; Howard, S. J.; Rogers, P. D.; Perlin, D. S., Mechanisms of Antifungal Drug Resistance. *Cold Spring Harbor perspectives in medicine* **2014,** *5* (7), a019752.

4. Brown, G. D.; Denning, D. W.; Gow, N. A. R.; Levitz, S. M.; Netea, M. G.; White, T. C., Hidden Killers: Human Fungal Infections. *Science Translational Medicine* **2012,** *4* (165), 165rv13.

5. Bongomin, F.; Gago, S.; Oladele, R. O.; Denning, D. W., Global and Multi-National Prevalence of Fungal Diseases-Estimate Precision. *Journal of fungi (Basel, Switzerland)* **2017,** *3* (4).

6. Savary, S.; Ficke, A.; Aubertot, J.-N.; Hollier, C., Crop losses due to diseases and their implications for global food production losses and food security. *Food Security* **2012,** *4* (4), 519-537.

7. Casadevall, A., Don't Forget the Fungi When Considering Global Catastrophic Biorisks. *Health security* **2017,** *15* (4), 341-342.

8. Fisher, M. C.; Henk, D. A.; Briggs, C. J.; Brownstein, J. S.; Madoff, L. C.; McCraw, S. L.; Gurr, S. J., Emerging fungal threats to animal, plant and ecosystem health. *Nature* **2012,** *484* (7393), 186-194.

9. Garcia-Solache, M. A.; Casadevall, A., Global Warming Will Bring New Fungal Diseases for Mammals. *mBio* **2010,** *1* (1), e00061-10.

10. Jeffery-Smith, A.; Taori, S. K.; Schelenz, S.; Jeffery, K.; Johnson, E. M.; Borman, A.; Manuel, R.; Brown, C. S., Candida auris: a Review of the Literature. *Clinical microbiology reviews* **2018,** *31* (1).

11. Satoh, K.; Makimura, K.; Hasumi, Y.; Nishiyama, Y.; Uchida, K.; Yamaguchi, H., Candida auris sp. nov., a novel ascomycetous yeast isolated from the external ear canal of an inpatient in a Japanese hospital. *Microbiology and immunology* **2009,** *53* (1), 41-4.

12. Rhodes, J.; Fisher, M. C., Global epidemiology of emerging Candida auris. *Current opinion in microbiology* **2019,** *52*, 84-89.

13. Lockhart, S. R.; Etienne, K. A.; Vallabhaneni, S.; Farooqi, J.; Chowdhary, A.; Govender, N. P.; Colombo, A. L.; Calvo, B.; Cuomo, C. A.; Desjardins, C. A.; Berkow, E. L.; Castanheira, M.; Magobo, R. E.; Jabeen, K.; Asghar, R. J.; Meis, J. F.; Jackson, B.; Chiller, T.; Litvintseva, A. P., Simultaneous Emergence of Multidrug-Resistant Candida auris on 3 Continents Confirmed by Whole-Genome Sequencing and Epidemiological Analyses. *Clinical infectious diseases : an official publication of the Infectious Diseases Society of America* **2017,** *64* (2), 134-140.

14. Schelenz, S.; Hagen, F.; Rhodes, J. L.; Abdolrasouli, A.; Chowdhary, A.; Hall, A.; Ryan, L.; Shackleton, J.; Trimlett, R.; Meis, J. F.; Armstrong-James, D.; Fisher, M. C., First hospital outbreak

of the globally emerging Candida auris in a European hospital. *Antimicrob Resist Infect Control* **2016,** *5*, 35-35.

15.   Chowdhary, A.; Anil Kumar, V.; Sharma, C.; Prakash, A.; Agarwal, K.; Babu, R.; Dinesh, K. R.; Karim, S.; Singh, S. K.; Hagen, F.; Meis, J. F., Multidrug-resistant endemic clonal strain of Candida auris in India. *European journal of clinical microbiology & infectious diseases : official publication of the European Society of Clinical Microbiology* **2014,** *33* (6), 919-26.

16.   Spivak, E. S.; Hanson, K. E., Candida auris: an Emerging Fungal Pathogen. *Journal of clinical microbiology* **2018,** *56* (2).

17.   Coelho, C.; Casadevall, A., Cryptococcal therapies and drug targets: the old, the new and the promising. *Cellular microbiology* **2016,** *18* (6), 792-9.

18.   Chowdhary, A.; Prakash, A.; Sharma, C.; Kordalewska, M.; Kumar, A.; Sarma, S.; Tarai, B.; Singh, A.; Upadhyaya, G.; Upadhyay, S.; Yadav, P.; Singh, P. K.; Khillan, V.; Sachdeva, N.; Perlin, D. S.; Meis, J. F., A multicentre study of antifungal susceptibility patterns among 350 Candida auris isolates (2009-17) in India: role of the ERG11 and FKS1 genes in azole and echinocandin resistance. *The Journal of antimicrobial chemotherapy* **2018,** *73* (4), 891-899.

19.   Escandón, P.; Chow, N. A.; Caceres, D. H.; Gade, L.; Berkow, E. L.; Armstrong, P.; Rivera, S.; Misas, E.; Duarte, C.; Moulton-Meissner, H.; Welsh, R. M.; Parra, C.; Pescador, L. A.; Villalobos, N.; Salcedo, S.; Berrio, I.; Varón, C.; Espinosa-Bode, A.; Lockhart, S. R.; Jackson, B. R.; Litvintseva, A. P.; Beltran, M.; Chiller, T. M., Molecular Epidemiology of Candida auris in Colombia Reveals a Highly Related, Countrywide Colonization With Regional Patterns in Amphotericin B Resistance. *Clinical infectious diseases : an official publication of the Infectious Diseases Society of America* **2019,** *68* (1), 15-21.

20.   Rhodes, J.; Abdolrasouli, A.; Farrer, R. A.; Cuomo, C. A.; Aanensen, D. M.; Armstrong-James, D.; Fisher, M. C.; Schelenz, S., Genomic epidemiology of the UK outbreak of the emerging human fungal pathogen Candida auris. *Emerging microbes & infections* **2018,** *7* (1), 43.

21.   Berkow, E. L.; Lockhart, S. R., Activity of CD101, a long-acting echinocandin, against clinical isolates of Candida auris. *Diagnostic microbiology and infectious disease* **2018,** *90* (3), 196-197.

22.   Franci, G.; Falanga, A.; Galdiero, S.; Palomba, L.; Rai, M.; Morelli, G.; Galdiero, M., Silver nanoparticles as potential antibacterial agents. *Molecules (Basel, Switzerland)* **2015,** *20* (5), 8856-74.

23.   Mallakpour, S.; Abdolmaleki, A.; Borandeh, S.; Sabzalian, M., One pot fabrication of optically active and efficient antibacterial poly(amide-benzimidazole-imide)/Ag bionanocomposite. *Journal of Polymer Research* **2015,** *22*.

24.   Rajendran, S. P.; Sengodan, K., Synthesis and Characterization of Zinc Oxide and Iron Oxide Nanoparticles Using<i> Sesbania grandiflora</i> Leaf Extract as Reducing Agent. *Journal of Nanoscience* **2017,** *2017*, 8348507.

25.   Sankaralingam, K.; Kadirvelu, K., Green synthesis of Iron oxide nanoparticles using Lagenaria siceraria and evaluation of its Antimicrobial activity. *Defence Life Science Journal* **2017,** *2*, 422.

26.   Jadhav, M. S.; Kulkarni, S.; Raikar, P.; Barretto, D. A.; Vootla, S. K.; Raikar, U. S., Green biosynthesis of CuO & Ag–CuO nanoparticles from Malus domestica leaf extract and evaluation of

antibacterial, antioxidant and DNA cleavage activities. *New Journal of Chemistry* **2018,** *42* (1), 204-213.

27.   Karthik, K.; Dhanuskodi, S.; Seetharaman, P. K.; Chandrakasan, G.; Sivaramakrishnan, S., Microwave Assisted Green Synthesis of MgO Nanorods and Their Antibacterial and Anti-breast Cancer Activities. *Materials Letters* **2017,** *206*, 217-220.

28.   Martinez, L. R.; Han, G.; Chacko, M.; Mihu, M. R.; Jacobson, M.; Gialanella, P.; Friedman, A. J.; Nosanchuk, J. D.; Friedman, J. M., Antimicrobial and healing efficacy of sustained release nitric oxide nanoparticles against Staphylococcus aureus skin infection. *The Journal of investigative dermatology* **2009,** *129* (10), 2463-9.

29.   Bahadar, H.; Maqbool, F.; Niaz, K.; Abdollahi, M., Toxicity of Nanoparticles and an Overview of Current Experimental Models. *Iranian biomedical journal* **2016,** *20* (1), 1-11.

30.   Wang, X.; Liu, X.; Chen, J.; Han, H.; Yuan, Z., Evaluation and mechanism of antifungal effects of carbon nanomaterials in controlling plant fungal pathogen. *Carbon* **2014,** *68*, 798-806.

31.   Benincasa, M.; Pacor, S.; Wu, W.; Prato, M.; Bianco, A.; Gennaro, R., Antifungal activity of amphotericin B conjugated to carbon nanotubes. *ACS nano* **2011,** *5* (1), 199-208.

32.   Miao, H.; Teng, Z.; Wang, C.; Chong, H.; Wang, G., Recent Progress in Two-Dimensional Antimicrobial Nanomaterials. *Chemistry – A European Journal* **2019,** *25* (4), 929-944.

33.   Zhu, Y.; Murali, S.; Cai, W.; Li, X.; Suk, J. W.; Potts, J. R.; Ruoff, R. S., Graphene and Graphene Oxide: Synthesis, Properties, and Applications. *Advanced Materials* **2010,** *22* (35), 3906-3924.

34.   Mallakpour, S.; Abdolmaleki, A.; Borandeh, S., Covalently functionalized graphene sheets with biocompatible natural amino acids. *Applied Surface Science* **2014,** *307*, 533-542.

35.   Mohammed, H.; Kumar, A.; Bekyarova, E.; Al-Hadeethi, Y.; Zhang, X.; Chen, M.; Ansari, M. S.; Cochis, A.; Rimondini, L., Antimicrobial Mechanisms and Effectiveness of Graphene and Graphene-Functionalized Biomaterials. A Scope Review. *Frontiers in Bioengineering and Biotechnology* **2020,** *8* (465).

36.   Yang, Y.; Liu, T.; Cheng, L.; Song, G.; Liu, Z.; Chen, M., MoS2-Based Nanoprobes for Detection of Silver Ions in Aqueous Solutions and Bacteria. *ACS Applied Materials & Interfaces* **2015,** *7* (14), 7526-7533.

37.   Zhang, W.; Mou, Z.; Wang, Y.; Chen, Y.; Yang, E.; Guo, F.; Sun, D.; Wang, W., Molybdenum disulfide nanosheets loaded with chitosan and silver nanoparticles effective antifungal activities: in vitro and in vivo. *Materials science & engineering. C, Materials for biological applications* **2019,** *97*, 486-497.

38.   Kurapati, R.; Muzi, L.; de Garibay, A. P. R.; Russier, J.; Voiry, D.; Vacchi, I. A.; Chhowalla, M.; Bianco, A., Enzymatic Biodegradability of Pristine and Functionalized Transition Metal Dichalcogenide MoS2 Nanosheets. *Advanced Functional Materials* **2017,** *27* (7), 1605176.

39.   Roy, S.; Mondal, A.; Yadav, V.; Sarkar, A.; Banerjee, R.; Sanpui, P.; Jaiswal, A., Mechanistic Insight into the Antibacterial Activity of Chitosan Exfoliated MoS2 Nanosheets: Membrane Damage, Metabolic Inactivation, and Oxidative Stress. *ACS Applied Bio Materials* **2019,** *2* (7), 2738-2755.

40.   Pandit, S.; Karunakaran, S.; Boda, S. K.; Basu, B.; De, M., High Antibacterial Activity of Functionalized Chemically Exfoliated MoS2. *ACS Applied Materials & Interfaces* **2016,** *8* (46), 31567-31573.

41.   Cao, F.; Ju, E.; Zhang, Y.; Wang, Z.; Liu, C.; Li, W.; Huang, Y.; Dong, K.; Ren, J.; Qu, X., An Efficient and Benign Antimicrobial Depot Based on Silver-Infused MoS2. *ACS nano* **2017,** *11* (5), 4651-4659.

42.   Liu, X.; Duan, G.; Li, W.; Zhou, Z.; Zhou, R., Membrane destruction-mediated antibacterial activity of tungsten disulfide (WS2). *RSC Advances* **2017,** *7* (60), 37873-37880.

43.   Rasool, K.; Helal, M.; Ali, A.; Ren, C. E.; Gogotsi, Y.; Mahmoud, K. A., Antibacterial Activity of Ti3C2Tx MXene. *ACS nano* **2016,** *10* (3), 3674-3684.

44.   Bang, G. S.; Cho, S.; Son, N.; Shim, G. W.; Cho, B.-K.; Choi, S.-Y., DNA-Assisted Exfoliation of Tungsten Dichalcogenides and Their Antibacterial Effect. *ACS Applied Materials & Interfaces* **2016,** *8* (3), 1943-1950.

45.   Das, B.; Khan, M. I.; Jayabalan, R.; Behera, S. K.; Yun, S.-I.; Tripathy, S. K.; Mishra, A., Understanding the Antifungal Mechanism of Ag@ZnO Core-shell Nanocomposites against Candida krusei. *Scientific Reports* **2016,** *6* (1), 36403.

46.   Debnath, A.; Saha, S.; Li, D. O.; Chu, X. S.; Ulissi, Z. W.; Green, A. A.; Wang, Q. H., Elimination of Multidrug-Resistant Bacteria by Transition Metal Dichalcogenides Encapsulated by Synthetic Single-Stranded DNA. *ACS Applied Materials & Interfaces* **2021,** *13* (7), 8082-8094.

47.   Alimardani, V.; Abolmaali, S.; Borandeh, S., Antifungal and Antibacterial Properties of Graphene-based Nanomaterials: A Mini-review. *Journal of Nanostructures* **2019,** *9*, 402-413.

48.   Sawangphruk, M.; Srimuk, P.; Chiochan, P.; Sangsri, T.; Siwayaprahm, P., Synthesis and antifungal activity of reduced graphene oxide nanosheets. *Carbon* **2012,** *50* (14), 5156-5161.

49.   Bhatt, V. K.; Patel, M.; Pataniya, P. M.; Iyer, B. D.; Sumesh, C. K.; Late, D. J., Enhanced Antifungal Activity of WS2/ZnO Nanohybrid against Candida albicans. *ACS Biomaterials Science & Engineering* **2020,** *6* (11), 6069-6075.

50.   Amato, D. V.; Amato, D. N.; Blancett, L. T.; Mavrodi, O. V.; Martin, W. B.; Swilley, S. N.; Sandoz, M. J.; Shearer, G.; Mavrodi, D. V.; Patton, D. L., A bio-based pro-antimicrobial polymer network via degradable acetal linkages. *Acta biomaterialia* **2018,** *67*, 196-205.

51.   Fan, X.; Ngo, H.; Wu, C., Natural and Bio-based Antimicrobials: A Review. In *Natural and Bio-Based Antimicrobials for Food Applications*, American Chemical Society: 2018; Vol. 1287, pp 1-24.

52.   Shankar, S.; Rhim, J.-W., Preparation of sulfur nanoparticle-incorporated antimicrobial chitosan films. *Food Hydrocolloids* **2018,** *82*, 116-123.

53.   Park, Y.; Kim, M. H.; Park, S. C.; Cheong, H.; Jang, M. K.; Nah, J. W.; Hahm, K. S., Investigation of the antifungal activity and mechanism of action of LMWS-chitosan. *Journal of microbiology and biotechnology* **2008,** *18* (10), 1729-34.

54.   Ing, L. Y.; Zin, N. M.; Sarwar, A.; Katas, H., Antifungal Activity of Chitosan Nanoparticles and Correlation with Their Physical Properties. *International Journal of Biomaterials* **2012,** *2012*, 632698.

55.   Sundaram, J.; Pant, J.; Goudie, M. J.; Mani, S.; Handa, H., Antimicrobial and Physicochemical Characterization of Biodegradable, Nitric Oxide-Releasing Nanocellulose–Chitosan Packaging Membranes. *Journal of Agricultural and Food Chemistry* **2016,** *64* (25), 5260-5266.

56.   Kumar, S.; Ye, F.; Dobretsov, S.; Dutta, J., Chitosan Nanocomposite Coatings for Food, Paints, and Water Treatment Applications. *Applied Sciences* **2019,** *9,* 2409.

57.   Li, C.; Wang, X.; Chen, F.; Zhang, C.; Zhi, X.; Wang, K.; Cui, D., The antifungal activity of graphene oxide-silver nanocomposites. *Biomaterials* **2013,** *34* (15), 3882-90.

58.   Hu, Y.; Qi, X.; Sun, H.; Lu, Y.; Hu, Y.; Chen, X.; Liu, K.; Yang, Y.; Mao, Z.; Wu, Z.; Zhou, X., Photodynamic therapy combined with antifungal drugs against chromoblastomycosis and the effect of ALA-PDT on Fonsecaea in vitro. *PLoS neglected tropical diseases* **2019,** *13* (10), e0007849.

59.   Zhang, Y.; Huang, P.; Wang, D.; Chen, J.; Liu, W.; Hu, P.; Huang, M.; Chen, X.; Chen, Z., Near-infrared-triggered antibacterial and antifungal photodynamic therapy based on lanthanide-doped upconversion nanoparticles. *Nanoscale* **2018,** *10* (33), 15485-15495.

60.   Liu, J.; Li, F.; Zheng, J.; Li, B.; Zhang, D.; Jia, L., Redox/NIR dual-responsive MoS(2) for synergetic chemo-photothermal therapy of cancer. *J Nanobiotechnology* **2019,** *17* (1), 78-78.

61.   Chowdhary, A.; Sharma, C.; Meis, J. F., Candida auris: A rapidly emerging cause of hospital-acquired multidrug-resistant fungal infections globally. *PLoS pathogens* **2017,** *13* (5), e1006290.

62.   Abdolrasouli, A.; Armstrong-James, D.; Ryan, L.; Schelenz, S., In vitro efficacy of disinfectants utilised for skin decolonisation and environmental decontamination during a hospital outbreak with Candida auris. *Mycoses* **2017,** *60* (11), 758-763.

63.   Vallabhaneni, S.; Kallen, A.; Tsay, S.; Chow, N.; Welsh, R.; Kerins, J.; Kemble, S. K.; Pacilli, M.; Black, S. R.; Landon, E.; Ridgway, J.; Palmore, T. N.; Zelzany, A.; Adams, E. H.; Quinn, M.; Chaturvedi, S.; Greenko, J.; Fernandez, R.; Southwick, K.; Furuya, E. Y.; Calfee, D. P.; Hamula, C.; Patel, G.; Barrett, P.; Lafaro, P.; Berkow, E. L.; Moulton-Meissner, H.; Noble-Wang, J.; Fagan, R. P.; Jackson, B. R.; Lockhart, S. R.; Litvintseva, A. P.; Chiller, T. M., Investigation of the First Seven Reported Cases of Candida auris, a Globally Emerging Invasive, Multidrug-Resistant Fungus-United States, May 2013-August 2016. *American journal of transplantation : official journal of the American Society of Transplantation and the American Society of Transplant Surgeons* **2017,** *17* (1), 296-299.

64.   Lee, W. G.; Shin, J. H.; Uh, Y.; Kang, M. G.; Kim, S. H.; Park, K. H.; Jang, H. C., First three reported cases of nosocomial fungemia caused by Candida auris. *Journal of clinical microbiology* **2011,** *49* (9), 3139-42.

65.   Piedrahita, C. T.; Cadnum, J. L.; Jencson, A. L.; Shaikh, A. A.; Ghannoum, M. A.; Donskey, C. J., Environmental Surfaces in Healthcare Facilities are a Potential Source for Transmission of Candida auris and Other Candida Species. *Infection control and hospital epidemiology* **2017,** *38* (9), 1107-1109.

66.   Welsh, R. M.; Bentz, M. L.; Shams, A.; Houston, H.; Lyons, A.; Rose, L. J.; Litvintseva, A. P., Survival, Persistence, and Isolation of the Emerging Multidrug-Resistant Pathogenic Yeast Candida auris on a Plastic Health Care Surface. *Journal of clinical microbiology* **2017,** *55* (10), 2996-3005.

67.   Saeed, S.; Rashid, N.; Jones, P. G.; Ali, M.; Hussain, R., Synthesis, characterization and biological evaluation of some thiourea derivatives bearing benzothiazole moiety as potential antimicrobial and anticancer agents. *European journal of medicinal chemistry* **2010,** *45* (4), 1323-31.

68.   Wu, R.; Ou, X.; Tian, R.; Zhang, J.; Jin, H.; Dong, M.; Li, J.; Liu, L., Membrane destruction and phospholipid extraction by using two-dimensional MoS(2) nanosheets. *Nanoscale* **2018,** *10* (43), 20162-20170.

Chapter 5

1.   Garcia-Viloca, M.; Gao, J.; Karplus, M.; Truhlar, D. G., How Enzymes Work: Analysis by Modern Rate Theory and Computer Simulations. *Science* **2004,** *303* (5655), 186.

2.   Jun, L. Y.; Yon, L. S.; Mubarak, N. M.; Bing, C. H.; Pan, S.; Danquah, M. K.; Abdullah, E. C.; Khalid, M., An overview of immobilized enzyme technologies for dye and phenolic removal from wastewater. *Journal of Environmental Chemical Engineering* **2019,** *7* (2), 102961.

3.   Parameswaran, B.; Papamichael, E.; Varjani, S.; Raveendran, S., Introduction to Green Bioprocesses: Industrial Enzymes for Food Applications: Enzymes in Industrial Food Processing. 2019; pp 1-8.

4.   Shrivastava, A.; Shrivastava, N.; Singh, P. K., Chapter 34 - Enzymes in Pharmaceutical Industry. In *Enzymes in Food Biotechnology*, Kuddus, M., Ed. Academic Press: 2019; pp 591-602.

5.   Lin, Y.; Ren, J.; Qu, X., Catalytically Active Nanomaterials: A Promising Candidate for Artificial Enzymes. *Accounts of Chemical Research* **2014,** *47* (4), 1097-1105.

6.   Gao, L.; Zhuang, J.; Nie, L.; Zhang, J.; Zhang, Y.; Gu, N.; Wang, T.; Feng, J.; Yang, D.; Perrett, S.; Yan, X., Intrinsic peroxidase-like activity of ferromagnetic nanoparticles. *Nature Nanotechnology* **2007,** *2* (9), 577-583.

7.   Liang, M.; Yan, X., Nanozymes: From New Concepts, Mechanisms, and Standards to Applications. *Accounts of Chemical Research* **2019,** *52* (8), 2190-2200.

8.   Manea, F.; Houillon, F. B.; Pasquato, L.; Scrimin, P., Nanozymes: Gold-Nanoparticle-Based Transphosphorylation Catalysts. *Angewandte Chemie International Edition* **2004,** *43* (45), 6165-6169.

9.   Manea, F.; Houillon, F. B.; Pasquato, L.; Scrimin, P., Nanozymes: gold-nanoparticle-based transphosphorylation catalysts. *Angewandte Chemie (International ed. in English)* **2004,** *43* (45), 6165-9.

10.   Huang, Y.; Ren, J.; Qu, X., Nanozymes: Classification, Catalytic Mechanisms, Activity Regulation, and Applications. *Chemical Reviews* **2019,** *119* (6), 4357-4412.

11.   Temoçin, Z.; İnal, M.; Gökgöz, M.; Yiğitoğlu, M., Immobilization of horseradish peroxidase on electrospun poly(vinyl alcohol)–polyacrylamide blend nanofiber membrane and its use in the conversion of phenol. *Polymer Bulletin* **2018,** *75* (5), 1843-1865.

12.   Zhang, Z.; Lai, J.; Wu, K.; Huang, X.; Guo, S.; Zhang, L.; Liu, J., Peroxidase-catalyzed chemiluminescence system and its application in immunoassay. *Talanta* **2018,** *180*, 260-270.

13.   Kim, M. S.; Cho, S.; Joo, S. H.; Lee, J.; Kwak, S. K.; Kim, M. I.; Lee, J., N- and B-Codoped Graphene: A Strong Candidate To Replace Natural Peroxidase in Sensitive and Selective Bioassays. *ACS nano* **2019,** *13* (4), 4312-4321.

14.   Wang, X.; Hu, Y.; Wei, H., Nanozymes in bionanotechnology: from sensing to therapeutics and beyond. *Inorganic Chemistry Frontiers* **2016,** *3* (1), 41-60.

15.   Li, W.; Chen, B.; Zhang, H.; Sun, Y.; Wang, J.; Zhang, J.; Fu, Y., BSA-stabilized Pt nanozyme for peroxidase mimetics and its application on colorimetric detection of mercury(II) ions. *Biosensors & bioelectronics* **2015,** *66*, 251-8.

16. Liu, Y.; Xiang, Y.; Ding, D.; Guo, R., Structural effects of amphiphilic protein/gold nanoparticle hybrid based nanozyme on peroxidase-like activity and silver-mediated inhibition. *RSC Advances* **2016,** *6* (113), 112435-112444.

17. Chen, T.; Zou, H.; Wu, X.; Liu, C.; Situ, B.; Zheng, L.; Yang, G., Nanozymatic Antioxidant System Based on MoS2 Nanosheets. *ACS Applied Materials & Interfaces* **2018,** *10* (15), 12453-12462.

18. Huang, X.-W.; Wei, J.-J.; Liu, T.; Zhang, X.-L.; Bai, S.-M.; Yang, H.-H., Silk fibroin-assisted exfoliation and functionalization of transition metal dichalcogenide nanosheets for antibacterial wound dressings. *Nanoscale* **2017,** *9* (44), 17193-17198.

19. Li, Z.; Liu, X.; Liang, X. H.; Zhong, J.; Guo, L.; Fu, F., Colorimetric determination of xanthine in urine based on peroxidase-like activity of WO(3) nanosheets. *Talanta* **2019,** *204*, 278-284.

20. Zhu, J.; Peng, X.; Nie, W.; Wang, Y.; Gao, J.; Wen, W.; Selvaraj, J. N.; Zhang, X.; Wang, S., Hollow copper sulfide nanocubes as multifunctional nanozymes for colorimetric detection of dopamine and electrochemical detection of glucose. *Biosensors and Bioelectronics* **2019,** *141*, 111450.

21. Sun, H.; Gao, N.; Dong, K.; Ren, J.; Qu, X., Graphene Quantum Dots-Band-Aids Used for Wound Disinfection. *ACS nano* **2014,** *8* (6), 6202-6210.

22. Chen, S.; Wang, Y.; Zhong, M.; Yu, D.; Wang, C.; Lu, X., Fe(III)-Tannic Acid Complex Derived Fe3C Decorated Carbon Nanofibers for Triple-Enzyme Mimetic Activity and Their Biosensing Application. *ACS Biomaterials Science & Engineering* **2019,** *5* (3), 1238-1246.

23. Yin, W.; Yu, J.; Lv, F.; Yan, L.; Zheng, L. R.; Gu, Z.; Zhao, Y., Functionalized Nano-MoS(2) with Peroxidase Catalytic and Near-Infrared Photothermal Activities for Safe and Synergetic Wound Antibacterial Applications. *ACS nano* **2016,** *10* (12), 11000-11011.

24. Yang, Y.; Li, T.; Qin, Y.; Zhang, L.; Chen, Y., Construct of Carbon Nanotube-Supported Fe2O3 Hybrid Nanozyme by Atomic Layer Deposition for Highly Efficient Dopamine Sensing. *Frontiers in Chemistry* **2020,** *8* (876).

25. Singh, N.; Savanur, M. A.; Srivastava, S.; D'Silva, P.; Mugesh, G., A Redox Modulatory Mn3O4 Nanozyme with Multi-Enzyme Activity Provides Efficient Cytoprotection to Human Cells in a Parkinson's Disease Model. *Angewandte Chemie International Edition* **2017,** *56* (45), 14267-14271.

26. Chen, Y.; Chen, T.; Wu, X.; Yang, G., CuMnO2 nanoflakes as pH-switchable catalysts with multiple enzyme-like activities for cysteine detection. *Sensors and Actuators B: Chemical* **2019,** *279*, 374-384.

27. Li, H.; Wang, T.; Wang, Y.; Wang, S.; Su, P.; Yang, Y., Intrinsic Triple-Enzyme Mimetic Activity of V6O13 Nanotextiles: Mechanism Investigation and Colorimetric and Fluorescent Detections. *Industrial & Engineering Chemistry Research* **2018,** *57* (6), 2416-2425.

28. Zhang, W.; Hu, S.; Yin, J.-J.; He, W.; Lu, W.; Ma, M.; Gu, N.; Zhang, Y., Prussian Blue Nanoparticles as Multienzyme Mimetics and Reactive Oxygen Species Scavengers. *Journal of the American Chemical Society* **2016,** *138* (18), 5860-5865.

29. Lim, H.; Yoon, S. I.; Kim, G.; Jang, A. R.; Shin, H. S., Stacking of Two-Dimensional Materials in Lateral and Vertical Directions. *Chemistry of Materials* **2014,** *26* (17), 4891-4903.

30.   Wang, Q. H.; Kalantar-Zadeh, K.; Kis, A.; Coleman, J. N.; Strano, M. S., Electronics and optoelectronics of two-dimensional transition metal dichalcogenides. *Nature Nanotechnology* **2012,** *7* (11), 699-712.

31.   Puthirath Balan, A.; Radhakrishnan, S.; Woellner, C. F.; Sinha, S. K.; Deng, L.; Reyes, C. d. l.; Rao, B. M.; Paulose, M.; Neupane, R.; Apte, A.; Kochat, V.; Vajtai, R.; Harutyunyan, A. R.; Chu, C.-W.; Costin, G.; Galvao, D. S.; Martí, A. A.; van Aken, P. A.; Varghese, O. K.; Tiwary, C. S.; Malie Madom Ramaswamy Iyer, A.; Ajayan, P. M., Exfoliation of a non-van der Waals material from iron ore hematite. *Nature Nanotechnology* **2018,** *13* (7), 602-609.

32.   Yu, J.; Ma, D.; Mei, L.; Gao, Q.; Yin, W.; Zhang, X.; Yan, L.; Gu, Z.; Ma, X.; Zhao, Y., Peroxidase-like activity of MoS2 nanoflakes with different modifications and their application for H2O2 and glucose detection. *Journal of Materials Chemistry B* **2018,** *6* (3), 487-498.

33.   Sani, E.; Mercatelli, L.; Meucci, M.; Silvestroni, L.; Balbo, A.; Sciti, D., Process and composition dependence of optical properties of zirconium, hafnium and tantalum borides for solar receiver applications. *Solar Energy Materials and Solar Cells* **2016,** *155*, 368-377.

34.   Gilliam, M. S.; Yousaf, A.; Guo, Y.; Li, D. O.; Momenah, A.; Wang, Q. H.; Green, A. A., Evaluating the Exfoliation Efficiency of Quasi-2D Metal Diboride Nanosheets Using Hansen Solubility Parameters. *Langmuir* **2021,** *37* (3), 1194-1205.

35.   Yousaf, A.; Gilliam, M. S.; Chang, S. L. Y.; Augustin, M.; Guo, Y.; Tahir, F.; Wang, M.; Schwindt, A.; Chu, X. S.; Li, D. O.; Kale, S.; Debnath, A.; Liu, Y.; Green, M. D.; Santos, E. J. G.; Green, A. A.; Wang, Q. H., Exfoliation of Quasi-Two-Dimensional Nanosheets of Metal Diborides. *The Journal of Physical Chemistry C* **2021,** *125* (12), 6787-6799.

36.   Wagner, F. R.; Baranov, A. I.; Grin, Y.; Kohout, M., A Position-Space View on Chemical Bonding in Metal Diborides with AlB2 Type of Crystal Structure. *Zeitschrift für anorganische und allgemeine Chemie* **2013,** *639* (11), 2025-2035.

37.   Backes, C.; Higgins, T. M.; Kelly, A.; Boland, C.; Harvey, A.; Hanlon, D.; Coleman, J. N., Guidelines for Exfoliation, Characterization and Processing of Layered Materials Produced by Liquid Exfoliation. *Chemistry of Materials* **2017,** *29* (1), 243-255.

38.   Debnath, A.; Saha, S.; Li, D. O.; Chu, X. S.; Ulissi, Z. W.; Green, A. A.; Wang, Q. H., Elimination of Multidrug-Resistant Bacteria by Transition Metal Dichalcogenides Encapsulated by Synthetic Single-Stranded DNA. *ACS Applied Materials & Interfaces* **2021,** *13* (7), 8082-8094.

39.   Yousaf, A.; Gilliam, M.; Chang, S.; Augustin, M.; Guo, Y.; Tahir, F.; Wang, M.; Schwindt, A.; Chu, X.; Li, D.; Kale, S.; Debnath, A.; Liu, Y.; Green, M.; Santos, E.; Green, A.; Wang, Q. H., *Exfoliation of Two-Dimensional Nanosheets of Metal Diborides*. 2020.

40.   Pitto-Barry, A.; Barry, N. P. E., Pluronic® block-copolymers in medicine: from chemical and biological versatility to rationalisation and clinical advances. *Polymer Chemistry* **2014,** *5* (10), 3291-3297.

41.   Seo, J.-W. T.; Green, A. A.; Antaris, A. L.; Hersam, M. C., High-Concentration Aqueous Dispersions of Graphene Using Nonionic, Biocompatible Block Copolymers. *The Journal of Physical Chemistry Letters* **2011,** *2* (9), 1004-1008.

42.   Nečas, D.; Klapetek, P., Gwyddion: an open-source software for SPM data analysis. *Central European Journal of Physics* **2012,** *10* (1), 181-188.

43.   Hernandez, Y.; Nicolosi, V.; Lotya, M.; Blighe, F. M.; Sun, Z.; De, S.; McGovern, I. T.; Holland, B.; Byrne, M.; Gun'Ko, Y. K.; Boland, J. J.; Niraj, P.; Duesberg, G.; Krishnamurthy, S.; Goodhue, R.; Hutchison, J.; Scardaci, V.; Ferrari, A. C.; Coleman, J. N., High-yield production of graphene by liquid-phase exfoliation of graphite. *Nature Nanotechnology* **2008,** *3* (9), 563-568.

44.   Chatakondu, K.; Green, M. L. H.; Thompson, M. E.; Suslick, K. S., The enhancement of intercalation reactions by ultrasound. *Journal of the Chemical Society, Chemical Communications* **1987,** (12), 900-901.

45.   Gupta, A.; Arunachalam, V.; Vasudevan, S., Water Dispersible, Positively and Negatively Charged MoS2 Nanosheets: Surface Chemistry and the Role of Surfactant Binding. *The Journal of Physical Chemistry Letters* **2015,** *6* (4), 739-744.

46.   Guo, Y.; Gupta, A.; Gilliam, M. S.; Debnath, A.; Yousaf, A.; Saha, S.; Levin, M. D.; Green, A. A.; Singh, A. K.; Wang, Q. H., Exfoliation of boron carbide into ultrathin nanosheets. *Nanoscale* **2021,** *13* (3), 1652-1662.

47.   Marquez, L. A.; Dunford, H. B., Mechanism of the Oxidation of 3,5,3',5'-Tetramethylbenzidine by Myeloperoxidase Determined by Transient- and Steady-State Kinetics. *Biochemistry* **1997,** *36* (31), 9349-9355.

48.   Xia, X.; Zhang, J.; Lu, N.; Kim, M. J.; Ghale, K.; Xu, Y.; McKenzie, E.; Liu, J.; Ye, H., Pd–Ir Core–Shell Nanocubes: A Type of Highly Efficient and Versatile Peroxidase Mimic. *ACS nano* **2015,** *9* (10), 9994-10004.

49.   Porter, D. J.; Bright, H. J., The mechanism of oxidation of nitroalkanes by horseradish peroxidase. *The Journal of biological chemistry* **1983,** *258* (16), 9913-24.

50.   Song, Y.; Qu, K.; Zhao, C.; Ren, J.; Qu, X., Graphene Oxide: Intrinsic Peroxidase Catalytic Activity and Its Application to Glucose Detection. *Advanced Materials* **2010,** *22* (19), 2206-2210.

51.   Ji, H.; Sun, H.; Qu, X., Antibacterial applications of graphene-based nanomaterials: Recent achievements and challenges. *Advanced drug delivery reviews* **2016,** *105* (Pt B), 176-189.

52.   Liu, S.; Zeng, T. H.; Hofmann, M.; Burcombe, E.; Wei, J.; Jiang, R.; Kong, J.; Chen, Y., Antibacterial Activity of Graphite, Graphite Oxide, Graphene Oxide, and Reduced Graphene Oxide: Membrane and Oxidative Stress. *ACS nano* **2011,** *5* (9), 6971-6980.

53.   Rasool, K.; Helal, M.; Ali, A.; Ren, C. E.; Gogotsi, Y.; Mahmoud, K. A., Antibacterial Activity of Ti3C2Tx MXene. *ACS nano* **2016,** *10* (3), 3674-3684.

54.   Roy, S.; Mondal, A.; Yadav, V.; Sarkar, A.; Banerjee, R.; Sanpui, P.; Jaiswal, A., Mechanistic Insight into the Antibacterial Activity of Chitosan Exfoliated MoS2 Nanosheets: Membrane Damage, Metabolic Inactivation, and Oxidative Stress. *ACS Applied Bio Materials* **2019,** *2* (7), 2738-2755.

55.   Wang, Z.; Dong, K.; Liu, Z.; Zhang, Y.; Chen, Z.; Sun, H.; Ren, J.; Qu, X., Activation of biologically relevant levels of reactive oxygen species by Au/g-C(3)N(4) hybrid nanozyme for bacteria killing and wound disinfection. *Biomaterials* **2017,** *113*, 145-157.

56.   Liu, J.; Li, F.; Zheng, J.; Li, B.; Zhang, D.; Jia, L., Redox/NIR dual-responsive MoS(2) for synergetic chemo-photothermal therapy of cancer. *J Nanobiotechnology* **2019,** *17* (1), 78-78.

57.   Notley, S. M., Highly Concentrated Aqueous Suspensions of Graphene through Ultrasonic Exfoliation with Continuous Surfactant Addition. *Langmuir* **2012,** *28* (40), 14110-14113.

58.   Johnson, K. A.; Goody, R. S., The Original Michaelis Constant: Translation of the 1913 Michaelis–Menten Paper. *Biochemistry* **2011,** *50* (39), 8264-8269.

59.   Cho, Y. S.; Lim, H. S., Comparison of various estimation methods for the parameters of Michaelis-Menten equation based on in vitro elimination kinetic simulation data. *Translational and clinical pharmacology* **2018,** *26* (1), 39-47.

60.   Markides, H.; Rotherham, M.; El Haj, A. J., Biocompatibility and Toxicity of Magnetic Nanoparticles in Regenerative Medicine. *Journal of Nanomaterials* **2012,** *2012*, 614094.

Chapter 6

1.   Novoselov, K. S.; Geim, A. K.; Morozov, S. V.; Jiang, D.; Zhang, Y.; Dubonos, S. V.; Grigorieva, I. V.; Firsov, A. A., Electric Field Effect in Atomically Thin Carbon Films. *Science* **2004,** *306* (5696), 666.

2.   Mas-Ballesté, R.; Gómez-Navarro, C.; Gómez-Herrero, J.; Zamora, F., 2D materials: to graphene and beyond. *Nanoscale* **2011,** *3* (1), 20-30.

3.   Banerjee, A. N., Graphene and its derivatives as biomedical materials: future prospects and challenges. *Interface focus* **2018,** *8* (3), 20170056.

4.   Rohaizad, N.; Mayorga-Martinez, C. C.; Fojtů, M.; Latiff, N. M.; Pumera, M., Two-dimensional materials in biomedical, biosensing and sensing applications. *Chemical Society Reviews* **2021,** *50* (1), 619-657.

5.   Debnath, A.; Saha, S.; Li, D. O.; Chu, X. S.; Ulissi, Z. W.; Green, A. A.; Wang, Q. H., Elimination of Multidrug-Resistant Bacteria by Transition Metal Dichalcogenides Encapsulated by Synthetic Single-Stranded DNA. *ACS Applied Materials & Interfaces* **2021,** *13* (7), 8082-8094.

6.   Gilliam, M. S.; Yousaf, A.; Guo, Y.; Li, D. O.; Momenah, A.; Wang, Q. H.; Green, A. A., Evaluating the Exfoliation Efficiency of Quasi-2D Metal Diboride Nanosheets Using Hansen Solubility Parameters. *Langmuir* **2021,** *37* (3), 1194-1205.

7.   Yousaf, A.; Gilliam, M. S.; Chang, S. L. Y.; Augustin, M.; Guo, Y.; Tahir, F.; Wang, M.; Schwindt, A.; Chu, X. S.; Li, D. O.; Kale, S.; Debnath, A.; Liu, Y.; Green, M. D.; Santos, E. J. G.; Green, A. A.; Wang, Q. H., Exfoliation of Quasi-Two-Dimensional Nanosheets of Metal Diborides. *The Journal of Physical Chemistry C* **2021,** *125* (12), 6787-6799.

8.   Guo, Y.; Gupta, A.; Gilliam, M. S.; Debnath, A.; Yousaf, A.; Saha, S.; Levin, M. D.; Green, A. A.; Singh, A. K.; Wang, Q. H., Exfoliation of boron carbide into ultrathin nanosheets. *Nanoscale* **2021,** *13* (3), 1652-1662.

9.   Imani, S. M.; Ladouceur, L.; Marshall, T.; Maclachlan, R.; Soleymani, L.; Didar, T. F., Antimicrobial Nanomaterials and Coatings: Current Mechanisms and Future Perspectives to Control the Spread of Viruses Including SARS-CoV-2. *ACS Nano* **2020,** *14* (10), 12341-12369.

10.   Li, X.; Huang, T.; Heath, D. E.; O'Brien-Simpson, N. M.; O'Connor, A. J., Antimicrobial nanoparticle coatings for medical implants: Design challenges and prospects. *Biointerphases* **2020,** *15* (6), 060801.

11.   Vasilev, K., Nanoengineered Antibacterial Coatings and Materials: A Perspective. *Coatings* **2019,** *9* (10).

12.   Han, G.; Ceilley, R., Chronic Wound Healing: A Review of Current Management and Treatments. *Advances in therapy* **2017,** *34* (3), 599-610.

13.   Blanco-Fernandez, B.; Castaño, O.; Mateos-Timoneda, M.; Engel, E.; Pérez-Amodio, S., Nanotechnology Approaches in Chronic Wound Healing. *Advances in wound care* **2021,** *10* (5), 234-256.

14.   Klein, S.; Müller, T. G.; Khalid, D.; Sonntag-Buck, V.; Heuser, A.-M.; Glass, B.; Meurer, M.; Morales, I.; Schillak, A.; Freistaedter, A.; Ambiel, I.; Winter, S. L.; Zimmermann, L.; Naumoska, T.; Bubeck, F.; Kirrmaier, D.; Ullrich, S.; Barreto Miranda, I.; Anders, S.; Grimm, D.; Schnitzler, P.;

Knop, M.; Kräusslich, H.-G.; Dao Thi, V. L.; Börner, K.; Chlanda, P., SARS-CoV-2 RNA Extraction Using Magnetic Beads for Rapid Large-Scale Testing by RT-qPCR and RT-LAMP. *Viruses* **2020,** *12* (8), 863.

APPENDIX A

SUPPLEMENTAL MATERIAL FOR CHAPTER 2

Table of contents

S1. Materials and supplies

S2. Preparation of MoSe$_2$/PLL/F77 dispersions and characterization

S3. Antibacterial study

S4. Biocompatibility study

S5. Morphology

S.6 Resistance Study

S7. Supplementary figures

S1. Materials and supplies

Chemicals

Molybdenum disulfide (MoS_2), molybdenum diselenide ($MoSe_2$), tungsten disulfide (WS_2), tungsten diselenide (WSe_2), tin sulfide (SnS), tin diselenide (SnS), bismuth disulfide (Bi_2S_3) and bismuth diselenide (Bi_2Se_3), poly-L-lysine (PLL), phosphate buffer saline solution (PBS, pH 7.4), Dulbecco's phosphate buffered saline (DPBS), Muller-Hilton broth (MHB), Muller-Hilton agar (MHA), brain heart infusion (MHI) broth, brain heart infusion (BHI) agar, Dulbecco's modified Eagle's medium (DMEM), trypsin-EDTA, tryptic soy agar (TSA), tryptic soy broth (TSB), Luria-Bertani (LB) broth and LB agar were purchased from Sigma-Aldrich. T_{20} ssDNA was purchased from Integrated DNA Technologies (IDT). RAW 264.7 (TIB-71™) macrophage cells were purchased from ATCC. Whole red blood cells (RBCs) from a single donor were purchased from Innovative Research. The alamarBlue reagent cell proliferation assay was purchased from G-Biosciences. Acetone and ethanol were purchased from VWR. Osmium tetroxide (OsO_4, 98% purity) was purchased from Combi-Blocks Inc. Pluronic F77 was obtained from BASF Corporation.

Bacteria strains

Escherichia coli (*E. coli*) strain MG1655 (ATCC, 700926), *Staphylococcus aureus* (*S. aureus*) (ATCC, 29213), *Methicillin resistant Staphylococcus aureus* (MRSA) (ATCC, BAA 1720), *Pseudomonas aeruginosa* (*P. aeruginosa*) (ATCC, BAA 2113), *Klebsiella pneumoniae* (*K. pneumoniae*) (ATCC, BAA 2342), *Vancomycin-resistant Enterococcus faecium* (*E. faecium*) (ATCC, 51299), *Acinetobacter baumannii* (*A. baumannii*) (ATCC, BAA 1797) and Enterobacter cloacae (*E. cloacea*) (ATCC, BAA 2468).

2. Preparation of TMC dispersions and characterization

Preparation of TMC/ssDNA

The T_{20} ssDNA aqueous solution (1.6 mg ml^{-1}) was dissolved in 8 ml of autoclaved water and 200 mg of bulk power source material was added. The mixture was probe sonicated with a 13 mm tip with Branson Digital Sonifier SFX 550 for 2 h at 11 W power under. After sonication, the dispersion was centrifuged at 5000 rpm for 5 mins followed by 21,000 g for 1 minute to

remove the excess bulk powder flakes using an Eppendorf 5424 Microcentrifuge and the supernatant was collected. The concentration of nanosheets in the final dispersion was determined using ICP-MS. The MoSe$_2$/PLL/F77 dispersions were stable for several weeks. Liquid dispersions for ICP-MS analysis were first acidified in nitric acid overnight and diluted to a final nitric acid concentration of 2 wt%. The samples were then analyzed by a Thermo Fisher iCap Q quadrupole instrument. The color of the resulting dispersions varied from brown to green depending on the material.

Preparation of MoSe$_2$/PLL/F77

We ultrasonicated 200 mg of TMC were added to 8 ml aqueous solution containing 1 mg ml^{-1} of PLL with a 13 mm tip at a power level of 12 W for 2 hours using a Branson Digital Sonifier 450D. After ultrasonication, the sample was centrifuged at 5000 g for 5 minutes followed by 21,000 g for 1 minute to remove the excess bulk powder using an Eppendorf 5424 Microcentrifuge. The supernatant then was further ultrasonicated for 30 minutes with 3% (w/v%) Pluronic F77 added to a concentration of 0.5% w/v for 30 minutes. The resulting solution was than dialyzed for 24 h using 100 kD molecular weight cutoff cellulose ester membrane. The concentration of nanosheets in the final dispersion was determined using ICP-MS. The MoSe$_2$/PLL/F77 dispersions were stable for several weeks. Liquid dispersions for ICP-MS analysis were first acidified in nitric acid overnight and diluted to a final nitric acid concentration of 2 wt%. The samples were then analyzed by a Thermo Fisher iCap Q quadrupole instrument.

Characterization

Absorbance (UV-Vis) spectra for the dispersed 2D MoSe$_2$/PLL/F77 were acquired using a Jasco V-670 Spectrophotometer using a quartz cell with a path length of 1.0 cm. Transmission electron microscopy (TEM) samples were prepared by drop-casting 10 µl of dilute MoSe$_2$/PLL/F77 dispersion on a holey carbon grid followed by washing with 10 µl of water and dried with filter paper. Images were acquired on a Philips CM-12 TEM operated at 80 kV with the help of a Gatan model 791 CCD camera.

S3. Antibacterial studies

Overnight cultures of bacteria were grown in their respective medium at 37 °C. *E. coli* strain MG1655 was grown in LB broth. TSB broth (Sigma Aldrich) and TSB agar (Sigma Aldrich) were used to grow *S. aureus*, MRSA, *P. aeruginosa* and *A. baumannii* whereas *E. faecium* were grown in BHI broth and BHI agar in presence of 4mcg/ml of vancomycin. *K. pneumoniae* was grown in MHB. They were harvested at the mid-exponential growth phase (optical density (OD) at 600 nm wavelength, OD_{600} = 0.33). Cells were centrifuged at 2500 rpm for 5 min and the pellets were washed with 1×PBS. The final pellet was resuspended in minimal essential medium (MEM) and OD_{600} was measured on a spectrometer, then diluted to 10^7 cell-forming units (CFU)/mL in MEM medium. Bacteria at concentrations of 10^7 CFU/ml were incubated with different concentrations of nanomaterials (TMC/ssDNA and MoSe$_2$/PLL/F77) for 4 h and 2 h respectively. After incubation, bacteria were plated in agar plates using serial dilution method and after overnight growth remaining bacterial was calculated by colony counting method.

S4. Biocompatibility

Hemolysis assay

Fresh RBC was diluted in 1x PBS to dilute it to the concentration of 2×10^7 and centrifuged at 5000 g for 10 minutes. The supernatant was collected, and pellet was washed with 1x PBS three times to remove any hemoglobin from lysed cell. The diluted cell was than incubated with varying concentrations of nanomaterials in presence of humidity containing 5% CO_2 at 37 °C for 2 hours. After incubation, solution was centrifuged, and absorbance of supernatant was measured at 570 nm. RBC suspension in 1x PBS was used as a negative control whereas RBC lysed with 0.5% Triton X-100 was taken as a positive control.

Cell viability of mammalian cell

Rat macrophage 264.7 cell cell line was cultivated in DMEM medium containing 10% FBS and 1% antibiotics. The cells were cultured in presence of humidity containing 5% CO_2 at 37 °C. The cells were passaged thrice a week before performing cell experiments. Cell viability was determined by seeding mammalian cells to the order of 1×10^5 order in 96 well plate for 24 h. The cells were incubated with varied concentrations of nanomaterials for 24 h. After incubations, supernatant was removed and replaced with 10% alamerBlue solution in DMEM. After 4 hours

incubation with 10% alamerBlue solution, the fluorescence was measured (excitation/emission: 560 nm/610nm). Cells without nanomaterials were considered as 100% viable. All experiments were performed in quadruplicate.

S5. Morphology study

SEM Imaging

For scanning electron microscopy (SEM) imaging, cells were initially fixed and washed following the same method used for TEM samples. Washed cells were then concentrated into a small volume of DPBS and applied to poly-L-lysine (PLL)-coated coverslips for 10 min. Excess cells were removed by briefly rinsing in DPBS and the coverslips were transferred to a solution of 1% OsO_4 in DPBS for 1 h at room temperature, followed by thorough washing with deionized water. Samples were dehydrated in a graded ethanol series (20%, 40%, 60%, 75%, 90% and 100%) and critical-point dried in a Balzers-Union CPD-020 unit using carbon dioxide as the transition fluid. After routine mounting on aluminum stubs, samples were sputtered-coated with 10-12 nm of gold-palladium in a Technics Hummer-II unit. Images were generated on a JEOL JSM6300 SEM operated at 15 kV and acquired with an IXRF model 500 digital processor.

TEM Imaging

For transmission electron microscopy (TEM) imaging, samples treated by $MoSe_2$/CS and control samples were initially fixed in a suspension with 2.5% glutaraldehyde in Dulbecco's phosphate buffered saline (DPBS) overnight at 4°C, followed by washing in DPBS. Cells were then placed into a drop of 1% agarose on a glass slide and treated with 1% osmium tetroxide (OsO_4) in DPBS for 1 h, washed thoroughly with deionized water, and dehydrated in a graded acetone series (20%, 40%, 60%, 80% and 100%). Spurr's epoxy resin was used to infiltrate and embed the samples. 70-nm-thick sections were cut on a Leica Ultra cut-R microtome followed by post-staining with uranyl acetate and lead citrate. Images were generated on a Philips CM-12 TEM operated at 80 kV and acquired with a Gatan model 791 CCD camera.

S 6. Resistance study

S. aureus (ATCC-BAA 1720) and *A. baumannii* (ATCC- BAA 1797) was inoculated in TSB medium and cultured overnight at 37 °C at 200 rpm. The overnight culture was further diluted in TSB medium and incubated with $MoSe_2$/PLL/F77 or antibiotics solutions in TSB medium. The plates were sealed and incubated for 16 hours. The MIC was determined. The bacteria from 25 concentration of $MoSe_2$/PLL/F77 or antibiotics was further diluted in TSB medium and treated with fresh solution of $MoSe_2$/PLL/F77 or antibiotics and incubated as above. This process was repeated for 20 passages.

S7. Supplementary figures
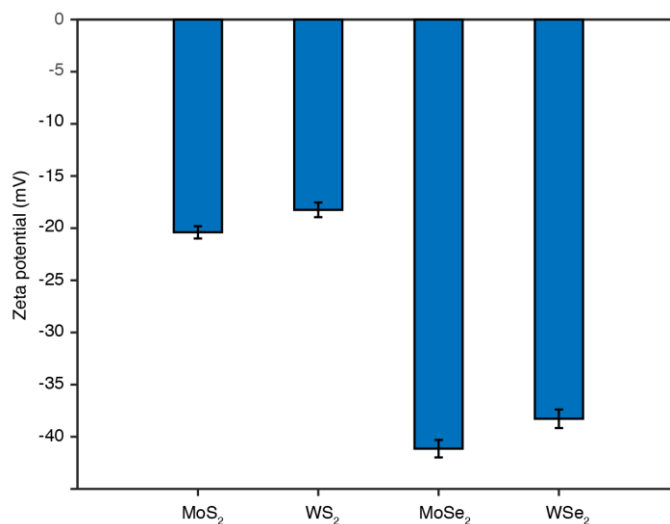
Figure S 2.1. Zeta potentials of dispersions of 2D TMCs in ssDNA.[38]
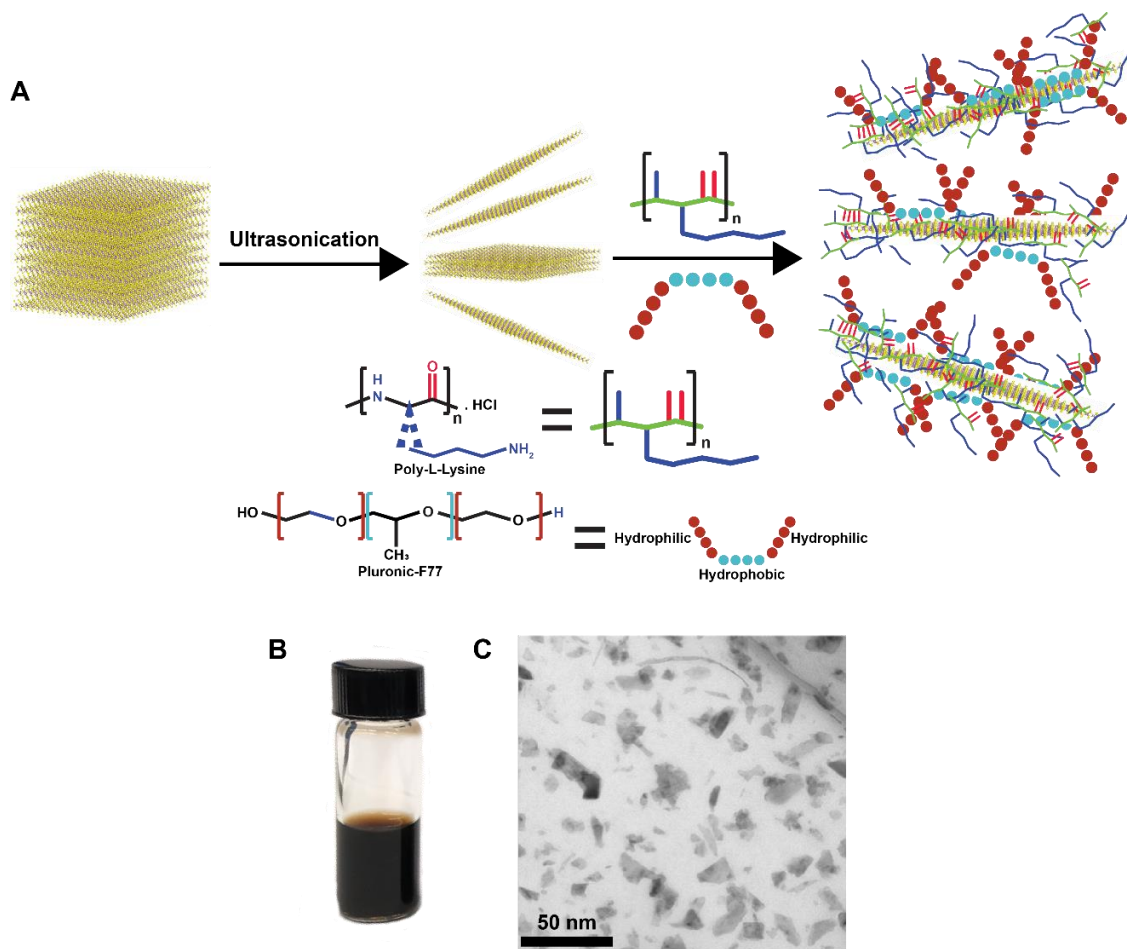
Figure S 2.2. Synthesis and characterization of MoSe$_2$/PLL/F77. (A) Schematic illustration of exfoliation of bulk MoSe$_2$ in PLL and Pluronic F77 solution to form MoSe$_2$/PLL/F77 nanosheets. The structure of PLL is shown at bottom along with Pluronic F77. (B) Glass vial containing a dark brown MoSe$_2$/PLL/F77 dispersion. (C) TEM image showing dispersed MoSe$_2$/PLL/F77 nanosheets.
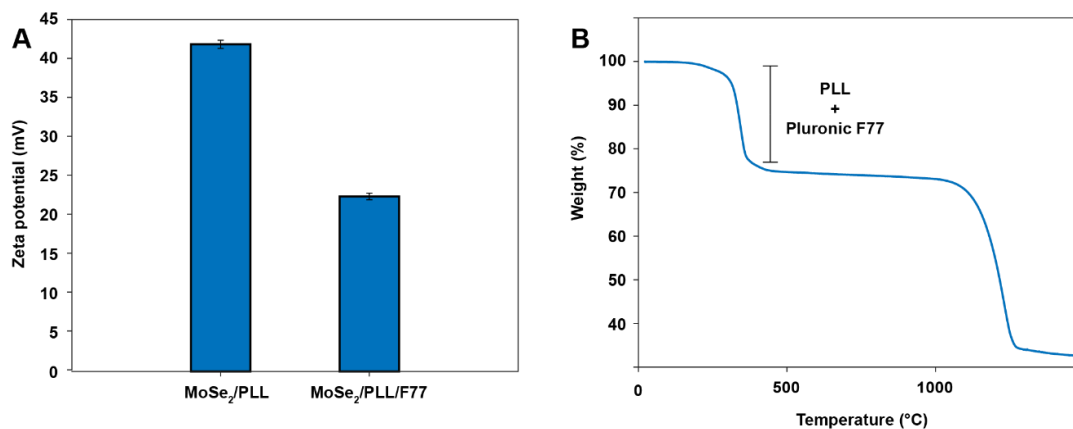
Figure S2.3. Zeta potential and TGA. (A). Comparison of zeta potential of MoSe$_2$/PLL and MoSe$_2$/PLL/F77. (B) TGA data of MoSe$_2$/PLL/F77. (Experiment credit: Abhishek Debnath).
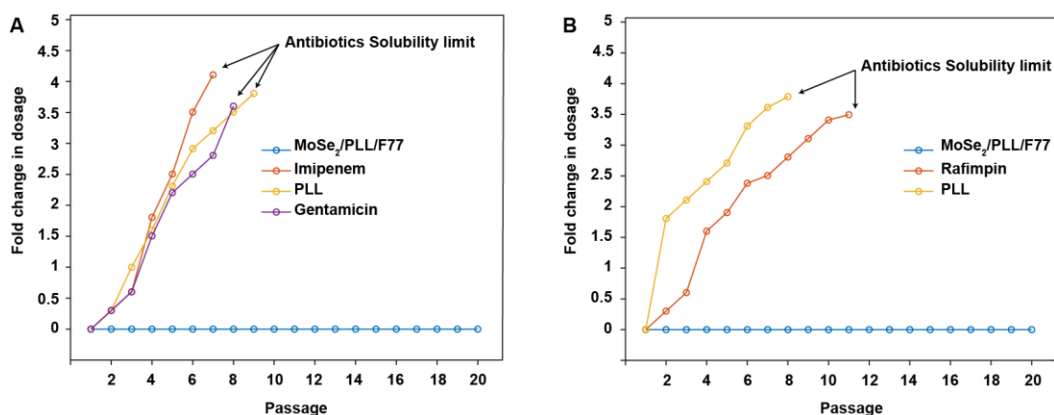
Figure S 2.4. (A) Development of resistance by *Pseudomonas aeruginosa* against imipenem, gentamicin, PLL and MoSe$_2$/PLL/F77 after treatment at 0.5 x MIC concentrations. (B) Development of resistance by *Staphylococcus aureus* against antibiotic rifampin, PLL, and MoSe$_2$/PLL/F77 after treatment at 0.5 x MIC concentrations. (Experiment credit: Abhishek Debnath).

APPENDIX B

SUPPLEMENTAL MATERIAL FOR CHAPTER 3

Eradication and inhibition of bacterial biofilms using 2D $MoSe_2$ wrapped in biopolymers

Sanchari Saha,[1,2] Abhishek Debnath,[1,2] Qing Hua Wang,*[3] and Alexander A. Green*[4]

1. Biodesign Center for Molecular Design and Biomimetics, The Biodesign Institute, Arizona State University, Tempe, Arizona 85287, United States

2. School of Molecular Sciences, Arizona State University, Tempe, Arizona 85287, United States

3. Materials Science and Engineering, School for Engineering of Matter, Transport and Energy, Arizona State University, Tempe, Arizona 85287, United States

4. Department of Biomedical Engineering, Boston University, Boston, MA 02215, United States

* Corresponding author: alexgreen@bu.edu, qhwang@asu.edu

Table of contents

S1. Materials and supplies

Materials

Molybdenum (IV) selenide (MoSe$_2$, 325 mesh, 99.9% trace metals basis, item number: 778087), poly-L-lysine hydrochloride (PLL, mol. Wt. >30,000), phosphate buffer saline solution (PBS, pH 7.4), Dulbecco's phosphate buffered saline (DPBS), Dulbecco's modified Eagle's medium (DMEM), tryptic soy broth, tryptic soy agar, crystal violet (CV, 548-62-9), **Poly(methacrylic acid methyl ester)** (PMMA, 9011-14-7), hydrophilic polytetrafluoroethylene membrane (PTFE, **JAWP04700,** 1.0 um pore size, 47 mm diameter) and (sodium 3′-[1-[(phenylamino)-carbony]-3,4-tetrazolium]-bis(4-methoxy-6-nitro)benzene-sulfoni acid hydrate) (XTT, 111072-31-2) salt were purchased from Sigma-Aldrich. Glutaraldehyde solution (25% in H$_2$O) was purchased from Thomas Scientific Holdings LLC. Human embryonic kidney 293 cells (HEK293) were purchased from ATCC. Osmium tetroxide (OsO$_4$, 98% purity) was purchased from Combi-Blocks Inc. LIVE/DEAD BacLight Bacterial Viability Kits was purchased from Thermo Fisher Scientific. Minimum biofilm eradication concentration (MBEC) assay plates with stubs were purchased from Innovotech's MBEC Assay® (Product Codes 19132). Pluronic F77 was obtained from BASF Corporation. Medical grade titanium alloy (Ti-alloy, 6-4 Eli Grade 23 Titanium Grade) was obtained from TMS Titanium.

Bacterial strains

The antibacterial activity of MoSe$_2$/PLL/F77 was studied using the *Methicillin resistant Staphylococcus aureus* (MRSA, ATCC, BAA 1720), *Acinetobacter baumannii* (*A. baumannii*, ATCC, BAA 1797) and *Pseudomonas aeruginosa* (*P. aeruginosa*, ATCC, BAA 2113).

S2. Preparation and characterization of MoSe$_2$/PLL/F77

Preparation of MoSe$_2$/PLL/F77 dispersions

The MoSe$_2$/PLL/F77 dispersions were prepared by first probe sonicating 200 mg of MoSe$_2$ in the presence of 1.6 mg ml^{-1} PLL in 8 ml of water, to make a dispersion of MoSe$_2$/PLL. The sonication was done for 2 h at 25 W power using Branson Digital Sonifier SFX 550. The sonicated sample was centrifuged for 5 mins at 5000 rcf followed by 1 min at 21000 rcf using an Eppendorf

5424 Microcentrifuge. The supernatant was collected leaving the pellet which contained excess MoSe$_2$ and PLL. The MoSe$_2$/PLL dispersion was further sonicated in 0.5% Pluronic F77, an amphiphilic nonionic biocompatible surfactant for 30 mins at 11 W power. The resultant dispersion was then dialyzed for 36 h in water to remove excess the PLL and Pluronic F77. The MoSe$_2$/PLL/F77 dispersions were stable for several weeks. The concentration of nanosheets in the final dispersion was determined using inductively coupled mass spectrometry (ICP-MS). Liquid dispersions for ICP-MS analysis were first acidified in nitric acid overnight and diluted to a final nitric acid concentration of 2 wt%. The samples were then analyzed by a Thermo Fisher iCap Q quadrupole instrument.

Optical characterization and transmission electron microscopy

Absorbance (UV-Vis) spectra for the dispersed 2D MoSe$_2$/PLL/F77 were acquired using a Jasco V-670 Spectrophotometer using a quartz cell with a path length of 1.0 cm. Transmission electron microscopy (TEM) samples were prepared by drop-casting 10 µl of dilute MoSe$_2$/PLL/F77 dispersion on a holey carbon grid and left to dry under ambient conditions. Images were acquired on a Philips CM-12 TEM operated at 80 kV with the help of a Gatan model 791 CCD camera.

S3. Bacterial cell preparation and biofilm quantification assay

Biofilm growth

Overnight cultures of MRSA, *A. baumannii*, and *P. aeruginosa* were grown in tryptic soy broth (TSB) at 37°C and harvested at mid-exponential growth phase (optical density (OD) at 600 nm wavelength, OD$_{600}$ = 0.33). Bacteria samples were diluted in TSB medium to obtain an of OD$_{600}$ = 0.01. Then, 150 µl of this stock solution from each strain was incubated in 96-well plates or minimum biofilm eradication concentration (MBEC) assay plates coated with hydroxyapatite. Cells were incubated at 37°C for 48 h and the growth medium was changed after 24 h. All the experiments were done in triplicate.

Measurement of minimal bactericidal concentration (MBC)

Different concentrations of MoSe$_2$/PLL/F77 were made by serial dilution. Bacterial cells were grown to OD$_{600}$ of ~0.4 and ~0.33, respectively, and diluted to 10^6 CFU (cell-forming units) ml$^-$

[1] in their respective growth medium. Equal volumes of cell culture and nanomaterial at different concentrations were then added to a 96 deep-well plate. The 96 deep-well plate was then incubated at 37 °C for 2 h. The final cell viability was determined using the microdilution method on agar plates. For MRSA, *A. baumannii and P. aeruginosa* agar plates were incubated for 16 h at 37 °C.

Minimum biofilm eradication concentration (MBEC)

The 96-well plates were used to grow biofilms of MRSA, *A. baumannii and P. aeruginosa* as mentioned above. The biofilms were washed three times with 1x PBS, followed by incubation at different concentrations of $MoSe_2$/PLL/F77 solution. 1x PBS was used as positive control. It was treated for 6 h at 37°C. After treatment, the wells were pipetted gently to mix the biofilm adhered at the bottom of the 96 well plate. The MBEC was calculated using the microdilution method on TSB agar plates. The final cell colonies were counted after 16 h at 37 °C to determine the MBEC.

Biofilm formation assay (crystal violet assay)

Biofilms of MRSA, *A. baumannii*, and *P. aeruginosa* were grown on 96-well plates as described above. MBEC stubs were washed three times in 1x PBS to remove unattached cells. The biofilm was incubated with different concentrations of $MoSe_2$/PLL/F77 solutions at 37°C for 6 h. After incubation, the $MoSe_2$/PLL/F77 solution was discarded, and the 96-well plate was washed with 1x PBS. The plate was then incubated with 150 µl of 0.1% crystal violet (CV) solution and incubated for 30 mins at room temperature. The plate was rinsed and washed with 1x PBS and kept upside down for it to dry out completely for 2-3 h. Each well was treated with 150 µl of 30 % acetic acid for 30 mins at room temperature to dissolve the crystal violet attached to the biomass. Then, 100 µl of the solubilized crystal violet solution was transferred to a new flat bottom plate and absorbance was taken at 550 nm on a microplate spectrophotometer with acetic acid in water as blank.

Metabolic activity (XTT assay)

Biofilms of MRSA, *A. baumannii*, and *P. aeruginosa* were grown on 96-well plates as described above. They were washed 3 times with 1x PBS to remove unattached cells, and then incubated with different concentrations of $MoSe_2$/PLL/F77 solution at 37°C for 4 h. After incubation the $MoSe_2$/PLL/F77 solution was discarded and the 96-well plate was washed with 1x PBS. The

163

plate was then incubated with a 150 µl of 1 mg ml^{-1} solution of XTT salt and 12 µl of 1mM menadione salt at 37°C for 5 hours in dark. The solution from each well was taken individually and centrifuged at 2500 rcf using an Eppendorf 5424 Microcentrifuge to remove any nanomaterial particle or biomass that might have been present in the solution. 100 µl of the supernatant was transferred to a new plate and the absorbance was measured at 490 nm on a microplate spectrophotometer.

S4. Electron microscopy study

Confocal scanning laser microscopy (CSLM)

For biofilm visualization by confocal laser scanning microscopy. Biofilms of MRSA, *A. baumannii*, and *P. aeruginosa* were grown for 48 h on 8-well µ-slides from ibidi. They were incubated with different concentrations of MoSe$_2$/PLL/F77 for 6 h at 37°C. The stains SYTO9 (excitation/emission maxima at 480/500 nm) and propidium iodide (PI, excitation/emission maxima at 490/635 nm) from a LIVE/DEAD BacLight bacterial viability kit were added to treated and untreated (control) biofilms individually. The stained cells were incubated at room for 30 mins followed by imaging. Stained samples were observed with a Nikon C2 confocal scanning laser microscope equipped with argon and He lasers and mounted on a Zeiss Axiovert100 M microscope (Carl Zeiss, Inc.).

Biofilm treatment for scanning electron microscope (SEM):

Biofilms were grown on stubs of MBEC assay plates as mentioned above with gentle shaking at 110 rpm. The stubs were then incubated in a 150 µg ml^{-1} concentration of MoSe$_2$/PLL/F77 solution for the treated samples and 1x PBS for the untreated control sample at 37°C for 4 h. After the incubation, each individual stub was detached from the plate and fixed in 2.5% glutaraldehyde in DPBS for 12 h and kept at 4°C.

SEM imaging:

After fixing the samples in suspension with 2.5% glutaraldehyde in DPBS overnight at 4°C, they were washed in DPBS three times to remove excess cells. The MBEC stubs were then transferred to a solution of 1% osmium tetroxide in DPBS for 30 mins, followed by thorough washing with deionized water. Samples were dehydrated in a graded ethanol series and critical-point dried in a Balzers-Union CPD-020 unit using carbon dioxide as the transition fluid. After mounting on

aluminum stubs, samples were sputter-coated with 10-12 nm of gold-palladium in a Technics Hummer-II unit. Images were generated on a JEOL JSM6300 SEM operated at 15kV and acquired with an IXRF model 500 digital processor.

S5. Biofilm inhibition study

Biofilm growth on pre-coated substrates:

The MBEC assay plate was dipped in 200 µl of $MoSe_2$/PLL/F77 solution at the MBEC concentration for the coated stubs and 1x PBS for the untreated or control stub at 37°C for 48 h. The solution was allowed to dry out, resulting into a uniform coating around the MBEC stubs. It was them washed 3 times in 1x PBS to remove any excess nanomaterial. Then biofilm was grown following the usual protocol as mentioned above. After growing biofilm, it was then washed in 1x PBS and fixed with the help of glutaraldehyde in DPBS. Another set of samples was made by dipping the MBEC stubs in 100 µl of the $MoSe_2$/PLL/F77 to ensure coating of approximately half of the stub, followed by biofilm growth on the entire of the stub. This experiment was performed to demonstrate inhibition of biofilm growth by $MoSe_2$/PLL/F77 coating as well as biofilm growth on the same stub around the untreated area. These samples were then prepared for SEM imaging mentioned above.

Energy dispersive X-ray (EDX) spectroscopy analysis:

The half $MoSe_2$/PLL/F77 coated stubs of MBEC assay plates with biofilm grown on them were prepared for SEM imaging as mentioned above. EDX was carried in an SEM system (XL30 Environmental FEG, FEI) with accelerating voltage at 20kV and spot size of 3 pixels wide (1.2 nm).

Biofilm growth on different samples:

Hydrophilic poly-tetrafluoroethylene (PTFE) films, poly(methyl methacrylate) (PMMA) coated coverslips obtained by spin coating glass coverslips with PMMA five times at 1500 rpm for 60 s, and medical grade titanium alloy (Ti-alloy) cubes were dipped in 300 µl of $MoSe_2$/PLL/F77 solution in 12-well plates. 1x PBS was used for the uncoated or control samples. The samples were incubated at 37°C for 48 h until completely dried out. These coated and uncoated samples were

washed three times with 1x PBS followed by biofilm growth as mentioned above. They were then fixed in 2.5% glutaraldehyde in DPBS and prepared for SEM imaging.

S6. Biocompatibility of coating

Biocompatibility of coatings:

The cytotoxicity of MoSe$_2$/PLL/F77 coatings toward HEK 293 cells was evaluated by alamarBlue assay and LDH assay. Cells were seeded in 24-well microplates at a density of 1 × 10^5 cells ml^{-1} in a 500-μl volume with DMEM medium. After 24 h of cell attachment, the plates were washed with DPBS and the MoSe$_2$/PLL/F77-coated hydrophilic PTFE films were introduced into the DMEM solution. Cells were incubated for 24 h. The wells were washed 3 times with 1x DPBS to remove any unattached cells. To check the viability of the attached cells, they were incubated with 500 μl of 10% alamarBlue solution in DMEM at 37°C for 5 h. The fluorescence intensity was measured at 530 nm (excitation) and 590 nm (emission) using a microplate reader. To determine the cytotoxicity of MoSe$_2$/PLL/F77 through damaged cells, the supernatants from each well were pipetted out into a 96-well plate for the lactate dehydrogenase (LDH) assay. 50 μl of supernatant and 50 μl of reaction mixture were incubated at room temperature for 4 h. The absorbance was measured at 490 nm and 680 nm using a microplate reader. Cell damage was expressed as a relative absorbance relative to that of Triton X-100 as a negative control and DMEM medium as a positive control.
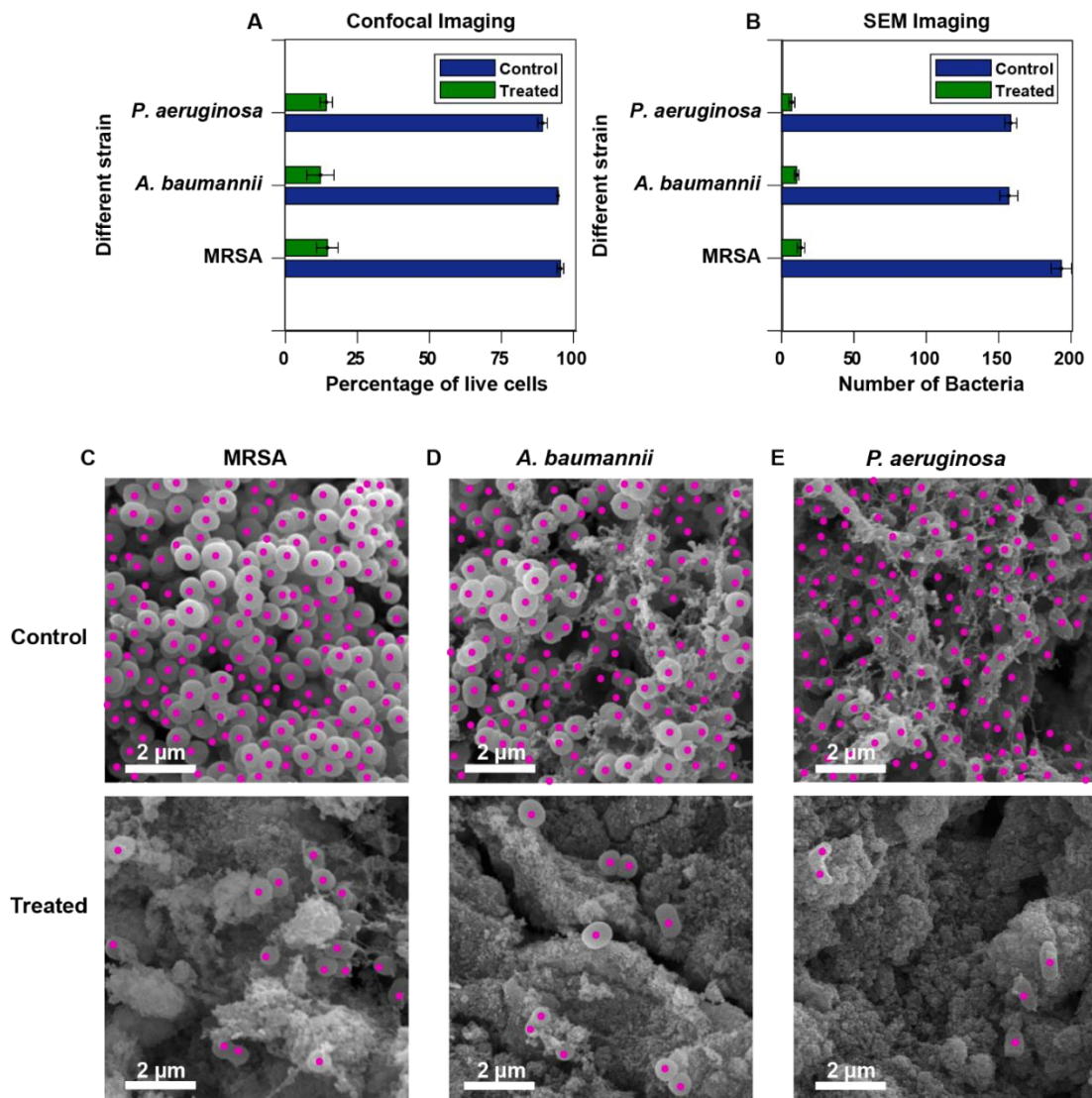
Figure S1: Analysis of effects of MoSe$_2$/PLL/F77 solution on biofilm growth. (A) Percent of live cells present in control samples in comparison to samples treated with MoSe$_2$/PLL/F77 obtained by confocal imaging. (B) Number of cells present before and after treatment with MoSe$_2$/PLL/F77 for 6 h on hydroxyapatite coated MBEC stubs covered with biofilm of different strains. (C-F) Manual counting of bacteria with the help of SEM imaging before and after treatment with MoSe$_2$/PLL/F77 for 6 h on hydroxyapatite coated MBEC stubs covered with MRSA (C), *A. baumannii* (D), and *P. aeruginosa* (E).
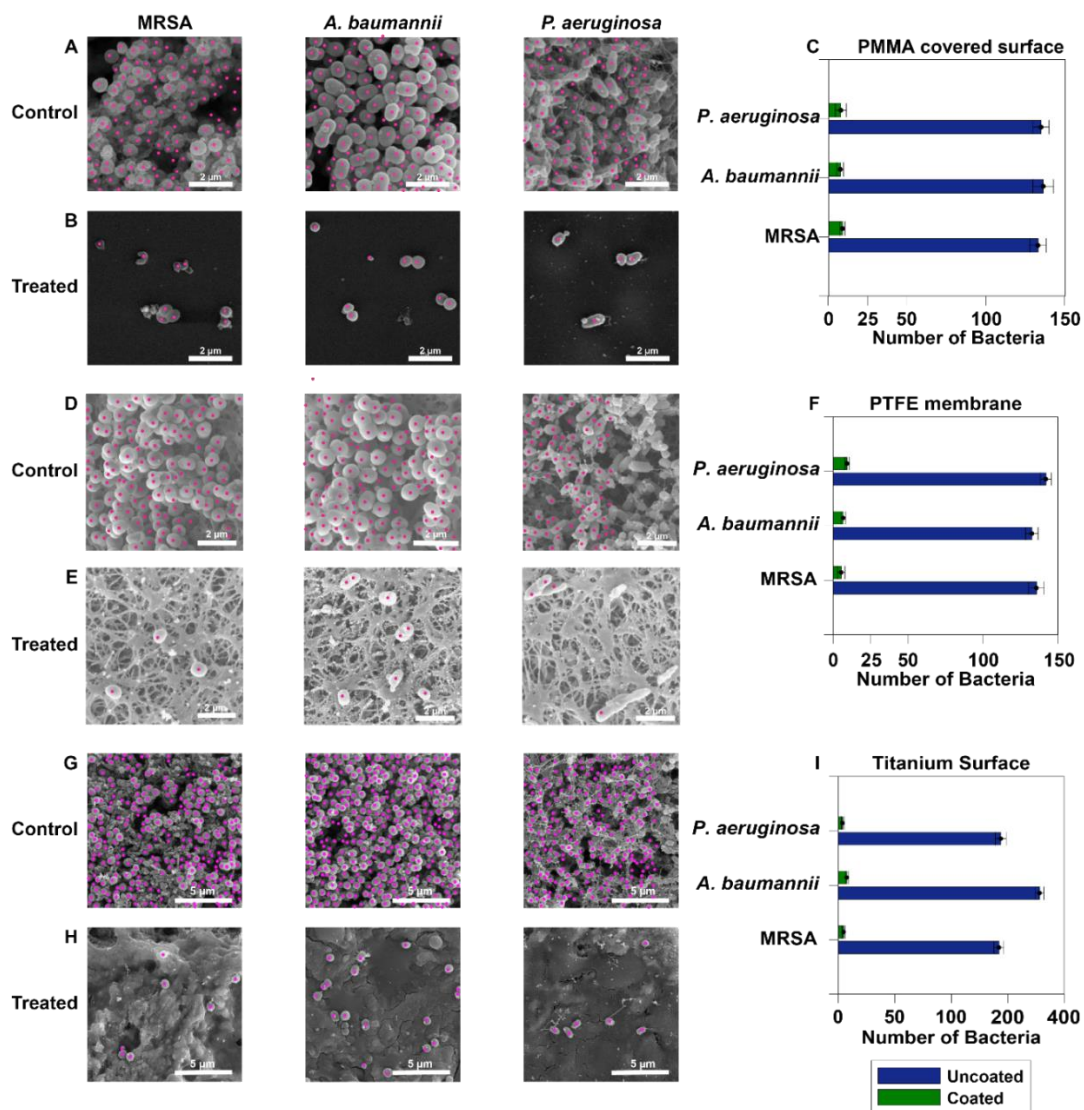
Figure S2: Analysis of inhibition of biofilm growth on different medically relevant surfaces precoated with MoSe₂/PLL/F77. (A-C) Poly(methyl methacrylate) (PMMA) covered glass slides. Manual counting of bacteria with the help of SEM imaging on PMMA surface, uncoated (A) and precoated with MoSe₂/PLL/F77 (B). (C) Bar plot showing number of bacteria cells present on uncoated and coated regions. (D-F) Hydrophilic polytetrafluoroethylene (PTFE) membrane. Manual counting of bacteria with the help of SEM imaging on PMMA surface, uncoated (D) and precoated with MoSe₂/PLL/F77 (E). (F) Bar plot showing number of bacteria cells present on uncoated and coated regions. (G-I) Medical grade titanium alloy (Ti-alloy) surface. Manual counting of bacteria with the

help of SEM imaging on PMMA surface, uncoated (G) and precoated with MoSe$_2$/PLL/F77 (H). (I)

Bar plot showing number of bacteria cells present on uncoated and coated regions.
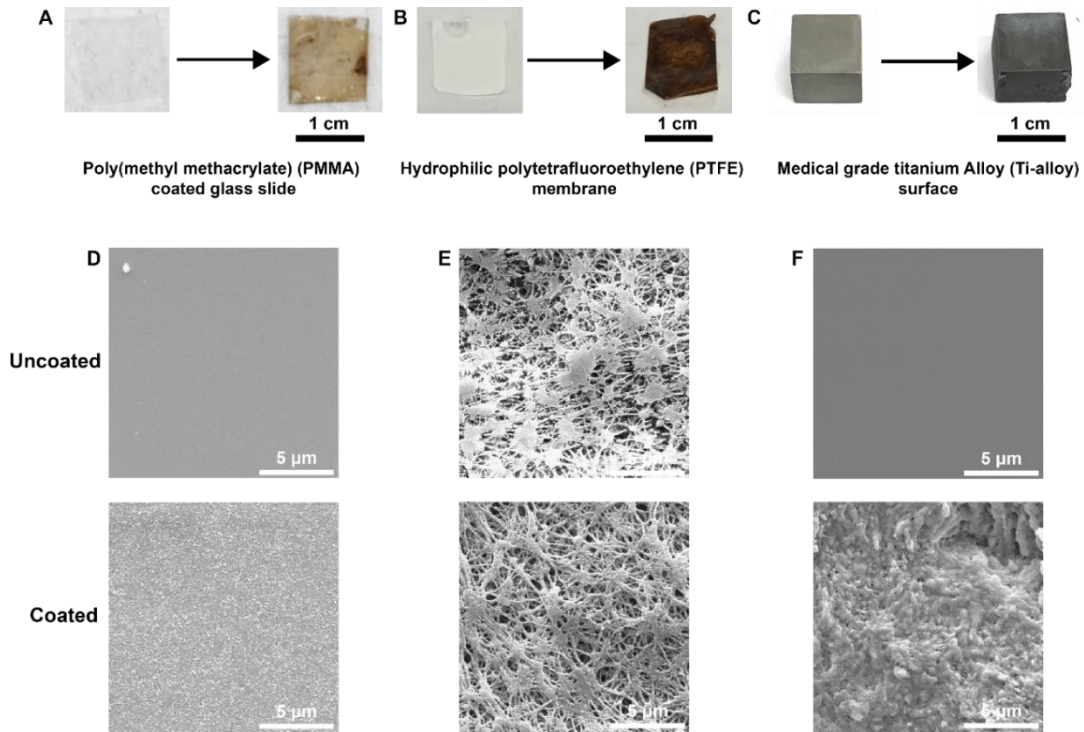
Figure S3: Analysis of different surfaces to grow biofilm on. (A-C) Camera images of different surfaces uncoated (left) and coated (right) with MoSe$_2$/PLL/F77. (A) Confocal images of the MRSA (A), *A. baumannii* (B), and *P. aeruginosa* (C) untreated control films. The surfaces are poly(methyl methacrylate) (PMMA) covered glass slides (A), hydrophilic polytetrafluoroethylene (PTFE) membrane (B) and medical grade titanium alloy (Ti-alloy) surface (C). (D-F) SEM images of surfaces with no coating and coated with MoSe$_2$/PLL/F77. The surfaces are poly (methyl methacrylate) (PMMA) covered glass slides (D), hydrophilic polytetrafluoroethylene (PTFE) membrane (E) and medical grade titanium alloy (Ti-alloy) surface (F).
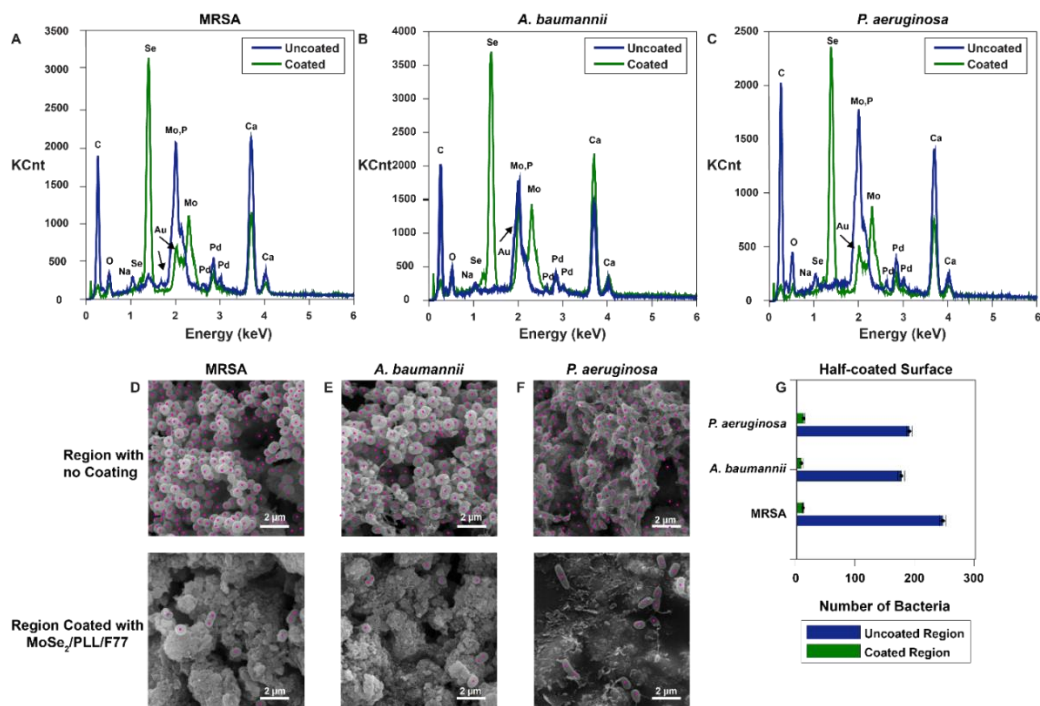
Figure S4: Analysis of inhibition of biofilm growth on MBEC stub half uncoated (top part) and the other half precoated with on MoSe₂/PLL/F77. (A-C) EDX analysis of half-coated MBEC stub with MoSe₂/PLL/F77 showing the absence and presence of Mo and Se elements on uncoated and coated region with MRSA (A), *A. baumannii* (B), and *P. aeruginosa* (C). (D-F) Manual counting of bacteria on SEM images at regions with no coating and coating with MoSe₂/PLL/F77 on the same MBEC stubs with MRSA (D), *A. baumannii* (E), and *P. aeruginosa* (F). (G) Number of cells present on the uncoated region against the coated region on the same MBEC stub for different strains.

Table S1. Percentage inhibition of biofilm on different surfaces.

Different Surfaces	Percentage inhibition of biofilm growth		
	MRSA	***A. baumannii***	***P. aeruginosa***
MBEC assay with Hydroxyapatite coated stubs	93.10	93.42	95.58
PMMA coated glass slides	93.46	94.60	94.30
PTFE membrane	96.06	94.97	93.42
Ti-alloy	96.71	95.69	97.33

Half-coated hydroxyapatite stubs	95.91	95.80	94.15

Table S2. Atomic percent of elements present on uncoated region against region coated with MoSe$_2$/PLL/F77 on the same hydroxyapatite stub.

Elements	Uncoated Region			Coated Region		
	MRSA	*A. baumannii*	*P. aeruginosa*	MRSA	*A. baumannii*	*P. aeruginosa*
Carbon (C)	76.53	74.59	80.36	45.05	39.95	40.93
Oxygen (O)	11.5	9.36	9.64	10.79	9.35	7.22
Sodium (Na)	0.76	0.71	0.69	0	0.76	0
Phosphorous (P)	4.5	5.05	3.26	7.19	5.93	5.58
Calcium (Ca)	4.85	7.03	2.88	11.86	10.66	8.97
Selenium (Se)	**0.02**	**0.28**	**0**	**15.82**	**21.15**	**7.42**
Molybdenum (Mo)	**0**	**0**	**0**	**6.24**	**8.11**	**7.52**
Palladium (Pd)	0.74	0.92	0.87	1.22	1.82	1.37
Gold (Au)	1.06	1.22	1.26	1.83	2.1	1.99

Table S3. Comparison of efficacy of different nanomaterials against biofilms.

Drug or Antibiofilm Agent	Microbe Strain	Dosage	Anti-biofilm Assay	Incubation Time	Percent Inhibition	Year	Ref.
Zinc oxide particle (ZnO) of diameter 12 nm	*S. aureus*	30% (wt/vol%)	Colony counting method	24 h	87	2013	42
Chitosan (CS)-molybdenum disulfide (MoS$_2$) nanosheets-tetracycline hydrochloride	*S. aureus*	80 µg/ml	Crystal violet (CV) staining assay	16-18 h	>80	2017	40

drugs (CM-TH)							
CM-TH	*Salmonella*	80 µg/ml	CV staining assay	16-18 h	>80	2017	40
Graphene quantum dots (GQDs)	*S. aureus*	500 µg/ml	Biofilm mass	24 h	48.85	2018	41
Graphene oxide (GO)	*S. aureus*	50 µg/ml	Safranin staining	24 h	20.16	2018	39
GO	*P. aeruginosa*	50 µg/ml	Safranin staining	24 h	10.22	2018	39
Poly(oxanorborneneimide)-stabilized oil-in-water nanocomposites (X-BNCs)	*P. aeruginosa*	16%	Coculture model and colony counting method	3 h	99.5	2018	45
dextran-block-poly((3-acrylamidopropyl) trimethylammonium chloride (AMPTMA)-co-butylmethacrylate (BMA)) (DA95B5)	MRSA	32 µg/ml	MBEC assay	18-24 h	99	2018	46
DA95B5	Vancomycin-resistant *E. faecalis* (VRE)	512 µg/ml	MBEC assay	18-24 h	99.68	2018	46
Quaternary ammonium poly(oxanorborneneimides) (PNPs)	*P. aeruginosa*	900 nM	Alamar Blue assay	3 h	90	2018	32
PNPs	MRSA	1500 nM	Alamar Blue assay	3 h	90	2018	32
Graphene oxide–silver nanoparticles (GO–AgNPs)	*P. aeruginosa*	25 µg/ml	Confocal Assay	12 h	98	2018	39

Polyethylenei mine (PEI)-modified and AgNP-decorated GO nanocomposit e (GO−PEI−Ag)	*E. coli*	10 µg/ml	CV staining assay	2.5 h	~89.96	201 8	44
GO-PEI-Ag	*S. aureus*	10 µg/ml	CV staining assay	2.5 h	~93.45	201 8	44
Ultra-high molecular weight (uHMW) poly(N,N-dimethylacryla mide) (PDMA)	*S. aureus*	2 mg/ml (dopamin e) + 10 mg/ml (PDMA)	Flowcyt ometry	48 h	>99.3	201 8	47
Molybdenum disulfide-penicillin-near infrared (MoS$_2$-Pen-NIR)	*S. aureus*	0.171 mg/ml (MoSe$_2$) + 0.366 mg/ml (Pen)	Colony counting method	6 h	~86.15	201 8	49
MoS$_2$-Pen-NIR	*E. coli*	0.171 mg/ml (MoSe$_2$) + 0.366 mg/ml (Pen)	Colony counting method	6 h	~84.05	201 8	49
Lanthanum hydroxide and graphene oxide nanocomposit es (La@GO)	*E. coli*	500 µg/ml	Colony counting method	2 h	100	201 9	94
CS-MoS$_2$	*S. aureus*	225 µg/ml	Resazur in reductio n test	24 h	80	201 9	87
MoS$_2$ surfaces (MoS$_{2SUR}$) produced using MoS$_2$ particle (MoS$_{2PAR}$)	*S. aureus*	20%	CV staining assay	24 h	28.5	202 0	94
MoS$_{2SUR}$ produced using MoS$_{2PAR}$	*P. aeruginosa*	20%	CV staining assay	24 h	34.8	202 0	94

173

MoSe$_2$/PLL/F77	MRSA	150 µg/ml	MBEC assay	6 h	100	2021	This work
MoSe$_2$/PLL/F77	*A. baumannii*	150 µg/ml	MBEC assay	6 h	100	2021	This work
MoSe$_2$/PLL/F77	*P. aeruginosa*	150 µg/ml	MBEC assay	6 h	100	2021	This work

APPENDIX C

SUPPLEMENTAL MATERIAL FOR CHAPTER 4

Eradication of Fungi Using MoSe$_2$/Chitosan Nanosheets

Sanchari Saha,[1,2] Matthew S. Gilliam,[1,2] Qing Hua Wang,[3*] and Alexander A. Green[1,2,4*]

1. Biodesign Center for Molecular Design and Biomimetics, The Biodesign Institute, Arizona State University, Tempe, Arizona 85287, United States

2. School of Molecular Sciences, Arizona State University, Tempe, Arizona 85287, United States

3. Materials Science and Engineering, School for Engineering of Matter, Transport and Energy, Arizona State University, Tempe, Arizona 85287, United States

4. Department of Biomedical Engineering, Boston University, Boston, MA 02215, United States

* Corresponding author: alexgreen@bu.edu, qhwang@asu.edu

Table of contents

S1. Materials and supplies

S2. Preparation and characterization of MoSe$_2$/Chitosan (CS) dispersions

S3. Fungal cell preparation and antifungal assay

S4. Biocompatibility study

S5. Mechanistic study

S6. Supplementary information

S1. Materials and supplies

Chemicals

Molybdenum (IV) selenide (MoSe$_2$, -325 mesh, 99.9% trace metals basis, item number: 778087), low molecular weight chitosan (LMW CS) (50,000-190,000 Da, 75-85% deacetylated, item number: 448869), phosphate buffer saline solution (PBS, pH 7.4), Dulbecco's phosphate buffered saline (DPBS), potato dextrose broth (PDB) medium, PDB agar, Dulbecco's modified Eagle's medium (DMEM), trypsin-EDTA, poly-L-lysine, and propidium iodide (PI) were purchased from Sigma-Aldrich. Glacial acetic acid, yeast malt (YM) broth, YM agar, glutaraldehyde solution (25% in H$_2$O) were purchased from Thomas Scientific Holdings LLC. Difco Sabouraud dextrose broth (SDB) medium and Difco SDB agar were purchased from Spectrum Chemical Mfg. Corp. Human embryonic kidney 293 cells (HEK293) were purchased from ATCC. Whole red blood cells (RBCs) from a single donor were purchased from Innovative Research. The alamarBlue reagent cell proliferation assay was purchased from G-Biosciences. Acetone and ethanol were purchased from VWR. Osmium tetroxide (OsO$_4$, 98% purity) was purchased from Combi-Blocks Inc. Concavalin A, Alexa Fluor 488 conjugate (ConA), Invitrogen FUN 1 cell stain (Fun 1) and Invitrogen (Bis-(1,3-Dibutylbarbituric Acid) Trimethine Oxonol) (DiBaC$_4$) were purchased from Thermo Fisher Scientific.

Fungal strains

Issatchenkia orientalis (*I. orientalis*, ATCC 6258), *Saccharomyces cerevisiae* (*S. cerevisiae*, ATCC 9763), *Candida parapsilosis* (*C. parapsilosis*, ATCC 22019), *Candida albicans* (*C. albicans*, ATCC 76485), *Cryptococcus neoformans* (*C. neoformans*, ATCC 208821), *Cryptococcus gattii* (*C. gattii*, ATCC MYA-4071), *Aspergillus fumigatus* (*A. fumigatus* ATCC, MYA-4609), *Fusarium verticillioides* (*F. verticillioides,* ATCC MYA-3629) *and Fusarium falciforme* (*F. falciforme*, ATCC MYA-3636) were purchased from ATCC. The *Candida auris* panel including *Candida auris* (*C.* auris, 0386), *C. auris* (0388), *C. auris* (0389), *Candida duobushaemulonii* (*C. duobushaemulonii*, 0394), *Candida haemulonii* (*C. haemulonii*, 0395), *Krusei ohmeri* (*K.* ohmeri, 0396), *Candida krusei* (*C. krusei,* 0397), *Candida lusitaniae* (*C. lusitaniae*, 0398) and

Saccharomyces cerevisiae (*S. cerevisiae*, 0399) were obtained from the CDC & FDA Antibiotic Resistance (AR) Isolate Bank.

S2. Preparation of MoSe$_2$/Chitosan (CS) dispersions and characterization

Preparation of MoSe$_2$/Chitosan (CS) dispersions

A 0.5% (w/v) solution of chitosan (CS) was made by dissolving the solid polymer in 1% acetic acid. 500 mg of bulk MoSe$_2$ powder was ultrasonicated in 20 ml of the 0.5% CS solution for 2 h at 25 W power using a 1/8" microtip probe in a Branson Digital Sonifier SFX 550. The sonicated sample was centrifuged at 5,000 rcf for 10 min followed by centrifuging at 21,000 rcf for 5 min using an Eppendorf 5424 Microcentrifuge with a fixed angle (45°) rotor. The supernatant was then collected for subsequent experiments. For control experiments, a 0.5% CS solution was sonicated and centrifuged following the same protocol but without any MoSe$_2$. The concentration of MoSe$_2$ was calculated with the help of inductively coupled plasma mass spectrometry (ICP-MS). Liquid dispersions for ICP-MS analysis were first acidified in nitric acid overnight and diluted to a final nitric acid concentration of 2 wt%. The samples were then analyzed by a Thermo Fisher iCap Q quadrupole instrument.

Optical characterization and electron microscopy

Absorbance (UV-Vis) spectra for the dispersed 2D MoSe$_2$/CS were acquired using a Jasco V-670 Spectrophotometer using a quartz cell with a path length of 1.0 cm. TEM samples were prepared by drop-casting 10 µl of dilute MoSe$_2$/CS dispersion on a holey carbon grid and dried with edge of filter paper followed by washed with water and the same drying process. Images were acquired on a Philips CM-12 TEM operated at 80 kV with the help of a Gatan model 791 CCD camera.

S3. Fungal cell preparation and antifungal assay

Fungal cell preparation

Overnight cultures of *I. orientalis*, *S. cerevisiae* and *C. parapsilosis* were grown in YM broth at 30°C. *C. albicans*, *C. neoformans* and *C. gattii* were grown in SDB medium at 30°C for 16 h. *A.*

fumigatus, *F. falciforme* and *F. verticillioides* were grown in the PDB medium at 26°C for 48 h. They were grown to mid-exponential growth phase with 0.4 optical density (OD) at 600 nm. Cells were centrifuged at 2,500 rpm for 5 min and the pellets were washed with 1x phosphate buffered saline (PBS). The final pellet was resuspended in their respective growth medium and OD_{600} was measured. Cells were then diluted to 10^7 colony forming units per milliliter (CFU ml^{-1}). All experiments were performed in triplicate.

Measurement of minimum fungicidal concentration (MFC)

MFC values against different fungal strains were determined using varying concentrations of MoSe$_2$/CS. The fungal cell samples were diluted 100-fold in medium and allowed to grow until they reached OD_{600} = 0.4 while shaking at 250 rpm. After washing and redispersion, fungal cultures were incubated with different concentrations of MoSe$_2$/CS nanomaterials (1.56 to 150 µg ml^{-1}) for 3 h. After incubation, fungi were plated in agar plates using the serial dilution method and allowed to grow overnight to enable counting of the surviving colonies. All the experiments were done in triplicate.

Measurement of minimum inhibitory concentration (MIC)

MIC values of MoSe$_2$/CS were determined using varying concentrations of nanomaterials, including the MFC value for each fungal strain. 100 µl of the fungal cell culture at a concentration of 10^5 CFU ml^{-1} and 100 µl of MoSe$_2$/CS were incubated together at 30°C in a 96-well plate in their respective growth media while shaking at 250 rpm. The OD of each well at 600 nm were measured and recorded as a function of time using a microplate reader for 24 h at 30 min intervals. Negative controls containing cells without MoSe$_2$/CS were measured in parallel. OD measurements were plotted for each MoSe$_2$/CS concentration to determine the lowest concentration at which the optical density reading remained constant, indicating full inhibition of cell growth over time. This concentration is defined as the MIC. All experiments were performed in triplicate.

S4. Biocompatibility study

Mammalian cell viability of MoSe$_2$/CS

The cytotoxicity of MoSe$_2$/CS toward human embryonic kidney 293 cells (HEK293) cells was evaluated by alamarBlue and cell counting assays (CCK-8). Cells were seeded in 96-well microplates at a density of 1×10^5 cells ml^{-1} in a 200-µl volume with DMEM medium. After 24 h of cell attachment at 37°C in presence of 5% CO$_2$, the plates were washed with DPBS and the MoSe$_2$/CS at different concentration were incubated with the mammalian cells for 3 h at 37°C in presence of 5% CO$_2$. Then, the wells were washed three times with 1x DPBS to remove any unattached cells. To check the viability of the attached cells, they were incubated with 200 µl of 10% (v%) alamarBlue solution in DMEM at 37°C in presence of 5% CO$_2$ for 5 h. The fluorescence intensity (FI 590) was measured at 530 nm (excitation) and 590 nm (emission) using a microplate reader. Cell damage was expressed as the fluorescence relative to that of DMEM medium alone as a control sample.

Similarly, XTT assays were also performed to check the biocompatibility of MoSe$_2$/CS against HEK293 cells. A 10 v% CCK-8 solution was added to the treated and washed mammalian cells to reach a 200-µl total volume, followed by 2 h incubation at 37°C in the presence of 5% CO$_2$. After incubation with the CCK-8 solution, 180 µl of supernatant was collected in a fresh 96-well microplate and absorbance at 450 nm was collected using a microplate reader. Mammalian cells treated with just DMEM without any MoSe$_2$/CS were measured as control samples. The absorbance of DMEM was subtracted from all the above values as blank. All the experiments were performed in triplicate.

The percentage difference in reduction between treated and control cells in the alamarBlue cytotoxicity assay was calculated using the formula:

$$\% \, Biocompatibility = \frac{FI \, 590 \, (treated \, sample)}{FI \, 590 \, (control \, sample)} \times 100 \tag{1}$$

Where, FI 590 (treated sample) and FI 590 (control sample) are the fluorescence intensity obtained at 590 nm emission and 530 nm excitation for the treat and control samples, respectively.

The percentage of viable cells in the cell counting proliferation assay was calculated using the formula:

$$\% \ Cell \ Viability = \frac{Abs \ (treated \ sample)}{Abs \ (control \ sample)} \times 100 \qquad (2)$$

Where, Abs (treated sample) and Abs (control sample) are the absorbance at 450 nm of the treated and control samples, respectively.

Hemolysis assay

Fresh single-donor human red blood cells (RBCs) were diluted 1:20 in PBS (pH 7.4), pelleted by centrifugation (1,000 rcf, 10 min), and washed three times in PBS. The RBCs were counted using a cell counter and diluted to a final concentration of 2×10^7 cells ml^{-1}. Equal volumes of RBCs were incubated with varying concentrations of MoSe$_2$/CS in a 96-well plate in a humidified atmosphere containing 5% CO$_2$ at 37 °C for 3 h. Following incubation, the 96-well plate was centrifuged (1,000 rcf, 10 mins) and 100 µl of supernatant were transferred to a black 96-well plate. Hemoglobin release upon lysis of the RBCs was monitored through the optical absorbance at 405 nm (Abs) using a microplate reader. Positive and negative controls for hemolysis were taken as RBCs lysed with 1% Triton X-100 (1:1 vol/vol) and RBC suspension in PBS, respectively. The percent hemolysis was plotted against nanomaterial concentration, and the experiment was performed in triplicate.

The percentage of hemolysis was calculated using the formula:

$$\% \ Hemolysis = \frac{Abs \ (treated \ sample) - Abs \ (negative \ control)}{Abs \ (positive \ control) - Abs \ (negative \ control)} \times 100 \qquad (3)$$

S5. Mechanistic study

Electron microscopy of fungal cell morphology

For transmission electron microscopy (TEM) imaging, samples treated by MoSe$_2$/CS and control samples were initially fixed in a suspension with 2.5% glutaraldehyde in Dulbecco's phosphate buffered saline (DPBS) overnight at 4°C, followed by washing in DPBS. Cells were then placed into a drop of 1% agarose on a glass slide and treated with 1% osmium tetroxide (OsO$_4$) in DPBS for 1 h, washed thoroughly with deionized water, and dehydrated in a graded acetone series (20%, 40%, 60%, 80% and 100%). Spurr's epoxy resin was used to infiltrate and embed the samples. 70-nm-thick sections were cut on a Leica Ultra cut-R microtome followed by post-staining

with uranyl acetate and lead citrate. Images were generated on a Philips CM-12 TEM operated at 80 kV and acquired with a Gatan model 791 CCD camera. For scanning electron microscopy (SEM) imaging, cells were initially fixed and washed following the same method used for TEM samples. Washed cells were then concentrated into a small volume of DPBS and applied to poly-L-lysine (PLL)-coated coverslips for 10 min. Excess cells were removed by briefly rinsing in DPBS and the coverslips were transferred to a solution of 1% OsO_4 in DPBS for 1 h at room temperature, followed by thorough washing with deionized water. Samples were dehydrated in a graded ethanol series (20%, 40%, 60%, 75%, 90% and 100%) and critical-point dried in a Balzers-Union CPD-020 unit using carbon dioxide as the transition fluid. After routine mounting on aluminum stubs, samples were sputtered-coated with 10-12 nm of gold-palladium in a Technics Hummer-II unit. Images were generated on a JEOL JSM6300 SEM operated at 15 kV and acquired with an IXRF model 500 digital processor.

Confocal scanning laser microscopy (CSLM)

For fungal cell visualization by CSLM, fungal cells of *C. albicans* (unicellular) and *A. fumigatus (*filamentous) were grown overnight and then diluted in SDB medium to 3 x 10^7 CFU ml^{-1} and transferred to 4-well µ-slides from ibidi. They were incubated with different concentrations of $MoSe_2$/CS for 3 h at 30°C. At the end of incubation, each sample was incubated for 30-35 min at 30°C with fluorescent stain mixture containing 1 µl ml^{-1} of FUN-1 cell stain (Fun 1) and 5 µl ml^{-1} solution of concavalin A-Alexa Fluor 488 conjugate (ConA) in PBS. The stained cells were then imaged. FUN 1 (excitation at 543 nm and emission at 560 nm long-pass filter) is converted to orange-red intravacuolar structures by metabolically active cells, while ConA (excitation wavelength at 488 nm and emission at 505 nm long-pass filter) binds to glucose and mannose residues of cell wall polysaccharides with green fluorescence. Stained samples were observed with a Nikon C2 confocal scanning laser microscope equipped with argon and He lasers and mounted on a Zeiss Axiovert100 M microscope (Carl Zeiss, Inc.).

Membrane integrity and membrane polarization

Evaluation of the antifungal mechanism of MoSe$_2$/CS was determined using flow cytometric assays. For the analysis of membrane permeabilization, overnight cultures of *C. albicans* were diluted in the SDB medium to 3 x 10^7 CFU ml^{-1}. Aliquots of the fungal suspension were then incubated with or without MoSe$_2$/CS nanosheets at 37°C for 3 h. At the end of the incubation time, the fungal suspensions were incubated in the dark for 60 min at 37°C with bis-(1,3-dibutylbarbituric acid) trimethine oxonol (DiBAC$_4$) at a final concentration of 1 M, to evaluate changes in the transmembrane potential. To monitor modifications in membrane integrity following treatment with the MoSe$_2$/CS, a filtered solution of propidium iodide (PI) at a final concentration of 10 g ml^{-1}, was incubated for 60 min at 37°C with each sample. An untreated sample of fungal cells pelleted and resuspended in cold absolute ethanol for 30 min at -20°C was used as a positive control for permeabilization. After centrifugation at 1000 *g* for 10 min, the ethanol was removed by aspiration, the pellet was suspended in SDB medium, and the PI was added as described above. The fluorescence intensity of all samples was detected with a Stratedigm A600 HTAS cytometer equipped with an argon laser (488 nm, 5 mW) and using a photomultiplier tube fluorescence detector for green (525 nm) or red (610 nm) filtered light. The detectors were set on logarithmic amplification. Optical and electronic noise were eliminated by setting an electronic gating threshold on the forward scattering detector, while the flow rate was kept at a data rate below 200 events/second to avoid measurements of more than one cell at a time. For each sample, at least 20,000 events were acquired. All the experiments with the fluorescent probes were conducted in triplicate. The percentage of cells depolarized and disintegrated were calculated by comparing number of events in positive control sample as compared to the treated and negative control samples.

S6. Supplementary information
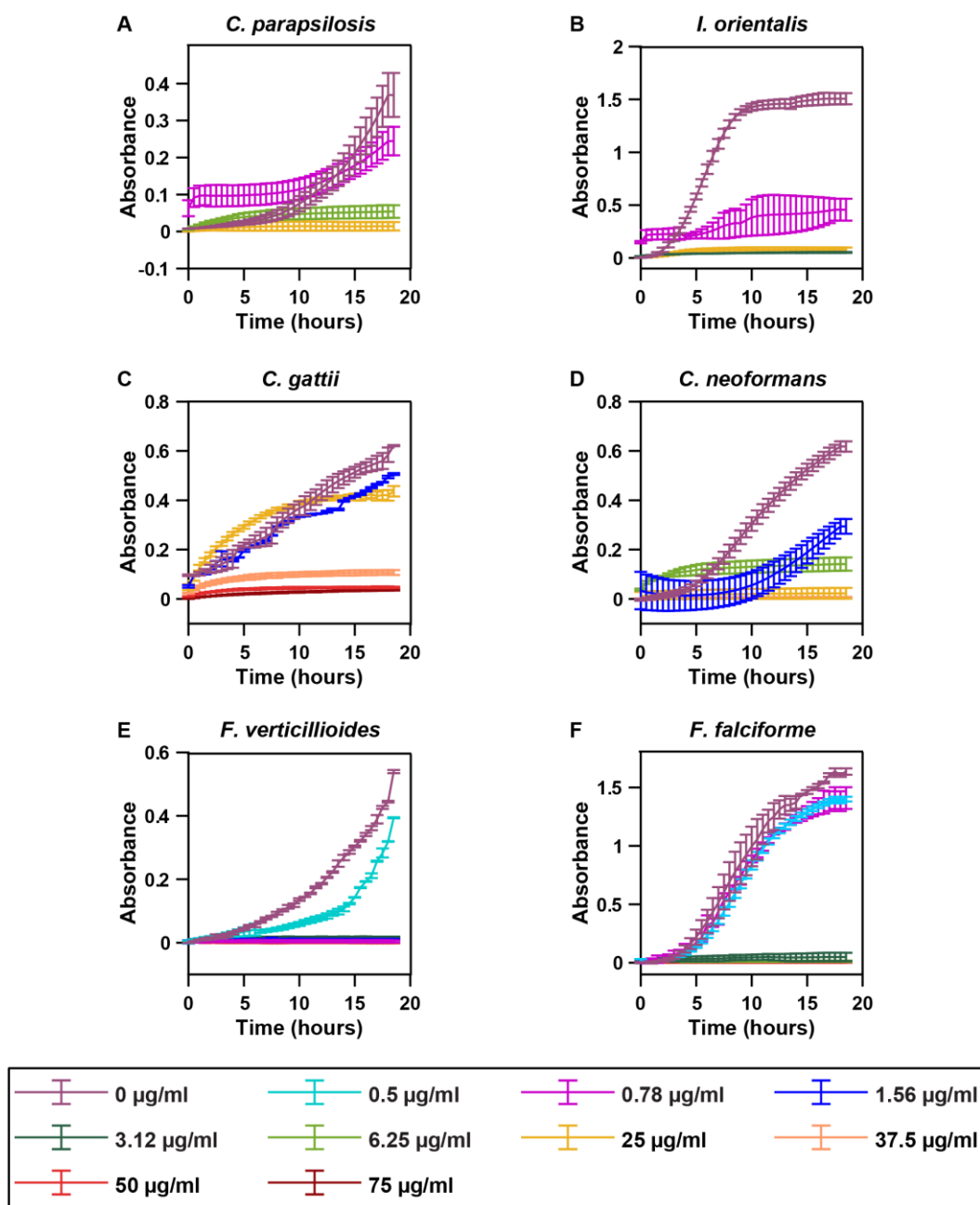
Figure S1: Antifungal efficiency of MoSe$_2$/CS against unicellular and filamentous fungi. (A-F) Time-course measurements of absorbance at 600 nm used for MoSe$_2$/CS MIC determination.

(A, B) The MIC of BSL-1 fungi *C. parapsilosis* and *I. orientalis is* 0.78 µg ml^{-1}. (C, D) The MIC of BSL-2 fungi *C. gattii*, and *C. neoformans* is 25 µg ml^{-1} and 1.56 µg ml^{-1}. (E, F) The MIC for BSL-2 filamentous fungi *F. verticillioides* is 0.5 µg ml^{-1} and *F. falciforme* is 0.78 µg ml^{-1}.
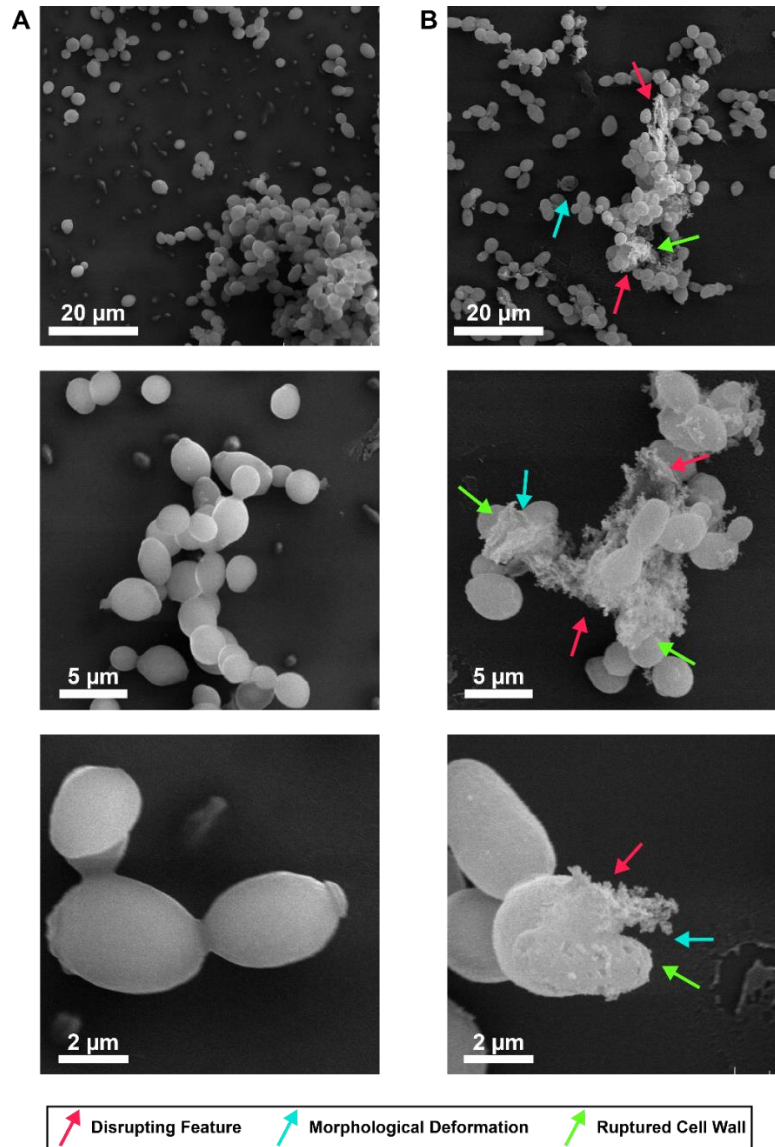
Figure S2: Multimodal killing mechanism of MoSe$_2$/CS against *C. albicans*. (A) SEM images of healthy control cells of *C. albicans* at different magnifications. (B) SEM images of cells treated with MoSe$_2$/CS at different magnifications showing disruptive features (**red arrows**), morphological deformation (**light blue arrows**) and broken outer membranes (**green arrows**).
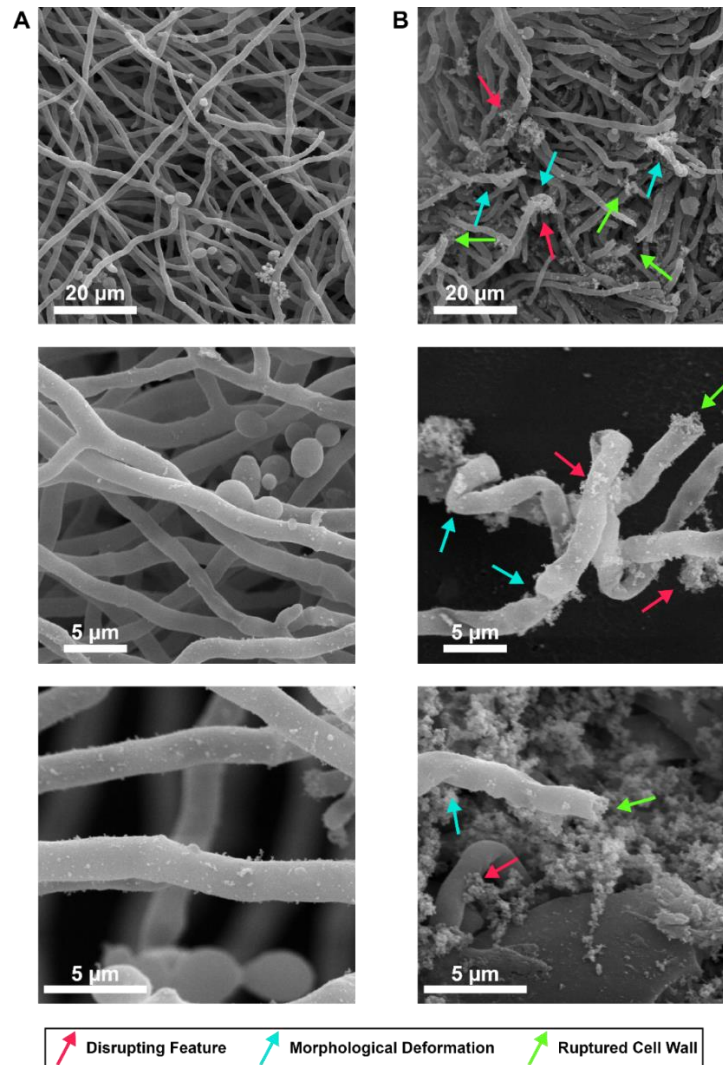
Figure S3: Multimodal killing mechanism of MoSe$_2$/CS against *A. fumigatus*. (A) SEM images of healthy control cells of *C. albicans* at different magnifications. (B) SEM images of cells treated with MoSe$_2$/CS at different magnifications showing disruptive features (**red arrows**), morphological deformation (**light blue arrows**) and broken outer membranes (**green arrows**).
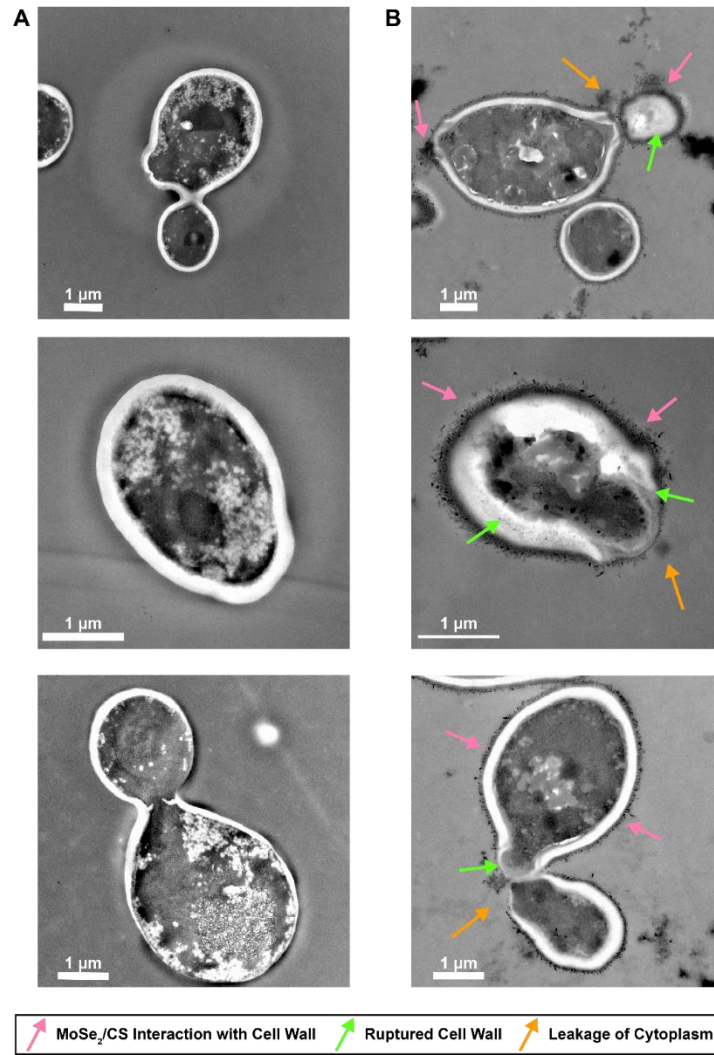
Figure S4: Multimodal killing mechanism of MoSe$_2$/CS against *C. albicans*. (A) TEM images of healthy control cells of *C. albicans*. (B) TEM images of cells treated with MoSe$_2$/CS showing sharp edges of MoSe$_2$ flakes interacting with cell wall (**pink**) leading to rupturing of cell wall (**green**) and cytoplasmic leakage (**orange**).
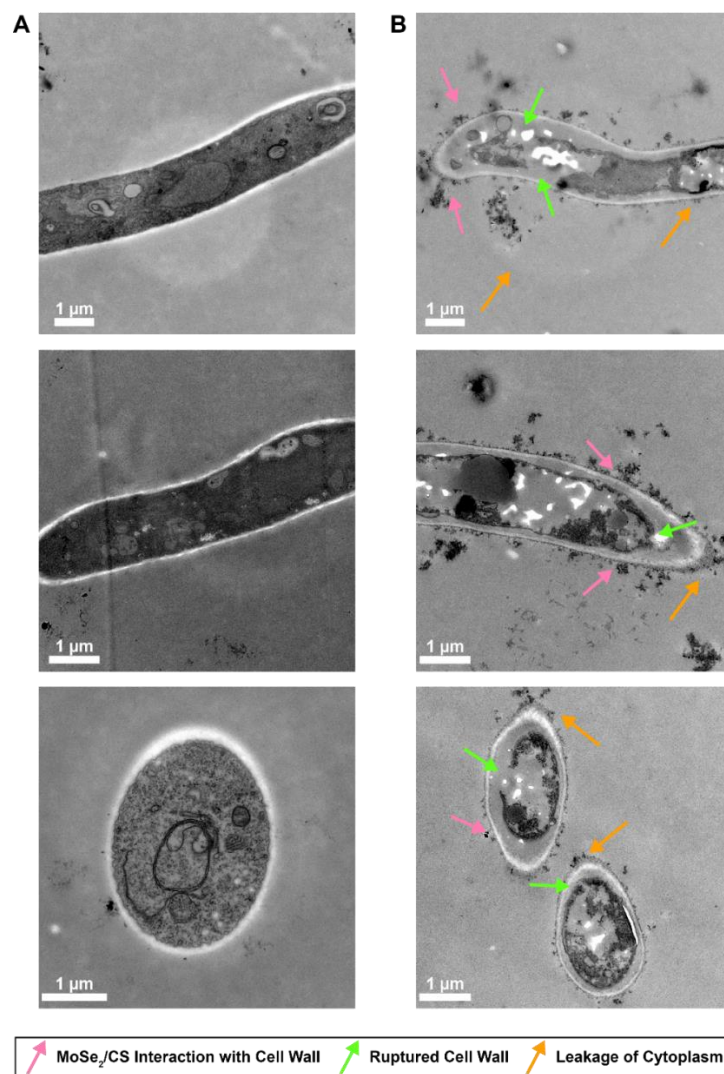
Figure S5: Multimodal killing mechanism of MoSe$_2$/CS against *A. fumigatus*. (A) TEM images of healthy control cells of *C. albicans*. (B) TEM images of cells treated with MoSe$_2$/CS showing sharp edges of MoSe$_2$ flakes interacting with cell wall (**pink**) leading to rupturing of cell wall (**green**) and cytoplasmic leakage (**orange**).
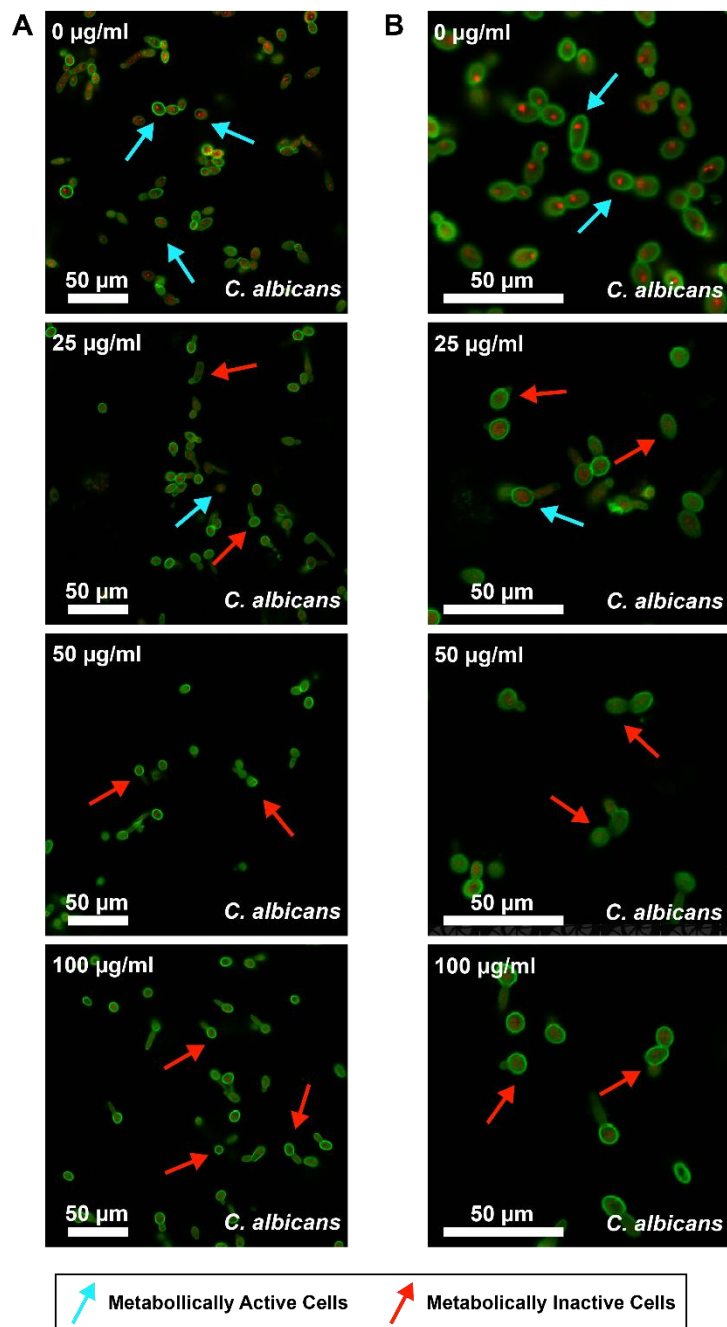
Figure S6: Confocal scanning laser microscopy (CSLM) of *C. albicans*. The green structures (Concanavalin A, Alexa Fluor 488 Conjugate) represent the fungal cell wall and the red structures (FUN 1 Cell Stain) are metabolically active cytoplasm. The viable cells have red fluorescent nuclei (**blue arrows**) and the absence of red aggregates signifies metabolically inactive cells (**red arrows**). (A) *C. albicans* (unicellular) cells after treatment with MoSe$_2$/CS at 0 µg ml^{-1} (negative

control), 25 µg ml^{-1}, 50 µg ml^{-1}, and 100 µg ml^{-1} after 3 h incubation. (B) Zoomed in images of *C. albicans* (unicellular) cells after treatment with MoSe$_2$/CS for 0 µg ml^{-1} (negative control), 25 µg ml^{-1}, 50 µg ml^{-1}, and 100 µg ml^{-1} after 3 h incubation.
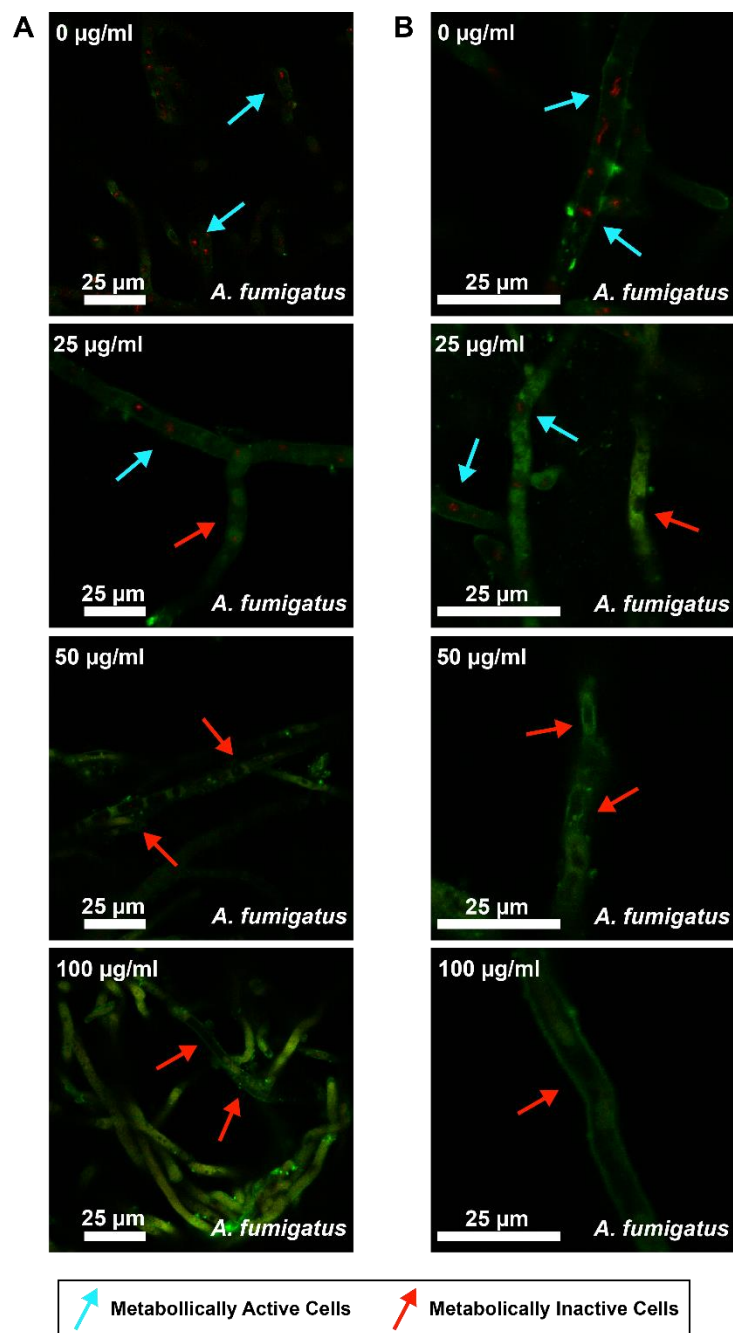
Figure S7: Confocal scanning laser microscopy (CSLM) of *A. fumigatus*. The green structures (Concanavalin A, Alexa Fluor 488 Conjugate) represent the fungal cell wall and the red structures (FUN 1 Cell Stain) are metabolically active cytoplasm. The viable cells have red fluorescent nuclei (**blue arrows**) and the absence of red aggregates signifies metabolically inactive cells (**red arrows**). (A) *A. fumigatus* (unicellular) cells after treatment with MoSe$_2$/CS for 0 μg ml^{-1} (negative

control), 25 µg ml^{-1}, 50 µg ml^{-1}, and 100 µg ml^{-1} after 3 h incubation. (B) Zoomed in images of *A. fumigatus* (unicellular) cells after treatment with MoSe$_2$/CS for 0 µg ml^{-1} (negative control), 25 µg ml^{-1}, 50 µg ml^{-1}, and 100 µg ml^{-1} after 3 h incubation.
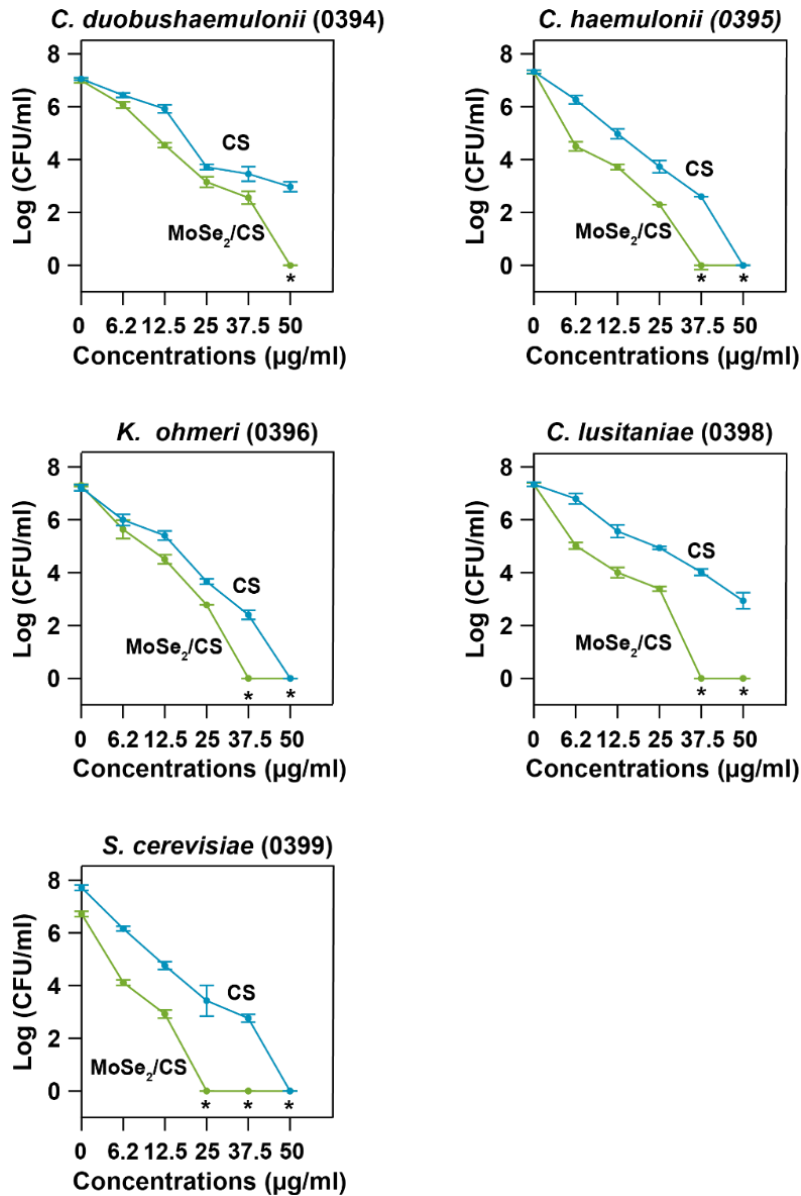
Figure S8: Antifungal efficiency of MoSe$_2$/CS against *Candida auris* (*C. auris*) panel. CFUs at different concentrations were used to determine MFC values of a BSL2 *C. auris* panel including (A) *C. duobushaemulonii* (0394), (B) *C. haemulonii* (0395), (C) *K. ohmeri* (0396), (D) *C. lusitaniae* (0398) and (E) *S. cerevisiae* (0399) was determined to be 50 µg ml^{-1}, 37.5 µg ml^{-1}, 37.5 µg ml^{-1},

37.5 µg ml^{-1} and 25 µg ml^{-1} respectively, using the microdilution method. * indicates complete

eradication of fungal cells.

Table S1. Comparison of efficacy of antifungal agents against different fungal strains.

Drug or Antifungal Agent	Fungal Strain	Dosage (µg/ml)	Antifungal Assay	Incubation Time	Killing Efficiency	Year	Ref.
fCNT-AMB	*C. albicans*	80	MIC	4 h	99.9%	2012	47
fCNT-AMB	*C. neoformans*	20	MIC	4 h	99.9%	2012	47
LMW CS (10 kDa) Water soluble	*C. albicans*	<40	MIC	24 h	-	2008	52
LMW CS (10 kDa) Water soluble	*C. albicans*	<40	MIC	24 h	-	2008	52
LMW CS (10 kDa) Water soluble	*C. albicans*	<40	MIC	24 h	-	2008	52
MoS$_2$-CS	*Saccharomyces uvarum*	18.1	MIC	72 h	-	2019	39
Ag NPs	*Saccharomyces uvarum*	9.8	MIC	72 h	-	2019	39
MoS$_2$-CS-Ag	*Saccharomyces uvarum*	6.8	MIC	72 h	-	2019	39
Amphotericin B (AMB)	*Saccharomyces uvarum*	2.3	MIC	72 h	-	2019	39
Voriconazole (VRC)	*Saccharomyces uvarum*	0.4	MIC	72 h	-	2019	39
Natamycin (NAT)	*Saccharomyces uvarum*	1.6	MIC	72 h	-	2019	39
MoS2-CS	*Aspergillus niger*	13.4	MIC	72 h	-	2019	39
Ag NPs	*Aspergillus niger*	7.4	MIC	72 h	-	2019	39
MoS2-CS-Ag	*Aspergillus niger*	4.2	MIC	72 h	-	2019	39
AMB	*Aspergillus niger*	1.1	MIC	72 h	-	2019	39
VRC	*Aspergillus niger*	2.6	MIC	72 h	-	2019	39
NAT	*Aspergillus niger*	0.2	MIC	72 h	-	2019	39
SWCNTs	*Fusarium graminearum*	500	MFC	3 h	>95.2%	2014	36
MWCNTs	*Fusarium graminearum*	500	MFC	3 h	85.1%	2014	36

GO	*Fusarium graminearum*	500	MFC	3 h	84.3%	2014	36
rGO	*Fusarium graminearum*	500	MFC	3 h	50%	2014	36
SWCNTs	*Fusarium poae*	500	MC	3 h	>90.8%	2014	36
MWCNTs	*Fusarium poae*	500	MFC	3 h	84.4%	2014	36
GO	*Fusarium poae*	500	MFC	3 h	82.1%	2014	36
rGO	*Fusarium poae*	500	MFC	3 h	32%	2014	36
AgNPs	*C. albicans*	40	MFC	48 h	90%	2018	55
AuNPs	*C. parapsilosis*	1	MIC	48 h	90%	2018	56
AgNPs	*C. parapsilosis*	0.5	MIC	48 h	90%	2018	56
AuAgNPs	*C. parapsilosis*	0.5	MIC	48 h	90%	2018	56
AuNPs	*C. krusei*	1	MIC	48 h	90%	2018	56
AgNPs	*C. krusei*	0.5	MIC	48 h	90%	2018	56
AuAgNPs	*C. krusei*	1	MIC	48 h	90%	2018	56
AuNPs	*C. glabrata*	1	MIC	48 h	90%	2018	56
AgNPs	*C. glabrata*	0.5	MIC	48 h	90%	2018	56
AuAgNPs	*C. glabrata*	0.5	MIC	48 h	90%	2018	56
AuNPs	*C. albicans*	2	MIC	48 h	90%	2018	56
AgNPs	*C. albicans*	0.5	MIC	48 h	90%	2018	56
AuAgNPs	*C. albicans*	0.5	MIC	48 h	90%	2018	56
ZnO NPs	*C. albicans*	1000	MFC	24 h	99.5%	2011	57
GO-AgNPs hybrid	*C. albicans*	8	MIC	24 h	-	2013	58
CNSs-AgNPs hybrid	*C. albicans*	8	MIC	24 h	-	2013	58
GO-AgNPs nanocomposite	*Fusarium graminearum*	9.37/ 4.68	MFC/MIC	3 h	99%-99.5%	2016	59
Ag@ZnO NC	*C. krusei*	250	MIC	18 h	100%	2016	60
rGO	*Aspergillus niger*	50	MIC	7 days	50%	2012	48
rGO	*Aspergillus oryzae*	100	MIC	7 days	50%	2012	48
rGO	*Fusarium oxysporum*	100	MIC	7 days	50%	2012	48
MoSe₂/CS	***F. falciforme***	**0.5**	**MIC**	**3 h**	**-**	**2020**	**This work**

MoSe$_2$/CS	C. parapsilosis	6.25/ 0.78	MFC/MIC	3 h	100%	2020	This work
MoSe$_2$/CS	A. fumigatus	12.5	MIC	3 h	-	2020	This work
MoSe$_2$/CS	C. albicans	75/ 37.5	MFC/MIC	3 h	100%	2020	This work
MoSe$_2$/CS	C. auris (0389)	150/ 50	MFC/MIC	3 h	100%	2020	This work
MoSe$_2$/CS	C. krusei (0397)	125/ 25	MFC/MIC	3 h	100%	2020	This work

Table S2. MIC of antifungal drugs against different *C. auris* strains.

ARBank Number	Species	Ampho-tericin B	Flucon-azole	Flucy-to-sine	Itracon-azole	Micafungin	Posacon-azole	Voricon-azole
386	*Candida auris*	0.5	>256	0.5	0.5	0.25	0.5	16
388	*Candida auris*	1.5	>256	0.125	0.5	0.125	0.25	2
389	*Candida auris*	4	256	128	0.25	0.25	0.125	4
394	*Candida duobushae-mulonii*		4	<0.125	0.06	0.06	0.016	0.125
396	*Kodameae ohmeri*		2	0.5	0.125	0.5	0.06	0.03
397	*Candida krusei*		64	2	1	0.125	1	1
398	*Candida lusitaniae*	0.38	1	<0.125	0.125	0.125	0.5	0.016
399	*Saccharo-myces cerevisiae*		2	<0.125	0.06	0.25	0.5	0.03

APPENDIX D

SUPPLEMENTAL MATERIAL FOR CHAPTER 5

Peroxidase-like Activity of Hafnium Diboride Nanozyme with Antibacterial Properties

Sanchari Saha,[1,2] Mahmoud Matar Abed,[1,3,+] Yuqi Guo,[1,3] Matthew S. Gilliam,[1,2] Qing Hua Wang,[3*] and Alexander A. Green[1,2,4*]

1. Biodesign Center for Molecular Design and Biomimetics, The Biodesign Institute, Arizona State University, Tempe, Arizona 85287, United States

2. School of Molecular Sciences, Arizona State University, Tempe, Arizona 85287, United States

3. Materials Science and Engineering, School for Engineering of Matter, Transport and Energy, Arizona State University, Tempe, Arizona 85287, United States

4. Department of Biomedical Engineering, Boston University, Boston, MA 02215, United States

+ Current address: The College of Science & Engineering, University of Minnesota, Minneapolis, Minnesota, United States.

* Corresponding author: alexgreen@bu.edu, qhwang@asu.edu

Table of contents

S1. Methods and supplies

Materials

Hafnium diboride powder (HfB$_2$, SKU:01542) was obtained from Smart Elements. Pluronic F68, Pluronic F68, Pluronic T1107 were obtained from BASF Corporation. Dulbecco's phosphate buffered saline (DPBS), Dulbecco's modified Eagle's medium (DMEM), phosphate buffer saline (PBS), tryptic soy broth (TSB), tryptic soy agar (TSA), Luria-Bertani (LB, Miller) medium, LB agar, 3,3,5,5-tetramethylbenzidine (TMB), o-phenylenediamine (OPD), 2,2'-azino-bis(3-ethylbenzothiazoline-6-sulphonic acid) (ABTS), di-azo-aminobenzene (DAB), 30 wt. % hydrogen peroxide solution and sodium acetate buffer solution were purchased from Sigma Aldrich. Glacial acetic acid was purchased from Thomas Scientific Holdings LLC. Human embryonic kidney 293 cells (HEK293) were purchased from ATCC. Whole red blood cells (RBCs) from a single donor were purchased from Innovative Research.

Bacterial strains

Escherichia coli (*E. coli*) MG1655 (700926) and methicillin-resistant *Staphylococcus aureus* (MRSA, BAA 1720) bacterial strains were obtained from ATCC.

S2. Preparation and characterization of HfB$_2$/F68 dispersions

HfB$_2$ Dispersion

HfB$_2$ nanoflakes were dispersed in Pluronic F68 by liquid-phase exfoliation by bath sonication in a Branson 5800 Digital Sonifier. 200 mg of HfB$_2$ powder was added to 5 ml of 3% (w/v) aqueous F68 solution, followed by bath sonication for 24 hours in ice water to avoid overheating. Then the bulk material was removed by centrifugation for 5 minutes at 5000 rcf. The mass concentration of HfB$_2$ was determined from the molar extinction coefficient obtained by inductively coupled plasma mass spectrometry (ICP-MS) and measuring absorbance at 600 nm in a Synergy H1 Hybrid Multi-Mode Reader (BioTek). Liquid dispersions for ICP-MS analysis were first acidified in nitric acid overnight and diluted to a final nitric acid concentration of 2 wt%. The samples were then analyzed by a Thermo Fisher iCap Q quadrupole instrument.

Characterization of HfB$_2$/F68

TEM samples were prepared by drop-casting 10 µl of dilute HfB$_2$/F68 dispersion on a holey carbon grid and left to dry under ambient conditions. Images were acquired on a Philips CM-12 TEM operated at 80 kV using a Gatan model 791 CCD camera. The surface area measurement on was done by measuring the thickness of 200 nanoflakes from TEM images employing ImageJ software.

HRTEM samples were prepared by drop-casting HfB$_2$/F68 dispersions onto lacey carbon grids (Cu-400LC, Pacific Grid Tech). Imaging and energy dispersive x-ray spectroscopy (EDS) analysis were performed using a FEI Titan operating at an accelerating voltage of 300 kV.

Samples for AFM imaging were prepared by spin-coating 20 µL of dispersion on a silicon substrate at 2500 rpm for one minute. This step was repeated three times. Then the sample was annealed under argon gas for three hours at 300°C to remove excess polymer and other organic residues. The images were obtained by a Bruker Multimode V AFM and processed by Gwyddion software.[42] The thickness distribution on was made by measuring the thickness of 200 nanoflakes from AFM images using Gwyddion.

S3. Catalytic activity of HfB$_2$/F68

Catalytic Activity Characterization

The peroxidase-like activity of HfB$_2$ nanozyme was studied with the colorimetric TMB substrate on 96-well plates and the absorbance of the oxidized TMB was measured with the Synergy H1 multi-plate reader at a wavelength of 652 nm.

For the optimization of nanozyme activity in terms of Pluronic F68 concentration, pH, temperature, H$_2$O$_2$ concentration and TMB concentration, just one parameter was varied at a time while the rest of the conditions were fixed, and absorbance was measured after 30 minutes of reaction. The highest absorbance was set as 100% relative activity in all the assays. The final working concentration of nanozyme was 9 µg ml^{-1} HfB$_2$ in all experiments. For the optimal pH determination, the experiment was carried out at 37 °C, 0.2 M sodium acetate buffer, 7 mM H$_2$O$_2$, 7 mM TMB, and

varying pH from pH 3.5 to 12. The relative activity at different TMB concentrations was studied at 37 ℃ with reaction mixtures of 0.2 M sodium acetate buffer at pH 4, 7 mM H_2O_2, and varying TMB concentrations from 0 mM to 20 mM. The catalytic activity at different H_2O_2 concentrations was studied at 37 ℃ with reaction mixtures of 0.2 M sodium acetate buffer at pH 4, 10 mM TMB, and varying H_2O_2 concentrations from 0 mM to 100 mM. For determining optimal Pluronic F68 concentration, the experiment was performed at 37 ℃ with F68 concentration ranging from 0.5% to 4% (w/v) in 0.2 M sodium acetate buffer at pH 4, 10 mM TMB, and 10mM H_2O_2. The optimal temperature was determined by studying different temperatures from 10 ℃ to 100 ℃ with F68 concentration ranging of 3% (w/v) in 0.2 M sodium acetate buffer at pH 4, 10 mM TMB, and 10mM H_2O_2.

Steady State Kinetics

The kinetic experiments were carried out by measuring the absorbance change with time. The initial rate velocity was determined by linear regression analysis of the change in absorbance and time on the early stage of the reaction. Then the initial velocity of the reaction and the substrate concentrations were fitted to the Michalis-Menten equation (***Equation 1***)

$$V = \frac{V_{max} \times [S]}{(K_M + [S])}$$

(1)

where V is the initial reaction rate, V_{max} is the maximum rate, K_M is the Michaelis constant, and [S] is the substrate concentration.

All the kinetic experiments were conducted with a fixed concentration of 7 μg ml^{-1} HfB$_2$ nanozyme, 0.2 M acetate buffer at pH 4 and 37℃. The kinetic parameters of TMB were determined by fixing the concentration of H_2O_2 tat10 mM. For determining H_2O_2 kinetic parameters, the concentration of TMB was fixed at 10 mM.

Reaction Mechanism

The reaction mechanism was studied with the double reciprocal plot of the initial rate velocity and substrate concentration using Lineweaver-Burk plots (***Equation 2***). These experiments were conducted with a fixed concentration of 10 μg ml^{-1} HfB$_2$ nanozyme, 3% F68, 0.2

M acetate buffer at pH 4 and 37ºC. For the double reciprocal plot of TMB, three different experiments were done having three different concentrations of H_2O_2 (1, 2 and 5 mM) and varying the concentration of TMB for each experiment. Similarly, the double reciprocal plot of H_2O_2 was obtained with three different concentrations of TMB (1 mM, 2 mM, and 5 mM).

$$\frac{1}{V} = \left(\frac{K_M}{V_{max}}\right)\left(\frac{1}{[S]}\right) + \frac{1}{V_{max}}$$

(2)

S4. Antibacterial activity of HfB$_2$/F68

Bacterial cell preparation

Cultures of *E. coli* was grown in LB medium and MRSA was grown in TSB medium for 16-18 h at 37 °C. They were then harvested to mid-exponential growth phase (optical density (OD) at 600 nm wavelength, OD_{600} = 0.33). At growth phase, cultures were centrifuged at 2500 rpm for 5 mins, and pellets were washed three times in PBS to remove dead cells. Finally, cell pellets were redispersed in 1x PBS and diluted to a cell concentration of 10^7 CFU ml^{-1}.

Measurement of minimum bactericidal concentration (MBC)

MBC values against *E. coli* and *S. aureus* bacterial strains were determined using varying concentrations of HfB$_2$/F68. Each strain at concentrations of 10^7 CFU ml^{-1} were used determined by taking OD_{600} = 0.4 while shaking at 250 rpm. 100 µl of bacteria cell was incubated with 100 µl of different concentrations of nanozyme (ranging from 0 to 15 µg ml^{-1} of HfB$_2$) at different time limit (ranging from 2 h to 5 h). After incubation, bacteria were plated in agar plates using the serial dilution method and allowed to grow overnight to enable counting of the surviving colonies. All the experiments were done in triplicate.

S5. Biocompatibility study HfB$_2$/F68

Biocompatibility of HfB$_2$/F68

The cytotoxicity of HfB$_2$/F68 toward human embryonic kidney 293 cells (HEK293) cells was determined with alamarBlue. 200 µl of cells were seeded in 96-well microplates at a density of 1 × 10^5 cells ml^{-1} in DMEM medium. After 24 h of cell attachment at 37°C in the presence of 5% CO_2,

the plates were washed with DPBS, and then various HfB$_2$/F68 concentrations (ranging from 0 to 15 µg ml^{-1} of HfB$_2$) were incubated with the mammalian cells for 24 h at 37°C in presence of 5% CO$_2$. Then, the wells were washed three times with 1x DPBS to remove any unattached cells. To check the viability of the attached cells, they were incubated with 200 µl of 10% (v%) alamarBlue solution in DMEM at 37°C in presence of 5% CO$_2$ for 5 h. The fluorescence intensity (FI 590) was measured at 530 nm (excitation) and 590 nm (emission) using a microplate reader. Cell damage was expressed as the fluorescence relative to that of DMEM medium alone as a control sample.

The percentage difference in reduction between treated and control cells in the alamarBlue cytotoxicity assay was calculated using the formula:

$$\% \, Biocompatibility = \frac{FI \, 590 \, (treated \, sample)}{FI \, 590 \, (control \, sample)} \times 100 \tag{3}$$

where, FI 590 (treated sample) and FI 590 (control sample) are the fluorescence intensity obtained at 590 nm emission and 530 nm excitation for the treated and control samples, respectively.

Hemolysis assay

Fresh single-donor human red blood cells (RBCs) were diluted 1:20 in PBS (pH 7.4), pelleted by centrifugation (1,000 rcf, 10 min), and washed three times in PBS. The RBCs were counted using a cell counter and diluted to a final concentration of 2×10^7 cells ml^{-1}. Equal volumes of RBCs were incubated with varying concentrations of HfB$_2$/F68 (ranging from 0 to 20 µg ml^{-1} of HfB$_2$) in a 96-well plate in a humidified atmosphere containing 5% CO$_2$ at 37 °C for 4 h. Following incubation, the 96-well plate was centrifuged (1,000 rcf, 10 mins) and 100 µl of supernatant was transferred to a black 96-well plate. Hemoglobin release upon lysis of the RBCs was monitored through the optical absorbance over a range of 300 to 700 nm (Abs) using a microplate reader. Positive and negative controls for hemolysis were taken as RBCs lysed with 1% Triton X (1:1 vol/vol) and RBC suspension in PBS, respectively. The percent hemolysis was plotted as a function of HfB$_2$/F68 concentration, and the experiment was performed in triplicate.

The percentage of hemolysis was calculated using the formula:

$$\% \, Hemolysis = \frac{Abs \, (treated \, sample) - Abs \, (negative \, control)}{Abs \, (positive \, control) - Abs \, (negative \, control)} \times 100 \tag{4}$$
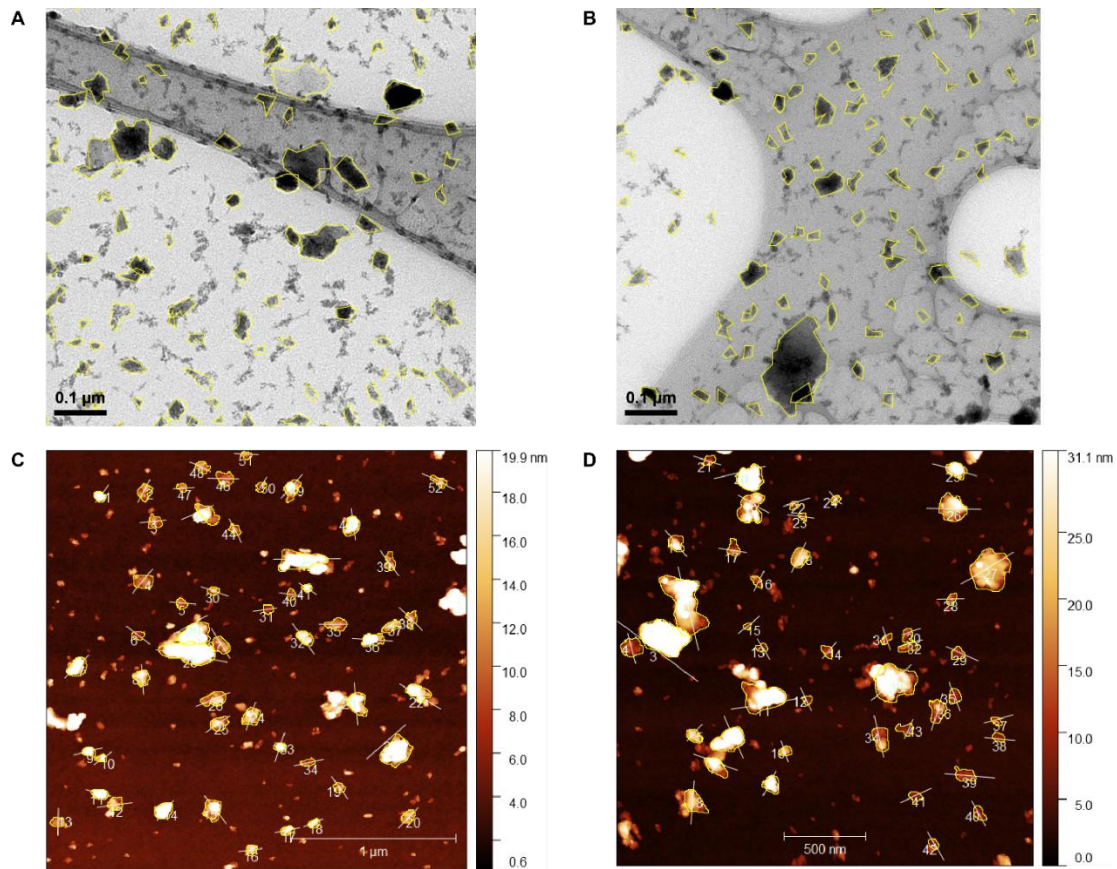
Figure S1: Size and thickness analysis of HfB$_2$/F68 nanozyme. (A, B) Examples of TEM images used for measuring the surface area of the HfB$_2$ nanoflakes. Surface area distribution was done with 500 flakes showing average area of nanoflakes is 503.30 nm^2. (C, D) Example of an AFM images used for thickness and surface area measurement of HfB$_2$ nanoflakes. Thickness distribution was obtained with 427 nanoflakes yielding 12.92 nm as the average thickness and 4000.81 nm^{2}a as the average surface area.

TMB ABTS OPD

After 3 mins

After 30 mins

10 mM 10 mM 20 mM
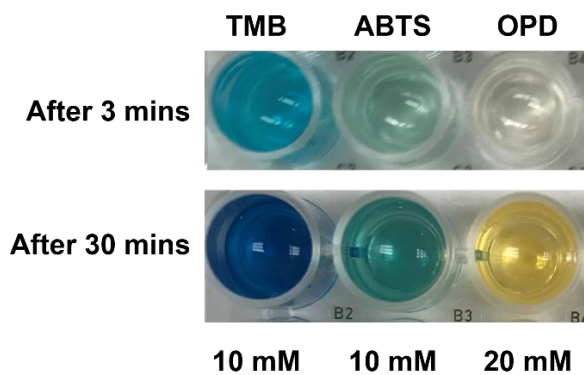
Figure S2: Screening for peroxidase-like activity of HfB$_2$/F68. Optical images taken after 3 and 30 mins of reaction with 10 μg/mL HfB$_2$/F68, 10 mM of substrate (substrate is listed above each well), and 10 mM H$_2$O$_2$ in 0.2 M acetate buffer at pH 4.

HfB$_2$/F68 Bulk HfB$_2$

After 3 mins
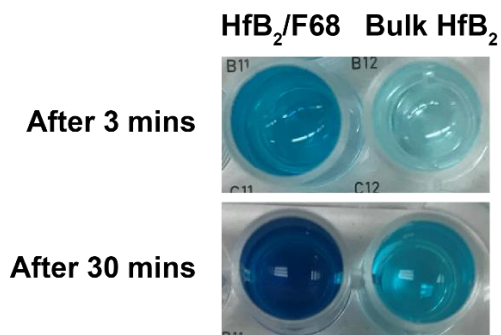
After 30 mins

Figure S3: Comparison with bulk HfB$_2$ powder. Catalytic activity of exfoliated HfB$_2$/F68 and HfB$_2$ powder were compared. Optical images taken after 3 and 30 mins of reaction with 10 μg/mL HfB$_2$/F68, 10 mM of substrate (material is listed above each well), and 10 mM H$_2$O$_2$ in 0.2 M acetate buffer at pH 4.
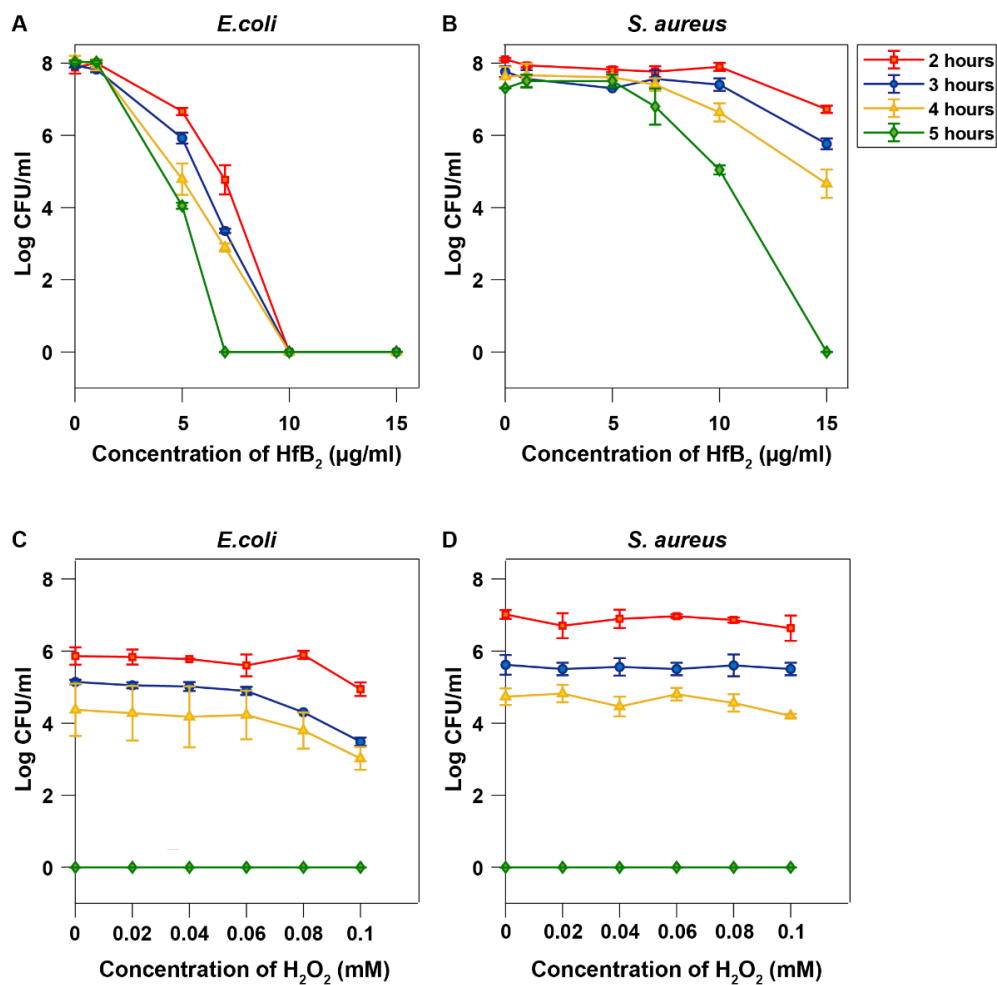
Figure S4: Antibacterial activity of HfB$_2$/F68 at different incubation times. (A) CFUs of *E. coli* after treatment with different HfB$_2$/F68 concentrations and 0.1 mM H$_2$O$_2$ at various incubation times of 2, 3, 4 and 5 h. (B) CFUs of *S. aureus* after treatment with HfB$_2$/F68 and 0.1 mM H$_2$O$_2$ concentrations at different incubation times of 2, 3, 4 and 5 h. (C) CFUs of *E. coli* after treatment with different H$_2$O$_2$ concentrations and 7 µg ml^{-1} HfB$_2$/F68 at various incubation times of 2, 3, 4 and 5 h. (D) CFUs of *S. aureus* after treatment with different H$_2$O$_2$ concentrations and 12 µg ml^{-1} HfB$_2$/F68 at various incubation times of 2, 3, 4 and 5 h.
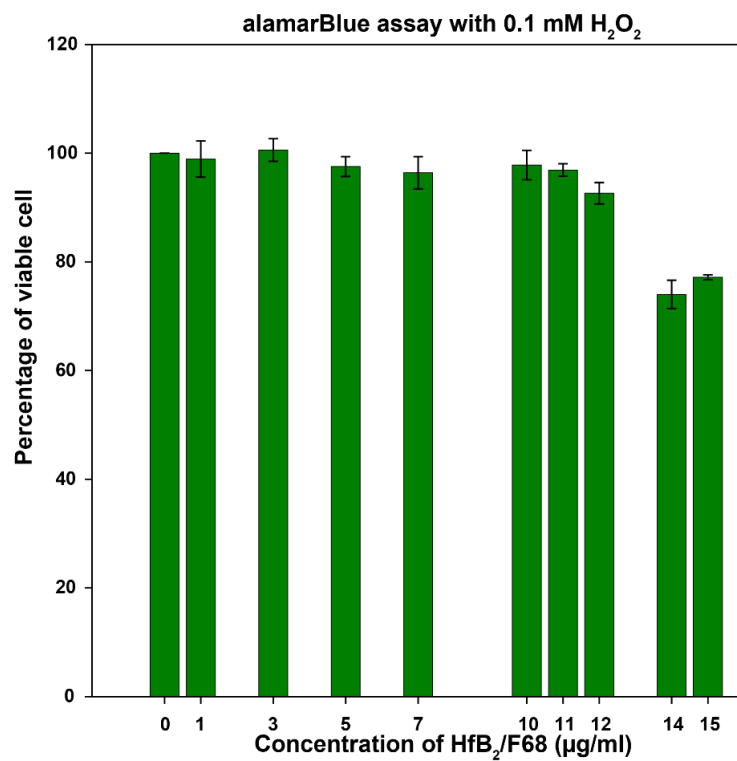
Figure S5: Biocompatibility test for HfB₂/F68 nanozyme in presence of 0.1 mM H₂O₂. Percent biocompatibility of A549 epithelial cells tested with the alamarBlue assay after incubating with different HfB₂/F68 concentrations and 0.1 mM H₂O₂. All the experiments were done in triplicate.
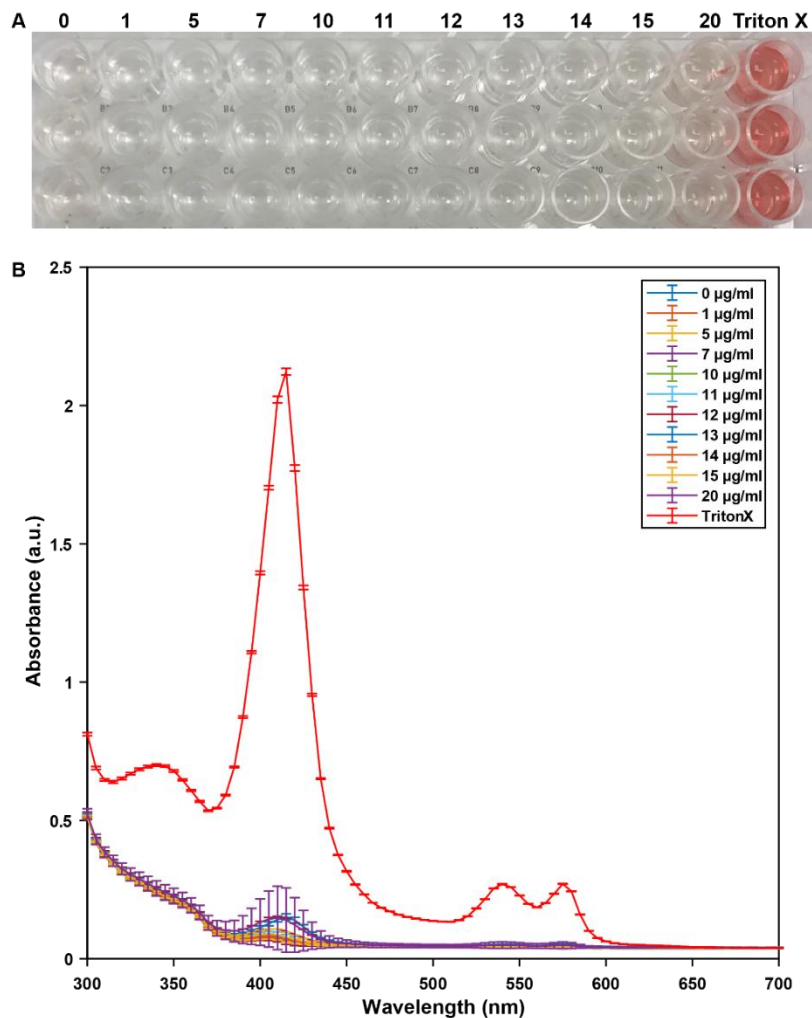
Figure S6: Hemolysis assay of HfB$_2$/F68 nanozyme. (A) Optical image of hemolysis assay to determine the toxicity of HfB$_2$/F68. (B) Spectra of samples after hemolysis assay over a range of wavelength ranging from 300 – 700 nm with different concentrations of HfB$_2$/F68. Triton X is used as the positive control against which the rest of the samples are compared. All the experiments were done in triplicate.
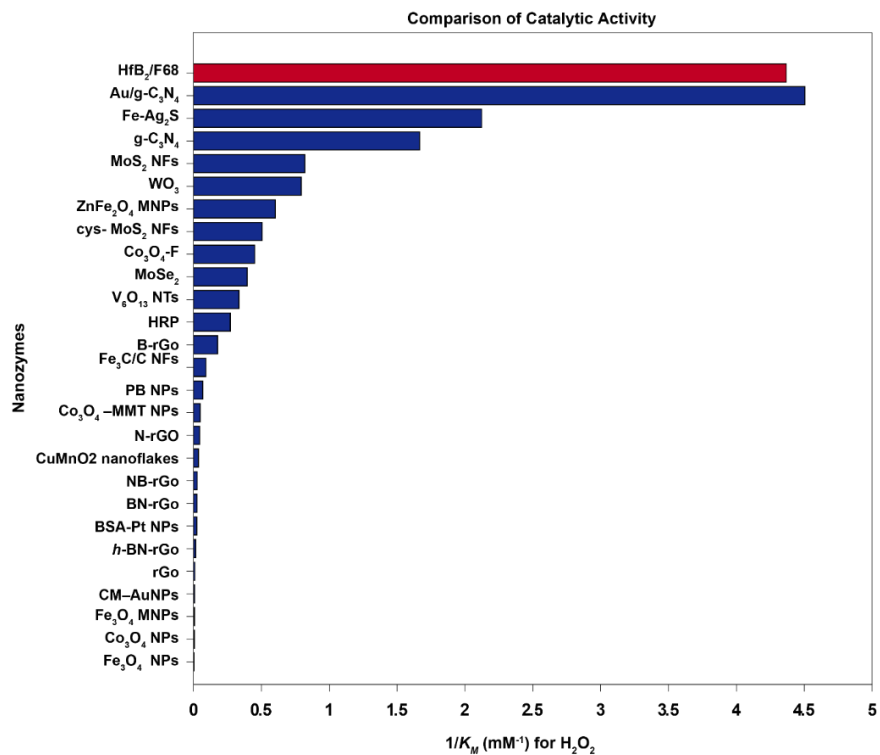
Figure S7: Affinity of catalysts for H_2O_2. The x-axis represents the reciprocal of the Michaelis constant (K_M) for H_2O_2. The higher the value, the higher the affinity of the catalyst towards H_2O_2.[1-17]
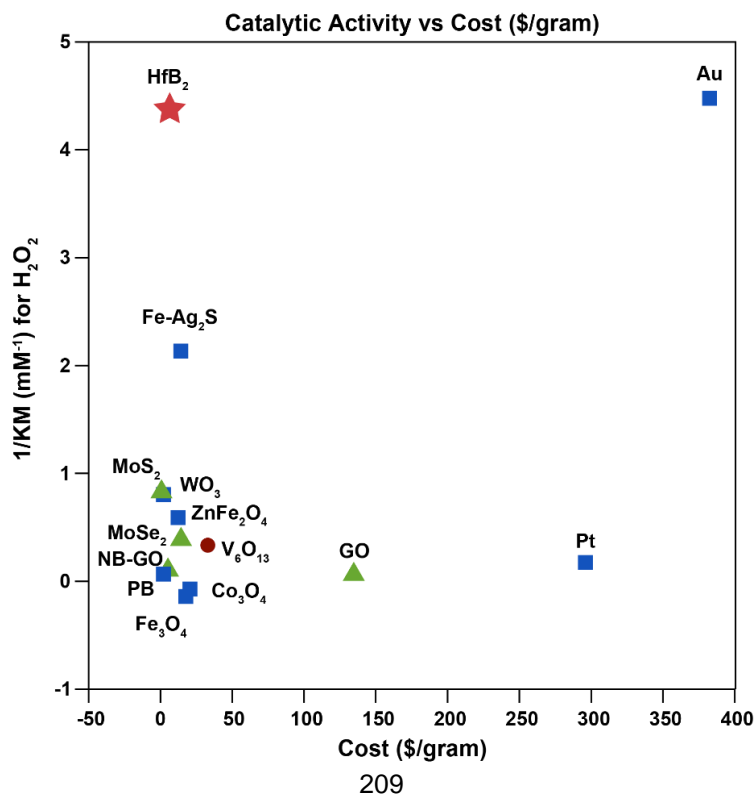
Figure S8: Catalytic performance and cost efficiency comparison of nanozymes. Relation between H_2O_2 affinity of nanozymes compared against their cost. The y-axis represents the reciprocal of the Michaelis constant (K_M) for H_2O_2 and the x-axis represents cost (\$/gram). Blue square represents nanoparticles, Brown circle represent nanofibers and green triangles represents 2D nanosheets, whereas red star represents our material HfB_2.[3-9, 11-18]

Table S1. Comparison of enzymatic efficacy of nanozymes against different fungal strains.

Nanozyme	Substrate	$1/K_M$ (mM^{-1})	K_M (mM)	V_{max} (M s^{-1})	Turnover number (K_{cat})	Year	Ref.
Ferromagnetic nanoparticles (Fe$_3$O$_4$ MNPs)	TMB	10.20	0.098	3.44×10^{-8}	3.02×10^4	2007	5
Fe$_3$O$_4$ MNPs	H$_2$O$_2$	0.006	154	9.78×10^{-8}	8.58×10^4	2007	5
ZnFe$_2$O$_4$ MNPs	TMB	1.176	0.85	13.31×10^{-8}	4.36×10^{10}	2012	11
ZnFe$_2$O$_4$ MNPs	H$_2$O$_2$	0.602	1.66	7.74×10^{-8}	2.54×10^{10}	2012	11
Cobalt oxide nanoparticle (Co$_3$O$_4$ NPs)	TMB	9.708	0.103	2.56×10^{-7}	101.19	2013	4
Co$_3$O$_4$ NPs	H$_2$O$_2$	0.005	173.51	1.89×10^{-7}	74.70	2013	4
Iron Oxide nanoparticles (Fe$_3$O$_4$ NPs)	TMB	4.291	0.233	1.76×10^{-7}	22.22	2013	4
Fe$_3$O$_4$	H$_2$O$_2$	0.002	479.91	2.75×10^{-7}	34.72	2013	4
Bovine serum albumin (BSA)-stabilized platinum (Pt) nanoparticles	TMB	8.40	0.119	21×10^{-8}	0.23	2015	9
BSA-Pt NPs	H$_2$O$_2$	0.023	41.8	16.7×10^{-8}	0.18	2015	9
Prussian blue (PB) nanoparticles	TMB	2.96	0.337	2.16×10^{-7}	1.16×10^5	2016	16

PB nanoparticles	H_2O_2	0.068	14.7	1.17×10^{-7}	5.87×10^4	2016	[16]
β-casein–gold nanoparticles (CM–AuNPs) (4.2 nm)	TMB	43.47	0.023	3.57×10^{-8}	1.42×10^{-6}	2016	[10]
CM–AuNPs (4.2 nm)	H_2O_2	0.007	130	4.05×10^{-8}	2.46×10^{-6}	2016	[10]
Ultrathin graphitic carbon nitride (g-C_3N_4)	TMB	38.31	0.0261	1.36×10^{-7}	0.125	2017	[13]
g-C_3N_4	H_2O_2	1.67	0.6	43.2×10^{-7}	4	2017	[13]
Gold nanoparticle with g-C_3N_4 (Au/g-C_3N_4)	TMB	3.38	0.295	8.6×10^{-7}	0.796	2017	[13]
Au/g-C_3N_4	H_2O_2	4.5	0.222	150.8×10^{-7}	13.96	2017	[13]
$MoSe_2$	TMB	4.61	0.2168	3.52×10^{-7}	0.357	2017	[6]
$MoSe_2$	H_2O_2	0.39	2.53	1.3×10^{-8}	0.013	2017	[6]
Co_3O_4 nanoparticles deposited on montmorillonite (Co_3O_4–MMT NPs)	TMB	462.31	0.002163	1.74×10^{-8}	0.014	2018	[17]
Co_3O_4–MMT NPs	H_2O_2	0.048	20.492	34.23×10^{-8}	0.276	2018	[17]
Porous Co_3O_4 nanoplates (Co_3O_4-F)	TMB	12.19	0.082	6.55×10^{-8}	1.57	2018	[12]
Co_3O_4-F	H_2O_2	0.45	2.22	11.82×10^{-8}	2.84	2018	[12]
Raw molybdenum disulfide nanoflakes (MoS_2 NFs)	TMB	4.54	0.22	1.37×10^{-7}	0.55×10^4	2018	[15]
MoS_2 NFs	H_2O_2	0.81	1.22	1.32×10^{-7}	0.52×10^4	2018	[15]
Cysteine (cys)- MoS_2 NFs	TMB	5.88	0.17	1.41×10^{-7}	0.56×10^4	2018	[15]
Cys- MoS_2 NFs	H_2O_2	0.50	1.98	1.52×10^{-7}	0.61×10^4	2018	[15]

Vanadium oxide nanotextiles (V_6O_{13} NTs)	TMB	6.53	0.153	1.51×10^{-8}	7.75×10^{-6}	2018	[8]
V_6O_{13} NTs	H_2O_2	0.33	2.99	3.12×10^{-8}	1.6×10^{-5}	2018	[8]
$CuMnO_2$ nanoflakes	TMB	1.733	0.577	8.15×10^{-8}	3.06×10^{-5}	2019	[2]
$CuMnO_2$ nanoflakes	H_2O_2	0.036	27.653	27.65×10^{-8}	1.04×10^{-4}	2019	[2]
Fe_3C decorated carbon nanofibers (Fe_3C/C NFs)	TMB	0.561	1.78	203.2×10^{-8}	5.49×10^{-5}	2019	[1]
Fe_3C/C NFs	H_2O_2	0.176	5.65	21.28×10^{-8}	5.75×10^{-6}	2019	[1]
Reduced graphene oxide (rGO sheets)	TMB	15.62	0.064	1.12×10^{-7}	94	2019	[7]
rGO sheets	H_2O_2	0.009	109	2.54×10^{-7}	2.12×10^2	2019	[7]
Nitrogen doped (N) rGO sheets	TMB	16.94	0.059	1.4×10^{-6}	1.17×10^3	2019	[7]
N-rGo sheets	H_2O_2	0.045	22	1.71×10^{-6}	1.43×10^3	2019	[7]
Boron doped (B) rGO sheets	TMB	1.82	0.548	5.58×10^{-6}	4.66×10^3	2019	[7]
B-rGo sheets	H_2O_2	0.09	11	2.63×10^{-6}	2.19×10^3	2019	[7]
h-BN-rGO sheets	TMB	26.31	0.038	3.80×10^{-7}	3.16×10^2	2019	[7]
h-BN-rGO sheets	H_2O_2	0.015	63	5.14×10^{-7}	4.28×10^2	2019	[7]
BN-rGO sheets	TMB	6.67	0.15	5.73×10^{-7}	4.77×10^4	2019	[7]
BN-rGO sheets	H_2O_2	0.025	39	6.01×10^{-7}	5.01×10^4	2019	[7]
NB-rGO sheets	TMB	6.71	0.149	7.87×10^{-7}	6.56×10^4	2019	[7]
NB-rGO sheets	H_2O_2	0.026	38	8.22×10^{-7}	6.85×10^4	2019	[7]
Tungsten oxide (WO_3)	TMB	100	0.01	1.53×10^{-8}	2.4×10^{-4}	2019	[18]
WO_3	H_2O_2	0.79	1.26	3×10^{-8}	4.8×10^{-4}	2019	[18]
$Fe-Ag_2S$	TMB	13.34	0.075	2.09×10^{-8}	1.81×10^{-5}	2019	[3]
$Fe-Ag_2S$	H_2O_2	2.12	0.471	37.40×10^{-8}	3.25×10^{-4}	2019	[3]
Horseradish peroxidase (HRP)	TMB	2.3	0.434	1.00×10^{-7}	4×10^4	2007	[5]

HRP	H_2O_2	2.7	3.7	8.78×10^{-8}	3.48×10^4	2007	5
HfB$_2$/F68	TMB	3.63	0.275	5.56×10^{-4}	15.90	2021	**This work**
HfB$_2$/F68	H_2O_2	4.36	0.229	3.26×10^{-4}	9.34	2021	**This work**

S7. References

1.   Chen, S.; Wang, Y.; Zhong, M.; Yu, D.; Wang, C.; Lu, X., Fe(III)-Tannic Acid Complex Derived Fe3C Decorated Carbon Nanofibers for Triple-Enzyme Mimetic Activity and Their Biosensing Application. *ACS Biomaterials Science & Engineering* **2019,** *5* (3), 1238-1246.

2.   Chen, Y.; Chen, T.; Wu, X.; Yang, G., CuMnO2 nanoflakes as pH-switchable catalysts with multiple enzyme-like activities for cysteine detection. *Sensors and Actuators B: Chemical* **2019,** *279*, 374-384.

3.   Ding, Y.; Liu, H.; Gao, L.-N.; Fu, M.; Luo, X.; Zhang, X.; Liu, Q.; Zeng, R.-C., Fe-doped Ag2S with excellent peroxidase-like activity for colorimetric determination of H2O2. *Journal of Alloys and Compounds* **2019,** *785*, 1189-1197.

4.   Dong, J.; Song, L.; Yin, J.-J.; He, W.; Wu, Y.; Gu, N.; Zhang, Y., Co3O4 Nanoparticles with Multi-Enzyme Activities and Their Application in Immunohistochemical Assay. *ACS Applied Materials & Interfaces* **2014,** *6* (3), 1959-1970.

5.   Gao, L.; Zhuang, J.; Nie, L.; Zhang, J.; Zhang, Y.; Gu, N.; Wang, T.; Feng, J.; Yang, D.; Perrett, S.; Yan, X., Intrinsic peroxidase-like activity of ferromagnetic nanoparticles. *Nature Nanotechnology* **2007,** *2* (9), 577-583.

6.   Huang, X.-W.; Wei, J.-J.; Liu, T.; Zhang, X.-L.; Bai, S.-M.; Yang, H.-H., Silk fibroin-assisted exfoliation and functionalization of transition metal dichalcogenide nanosheets for antibacterial wound dressings. *Nanoscale* **2017,** *9* (44), 17193-17198.

7.   Kim, M. S.; Cho, S.; Joo, S. H.; Lee, J.; Kwak, S. K.; Kim, M. I.; Lee, J., N- and B-Codoped Graphene: A Strong Candidate To Replace Natural Peroxidase in Sensitive and Selective Bioassays. *ACS nano* **2019,** *13* (4), 4312-4321.

8.   Li, H.; Wang, T.; Wang, Y.; Wang, S.; Su, P.; Yang, Y., Intrinsic Triple-Enzyme Mimetic Activity of V6O13 Nanotextiles: Mechanism Investigation and Colorimetric and Fluorescent Detections. *Industrial & Engineering Chemistry Research* **2018,** *57* (6), 2416-2425.

9.   Li, W.; Chen, B.; Zhang, H.; Sun, Y.; Wang, J.; Zhang, J.; Fu, Y., BSA-stabilized Pt nanozyme for peroxidase mimetics and its application on colorimetric detection of mercury(II) ions. *Biosensors & bioelectronics* **2015,** *66*, 251-8.

10.   Liu, Y.; Xiang, Y.; Ding, D.; Guo, R., Structural effects of amphiphilic protein/gold nanoparticle hybrid based nanozyme on peroxidase-like activity and silver-mediated inhibition. *RSC Advances* **2016,** *6* (113), 112435-112444.

11.   Su, L.; Feng, J.; Zhou, X.; Ren, C.; Li, H.; Chen, X., Colorimetric Detection of Urine Glucose Based ZnFe2O4 Magnetic Nanoparticles. *Analytical Chemistry* **2012,** *84* (13), 5753-5758.

12.   Wang, Q.; Chen, J.; Zhang, H.; Wu, W.; Zhang, Z.; Dong, S., Porous Co3O4 nanoplates with pH-switchable peroxidase- and catalase-like activity. *Nanoscale* **2018,** *10* (40), 19140-19146.

13.   Wang, Z.; Dong, K.; Liu, Z.; Zhang, Y.; Chen, Z.; Sun, H.; Ren, J.; Qu, X., Activation of biologically relevant levels of reactive oxygen species by Au/g-C(3)N(4) hybrid nanozyme for bacteria killing and wound disinfection. *Biomaterials* **2017,** *113*, 145-157.

14.   Yin, W.; Yu, J.; Lv, F.; Yan, L.; Zheng, L. R.; Gu, Z.; Zhao, Y., Functionalized Nano-MoS(2) with Peroxidase Catalytic and Near-Infrared Photothermal Activities for Safe and Synergetic Wound Antibacterial Applications. *ACS nano* **2016,** *10* (12), 11000-11011.

15.   Yu, J.; Ma, D.; Mei, L.; Gao, Q.; Yin, W.; Zhang, X.; Yan, L.; Gu, Z.; Ma, X.; Zhao, Y., Peroxidase-like activity of MoS2 nanoflakes with different modifications and their application for H2O2 and glucose detection. *Journal of Materials Chemistry B* **2018,** *6* (3), 487-498.

16.   Zhang, W.; Hu, S.; Yin, J.-J.; He, W.; Lu, W.; Ma, M.; Gu, N.; Zhang, Y., Prussian Blue Nanoparticles as Multienzyme Mimetics and Reactive Oxygen Species Scavengers. *Journal of the American Chemical Society* **2016,** *138* (18), 5860-5865.

17.   Zhu, X.; Chen, W.; Wu, K.; Li, H.; Fu, M.; Liu, Q.; Zhang, X., A colorimetric sensor of H2O2 based on Co3O4–montmorillonite nanocomposites with peroxidase activity. *New Journal of Chemistry* **2018,** *42* (2), 1501-1509.

18.   Li, Z.; Liu, X.; Liang, X. H.; Zhong, J.; Guo, L.; Fu, F., Colorimetric determination of xanthine in urine based on peroxidase-like activity of WO(3) nanosheets. *Talanta* **2019,** *204*, 278-284.

APPENDIX E

PERMISSIONS TO USE COPYRIGHTED MATERIALS

Geim, A. K.; Novoselov, K. S. The Rise of Graphene. *Nat. Mater.* **2007**, *6* (3), 183–191. https://doi.org/10.1038/nmat1849. Copyright © 2007, Nature Publishing Group

Zhang, F., Zhu, J., Zhang, D., Schwingenschlögl, U. and Alshareef, H.N., 2017. Two-dimensional SnO anodes with a tunable number of atomic layers for sodium ion batteries. *Nano letters*, *17*(2), pp.1302-1311. Copyright © 2017, American Chemical Society

Zhu, B., Zhang, J., Jiang, C., Cheng, B. and Yu, J., 2017. First principle investigation of halogen-doped monolayer g-C3N4 photocatalyst. *Applied Catalysis B: Environmental*, *207*, pp.27-34. © 2017 Elsevier B.V. All rights reserved.

Lloyd-Hughes, J. and Jeon, T.I., 2012. A review of the terahertz conductivity of bulk and nano-materials. *Journal of Infrared, Millimeter, and Terahertz Waves*, *33*(9), pp.871-925. Copyright © 2012, Springer Science Business Media, LLC

He, Z. and Que, W., 2016. Molybdenum disulfide nanomaterials: structures, properties, synthesis and recent progress on hydrogen evolution reaction. *Applied Materials Today*, *3*, pp.23-56. © 2016 Elsevier Ltd. All rights reserved.

Hong, W., Wyatt, B.C., Nemani, S.K. and Anasori, B., 2020. Double transition-metal MXenes: Atomistic design of two-dimensional carbides and nitrides. *MRS Bulletin*, *45*(10), pp.850-861. Copyright © 2020, The Materials Research Society

Balan, A.P., Radhakrishnan, S., Woellner, C.F., Sinha, S.K., Deng, L., de Los Reyes, C., Rao, B.M., Paulose, M., Neupane, R., Apte, A. and Kochat, V., 2018. Exfoliation of a non-van der Waals material from iron ore hematite. *Nature nanotechnology*, *13*(7), pp.602-609. Copyright © 2018, The Author(s)

Yousaf, A., Gilliam, M.S., Chang, S.L., Augustin, M., Guo, Y., Tahir, F., Wang, M., Schwindt, A., Chu, X.S., Li, D.O. and Kale, S., 2021. Exfoliation of Quasi-Two-Dimensional Nanosheets of Metal Diborides. *The Journal of Physical Chemistry C*, *125*(12), pp.6787-6799. Copyright © 2021, American Chemical Society

Han, S.A., Sohn, A. and Kim, S.W., 2017. Recent advanced in energy harvesting and storage applications with two-dimensional layered materials. *FlatChem*, *6*, pp.37-47. © 2017 Elsevier B.V. All rights reserved.

Yin, W., Yan, L., Yu, J., Tian, G., Zhou, L., Zheng, X., Zhang, X., Yong, Y., Li, J., Gu, Z. and Zhao, Y., 2014. High-throughput synthesis of single-layer MoS2 nanosheets as a near-infrared photothermal-triggered drug delivery for effective cancer therapy. *ACS nano*, *8*(7), pp.6922-6933. Copyright © 2014, American Chemical Society

Zhang, X., Wu, J., Williams, G.R., Niu, S., Qian, Q. and Zhu, L.M., 2019. Functionalized MoS2-nanosheets for targeted drug delivery and chemo-photothermal therapy. *Colloids and Surfaces B: Biointerfaces*, *173*, pp.101-108. © 2018 Elsevier B.V. All rights reserved.

Meng, S., Zhang, Y., Wang, H., Wang, L., Kong, T., Zhang, H. and Meng, S., 2020. Recent advances on TMDCs for medical diagnosis. *Biomaterials*, p.120471. © 2020 Published by Elsevier Ltd*.*

Dou, W.T., Kong, Y., He, X.P., Chen, G.R., Zang, Y., Li, J. and Tian, H., 2017. GPCR activation and endocytosis induced by a 2D material agonist. *ACS applied materials & interfaces*, *9*(17), pp.14709-14715. Copyright © 2017, American Chemical Society

Debnath, A., Saha, S., Li, D.O., Chu, X.S., Ulissi, Z.W., Green, A.A. and Wang, Q.H., 2021. Elimination of Multidrug-Resistant Bacteria by Transition Metal Dichalcogenides Encapsulated by Synthetic Single-Stranded DNA. *ACS Applied Materials & Interfaces*, *13*(7), pp.8082-8094. Copyright © 2021, American Chemical Society

Wang, X., Li, T., Ma, H., Zhai, D., Jiang, C., Chang, J., Wang, J. and Wu, C., 2017. A 3D-printed scaffold with MoS 2 nanosheets for tumor therapy and tissue regeneration. *NPG Asia Materials*, *9*(4), pp.e376-e376. Copyright © 2017, The Author(s)

Huang, Y., Ren, J. and Qu, X., 2019. Nanozymes: classification, catalytic mechanisms, activity regulation, and applications. *Chemical reviews*, *119*(6), pp.4357-4412. Copyright © 2019, American Chemical Society

Gao, L., Zhuang, J., Nie, L., Zhang, J., Zhang, Y., Gu, N., Wang, T., Feng, J., Yang, D., Perrett, S. and Yan, X., 2007. Intrinsic peroxidase-like activity of ferromagnetic nanoparticles. *Nature nanotechnology*, *2*(9), pp.577-583. Copyright © 2007, Nature Publishing Group

Zu, Y., Yao, H., Wang, Y., Yan, L., Gu, Z., Chen, C., Gao, L. and Yin, W., 2021. The age of bioinspired molybdenum-involved nanozymes: Synthesis, catalytic mechanisms, and biomedical applications. *View*, p.20200188. © 2021 The Authors. VIEW published by John Wiley & Sons Australia, Ltd and Shanghai Fuji Technology Consulting Co., Ltd, authorized by Professional Community of Experimental Medicine, National Association of Health Industry and Enterprise Management (PCEM)